



**University of  
Nottingham**  
UK | CHINA | MALAYSIA

# **Development and characterization of a protein based mineralizing bio-ink**

Thesis submitted to the University of Nottingham for the degree of  
**Doctor of Philosophy, March 2023**

Author

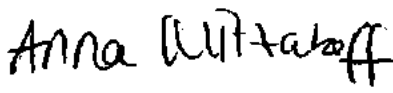
**Anna Marie-Thérèse Mitzakoff**

Supervised by

**Ricky Wildman**

**Derek Irvine**

**Alvaro Mata**

Signature: 

Submission date, original version: 28/03/2023

Submission date, corrected version: 04/03/2024

## **Acknowledgements**

I would like to thank my supervisors, Prof. Ricky Wildman, Prof. Derek Irvine, Prof. Alvaro Mata and Dr. Laura Ruiz Cantu for their advice and guidance. Their knowledge and experience have allowed me to broaden my knowledge in a multidisciplinary environment and allowed me to gain confidence in a chemical laboratory environment in a way that I had not experienced priorly.

I would also like to especially thank Dr. Abshar Hasan for the in-depth exchange of knowledge and for training me on a variety of instruments and methods related to my research. For the methodical recommendations and conduction of X-Ray diffraction experiments, I would like to thank Dr. Hannah Constantin. Furthermore, I would like to thank my colleagues who have become close friends, Maria Inês Evangelista Barreiros, Kevin Bandeira and Kristian Plender, not only for all the work-related brain storming, but also making my PhD- and Nottingham experience special.

I also want to thank the ESPRC for the provided funding, as well as the dedicated researchers and workers at Technical Proteins Nanobiotechnology, Valladolid, Spain, who have supplied me with the key material for my work and were always happy to answer questions and took the time to discuss research related matters with me.

Finally, I would like to express my gratitude to parents and my partner Laurie for the emotional support. I am immensely grateful for their encouragement and understanding, which has made it possible for me to complete my studies and built up my confidence tremendously.

## **Achievements**

### **Publications**

- Harry J. Harvey, Anna M. T. Mitzakoff, Ricky D. Wildman, Sacha J. Mooney, Simon V. Avery, 'Microbial Metal Resistance within Structured Environments is Inversely Related to Environmental Pore Size' in the Applied and Environmental Microbiology Journal.  
Full citation: Applied and Environmental Microbiology Journal 87(20), e01005-21 (2021) DOI: <https://doi.org/10.1128/AEM.01005-21>

### **Poster presentations**

- 2022, Advanced Functional Polymers for Medicine, Nice, France, 'Development of a 3D-printable polypeptide gel for bone regeneration'
- 2022, International Conference for Biofabrication, Pisa, Italy, 'A mineralizing bioink'
- 2022, University of Nottingham, Pharmacy School Research Day, 'Development of a 3D-printable polypeptide gel for bone regeneration'
- 2022, University of Nottingham, Biodiscovery Institute Research Day, 'Development of a 3D-printable polypeptide gel for bone regeneration'

### **Oral Presentations**

- 2022, Advanced Materials Research Group Showcase 3MT competition, Development of a 3D-printable gel for bone regeneration
- 2022, Engineering Research Showcase 3MT competition, Development of a 3D-printable gel for bone regeneration
- University wide 3MT competition, A novel approach to complex bone fracture therapy

### **Awards**

- Winner of the Advanced Materials Research Group Showcase 3MT competition
- Winner of the Engineering Research Showcase 3MT competition

## **i. Abstract**

Despite the outstanding mechanical properties of human bone, bone fractures to this day impose a challenge on bone repair therapy. In regenerative medicine, tissue engineering has gained increasing interest for the synthesis of biologically derived tissues. For bone synthesis, tissue engineering uses so-called scaffolds which mimic the structural bone environment. 3D-printing is a popular option for the fabrication of these complex scaffolds. Whilst some methods rely on the interplay between biological components and structurally distinct scaffolds, which can trigger osteogenesis, other methods explore the development of novel materials that can be processed to mimic the structural and mechanical properties of human bone. However, challenges such as biocompatibility, mechanical strength, and resolution, remain. Therefore, the development of biocompatible materials, which can exhibit desired biological and mechanical properties once processed into scaffolds, is crucial to satisfy the unmet needs in bone regeneration therapy research.

Previous studies show improvements with respect to biocompatibility and osteoinductivity of bone tissue engineering scaffolds through the synthesis of biomineralized scaffolds. A popular choice in the selection of biomaterials suitable for these scaffolds is Hydroxyapatite. However, three-dimensional scaffolds produced from pure Hydroxyapatite are highly brittle, making them unsuitable for load bearing applications. Through the development of composite materials, which integrate a polymeric phase into these inorganic constructs, the materials' durability can be enhanced. Even though this approach has improved the mechanical performance of mineralized scaffolds, issues such as interfacial bonding between the phases remain. Hence, the clinical need for the establishment of suitable biomaterials for bone tissue engineering remains. Polypeptides have been found to play a crucial role in biomineralization. In previous work, polypeptide-based membranes have been synthesized. The used polypeptide sequence can undergo stimuli triggered self-assembly that can template the growth of hierarchically mineralized structures that can exhibit the same mechanical properties as bone.

In this thesis, this proposed platform was extended to enable the controlled extrusion of shapely filaments that could undergo hierarchically structured biomineralization. The work ranged from formulation development and optimization to material characterization and process integration into an automated extrusion system. Two novel formulations were processed into membrane- and gel configurations. Control strategies were developed to understand parameters that contribute to self-assembly of the integrated polypeptide sequence. Furthermore, a mechanism that triggers biomineralization in the presented formulations was proposed. Two-dimensional grid structures were successfully printed. However, the rheological properties of the established bio inks were not fully understood, and further work is required to optimize the choice of print substrate.

# Table of contents

<b>I. ABSTRACT .....</b>	<b>3</b>
<b>II. LIST OF FIGURES.....</b>	<b>8</b>
<b>III. LIST OF TABLES.....</b>	<b>22</b>
<b>IV. LIST OF ACRONYMS AND ELEMENTS .....</b>	<b>23</b>
<b>1. INTRODUCTION .....</b>	<b>25</b>
1.1. HUMAN BONE.....	25
1.1.1. Chemical composition of human bone .....	26
1.1.2. Structural composition of human bone.....	28
1.1.3. History and challenges in bone defect repair .....	29
1.2. BIOMATERIALS IN BONE REGENERATION THERAPY .....	30
1.2.1. Classification of biomaterials .....	30
1.2.1.1. Bioactive biomaterials.....	31
1.2.1.2. Bioinert biomaterials.....	32
1.2.1.3. Biotolerant biomaterials .....	33
1.2.1.4. Biodegradable biomaterials .....	33
1.2.2. Biocompatibility assessment methods.....	34
1.2.3. Mechanical biocompatibility assessments .....	41
1.3. STATE-OF-THE-ART BONE TISSUE ENGINEERING .....	47
1.3.1. Conventional bone tissue engineering scaffold fabrication methods.....	49
1.3.1.1. Solvent casting and particulate leaching (SCPL) .....	49
1.3.1.2. Thermally induced phase separation (TIPS) .....	50
1.3.1.3. Freeze-drying.....	51
1.3.1.4. Sol-Gel Method .....	52
1.3.1.5. Gas foaming .....	53
1.3.1.6. Electrospinning.....	54
1.3.2. Additive Manufacturing techniques for bone tissue engineering .....	56
1.3.2.1. VAT polymerization (SLA-printing).....	57
1.3.2.2. Material jetting .....	58
1.3.2.3. Binder jetting .....	59
1.3.2.4. Powder bed fusion.....	60
1.3.2.5. Material extrusion.....	61
1.3.3. Common materials in tissue engineering scaffold fabrication .....	70
1.3.3.1. Metals in bone tissue engineering scaffold fabrication .....	70
1.3.3.2. Ceramics in bone tissue engineering scaffold fabrication .....	72
1.3.3.3. Polymers in bone tissue engineering scaffold fabrication .....	73
1.4. ELASTIN LIKE POLYPEPTIDES IN TISSUE ENGINEERING APPLICATIONS .....	77
1.4.1. Supramolecular self-assembly .....	78
1.4.1.1. Protein secondary structure.....	80

1.4.1.2.	Protein secondary structure analysis.....	83
1.4.2.	SN <sub>A</sub> 15 elastin like polypeptides in hard tissue engineering applications.....	86
1.4.2.1.	Optical and polarized light microscopy .....	92
1.4.2.2.	Scanning electron microscopy .....	93
1.4.2.3.	X Ray Diffraction .....	94
1.5.	AIMS AND OBJECTIVES.....	96
<b>2.</b>	<b>MATERIALS AND METHODS .....</b>	<b>98</b>
2.1.	MATERIALS.....	98
2.1.1.	SN <sub>A</sub> 15 ELP sequence .....	98
2.1.2.	Organic solvents .....	98
2.1.3.	Cross-linking agents.....	99
2.2.	METHODS .....	100
2.2.1.	Fourier transform infrared spectroscopy.....	100
2.2.2.	Assessment of sample shrinkage/swelling.....	101
2.2.3.	Preparation of biomineralization solution.....	102
2.2.4.	Optical light microscopy and polarized light microscopy .....	102
2.2.5.	Scanning electron microscopy .....	102
2.2.6.	X-Ray diffraction.....	103
2.2.7.	Plunger-based material extrusion.....	103
<b>3.</b>	<b>NOVEL MATERIAL FORMULATIONS FOR SN<sub>A</sub>15 ELP BASED SAMPLES .....</b>	<b>104</b>
3.1.	PROTEIN SECONDARY STRUCTURE FORMATION IN PMDI-ELP GELS .....	105
3.1.1.	PMDI-ELP gel synthesis .....	105
3.1.2.	Identification of supramolecular protein secondary structure formation triggers in PMDI-ELP gels.....	110
3.1.2.1.	Protein secondary structure in contained PMDI-ELP gel.....	111
3.1.2.2.	Protein secondary structure in cross-linked PMDI-ELP gels .....	112
3.1.2.3.	Investigation of gel shrink capacity.....	117
3.2.	PROTEIN SECONDARY STRUCTURE FORMATION IN GENIPIN-ELP GELS.....	119
3.2.1.	Identification of protein secondary structure formation triggers in genipin-ELP gels...	119
3.2.1.1.	Protein secondary structure in contained genipin-ELP gel.....	120
3.2.1.2.	Protein secondary structure in cross-linked genipin-ELP gels .....	121
3.3.	CHARACTERIZATION OF ELP-BASED MEMBRANES .....	124
3.3.1.	PMDI-ELP membrane characterization .....	125
3.3.1.1.	Protein secondary structure analysis of PMDI-ELP membranes .....	127
3.3.1.2.	Investigation of PMDI-ELP membrane swell capacity.....	130
3.3.2.	Genipin-ELP membrane characterization.....	131
3.3.2.1.	Protein secondary structure analysis of genipin-ELP membranes .....	131
3.3.2.2.	Investigation of genipin-ELP membrane swell capacity.....	135
3.3.3.	HDI-ELP membrane characterization .....	136
3.3.3.1.	Protein secondary structure analysis of HDI-ELP membranes.....	136

3.3.3.2.	Investigation of HDI-ELP membrane swell capacity .....	137
3.4.	SUMMARY .....	138
<b>4.</b>	<b>BIOMINERALIZATION AND UNDERLYING FORMATION MECHANISM IN ELP BASED MEMBRANES.....</b>	<b>139</b>
4.1.	OPTICAL GEOMETRY ASSESSMENT OF UNMINERALIZED ELP MEMBRANES.....	139
4.1.1.	Polarized light microscopy on PMDI and genipin cross-linked ELP membranes.....	140
4.1.2.	Scanning electron microscopy on unmineralized ELP membranes.....	140
4.1.2.1.	SEM imaging of unmineralized HDI-ELP membranes.....	140
4.1.2.2.	SEM imaging of unmineralized PMDI-ELP membranes.....	141
4.1.2.3.	SEM imaging of unmineralized genipin-ELP membranes .....	142
4.2.	BIOMINERALIZATION ASSESSMENT IN PMDI- AND GENIPIN-ELP MEMBRANES .....	144
4.2.1.	Optical imaging of mineralized ELP membranes .....	144
4.2.1.1.	Optical microscopy on mineralized HDI-ELP membranes .....	144
4.2.1.2.	Optical microscopy on mineralized PMDI-ELP membranes .....	145
4.2.1.3.	Optical microscopy on mineralized genipin-ELP membranes.....	145
4.2.2.	SEM imaging of mineralized ELP membranes .....	146
4.2.2.1.	SEM imaging of mineralized HDI-ELP membranes .....	146
4.2.2.2.	SEM imaging of mineralized PMDI-ELP membranes.....	149
4.2.2.3.	SEM imaging of mineralized genipin-ELP membranes.....	151
4.2.3.	Crystallographic assessment of mineralized ELP membranes <i>via</i> X-Ray diffraction ...	154
4.3.	UNDERSTANDING THE BIOMINERALIZATION MECHANISM IN PMDI- AND GENIPIN-ELP MEMBRANES .....	157
4.3.1.	Mineralization mechanism in genipin-ELP membranes.....	157
4.3.2.	Mineralization mechanism in PMDI-ELP membranes.....	163
4.3.3.	Summary of the mineralization mechanism in PMDI- and genipin-ELP membranes...	164
4.4.	SUMMARY .....	166
<b>5.</b>	<b>3D-PRINTING OF ELP-BASED CONSTRUCTS.....</b>	<b>167</b>
5.1.	PRELIMINARY EXPERIMENTS – PMDI-ELP GEL EXTRUSION .....	167
5.1.1.	Manual 0.3% PMDI 4% ELP gel extrusion.....	168
5.1.2.	Automated material extrusion of PMDI-ELP gel.....	171
5.1.2.1.	PMDI-ELP gel printability assessment.....	173
5.1.2.2.	Post-processing and assessment of shape maintenance in PMDI-ELP prints.....	174
5.1.2.3.	Assessment of biomineralization ability in 3D-printed PMDI-ELP samples.....	179
5.2.	CONCLUDING EXPERIMENTS – GENIPIN-ELP GEL EXTRUSION .....	181
5.2.1.	Printability assessment – 0.5 wt% genipin 4% ELP gel .....	182
5.2.1.1.	Post-processing of 0.5 wt% genipin 4% ELP prints .....	186
5.2.1.2.	Assessment of biomineralization ability in 0.5 wt% genipin 4% ELP prints .....	188
5.2.2.	Printability assessment of 1.0 wt% genipin 4% ELP gel.....	188
5.2.2.1.	Protein secondary structure analysis on 1.0 wt% genipin 4% ELP filaments.....	189
5.2.2.2.	Printability assessment – 1.0 wt% genipin 4% ELP gel.....	190

5.2.2.3.	Print accuracy in two-dimensional 1.0 wt% genipin 4% ELP grid structures .....	191
5.2.2.4.	Assessment of biomineralization ability in 1.0 wt% genipin 4% ELP prints .....	198
5.2.2.5.	3D-printing of 1.0 wt% genipin 4% ELP grid structures .....	200
5.3.	SUMMARY .....	201
<b>6.</b>	<b>CONCLUSION AND FUTURE WORK.....</b>	<b>202</b>
<b>V.</b>	<b>REFERENCES.....</b>	<b>207</b>
<b>VI.</b>	<b>APPENDICES .....</b>	<b>215</b>
	APPENDIX A .....	215
	APPENDIX B .....	216
	APPENDIX C .....	265
	APPENDIX D .....	266

## ii. List of figures

<b>Figure 1.1:</b> Pie chart representing the chemical composition of human bone, which can be divided into organic and inorganic materials, as well as water [2][5]. .....	26
<b>Figure 1.2:</b> Schematic of hierarchical bone structure, modified from [2]. .....	29
<b>Figure 1.3:</b> Depiction of biomaterial classifications. (A) Bioactive materials trigger biophysical and biochemical reactions between the surrounding tissue and the implant, leading to a mechanically strong chemical bond between the two components. (B) Bioinert materials get encapsulated by fibrous tissue, leading to isolation from the surrounding bone. (C) Biotolerant materials release corrosion products, chemical compounds, and ions, leading to the formation of fibrous tissue around the implant. (D) Biodegradable materials dissolve upon reaction with body fluids. ....	31
<b>Figure 1.4:</b> Flow chart depicting the four steps of biocompatibility testing. (A) Step I: Material development and characterization, (B) Step II: <i>In vitro</i> testing, (C) Step III: <i>In vivo</i> animal testing, (D) Step IV: Clinical human trials. ....	35
<b>Figure 1.5:</b> Schematic of flow cytometry principle, wherein (A) (dyed) cells in suspension are hydrodynamically focused and directed in an axial manner in a narrow stream, where they perpendicularly interact with a laser. (B) As the laser interacts with the single cells, the light is excited and scattered forwards and sideways, depending on the cells characteristics. ....	39
<b>Figure 1.6:</b> Schematic of multiple colour flow cytometry, showing how dichroic mirror filters separate specific wavelengths to capture the fluorescence emitted from cells at specific wavelengths, before they are directed towards photomultiplier tubes, which can also detect side scatter. A separate detector detects forward scatter. ....	40
<b>Figure 1.7:</b> Schematic of tensile strength testing, showing a sample clamped between two holding grips and pulled at a specific force until fracture occurs. (B) Typical stress-strain curves for three classes of materials. ....	42
<b>Figure 1.8:</b> Schematic of compression strength testing wherein a rectangular or cylindrical sample is compressed between two parallel plates in an axial manner. ....	42
<b>Figure 1.9:</b> Schematic of nanoindentation, where a pyramidal or spherical probe is indented under a continuously increased load ( $P$ ), until a predetermined level is reached ( $h_{max}$ ). Once the probe is removed, a residual impression ( $h_f$ ) remains on the sample surface. (B) The nanoindentation graph is comprised of a displacement axis (x-axis) which represents the probe displacement over the course of sample penetration. The y-axis displays the load applied on probe, which increases as the sample is penetrated. ....	43
<b>Figure 1.10:</b> Schematic of dynamic mechanical analysis, where a sample is positioned onto a stationary base as a force is applied to a moveable clamp, that applies a controlled strain. ....	45
<b>Figure 1.11:</b> Relationship between storage modulus ( $E'$ ), loss modulus ( $E''$ ) and dynamic modulus ( $E^*$ ), modified from [64] .....	46
<b>Figure 1.12:</b> Bone TE approach schematic, showing how cells and biological components are seeded into a bone TE scaffold before it is exposed to external stimuli that induce osteogenesis in a bioreactor	

or using a different cell culturing technique. Thereafter, the ossified scaffold is inserted into the damaged site to achieve recovery.....	48
<b>Figure 1.13:</b> Schematic of SCPL, wherein porogen is dispersed in a polymer-solvent solution. After the solvent is evaporated, the resulting matrix is immersed in a suitable porogen solvent, leading to porogen leaching and forming a porous network. Modified from [2]. .....	49
<b>Figure 1.14:</b> Schematic of temperature induced phase separation, wherein an initially stable polymeric solution is separated into a polymer-rich and a polymer-deficit phase <i>via</i> low temperature thermally induced phase separation. The fabrication of a porous structure is achieved through solvent evaporation. Modified from [2].....	50
<b>Figure 1.15:</b> Schematic of freeze drying, wherein an emulsion of water and polymer solution is mould-casted and thereafter freeze-dried to enable sublimation/evaporation of solid/liquid solvent phases to form a polymeric porous structure. ....	51
<b>Figure 1.16:</b> Schematic of sol-gel fabrication method, wherein (A) a sol is synthesized which forms a (B) gel through hydrolysis and condensation reactions. Depending on the desired final morphology, supercritical drying can be applied to achieve the formation of an (C) aerogel. Alternatively, slow evaporation can achieve the formation of a (D) xerogel, which can be processed to obtain sol-gel particles. ....	52
<b>Figure 1.17:</b> Schematic of sol-gel fabrication method for sol-gel foam scaffolds, wherein (A) a surfactant is added to the synthesized sol. (B) As the solution undergoes the sol-gel transition, it is poured into a mold that possesses the desired scaffold morphology. (C) By drying the molded structure, a solid scaffold can be obtained. ....	53
<b>Figure 1.18:</b> Schematic of gas foaming, wherein polymer discs are subjected to high-pressure <i>via</i> saturation with inert gas, causing the formation of foam. As the pressure drops, phase separation is induced, resulting in a porous structure.....	53
<b>Figure 1.19:</b> Schematic of electrospinning, wherein polymer solution is fed through a capillary tube, as high voltage is used to induce polarity to accelerate polymer filaments from the tip of a syringe to direct them towards a fibre collector. ....	54
<b>Figure 1.20:</b> Pie chart depicting the contribution of AM to different industries and fields of research [77]. ....	56
<b>Figure 1.21:</b> VAT polymerization printing schematic, showing laser beams curing photo polymeric resin in a VAT in a layer-by-layer fashion as the build platform moves in z-direction after each material layer is cured.....	57
<b>Figure 1.22:</b> Schematic of a regular inkjet printing system, wherein a piezoelectric actuator generates a pressure pulse to eject fluid droplets in a controlled manner onto a substrate. <i>Via</i> coordination between the motion system and actuator electronics, deposition of custom printed patterns can be achieved [84]. ....	58
<b>Figure 1.23:</b> Schematic of binder jetting 3D printing, showing a powder spreader distributing the material of choice across the powder build platform in an even manner. Thereafter, an inkjet printhead deposits binder droplets into distinct positions in a bed of powdered material to fuse the desired part. The print	

head is led by a X-Y positioning system, whilst the three-dimensionality of the fabricated part is achieved through movement of the build platform in Z-direction, modified from [88].	59
<b>Figure 1.24:</b> Schematic of PDF, wherein a powder roller evenly spreads loose powder material from the powder stock onto the powder bed. A thermal source, repeatedly traces the 2D-geometry of an individual layer of the desired 3D-model, forming the 3D-part in a layer-by-layer fashion [92].	60
<b>Figure 1.25:</b> Schematic of (A) plunger-based material extrusion: A plunger pushes extrudable feedstock through a nozzle through axial movement in Z-direction. (B) Filament-based material extrusion: a motor and bearing wheel rotate in opposite directions to push a filament through the container and a heated nozzle to melt the feedstock. (C) Screw-based material extrusion: A screw, driven by a motor, rotates around its own axis to feed pellets to the nozzle tip. In all processes, the material is in a liquid state when it exits the nozzle and transforms to a solid state once it is deposited onto the substrate to allow layer-by-layer fabrication [94].	61
<b>Figure 1.26:</b> Depiction of transition stages experienced during ME. (1) After extrusion is induced by applying appropriate forces onto the material stored in a cartridge (2) different velocities and shear stresses are exhibited onto the material as it passes through the nozzle. (3) Thereafter, the material undergoes recovery to achieve the fabrication of 3D constructs.	63
<b>Figure 1.27:</b> Flow chart depicting the categorization of fluid behaviour into Newtonian and Non-Newtonian.	64
<b>Figure 1.28:</b> Graph showing how the viscosity of non-Newtonian time-dependent fluids changes over time under application of a constant shear rate, whereas the viscosity of non-Newtonian time-independent fluids remains constant under such conditions.	65
<b>Figure 1.29:</b> Stress and strain wave relationships for purely (A) elastic, (B) viscoelastic and (C) viscous material.	66
<b>Figure 1.30:</b> Graph showing the relationship between viscosity and shear rate in different types of fluids (Newtonian and non-Newtonian) [102].	67
<b>Figure 1.31:</b> Three different stages of rheological bio ink evaluation (1) flow initiation (2) study of viscoelastic and thixotropic behaviour, (3) post-printing recovery assesses the materials viscosity recovery time.	67
<b>Figure 1.32:</b> Structural composition of a micelle, consisting of surfactant molecules with a hydrophilic head and a hydrophobic tail.	79
<b>Figure 1.33:</b> Ionic bonding in sodium chloride, wherein the donation of a sodium (Na) electron to chlorine (Cl) results in a positive Na <sup>+</sup> cation and a negative Cl <sup>-</sup> anion, forming a stable ionic bond. ....	79
<b>Figure 1.34:</b> Hydrogen bonding caused by intermolecular interactions between hydrogen (H) and oxygen (O), forming water (H <sub>2</sub> O).	80
<b>Figure 1.35:</b> Structural organization of a typical $\alpha$ -helix, wherein in the hydrogen bonds are represented as dotted lines between the residues n and n+4.	81
<b>Figure 1.36:</b> Structural organization of $\beta$ -pleated sheets, wherein H-bonds connect two or more polypeptide chains ( $\beta$ -strands). H-bonds are oriented perpendicularly to the polypeptide backbones. ...	82

**Figure 1.37:** Depiction of parallel vs. antiparallel orientation  $\beta$ -strands. (a) Parallel orientation:  $\beta$ -strands run in the same N- to C-terminal, as indicated by the arrows. (b) Antiparallel orientation:  $\beta$ -strands run in opposite N- to C-terminal direction, as indicated by the arrows. .... 82

**Figure 1.38:** Schematic of FTIR spectroscopy, wherein IR light is passed through the sample of interest, which causes molecules in the sample to vibrate. The amount of absorbed IR light at specific wavelengths is measured to create a spectral fingerprint of the sample which is represented in the FTIR spectrum.. 83

**Figure 1.39:** (A) Depiction of polarized light, wherein the vector of polarized light rotates in one plane as it passes through the sample. (B) Depiction of circularly polarized light which propagates at a constant amplitude whilst penetrating the sample. (C) Electric field vector of circularly polarized light, rotating clockwise ( $E_R$ ) and counter clockwise ( $E_L$ ) at different amplitudes and thereby creating elliptically polarized light, wherein angle alpha represents the optical rotation of the plane of polarization as light interacts with material with chiral properties. Modified from below [139] ..... 85

**Figure 1.40:** HDI-ELP membrane fabrication method, where ELP was dissolved in solvent mixture and subsequently HDI was added *via* pipetting before drop casting the HDI-ELP solution on PDMS. The far-right image shows a transparent, flexible HDI-ELP membrane that formed after overnight cross-linking in a low humidity glovebox environment. Scale bar: 500  $\mu\text{m}$ . .... 87

**Figure 1.41:** (A) Biomineralized HDI-ELP membrane (B) Optical microscopy image and (C) SEM image of biomineralized structures on the membrane surface. (D) SEM image of fluorapatite (FAP) nanocrystals in the membrane cross-section. (D) XRD results showing peak regions overlap with FAP control group (modified from [140]). Scale bars: (A): 500  $\mu\text{m}$ , (B): 20  $\mu\text{m}$ , (C): 5  $\mu\text{m}$ , (D): 250 nm. .. 87

**Figure 1.42:** SEM images depicting the resemblance between (A) nanocrystals present in enamel (image modified from [148]) and (B) nanocrystals in biomineralized ELP membranes. Scale bars: 250 nm.... 88

**Figure 1.43:** Illustration of the hierarchical structure of human dental enamel, wherein hydroxyapatite (HAP) nanocrystals bundle *via* proteins to form nanofibers that assemble to enamel rods. The 2 mm thick enamel layer is composed of multiple enamel rods. This hierarchical structure enables the strong mechanical properties in enamel [149]..... 88

**Figure 1.44:** Macroscale SEM images of (A) characteristic enamel rods, that are composed of nanocrystals. The shown SEM image was modified from [148]. (B) The formation of rods composed of nanocrystals was equally observed in biomineralized HDI-ELP membranes. Scale bars: 20  $\mu\text{m}$ ..... 89

**Figure 1.45:** Mechanical properties (hardness and young's modulus) of mineralized structures in HDI-ELP membranes in comparison with mineralized tissue in the human body. .... 90

**Figure 1.46:** Polarized light microscopy image of unmineralized HDI-ELP membrane, showing the presence of cross-patterned structures (organic spherulites). Scale bar: 3  $\mu\text{m}$ . Modified from [140] .... 91

**Figure 1.47:** Visualization of biomineralization mechanism in HDI-ELP membranes, proposing that organic spherulites, function as nuclei sites in the formation of biomineralized structures that emerge to the membrane surface and spread horizontally, in a circular manner. Image modified from [140]. ..... 91

**Figure 1.48:** Schematics of (A) optical light microscopy: light is passed through condenser lens to illuminate a sample and form an image that is transmitted through the objective lens. The objective lens can have different magnifications. The formed magnified imaged is passed through the ocular lens and can then be viewed by the operator; and (B) polarized light microscopy: the setup in PLM is similar to

conventional optical microscopy. However, the additional components are added. (1) Polarizer: only allows light waves to pass through which vibrate into a specific direction. (2) Analyzer: only allows light waves which vibrate at the perpendicular direction to the light transmitted by the polarizer. .... 92

**Figure 1.49:** Schematic of scanning electron microscopy principle, where an electron source passes an electron beam through condenser lenses and an aperture, which condense the beam, before it is deflected onto the sample surface by a scanning coil. The electrons that are backscattered from the sample are collected by a back-scattered electron detector, amplified, and processed by a computer system to form a high-resolution image [155]. .... 94

**Figure 1.50:** Schematic of X-Ray diffraction technique, wherein X-Rays are emitted from an X-Ray source onto a crystalline sample, which diffracts the X-Rays at angle  $2\theta$ . .... 95

**Figure 2.1:** Chemical structure of lysine with a primary amine group ( $\text{NH}_2$ ). .... 98

**Figure 2.2:** Chemical structure of Dimethyl formamide ( $\text{C}_3\text{H}_7\text{NO}$ ). .... 98

**Figure 2.3:** Chemical structure of Dimethyl sulfoxide ( $\text{CH}_3$ )<sub>2</sub>SO. .... 99

**Figure 2.4:** Chemical structure of hexamethylene diisocyanate,  $\text{OCN}(\text{CH}_2)_6\text{NCO}_2$ . .... 99

**Figure 2.5:** Chemical structure of Polymeric diphenylmethane diisocyanate [ $\text{C}_6\text{H}_5(\text{NCO})\text{CH}_2$ ]<sub>n</sub>. .... 99

**Figure 2.6:** Chemical structure of genipin,  $\text{C}_{11}\text{H}_{14}\text{O}_5$ . .... 100

**Figure 2.7:** Example of a deconvoluted FTIR spectra, showing the spectral bands of the protein secondary structure in accordance with the specified spectral bands (blue =  $\beta$ -sheets, red = random coils, purple =  $\beta$ -turns, green =  $\alpha$ -helices). .... 101

**Figure 2.8:** Cellink Inkredible bioprinter. .... 103

**Figure 3.1:** Fabrication method PMDI-ELP gels where ELP and PMDI were dissolved separately before mixing the constituents. The image shows the formed PMDI-ELP gel in an Eppendorf tube (A) and after removal from the tube (B). Scale bar: 2.5 mm. .... 105

**Figure 3.2:** Integration of 0.1 wt%, 0.2 wt% and 0.3 wt% PMDI were integrated into 4% ELP solution. At 0.1 wt% and 0.2 wt% PMDI, the solution remained liquid. At 0.3 wt% PMDI, material gelation occurred within 3 seconds. .... 106

**Figure 3.3:** Threshold determination for PMDI-ELP gel formation. Examining PMDI concentrations of 0.23 wt%, 0.24 wt% and 0.25 wt% PMDI showed that the threshold lay at approximately 0.25 wt%. 106

**Figure 3.4:** PMDI-ELP cross-linking mechanism illustration, wherein the cross-linking interactions between the functional isocyanate compound of PMDI and the cross-linking specific primary amine of lysine form an isourea compound [171]. .... 107

**Figure 3.5:** Interaction between functional isocyanate groups and water, leading to the formation of an intermediate carbamic acid and potential decomposition to an amine compound under the release of  $\text{CO}_2$  gas [172]. .... 109

**Figure 3.6:** FTIR spectra deconvolution of PMDI-ELP gel showing that the secondary structure showed no significant changes between the day the sample solidified (A) and the day after (B). .... 113

**Figure 3.7:** Visualization of changes in secondary structure in PMDI-ELP gels over time in different cross-linking environments, depicting how accelerated PMDI-ELP gel solidification sped up protein secondary formation but also decreased molecular order in the final protein secondary structure conformation. .... 114

<b>Figure 3.8:</b> Schematic of DMF hydrolysis to dimethylamine (DMA) and formic acid (FA) [181] ....	116
<b>Figure 3.9:</b> Visualization of changes in secondary structure in PMDI-ELP gels after immersion in DI water, showing the translation from a highly disordered protein secondary structure to a mostly ordered configuration. Corresponding FTIR spectra can be found in Appendix B. ....	116
<b>Figure 3.10:</b> PMDI-ELP gels shrinkage bar chart, showing significantly less shrinkage in DI water. Mean values: fume hood 38.6 %, glovebox 47.7 %, vacuum oven 33.3 %, DI water 15.8 %.....	118
<b>Figure 3.11:</b> PMDI-ELP gels before (left) and after shrinkage (right), depicting vertical sample collapse after cross-linking in different dry environments. Scale bars: 5 mm.....	118
<b>Figure 3.12:</b> 0.5 wt% genipin-ELP gel (200 $\mu$ m) that formed after 6 days of incubation. Scale bar: 5 mm. ....	119
<b>Figure 3.13:</b> Visualization of changes in secondary structure in genipin-ELP gels over time in different cross-linking environments, depicting how accelerated sample solidification sped up protein secondary formation but also caused higher disorder in the final protein secondary structure configuration. ....	121
<b>Figure 3.14:</b> Genipin-ELP cross-linking mechanism illustration depicting how the formation of cross-links can either occur between (1) one genipin molecule and two primary amine groups from the same ELP backbone, or (2) one genipin molecule and two primary amine groups from two separate ELP backbones.....	123
<b>Figure 3.15:</b> Example of scanning position (P) selection in ELP membrane samples (S), displayed on a genipin-ELP membrane. ....	124
<b>Figure 3.16:</b> Fabrication method PMDI-ELP membranes, where ELP and PMDI were dissolved separately in 50% solvent mixture before being mixed and drop casted onto PDMS. Scale bars: 500 $\mu$ m. ....	125
<b>Figure 3.17:</b> Images showing how drop casted ELP-CLA-membranes dry over time, from the edge of the membrane towards (A, B) the centre of it (C).....	126
<b>Figure 3.18:</b> Numerical values obtained through the deconvolution of FTIR spectra, translated into a bar chart, showing how the secondary structure in PMDI-ELP membranes changed with increasing PMDI volumes. Overall, a decrease of $\beta$ -sheet and $\beta$ -turn formation was observed, whilst $\alpha$ -helices increased. At a 0.2 wt% PMDI concentration, no random coils were detected upon FTIR deconvolution Appendix B. Hence, no error bar was added to this region. At a higher concentration (0.3 wt%) random coil presence increased. ....	127
<b>Figure 3.19:</b> PMDI-ELP formulation schematic, describing how exceeding the lysine saturation threshold in terms of cross-linker concentration caused increased disorder protein secondary structure formation.....	129
<b>Figure 3.20:</b> Membrane swell capacity in PMDI-ELP membrane formulations.....	130
<b>Figure 3.21:</b> Fabrication method of genipin-ELP membranes, where ELP and genipin were dissolved in separate Eppendorf tubes to enhance CLA integration, before being mixed and drop casted onto PDMS. Scale bar: 500 $\mu$ m.....	131
<b>Figure 3.22:</b> Bar chart of changes in secondary structure with increasing genipin volumes in ELP membranes. The results showed an overall decrease of $\beta$ -sheet and random coils formation whilst $\alpha$ -helices slightly increases with an increase in CLA concentration.....	132

<b>Figure 3.23:</b> Genipin-ELP formulation schematic, according to which exceeding the threshold of 100% lysine saturation resulted in a plateau with respect to order:disorder in the final supramolecular protein secondary structure configuration.....	134
<b>Figure 3.24:</b> Swell capacity in genipin-ELP membrane formulations, showing statistically significant stronger swelling in 0.5 wt% genipin-ELP membranes, compared to other formulations.....	135
<b>Figure 3.25:</b> Bar chart of change in secondary structure with increasing HDI volumes in ELP membranes. Results showed a decrease of $\beta$ -sheet and $\alpha$ -helices, whilst random coils and $\beta$ -turns slightly increased with HDI increase.....	136
<b>Figure 3.26:</b> Membrane swell capacity tests in HDI-ELP membranes showed no significant differences. ....	137
<b>Figure 4.1:</b> PLM images of unmineralized ELP membranes. (A) HDI-ELP membranes, confirming the presence of evenly distributed Maltese cross-patterned organic spherulites. (B) The spherulite diameter (approximately 3 $\mu\text{m}$ ) coincided with data reported by S. Elsharkawy et. al. (C) No cross-patterned structures were visible in PMDI-ELP membranes (D). In genipin-ELP membranes strongly defined cross-pattern structures with a comparatively large diameter (10 – 15 $\mu\text{m}$ ) were observed in distinct locations. Scale bars (A), (C), (D): 20 $\mu\text{m}$ , (D): 5 $\mu\text{m}$ . ....	140
<b>Figure 4.2:</b> SEM images of HDI-ELP membranes showing (A) a smooth surface. (B) At lower and (C) higher magnifications, no geometrical features were observed in the bulk. Scale bars (A), (B): 10 $\mu\text{m}$ , (C): 1 $\mu\text{m}$ . ....	141
<b>Figure 4.3:</b> SEM images of PMDI-ELP membranes showing (A) a smooth membrane surface. (B) The cross-section appeared smooth at first sight. However, at higher magnification (C), nanoscopic pores were detected in the sample bulk. Scale bars (A): 100 $\mu\text{m}$ , (B): 10 $\mu\text{m}$ , (C): 1 $\mu\text{m}$ .....	141
<b>Figure 4.4:</b> SEM images of genipin-ELP membranes showing (A) a smooth membrane surface with indistinct surficial impurities. (B, C) The formation of spherical, microscopic pores in the membrane bulk was observed. Scale bars (A): 100 $\mu\text{m}$ , (B): 10 $\mu\text{m}$ , (C): 1 $\mu\text{m}$ . ....	142
<b>Figure 4.5:</b> (A) PLM and (B) optical light microscopy images of the same area in a genipin cross-linked ELP membrane, showing a distinct geometrical feature in the same location, as indicated with a dotted circle. Scale bars: 10 $\mu\text{m}$ . ....	142
<b>Figure 4.6:</b> SEM imaging of vacuum oven cross-linked genipin-ELP membrane. (A) Macroscopic image of the cross-section showing a significant decrease in pore density, compared to fume hood cross-linked specimens. (B) Nanoscopic pores were mainly observed close to the membrane surface. Scale bars (A): 10 $\mu\text{m}$ , (B): 200 nm.....	144
<b>Figure 4.7:</b> Optical microscopy images of mineralized HDI-ELP membrane after eight days in mineralization solution, (A) showing full mineralization at 10 x magnification and (B) rod like structures at 20 x magnification. Scale bars (A): 50 $\mu\text{m}$ , (B): 20 $\mu\text{m}$ .....	145
<b>Figure 4.8:</b> Optical microscopy images of mineralized PMDI-ELP membrane after 31 days in mineralization solution, (A) showing sparse biomineralization, compared to the control group. (B) Ring like structures were observed at higher magnifications. Scale bars (A): 50 $\mu\text{m}$ , (B): 20 $\mu\text{m}$ . ....	145
<b>Figure 4.9:</b> Optical microscopy images of mineralized genipin-ELP membrane after 21 days in mineralization solution, showing mineralized structures at different focal points, that achieved high	

definition imaging at (A) higher levels in respect to the membranes' z axis and (B) lower levels. Scale bars: 50 $\mu\text{m}$ .....	146
<b>Figure 4.10:</b> SEM images of the surfaces (A, C, E) and cross-sections (B, D, F) of HDI-ELP membranes. (A) Ring like structures were observed on the surface of ratio 1 membranes. Mineralization in the (B) bulk region was revealed. Ratio 4 (C, D) and ratio 12 (E, F) showed defined rod-like structures on the surface and no bulk mineralization. The morphology of surface mineralization became more condensed with an increase in cross-linker volume. Scale bars: 10 $\mu\text{m}$ .....	147
<b>Figure 4.11:</b> Close up SEM images of ratio 1 HDI-ELP membranes showing nanocrystals in the sample bulk, (A) covered with a thin layer of unmineralized organic matter. (B) Nanocrystals in the sample bulk were observed to have a dumbbell shape at an early stage of mineralization. Scale bars: 500 nm. ....	148
<b>Figure 4.12:</b> Close up SEM images of coinciding mineralized structures on the surface of (A) ratio 4 HDI-ELP membranes and (B) ratio 1 HDI-ELP membranes, highlighting 'folding' of the thin unmineralized blanked in volcano growth direction. Scale bar: 1 $\mu\text{m}$ .....	148
<b>Figure 4.13:</b> SEM images of the surfaces (A, C, E) and cross-sections (B, D, F) of PMDI-ELP membranes. All formulations showed bulk mineralization. No defined volcano morphology was observed on the surface of 0.1 wt% PMDI-ELP membranes (A), due to unmineralized blankets (approximately 3 – 5 $\mu\text{m}$ ) covering nanocrystals in the bulk (B). More extensive mineralization and defined volcano morphologies were observed on the surface of 0.2 wt% (C) and 0.3 wt% PMDI (E) ELP membranes. Scale bars (A, C, E): 100 $\mu\text{m}$ , (B, D, F): 10 $\mu\text{m}$ .....	149
<b>Figure 4.14:</b> SEM images showing how increasing in cross-linker volume caused the volcano morphology to become more distinct on the surface of 0.1 wt% (A), 0.2 wt% (B) and 0.3 wt% (C) PMDI-ELP membranes. Scale bars: 10 $\mu\text{m}$ .....	150
<b>Figure 4.15:</b> Close up images of (A) nanocrystals in a 0.3 wt% PMDI 4% ELP membrane, (B) covered by an unmineralized blanket. Scale bars: 1 $\mu\text{m}$ .....	151
<b>Figure 4.16:</b> Images showing how the unmineralized blanket 'folded' between two adjacent volcanoes. (A) Macroscopic image of mineralized structures emerging in proximity. (B) Close up image of folding motion occurring between two volcanos. Scale bars (A): 10 $\mu\text{m}$ , (B): 1 $\mu\text{m}$ .....	151
<b>Figure 4.17:</b> SEM images of the surfaces (A, C, E) and cross-sections (B, D, F) of genipin-ELP membranes. All formulations showed bulk mineralization. (A) Comparatively low mineralization density was observed in 0.5 wt% genipin-ELP membranes, whilst comprehensive mineralization was achieved in (C) 1.0 wt% and (D) 1.5 wt% genipin-ELP formulations. Scale bars (A, C, E): 100 $\mu\text{m}$ , (B, D, F): 10 $\mu\text{m}$ .....	152
<b>Figure 4.18:</b> Cross-sectional SEM images of mineralized structure close to the surface of a genipin-ELP membrane, revealing (A, C) nanocrystals, covered by a (B) thin layer of organic matter. Scale bars: 1 $\mu\text{m}$ . .....	153
<b>Figure 4.19:</b> SEM images of singular volcanoes in mineralized genipin-ELP membranes. (A) At a 0.5 wt% genipin concentration, 'bubble' shaped subunits were observed within the 'main' volcano. No major difference in morphology was observed between (B) 1.0 wt% (B) and (C) 1.5 wt% genipin formulations. Scale bars: 10 $\mu\text{m}$ .....	153

<b>Figure 4.20:</b> Cross-sectional SEM image of a mineralizing ‘main’ volcano with several underlying ‘subunits’ in the bulk region. Scale bar: 10 $\mu\text{m}$ . .....	154
<b>Figure 4.21:</b> SEM close up images of (A) mineralizing sphere in the sample bulk of mineralized genipin-ELP membranes, revealing the (B) presence of hexagonal nanocrystals, suggesting apatite mineralization. Scale bars (A): 1 $\mu\text{m}$ , (B): 100 nm. ....	155
<b>Figure 4.22:</b> XRD spectra of mineralized genipin- (blue), PMDI- (red) and HDI- (black) ELP membranes, showing peaks in the same regions and thereby confirming the presence of FAp. ....	156
<b>Figure 4.23:</b> SEM images of (A) spherically aligned nanocrystals at an early mineralization stage, engulfed in individual pockets. (B) As the spheres expanded, a hollow centre formed. Scale bars: 1 $\mu\text{m}$ . ....	157
<b>Figure 4.24:</b> SEM images from the top view of biomineralizing structures, which (A) appear as bubbles underneath the surface at an early stage (B) and grew closer to the surface as they increased in diameter. (C) The thickness of the unmineralized blanket covering the nanocrystals decreased as the structures expanded, causing a more distinct volcano morphology. Scale bars: 10 $\mu\text{m}$ .....	158
<b>Figure 4.25:</b> Cross-sectional SEM images of (A) mineralized structure that expanded towards the membrane surface, which caused nanocrystals to (B) divert away from the surface. Scale bars (A): 5 $\mu\text{m}$ , (B): 1 $\mu\text{m}$ . ....	159
<b>Figure 4.26:</b> Cross-sectional SEM images of (A) two colliding volcanoes at the membrane surface, causing (B) nanocrystals to grow back into the previously formed organic blanket. Scale bars: 1 $\mu\text{m}$ . ....	159
<b>Figure 4.27:</b> SEM images showing how different circumstances can affect the geometry of hollow structures in the centre of mineralizing spheres. Initially circular spheres turn oval upon (A) collision with adjacent mineralizing spheres. (B) When mineralizing spheres emerged to the surface uninterrupted, initially hollow centres transformed into the volcano centre. Scale bars: 10 $\mu\text{m}$ . ....	160
<b>Figure 4.28:</b> SEM images of mineralized vacuum-oven (left) and fume hood (right) 1.0 wt% genipin 4% ELP membranes that were immersed in mineralization solution for 3 weeks. (A) Compared to vacuum oven cross-linked samples, more extensive biomineralization was observed in fume hood cross-linked samples. (B) The cross-linking environment affected the volcano morphology. (C) Whilst in fume hood cross-linked samples, nanocrystals remained covered by a blanket of unmineralized matter, nanocrystals in vacuum oven cross-linked samples were exposed to the surface. Scale bars (A): 100 $\mu\text{m}$ , (B): 10 $\mu\text{m}$ , (C): 1 $\mu\text{m}$ . ....	161
<b>Figure 4.29:</b> Cross-sectional SEM images of mineralized 1.0 wt% genipin 4% ELP membranes after experiencing (A) vacuum oven cross-linking and (B) cross-linking under a fume hood, showing that fume hood cross-linked samples stronger mineralization capability. Scale bars: 10 $\mu\text{m}$ . ....	162
<b>Figure 4.30:</b> SEM images of early-stage bulk mineralization in PMDI-ELP membranes showing (A) spherically aligned nanocrystals, tightly engulfed in unmineralized matter. (B) Nanocrystals emerged to the surface as they grew in diameter, (C) remaining covered by an unmineralized blanket. Scale bars (A, B): 10 $\mu\text{m}$ , (C): 1 $\mu\text{m}$ .....	163
<b>Figure 4.31:</b> SEM image of (A) mineralizing PMDI-ELP membrane at an advanced biomineralization stage, showing redirected horizontal nanocrystal growth. (B) Nanocrystals remained covered by an unmineralized blanket. Scale bars: 1 $\mu\text{m}$ .....	164

**Figure 4.32:** Visualization of proposed mineralization mechanism in PMDI- and genipin-ELP membranes, wherein (i) ions from the mineralization solution came to an arrest at the interface between the pore and the organic matter. (ii) The interface between nucleic pore and the organic matter was assumed to promote spherical nanocrystal growth, away from circumference surface of the pore..... 165

**Figure 5.1:** Air in manual extrusion system causing discontinuous PMDI-ELP filament extrusion. Scale bar: 1 mm. .... 168

**Figure 5.2:** Experimental set-up for manual PMDI-ELP gel extrusion that minimizes air turbulence in the gel. (A) A conventional syringe, that was cut to match the prepared material volume. (B) A 25G needle was attached to syringe before ELP gel was transferred into the it *via* manual flicking, (C) Extruded PMDI-ELP filament on PDMS, handled with tweezers after extrusion and (D) in mineralization solution. Scale bars: 5 mm. .... 168

**Figure 5.3:** PMDI-ELP filament extruded through 25G needle showed irregular filament thickness across the sample length. Scale bar: 500  $\mu\text{m}$ ..... 169

**Figure 5.4:** Close up of extruded PMDI-ELP filament revealing the presence of biomineralized structures on the surface of the sample. Scale bars (A, B): 50  $\mu\text{m}$ ; (C): 10  $\mu\text{m}$ ..... 170

**Figure 5.5:** SEM images of PMDI-ELP filament after ten days in mineralization solution highlighting (A) gaps at the edge of the filament and (B) holes in the bulk, which stemmed from air in the extrusion system that resulted from manual transfer from the mixing container into the extrusion syringe. Scale bars: (A) 100  $\mu\text{m}$ ; (B) 5  $\mu\text{m}$ ..... 170

**Figure 5.6:** SEM images of mineralized PMDI-ELP filament, showing (A) mineralized structures on the sample surface, that are composed of (B) spherically arranged aligned nanocrystals in the filament bulk. (C) Nanocrystals were covered by a thin layer of unmineralized matter. Scale bars (A) (B): 5  $\mu\text{m}$ ; (C): 500 nm. .... 171

**Figure 5.7:** Setup for PMDI-ELP solution transfer to achieve homogenous gelation. (A) Two 1 ml syringes feeding into a mixer device that is connected to a printing cartridge *via* a female lure lock. (B) PMDI-ELP gel in 3mL printing cartridge. Scale bars: 1 cm..... 172

**Figure 5.8:** Print nozzles variants considered for PMDI-ELP extrusion printing. (A) 22G conical precision nozzle. (B) 22G conical standard nozzle. Scale bar: 1 mm..... 172

**Figure 5.9:** Printing speed tests, concluding an idea print speed of 4.4 mm s<sup>-1</sup> for continuous filament deposition onto PDMS substrate whilst applying a pneumatic pressure of 40-50 kPa. Scale bar: 10 mm. .... 173

**Figure 5.10:** Translation of an STL file into a 3D-printed PMDI-ELP gel sample. (A) STL file of a hollow circular structure (10 x 10 x 1 mm). (B) Additively manufactured, three layered PMDI-ELP gel, showing (C) offset layer heights and undefined filament edges. Scale bars: 1 mm. .... 173

**Figure 5.11:** Collapse of (A) a printed PMDI-ELP gel sample after fabrication (B) upon immersion in mineralization solution, leading to (C) strong disintegration after 1h in solution. Scale bar: 1 mm .... 174

**Figure 5.12:** Printed PMDI-ELP gel samples after 3 days of cross-linking in a parafilm sealed petri dish, showing (A) maintained three-dimensional shape and (B) gel conformation, as highlighted upon touching the gel with a spatula. (C, D) The sample remained stable upon immersion in mineralization solution (sol.) Scale bar: 1mm. .... 175

<b>Figure 5.13:</b> PMDI-ELP prints after 3 days in an open petri dish in a (A) glovebox and (B) fume hood, showing maintenance of the circular filament arrangement. However, sample collapse was experienced. The fume hood cross-linked sample showed stronger collapse than the glovebox cross-linked print. Scale bar: 1 mm. ....	176
<b>Figure 5.14:</b> SEM images of glovebox cross-linked PMDI-ELP prints. (A) Top view showing a measured filament thickness of approximately 365 $\mu\text{m}$ , (B) Cross-sectional view showing a sample peak height of approximately 580 $\mu\text{m}$ . (C) Close up image, revealing the presence of circular in the sample bulk. Scale bars (A, B): 100 $\mu\text{m}$ , (C): 1 $\mu\text{m}$ . ....	177
<b>Figure 5.15:</b> SEM images of fume hood cross-linked PMDI-ELP prints. (A) Top view showing a measured filament thickness of approximately 450 $\mu\text{m}$ , (B) Cross-sectional view showing a sample peak height of approximately 280 $\mu\text{m}$ . (C) Close up image, revealing the presence of oval shaped pores in the sample bulk. Scale bars (A, B): 100 $\mu\text{m}$ , (C): 1 $\mu\text{m}$ . ....	177
<b>Figure 5.16:</b> Circular PMDI-ELP print after 10 days in biomineralization solution and overnight drying at 60°C, maintaining its shape as it was held by a spatula. Scale bar: 1mm. ....	179
<b>Figure 5.17:</b> Printed PMDI-ELP constructs, cross-linked in different environments. (A) Glovebox cross-linked samples in an open container showed more mineralization than (B) samples cross-linked in a sealed container. (C) The fume hood cross-linked sample (open container) showed less mineralization than the glovebox cross-linked sample, whilst the fume hood cross-linked sample that was contained in a sealed container (D) showed the weakest mineralization ability. Scale bars: 100 $\mu\text{m}$ . ....	180
<b>Figure 5.18:</b> Change of colour over time in an incubating genipin-ELP gel, progressing from a light orange that progressively turns into a dark blue. In the Day 2 image, an air bubble is highlighted, that is used to monitor gelation over-time. Scale bar: 1 cm. ....	181
<b>Figure 5.19:</b> (A) STL print file for the fabrication of a 10x10 mm grid (Scale bar: 5 mm) (B) Illustration of printhead movement, travelling along two perpendicular sets of lines. ....	182
<b>Figure 5.20:</b> (A) After incubating 0.5 wt% genipin-ELP gel for six days in a closed cartridge, uniform filament deposition was achieved under the application of a pneumatic pressure of 145 kPa, at print speeds between 4.4–4.7 mm s <sup>-1</sup> . (B) Optical microscopy images of extruded filaments, showing how printing speed did not significantly affect the filament diameter post cross-linking. Scale bars (A): 10 mm, (B): 500 $\mu\text{m}$ . ....	183
<b>Figure 5.21:</b> Grid structure prints after nine days of gel incubation in a closed cartridge, showing excessive material gelation that does not allow for high print accuracy through neither (A) precision nozzle nor (B) standard nozzle. Scale bar: 1mm. ....	184
<b>Figure 5.22:</b> Print accuracy in 0.5 wt% genipin 4% ELP prints (six days gel incubation in a closed cartridge). (A) Slower printing speed causing material build up and pore closure. (B) Print accuracy was improved at an increased print speed. Pores in the inner scaffold region were printed more accurately (C) than those at the sample edge (D), which were prone to close. Scale bars (A), (B): 1 mm; (C), (D): 500 $\mu\text{m}$ . ....	184
<b>Figure 5.23:</b> Negative effect of low surface roughness substrate on print accuracy in genipin-ELP gel. (A) High print accuracy of first deposited layer was achieved. However, (B) deposition of a second layer exerted traction on the below layer, affecting print accuracy. Scale bar: 1 mm. ....	185

<b>Figure 5.24:</b> Improved print accuracy was achieved by (A) printing larger scaffolds and (B) using masking tape to increase substrate surface roughness. Scale bars: 5mm.....	186
<b>Figure 5.25:</b> Comparison of print accuracy in (A, B, C) fume hood cross-linked and (D, E, F) glovebox cross-linked genipin-ELP prints after six days of gel incubation in a closed cartridge, showing sample collapse into 2D grid structures. Sample collapse did not cause a significant change in pore sizes post cross-linking (C, F), compared to post-extrusion (B, E). Scale bars (A, D): 1 mm, (B, C, E, F): 500 $\mu$ m. ....	187
<b>Figure 5.26:</b> SEM images of glovebox (A, B, C) and fume hood (D, E, F) cross-linked samples after 10 days in mineralization solution, showing the emergence of biomineralized structures. (B) More biomineralization is observed in glovebox cross-linked genipin-ELP prints, where also directional growth in accordance with the printing direction is assumed. Scale bars (A, B, D, E): 100 $\mu$ m; (C, F): 10 $\mu$ m. ....	188
<b>Figure 5.27:</b> After six days of gel incubation in a closed cartridge 1.0 wt% genipin-ELP gel showed uniform and continuous filament deposition at an applied pneumatic pressure of 115 kPa and a print speed of 4.6 – 4.7 mm s <sup>-1</sup> . Scale bar: 1 cm. ....	190
<b>Figure 5.28:</b> Depiction of considered top and bottom of print cartridge. Scale bar: 1 cm. ....	191
<b>Figure 5.29:</b> 2D grid structures extruded after six day of gel incubation in a closed cartridge (1.0 wt% genipin 4% ELP) at a print speed of 4.7 mm s <sup>-1</sup> at 115 kPa. (A) Sample 1 (i) post printing and (ii) after cross-linking in a glovebox. (B) Sample 2 (i) post printing and (ii) after cross-linking in a fume hood. (C, D) Optical microscopy images of Sample 1 and 2 pre- and post-crosslinking with white squares depicting where pores should be located if they were in line with STL print file. The sample contracted towards the filament centres. Perpendicular filaments did not maintain their circular cross-section and collapsed into another instead. Scale bars (A, B): 5 mm; (C, D): 500 $\mu$ m.....	192
<b>Figure 5.30:</b> 2D grid structures extruded after seven day of gel incubation in a closed cartridge (1.0 wt% genipin 4% ELP) at a print speed 3 mm s <sup>-1</sup> and an applied pneumatic pressure of 230 kPa for (A) Sample 1 and 270kPa for (B) Sample 2. (A) Sample 1 (i) post printing and (ii) after glovebox cross-linking. (B) Sample 2 (i) post printing and (ii) after fume hood cross-linking. (C, D) Optical microscopy images of Sample 1 and 2 pre- and post-crosslinking with white squares depicting where pores and filaments should be located according to the generated STL print file. The sample contracted towards the filament centres and changed colour from a light green to a dark blue, due to genipin oxidation. Filament shape maintenance was achieved in Sample 1 post printing. In Sample 2, due to the use of poor-quality, filaments were prone to collapse into another. Scale bars (A, B): 5 mm; (C, D): 500 $\mu$ m. ....	193
<b>Figure 5.31:</b> Bar graph, representing the count of successfully printed pores in 2D grid structures after six and seven days of 1.0 wt% genipin 4% ELP gel incubation in a closed cartridge. After 6 days an average§ of 10.5 printed pores (n = 2) were successfully printed. Improved shape fidelity after seven days of incubation enabled the successful printing of 15.5 pores (n = 2). The dotted line represents the desired pore count.....	194
<b>Figure 5.32:</b> Bar chart representing pore sizes in 2D grid structures, printed with 1.0 wt% genipin 4% ELP gel after 6 days of gel incubation in a closed cartridge. Printed samples showed a similar average pore size (0.98 mm <sup>2</sup> and 0.95 mm <sup>2</sup> ). Post cross-linking, extruded filaments in both samples underwent	

statistically significant contraction, leading to an increase in average pore sizes to 2.67 mm<sup>2</sup> (glovebox cross-linked) and 2.48 mm<sup>2</sup> (fume hood cross-linked) respectively. The dotted line represents the ideal pore size (2.56 mm<sup>2</sup>) that considered the grid dimensions and nozzle diameter. .... 195

**Figure 5.33:** Bar chart representing pore sizes in 2D grid structures, printed with 1.0 wt% genipin 4% ELP gel after seven days of gel incubation in closed cartridge. Printed samples showed a similar average pore size (0.96 mm<sup>2</sup> and 0.82 mm<sup>2</sup>). Post glovebox cross-linking in a glovebox, filaments in Sample 1 showed statistically significant contraction, leading to an average pore size of 1.98 mm<sup>2</sup>. Due to poor bio gel quality, pore sizes in the fume hood cross-linked sample showed less contraction, with average pore sizes only reaching 1.32 mm<sup>2</sup>. The dotted line represents the ideal pore size (2.56 mm<sup>2</sup>) that considered the grid dimensions and nozzle diameter. .... 196

**Figure 5.34:** Bar chart, showing how incubation time affected sample contraction post cross-linking. Results showed that filament contraction decreased as gel incubation in a closed cartridge time was extended, which led to decreased percentual pores increase less post cross-linking. Furthermore, the cross-linking environments was not found to impact filament contraction. .... 197

**Figure 5.35:** Bar chart summarizing pore size accuracy post printing and post cross-linking after different gel (1.0 wt% genipin 4% ELP) incubation periods (six days vs. seven days), showing that pore size accuracy post printing remained constant, whilst pore size accuracy post cross-linking decreases due to a decrease in filament contraction capacity. .... 198

**Figure 5.36:** SEM image of fume hood cross-linked 1.0 wt% genipin 4% ELP print sample (six days of gel incubation in a closed cartridge), showing mineral accretions that formed in super saturated biomineralization solution and deposited onto the sample surface, impeding ion diffusion into the sample and thereby avoiding biomineralization. Scale bars: (A) 100 μm, (B) 1 μm. .... 199

**Figure 5.37:** SEM image of glovebox cross-linked 1.0 wt% genipin 4% ELP print sample (seven days of gel incubation in a closed cartridge). (A) Filament three-dimensionality was maintained post cross-linking. (B) Emergence of biomineralized structures, which started growing in the sample bulk and rose to the surface was observed. Scale bars: 100 μm. .... 199

**Figure 5.38:** Fabrication of a four-layered 10 x10 mm grid scaffold showing (A) collapse of all pores as filaments were deposited on top of each other. (B) Fume hood cross-linking induced sample contraction towards the centre. Side views showed, that despite sample collapse, the sample did not fully collapse into a membrane configuration. (C) Upon close observation of the cross-linked sample, intended pores could be vaguely determined. Scale bars (A, B, C): 5 mm; (side view): 1 mm ..... 200

**Figure v.1:** 1.0 wt% genipin 4% ELP printed Sample 1 after 6 days of incubation, showing measured surface area of successfully printed pores. Scale bar: 500 μm. .... 266

**Figure v.2:** 1.0 wt% genipin 4% ELP printed Sample 1 after 6 days of incubation, showing measured surface area of printed pores post glovebox cross-linking. Scale bar: 500 μm. .... 266

**Figure v.3:** 1.0 wt% genipin 4% ELP printed Sample 2 after 6 days of incubation, showing measured surface area of successfully printed pores. Scale bar: 500 μm. .... 266

**Figure v.4:** 1.0 wt% genipin 4% ELP printed Sample 2 after 6 days of incubation, showing measured surface area of printed pores post glovebox cross-linking. Scale bar: 500 μm. .... 266

<b>Figure v.5:</b> 1.0 wt% genipin 4% ELP printed Sample 1 after 7 days of incubation, showing measured surface area of successfully printed pores. Scale bar: 500 $\mu\text{m}$ .....	268
<b>Figure v.6:</b> 1.0 wt% genipin 4% ELP printed Sample 1 after 7 days of incubation, showing measured surface area of printed pores post glovebox cross-linking. Scale bar: 500 $\mu\text{m}$ . .....	268
<b>Figure v.7:</b> 1.0 wt% genipin 4% ELP printed Sample 2 after 7 days of incubation, showing measured surface area of successfully printed pores. Scale bar: 500 $\mu\text{m}$ .....	268
<b>Figure v.8:</b> 1.0 wt% fenipin 4% ELP printed Sample 2 after 7 days of incubation, showing measured surface area of printed pores post fume hood cross-linking. Scale bar: 500 $\mu\text{m}$ . .....	268

### iii. List of tables

<b>Table 1.1:</b> Mechanical properties of cortical and trabecular bone tissue [1] .....	25
<b>Table 1.2:</b> Summary of the function of bone related growth factors and non-collagenous proteins.....	27
<b>Table 1.3:</b> Summary of the function of different specialized bone cells [2], [18] .....	28
<b>Table 1.4:</b> Advantages and disadvantage of conventional bone tissue engineering scaffold fabrication techniques.....	55
<b>Table 1.5:</b> Summary of advantages and disadvantage of AM bone TE scaffold fabrication techniques. ....	69
<b>Table 1.6:</b> Advantages, disadvantage and suitable fabrication methods for conventionally used bone tissue engineering scaffold fabrication materials [36] [1]. ....	75
<b>Table 1.7:</b> Order-disorder interplay of protein secondary structure in ELP based membranes, (A) determining the morphology of mineralized structures and their mechanical properties. An increase of cross-linker caused an increase in disorder (random coils) in the protein secondary structure (B), which resulted in more defined biom mineralized structures. (C, D) As disorder was increased, the mechanical hardness and stiffness was decreased. Images modified from [140]. ....	90
<b>Table 3.1:</b> Numerical values [%] obtained through the deconvolution of FTIR spectra of PMDI-ELP gel in a sealed container (Day 0 – Day 4), showing static disorder (random coils) in the ELP protein secondary structure over time. Corresponding FTIR spectra can be found in Appendix B.....	111
<b>Table 3.2:</b> Numerical values [%] of the underlying protein secondary structure of CLA-free ELP-solution, displaying a predominant presence of random coils. Approx. 20% $\beta$ -sheets were detected. Corresponding FTIR spectra can be found in Appendix B.....	111
<b>Table 3.3:</b> Numerical values [%] of FTIR spectra deconvolution from PMDI gel that was cross-linked in a fume hood (Day 1 – Day 3). Results revealed a sequential order in protein secondary structure formation, wherein on the first day, proteins were mainly randomly ordered, and then reached ordered conformations <i>via</i> the formation of $\alpha$ -helices (Day 2), $\beta$ -sheets and $\beta$ -turns (Day 3). Corresponding FTIR spectra can be found in Appendix B. ....	112
<b>Table 3.4:</b> Numerical values [%] of FTIR spectra deconvolution from ELP in solvent, dried on PDMS substrate in a fume hood (left column) and in a glovebox (right column). The results showed higher molecular disorder (more random coils) in glovebox dried, non-cross-linked ELP membranes. Corresponding FTIR spectra can be found in Appendix B. ....	115
<b>Table 3.5:</b> Numerical values [%] obtained through the deconvolution of FTIR spectra of genipin-ELP solution (Day 0 – 4) and the thereafter forming gel (Day 5 – 7), showing a static predominantly disordered protein secondary structure over time. Corresponding FTIR spectra can be found in Appendix B.....	120
<b>Table 3.6:</b> Numerical values secondary structure in 2.5 wt% genipin-ELP membranes, showing 100% protein secondary structure translation into ordered coils in five out of six scanned sample (S) positions (P). ....	133
<b>Table 5.1:</b> Protein secondary structure deconvolution in different locations of a fume hood cross-linked 1.0 wt% genipin-ELP filament showed strong variation across the sample length (Filament location 1 and 2) and significantly more random coils than observed in membrane configurations (Average membranes). ....	189

#### **iv. List of acronyms and elements**

3D	Three-dimensional
3DP	3D Printing
AFM	Atomic force microscopy
ALP	Alkaline phosphatase
AM	Additive Manufacturing
BMP	Bone morphogenetic proteins
C	Carbon
CAD	Computer aided design
CaP	Calcium phosphate
CD	Circular dichroism
CLA	Cross-linking agent
DI	Deionized (water)
DMF	Dimethylformamide
DMSO	Dimethyl sulfoxide
ECM	Extracellular matrix
ELISA	Enzyme-linked immunosorbent assay
ELP	Elastin like protein / Elastin like polypeptide
ELR	Elastin like recombinamers
F	Fluorine
FAp	Fluorapatite
FCM	Flow cytometry
FTIR	Fourier transform infrared spectroscopy
GF	Growth factor
HAp	Hydroxyapatite
HDI	Hexamethylene diisocyanate
HRP	Horseradish peroxidase
IHC	Immunohistochemistry
IGF	Insulin-like growth factors
IR	Infrared radiation

K	Potassium
LCST	Lower critical solution temperature
ME	Material extrusion
Mg	Magnesium
MTT	Methyl thiazolyl tetrazolium
Na	Sodium
NCP	Non collagenous proteins
PCL	Polycaprolactone
PDMS	Polydimethylsiloxane
PEG	Polyethylene glycol
PEEK	Polyether ether ketone
PLGA	Poly(lactic-co-glycolic acid)
PLM	Polarized light microscopy
PMDI	Polymeric diphenylmethane diisocyanate
PMMA	Poly(methyl methacrylate)
PMT	Photomultiplier tubes
SCPL	Solvent casting and particulate leaching
SEM	Scanning electron microscopy
Sr	Strontium
STL	Standard triangle language
Ta	Tantalum
TCP	Tricalcium phosphates
TE	Tissue engineering
TGF	Transforming growth factors
Ti	Titanium
TIPS	Thermally induced phase separation
XRD	X-Ray diffraction

# 1. Introduction

## 1.1. Human bone

Bone is a dense, living tissue, that comprises the main part of the human skeletal system. It plays an important role in providing structure, enabling locomotion, supporting, and protecting soft tissue, hosting blood cells, and functioning as a reservoir for bone marrow [1][2].

Mature bone is comprised of three tissue types, cortical tissue, cancellous tissue, and subchondral tissue. Cortical bone tissue forms the external, dense layer of all bone types and contains < 10% of soft tissue. Over 75% of the cancellous bone tissue volume is represented by bone marrow. Cancellous bone tissue, also known as spongy bone tissue, is made up of honeycomb-shaped trabeculae, which are interspersed between said bone marrow to form a porous structure. It is located on the interior of bone, surrounded by cortical bone tissue, and possesses a higher bone surface-to-bone volume ratio than cortical bone [2][3].

Subchondral tissue, also known as cartilage, provides a smooth, lubricated surface at joint interfaces, thereby enhancing bone resilience and enabling resistance to compressive forces [4].

The mechanical properties of each bone tissue type are strongly dependent on the body part. Generally, the robustness and stiffness of cortical bone is higher in longitudinal direction, compared to its transverse direction. The elastic modulus and the strength of bone are anisotropic. The mechanical properties in cancellous bone tissue are dependent on the arrangement of the individual trabeculae and the resulting porosity [1].

**Table 1.1** states the modulus and strength of human bone as reported in previous studies.

	Location	Elastic Modulus [GPa]	Strength [MPa]	
	Cortical bone	Longitudinal	17.9 ± 3.9	Tension
Compression				205 ± 17.3
Transverse		10.1 ± 2.4	Tension	53 ± 10.7
			Compression	131 ± 20.7
Cancellous bone	Vertebra	0.067 ± 0.045	2.4 ± 1.6	
	Tibia	0.445 ± 0.257	5.3 ± 2.9	
	Femur	0.441 ± 0.271	6.8 ± 4.8	

**Table 1.1:** Mechanical properties of cortical and trabecular bone tissue [1]

### 1.1.1. Chemical composition of human bone

Bone tissue is a composite material, composed of inorganic minerals (45-60%), organic materials (20-30%) and water (10-20%). The following pie chart depicts the chemical composition of bone.

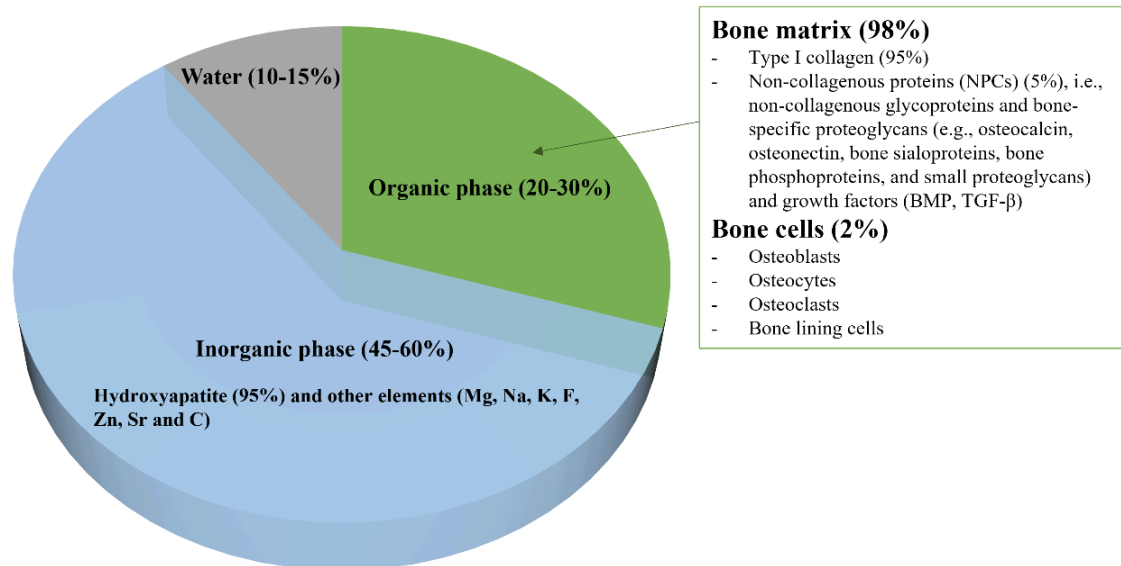


**Figure 1.1:** Pie chart representing the chemical composition of human bone, which can be divided into organic and inorganic materials, as well as water [2][5].

The majority of bone tissue, which is composed of an inorganic phase, mainly contains Hydroxyapatite (HAp) (approx. 95%). The remaining portion of the inorganic phase constitutes other elements, such as Magnesium (Mg), Sodium (Na), Potassium (K), Fluorine (F), Strontium (Sr) and Carbon (C). Most of the organic phase is composed of type I collagen. The remaining smaller portion of the bone matrix consists of specialized bone cells and non-collagenous proteins (NCPs).

NCPs are crucial in the bone mineralization process and play an important role in the association of cells and bone matrix with structural proteins. Less than 1% of NCPs account for growth factors (GFs), that are secreted by bone cells [2].

In the following table, the functions of several proteins and GFs are described.

	Name	Function	References
<b>Proteins</b>	Type I collagen	<ul style="list-style-type: none"> <li>- Acts as mechanical support and forms a bone cell scaffold</li> <li>- Forms a bond between mineralized collagen fibrils in the bone that improve bone toughness</li> </ul>	[6], [7]
	Osteonectin	<ul style="list-style-type: none"> <li>- Regulates extracellular matrix (ECM) assembly</li> <li>- Regulates osteoclast activity</li> <li>- Regulates osteoblast (bone forming cells) differentiation</li> </ul>	[8]
	Osteopontin	<ul style="list-style-type: none"> <li>- Promotes osteoclasts (bone remodelling cells) formation and activity</li> <li>- Regulates HAp growth</li> <li>- Inhibits mineralization of osteoblast cultures</li> </ul>	[9]
	Osteocalcin	<ul style="list-style-type: none"> <li>- Bone formation marker → Concentration directly correlates with bone formation</li> </ul>	[10]
	Proteoglycans	<ul style="list-style-type: none"> <li>- Contribute to ECM organisation</li> <li>- Contribute to bone tissue structuring <i>via</i> collagen fibrillogenesis</li> <li>- Modulate biological activity and bio-availability <i>via</i> interactions with other constituents, e.g., cytokines and growth factors</li> </ul>	[11]
	Alkaline phosphatase	<ul style="list-style-type: none"> <li>- Regulates bone mineralization <i>via</i> hydrolysis of a mineralization inhibitor (pyrophosphate)</li> <li>- Supports HAp synthesis by providing inorganic phosphate</li> </ul>	[12]
<b>Growth factors</b>	Transforming growth factor $\beta$ (TGF- $\beta$ )	<ul style="list-style-type: none"> <li>- Contributes to bone remodelling and bone formation <i>via</i> regulative interactions with osteoblasts and osteoclasts</li> <li>- Stimulates matrix protein synthesis</li> </ul>	[13], [14]
	Insulin-like growth factors (IGFs)	<ul style="list-style-type: none"> <li>- Contribute to skeletal homeostasis</li> <li>- Enhance osteoblast differentiation of mesenchymal stem cells, thereby contributing to bone formation</li> <li>- Regulate cell metabolism</li> </ul>	[15], [16]
	Bone morphogenetic proteins (BMPs)	<ul style="list-style-type: none"> <li>- Support production of bone matrix formation and neovascularization</li> <li>- Induce bone growth through recruitment of mesenchymal stem cells (MSCs) from adjacent tissue through               <ol style="list-style-type: none"> <li>(1) MSC differentiation into osteoblasts, or</li> <li>(2) MSC differentiation into cartilage cells, turning into bone cells</li> </ol> </li> </ul>	[17]

**Table 1.2:** Summary of the function of bone related growth factors and non-collagenous proteins

Specialized bone cells enable constant bone remodelling throughout a person's life to facilitate a balance between metabolic processes, including bone resorption and new bone formation [2].

In **Table 1.3**, the main functions of different bone cells are stated.

Bone cell type	Functions
Osteoblasts/bone forming cells (account for 4-6% of bone cells)	Responsible for synthesis of various bone proteins (e.g., type I collagen, osteonectin, osteopontin, osteocalcin, proteoglycans, and alkaline phosphatase) Responsible for synthesis of various growth factors (e.g., TGF- $\beta$ , IGF-I and IGF-II, and BMPs)
Osteoclasts/bone remodelling cells	Induce bone remodelling by engulfing aged or damaged bone matrix
Osteocytes/bone maintaining cells (account for 90 – 95% of bone cells)	Present on surfaces where bone is mostly metabolically inactive bone. Facilitate blood clotting in bone <i>via</i> <ul style="list-style-type: none"> <li>• Harmonization of the activity of bone forming (osteoblasts) and bone remodelling cells (osteoclasts)</li> <li>• Regulation of phosphate balance</li> <li>• Sensing of mechanical stress</li> </ul>
Bone-lining cells/inactive osteoblasts	Regulate in- and outflow of minerals where bone is in contact with other tissues Provide stem cells with appropriate signals to remain in an undifferentiated state
Osteogenic cells/stem cells	Present in bone marrow and the membrane of blood vessels and nerves surrounding bone. Precursors to more specialized bone cells, i.e., osteocytes and osteoblasts, thereby playing an important role in bone repair/growth.

**Table 1.3:** Summary of the function of different specialized bone cells [2], [18]

### 1.1.2. Structural composition of human bone

Bone owes its heterogenous and anisotropic properties to its complex hierarchical structure and its chemical composition. Bone has a macroscopic structure (e.g., cortical, and cancellous bone tissue) [19].

Whilst long limb bones, such as femur or tibia, are composed of an inner cancellous structure that is surrounded by outer compact (cortical) bone, flat bones, such as the skull, show a sandwich-like arrangement of the two macroscopic structures.

The macroscopic structure of bone is composed of repetitive microscopical units (10–500  $\mu\text{m}$ ), i.e., haversian systems, osteons, and single trabeculae, and sub-microscopic

lamellae (1–10  $\mu\text{m}$ ). Osteon are aligned concentric rings (200–250  $\mu\text{m}$ ) which run parallelly to the bone’s long axis. They are composed of planar arranged lamellae, that are concentrically arranged around a central canal, the haversian canal.

Fibrillar collagen (ranging from few hundred nanometers – 1  $\mu\text{m}$ ), minerals, elements, and non-collagenous proteins (NCPs) (below a few hundred nanometers) are embedded in the planar lamellae and constitute the nanostructure and sub-nanostructure of bone [2][19]. **Figure 1.2** shows the hierarchical structure and composition of bone.

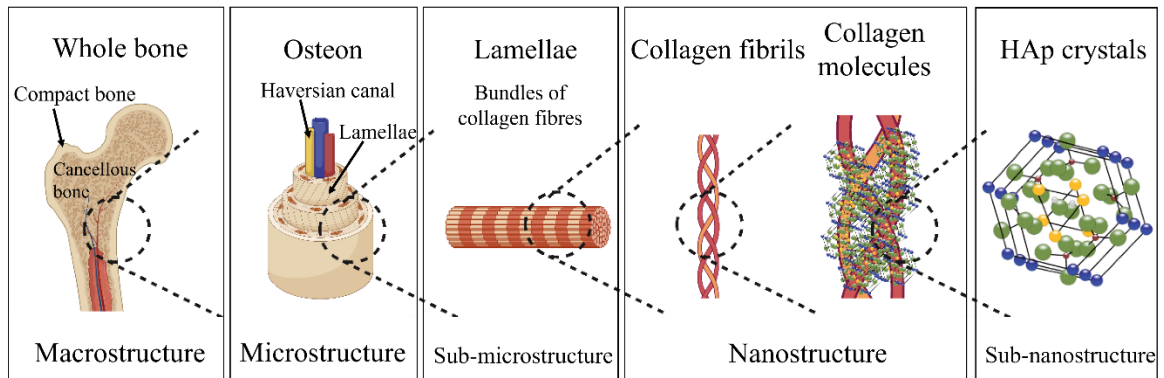


**Figure 1.2:** Schematic of hierarchical bone structure, modified from [2]

Despite the excellent mechanical properties of bone, bone fractures represent a global public health issue [20].

### 1.1.3. History and challenges in bone defect repair

Locomotive abilities as well as the structural stability can be impeded through bone defects. Often, bone defect treatment requires extensive surgical procedures, involving the use of bone-grafting techniques, resulting in a slow healing process. Despite advances in bone treatment therapy, the patient can experience significant pain whilst a high infection risk remains. Furthermore, complete recovery is not guaranteed. Hence, the search for alternative surgical procedures is an ongoing challenge [21].

Evidence shows, that for centuries, numerous biologically derived materials have been used to treat large bone defects [22][23]. In 1668, the first heterologous bone graft, harvested from a dog skull, was successfully implanted into a soldier’s injured head. The first successful autologous bone replacement was carried out in 1820 by the German surgeon Philips von Walter, who successfully carried out a cranium fragment replacement surgery [23].

To this day, the treatment of large bone defects, whether traumatic or disease induced, challenges medical practice [24]. Commonly, bone autografts (harvested from a patients' donor site) or allografts (harvested from another person) are mechanically fixated into the diseased or damaged site [22] [25]. However, this method bares a risk of complications, such as infection, disease transmission, graft rejection, or donor site morbidity. These complications can require secondary surgery to be resolved [26].

Alternatively, bone substitutes can be used, which are defined as a '*synthetic, inorganic or biologically organic combination which can be inserted for the treatment of a bone defect instead of autogenous or allogeneous bone* [23].' Even though the use of synthetic bone substitutes removes risks such as donor site morbidity or disease transmission, they impose different challenges, such as mainly promoting bone growth on the surface of the substitute and lacking osteogenesis potential [22][27][28]. This limits their role in fracture healing treatments [22].

In research, the development of suitable biomaterials which can be used for the fabrication of bone substitutes is constantly evolving to tackle these challenges [22].

## **1.2. Biomaterials in bone regeneration therapy**

Biomaterials are surfaces, or constructs, which are designed to interact with biological systems. They can be either naturally or synthetically derived [29] [30]. A minimum requirement of these materials is that they must be biocompatible to avoid the elicitation of unfavourable immune responses in the biological system; and sterilizable, to enable safe insertion into the host tissue [29]. The biocompatibility of biomaterials can be classified into different categories: bioactive, bioinert, biotolerant and/or biodegradable. Different available biomaterials for bone tissue engineering (TE) and their related classifications are elaborated on in the following section [31].

### **1.2.1. Classification of biomaterials**

Commonly studied bone biomaterials can be grouped into the following material categories: biomedical metals, bioceramics and polymers. By creating composites of these materials, their benefits can be combined.

Whilst bioceramics have a high elastic modulus, comparable to that of cortical bone, they typically have a low fracture toughness, leading to brittleness. Polymers, on the other hand, have a comparatively low mechanical strength and elastic modulus, which

makes them unsuitable for weight-bearing site applications. Success in creating composites of the two materials has been limited, as it is difficult to obtain strong interfacial bonding and uniform dispersion between the two components. Biomedical metals have stronger mechanical strength, but their elastic modulus is highly incompatible with that of natural bone. This can cause stress shielding upon implantation which can lead to bone loss and osteoporosis at the damaged site [32].

Depending on the material, different implant-tissue-interactions can be observed (**Figure 1.3**) [33].

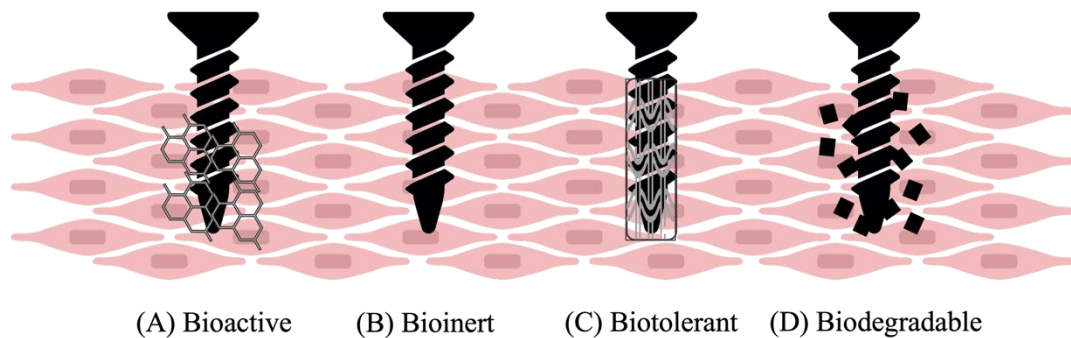


**Figure 1.3:** Depiction of biomaterial classifications. (A) Bioactive materials trigger biophysical and biochemical reactions between the surrounding tissue and the implant, leading to a mechanically strong chemical bond between the two components. (B) Bioinert materials get encapsulated by fibrous tissue, leading to isolation from the surrounding bone. (C) Biotolerant materials release corrosion products, chemical compounds, and ions, leading to the formation of fibrous tissue around the implant. (D) Biodegradable materials dissolve upon reaction with body fluids.

#### 1.2.1.1. *Bioactive biomaterials*

Bioactive materials in a bone tissue environment create chemical bonds with the bone tissue and thereby support osteogenetic activities (**Figure 1.3A**). They can be divided into two categories: osteoinductive and osteoconductive materials. Whilst osteoinductive materials (e.g., bioactive glasses or ceramics, and naturally derived polymers, such as collagen), stimulate osteogenesis, osteoconductive materials enable bone growth on the surface of the implanted material [31]. Biomaterials which lack bioactivity can often loosen or show signs of wear after long term implantation [32]. After the implantation of a bioactive material, a biological response from body is triggered, which leads to biophysical and biochemical reactions between the

surrounding tissue and the implant, leading to a mechanically strong chemical bond between the two components [31].

These biological responses are promoted through specific implant surface properties, such as surface roughness, implant porosity and the presence of bioactive materials. A popular material choice is Hydroxyapatite (HAp), which is a mineral that can be found in natural bone. Shortly after implantation of the bioactive component, proteins from the blood and extracellular matrix (ECM) attach to the implant surface. This interaction triggers a cascade of biological responses, which enable osteoblasts (bone-forming cells), to adhere to the surface. As these bone-forming cells begin to proliferate, they secrete an ECM that is composed of proteins, such as collagen. This matrix acts as a scaffold that enables the deposition of minerals, such as Calcium and Phosphate in an ordered manner to achieve the formation of HAp crystals. Over time, the mineralized matrix hardens and converts into mineralized bone tissue, which can integrate into the surrounding bone tissue and *vice versa*. As the surrounding bone penetrates the newly formed bone tissue, blood vessels grow into the new bone, which further enhances the interfacial connection [34].

However, most bioactive materials are too brittle to withstand the stress that bone is exposed to. Furthermore, shaping of bioactive glasses or ceramics into three-dimensional shapes is challenging [35].

#### *1.2.1.2. Bioinert biomaterials*

Unlike bioactive materials, bioinert materials e.g., metals, such as titanium or titanium alloys, stainless steel, or cobalt-chromium alloys; synthetic polymers, such as Poly(methyl methacrylate) (PMMA), Polyether ether ketone (PEEK) or Teflon; or ceramics, such as Alumina, Zirconia or Carbon, show low bioreactivity. They are mostly stable in the human body and do not interact with surrounding biological tissue or fluids. Instead, those implants are encapsulated by fibrous tissue (**Figure 1.3B**). This type of structural encapsulation can be achieved by different means. For example, by coating bioinert materials with biocompatible materials, such as HAp or biocompatible polymers, an interface can be created which can enable encapsulation as surrounding tissue interacts with the coating material, but not with the stable, bioinert bulk material. No chemical interaction occurs directly between the host tissue and the implant. By introducing an bioactive interface between a bioinert implant and the host tissue,

mechanical support can be enhanced and the risk of rejection by the host tissue can be decreased [31].

Major issues faced with bioinert materials, particularly metals, include the release of toxic metallic ions/particles upon wear or corrosion, which may lead to inflammation. Further drawbacks include associated properties, such as non-degradability and fatigue, as well as mechanical properties that mismatch those of bone [5][36].

The comparatively high stiffness of metals can impact the stress distribution between bone and implant, leading to stress shielding which can lead to bone degradation [35].

#### *1.2.1.3. Biotolerant biomaterials*

Biotolerant behaviour is often exhibited in metals and synthetic polymers. These materials interact with surrounding host tissue without compromising implant function. Fibrous tissue that encapsulates biotolerant materials is formed *via* corrosion products and chemical compounds from the implants, as well as release of ions (**Figure 1.3C**). Biotolerant materials are not functionally or structurally interconnected with the surrounding tissue and are often selected when bioinertness is not crucial to the application or other material properties outweigh the advantages of bioinertness [31].

#### *1.2.1.4. Biodegradable biomaterials*

Whilst the above-mentioned biomaterial classes remain in the host body after implantation, biodegradable implants, such as certain polymers (e.g., Polylactic or Polyglycolic acids and their co-polymers), ceramics (e.g., Calcium Phosphate or HAp) or biodegradable metals (e.g., Magnesium), dissolve upon reaction with body fluids (**Figure 1.3D**). The created by-products usually get removed from the body *via* the kidneys [31].

Numerous applications have been found for biodegradable materials, including biodegradable suture material, fracture repair devices, drug delivery devices, as well as TE scaffolds. But despite their advantageous resorb-ability, the rigidity of some biodegradable materials often does not match that of cortical bone. Furthermore, their degradation products can cause inflammatory reactions [35].

As previously mentioned, composite materials, which integrate two or more components, have gained increasing popularity in the development of next-generation

biomaterials [37]. Such composites shall ideally activate *in vivo* mechanisms which induce tissue regeneration, whilst stimulating healing mechanisms in the body and thereby achieving the replacement of scaffold with regenerated tissue [38]. This aim can for example be pursued through the development of bioactive and biodegradable composites [39].

By combining bioactive materials, such as bioceramics, with bioresorbable materials, such as biopolymers, the limitations of each material can be balanced out by the complementary material to design an interlaced material suited for bone regeneration. Herein, the bioactive phase can support *in vivo* mechanisms such as osteoconductivity and angiogenesis, whilst displaying mechanical properties that strongly resemble that of bone. The brittleness of the bioactive, inorganic phase can meanwhile be balanced out by the presence of the biodegradable, polymeric phase, which can provide resilience and improve the composites' processability into more complex shapes [35][39].

#### 1.2.2. Biocompatibility assessment methods

To successfully develop bone TE scaffolds, the constructs' behaviour within a living organism needs to be fully understood. *In vitro* as well as *in vivo* experiments can be conducted to understand interactions with surrounding tissues and the material and tissue transformations that are experienced during tissue regeneration. *In vitro* assays are carried out in a controlled laboratory environment. The development of three-dimensional models has opened new opportunities and allowed an increased accuracy of toxicology assays [40]. *In vitro* studies only measure the effect that the material has on specific cells during the first 12-24h. Therefore, they are considered less meaningful than *in vivo* data, which can obtain more complex information beyond 24h. In addition to that, unlike *in vitro* studies, *in vivo* studies are not restricted to a specific cell type. Instead, the material interacts with different cell types and takes interactions such as material-blood, -protein, -hormone and enzyme into consideration. For short term *in vivo* studies, animals with a short life span, such as mice and rats are often selected, whilst dogs, pigs or sheep are better suited for long-term testing [41].

Biocompatibility testing is usually conducted in four steps, as depicted in **Figure 1.4**.

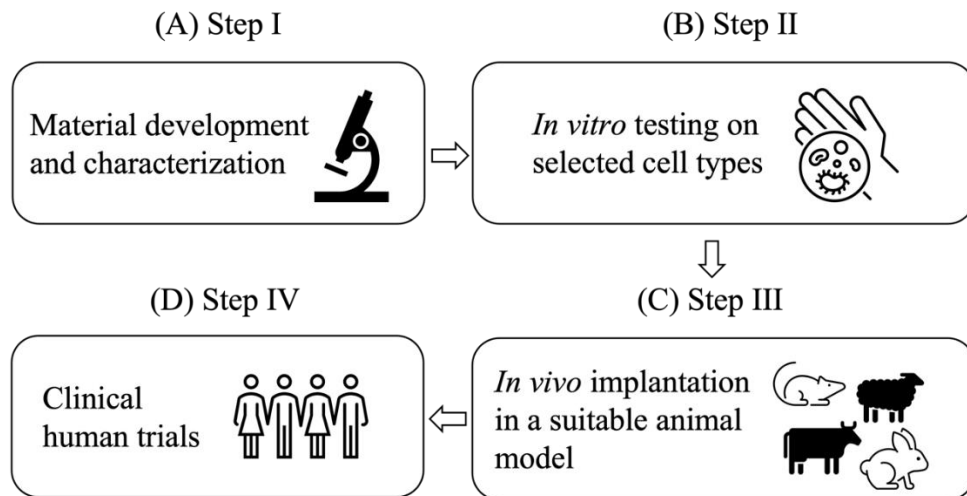


**Figure 1.4:** Flow chart depicting the four steps of biocompatibility testing. (A) Step I: Material development and characterization, (B) Step II: *In vitro* testing, (C) Step III: *In vivo* animal testing, (D) Step IV: Clinical human trials.

After the material is developed and characterized (**Figure 1.4A**), *in vitro* cytotoxicity and genotoxicity tests are carried out to test the effect on selected cell types (**Figure 1.4B**). Thereafter, *in vivo* implantation in an animal model, suited to the pathological implant location and the study time length, is conducted to test the effect the material has on the whole organism in terms of tissue viability and histology (**Figure 1.4C**). *In vivo* tests involve implanting the material in an animal model and the evaluation of its histocompatibility. Histological analysis is the gold standard used to assess the tissue response around the implanted material. This method can provide information about the inflammation response or the healing stage of the surrounding tissue. It can also visualise the degradation products that dissolved into the implantation site. After the site of interest is sectioned, different stains are used, depending on the properties of implanted material. The staining is used to identify different structures, such as tissues, cells, or metallic components. The stained samples can then be assessed under an optical microscope [42].

In the final step, human trials are conducted to gather information on interactions observed in a human organism (**Figure 1.4D**) [41].

In the following sections, different *in vitro* and *in vivo* methods are elaborated on which can be used to assess the physiological effects that the medical device of interest has on a living organism [43].

*In vitro* cytotoxicity testing is used to investigate cell proliferation and growth as well as to assess which morphological effects medical devices have on living cells. In the development of medical devices, cytotoxicity assays are preferred as pilot trials to gain an understanding of the device's toxicity. According to the International Organization for Standardization 109993-5, *in vitro* cytotoxicity tests are characterized into three main types: direct contact method, extract method and indirect contact test (e.g. agar diffusion test) [44].

#### (1) Extract method

In the extract method, a part of the scaffold is extracted, added to the cell culture medium, and incubated at specific conditions, allowing the release of soluble components from the extract. Subsequently, the cell culture medium with the released components is added to cultured cells to evaluate the cytotoxicity. A common method that is used to assess cell viability in the extract method is the colorimetric mitochondrial dehydrogenase performance measurement, which is also known as MTT (methyl thiazolyl tetrazolium) assay. Herein, MTT, a yellow tetrazolium dye, is added to the cell culture. Metabolically active cells can cleave the tetrazole ring, causing the MTT to turn into purple, crystalline formazan. These formazan crystals can be dissolved in organic solvents, such as DMSO (Dimethyl sulfoxide). By measuring the absorbance of the dissolved crystals, the number of surviving cells and their metabolic activity can be measured [44].

#### (2) Direct contact method

In this method, mammalian cells are cultured in direct contact with the medical device. After exposing the cells to the device for a specific incubation period, morphological changes are investigated and the change of numbers of cells is manually tracked to observe cell viability. Simultaneously, control groups are cultured to indicate and confirm cytotoxic effects. Assessments, such as live-dead assay or presto blue assay can subsequently be carried to evaluate cell viability and proliferation of bone cells [44].

- Live dead assay: In this assay, live cells are dyed with calcein-AM, whereas dead cells are stained with ethidium homodimer-1 (EthD-1). By conducting fluorescence microscopy on the device of interest, the distribution of live and dead cells is visualized [45].
- Presto blue assay: In this colorimetric assay, like the MTT assay, a scaffold is seeded with cells as well as presto blue, a redox indicator. When metabolically active cells get in touch with the redox indicator, a change of colour and fluorescence occurs. By subsequently measuring the fluorescence or absorbance, cell viability and proliferation can be evaluated [45].

### (3) Agar diffusion test

The qualitative agar diffusion test is used to evaluate soluble toxic components which can leach from the scaffold of interest. A scaffold or its extracts are placed on an agar plate onto which an individual layer of cells was priorly cultured. If cytotoxic extracts contact this cultured cell layer, cell death is induced locally on the agar plate, leading to the red agar dye to diffuse. This experimental setup makes this assay suitable for cytotoxicity testing of a wide range of large quantity of medical devices [44].

### *Evaluation of inflammatory response*

Post implantation of a medical device, immunological responses are triggered. When an immunological response is triggered, inflammatory factors are released which leads to the accumulation of macrophages in the affected area. Macrophages are cells that are responsible for the regulation of the inflammatory response and can break down foreign pathogens. After implantation, macrophages are recruited to the affected area and can differentiate to induce a favourable inflammatory response, thereby reducing the wound infection risk. Thereafter, a chronic inflammatory response is induced through the formation of foreign body giant cells. At later stages of implantation, macrophages can also promote tissue regeneration and the formation of new blood vessels. These responses are crucial to protect the living organism from foreign pathogens. Severe immune reactions, however, can lead to implant rejection. Hence, an important aspect of bone tissue engineering is to gain an understanding of how an immunoreaction can be triggered which does not lead to implant rejection, whilst simultaneously promoting osteogenesis. In the following, different approaches that can be used to evaluate the inflammatory response to bone scaffolds are specified [46].

### (1) Enzyme-linked immunosorbent assay (ELISA)

Antigen-antibody reactions are a key factor in the immune response that occurs post-implantation of a foreign object. ELISA is a quantitative method that specifies the immune-related molecules that are released by immune cells after the immune response occurs. It allows the detection and quantification of specific inflammatory mediators in the culture medium after incubation with the scaffold. To detect immune-related molecules, antigens, or antibodies, such as Alkaline Phosphatase (ALP), horseradish peroxidase (HRP), and  $\beta$ -galactosidase, are labelled *via* enzymes, thereby creating an enzyme immunoassay. The fluid antigen is immobilized on a rigid plane, such as a polystyrene plate, and subsequently allowed to interact with a specific antibody. This antibody is detected by an enzyme-labelled secondary antibody. Depending on the selected antigen, a chromogenic substrate develops a specific colour. For instance, *p*-nitrophenol, which is produced by ALP, is detected at 405 nm, leading to yellow colouring [47].

### (2) Immunohistochemistry

In immunohistochemistry (IHC), inflammatory markers are detected and visualized by monitoring antigen-antibody interactions. Herein, the antibody binding site is either identified by antibody labelling or a secondary labelling method. Thereafter, by using staining methods that include fluorophore-labelled (immunofluorescence) and enzyme-labelled (immunoperoxidase) antibodies, the proteins, and molecules of the cells in question are identified. Thereby, information on the distribution and localization of immune cells in the tissue, at the scaffold site can be obtained [48].

### (3) Flow cytometry

Flow cytometry (FCM) is an analytical technique that is used to rapidly analyse single cells, based on their morphology and fluorescence staining. To be able to employ this technique, the scaffold/cell culture or tissue sample of interest must be soluble to obtain a single cell suspension [49].

Typical FCM equipment is composed of a fluidic component, which enables the transport of cells, an optical component, composed of lasers, lenses and collection units, such as filters and mirrors, and electronics which convert light scatter and, in the case of a multicolour FCM, fluorescence emission signals from the optical laser component into are translated into digital signals.

The method is based on light scattering and, in multicolour FCM, fluorescence emission that occurs as a laser beam perpendicularly interacts with cells in the suspension that are injected into the FCM flow cell and move in a directed narrow fluid stream, allowing cells to interact with the laser beam one at a time. Using an isotonic buffer, also known as a sheath fluid, the sample stream is hydrodynamically focussed (**Figure 1.6A**).

Depending on the type of experiment and its aim, the cell rate flow can be adjusted. For example, higher flow rates are desirable when performing qualitative measurements such as immunophenotyping.

The laser beam that perpendicularly passes through the cell suspension stream is focused *via* cylindrical lenses. Commonly used laser excitation wave lengths in FCM include ultraviolet (350 nm), violet (405 nm), blue (488 nm) and red (640 nm). Interactions between the detected cells and the focussed laser cause the excitation light to be scattered both forwards as well as sideways (**Figure 1.6B**). Forward scatter (FSC) is recorded by detectors placed in front of the laser, whilst side scatter (SSC) is recorded by detectors placed on the side of the laser beam [50].

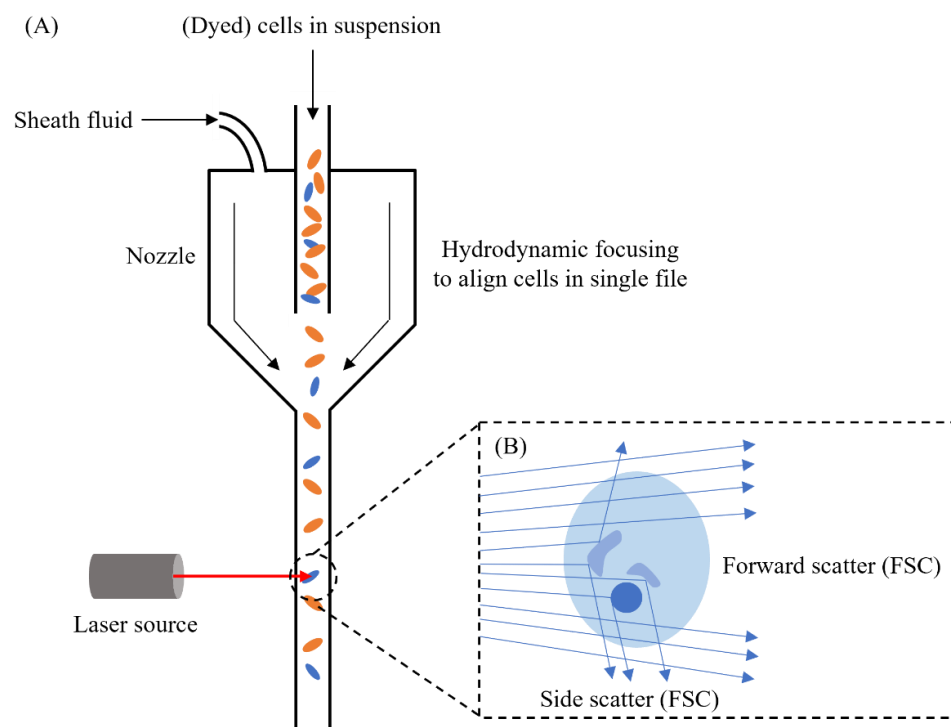


**Figure 1.5:** Schematic of flow cytometry principle, wherein (A) (dyed) cells in suspension are hydrodynamically focused and directed in an axial manner in a narrow stream, where they perpendicularly interact with a laser. (B) As the laser interacts with the single cells, the light is excited and scattered forwards and sideways, depending on the cells characteristics.

Whilst the cell size correlates with the FSC, the granularity of the cells is proportional with the SSC. Thereby, different cell types can be distinguished.

In multicolour FCM, fluorescence emitted from stained cells can additionally be detected at this stage. Therefore, cells must be fluorescently labelled to allow the laser to excite the fluorescent dye. The emitted light is consequently collected by a set of dichroic mirrors and suitable filters. Whilst band pass filters transmit only a specific range of wavelengths, short pass filters transmit wavelengths equal or shorter than a specific wavelength, and long pass filters respectively transmit wavelengths equal or longer than a specific wavelength. This setup enables the separation of specific wavelengths to capture the fluorescence emitted from the cells at specific wavelengths and allow the signals to be directed towards the designated optical detectors (**Figure 1.6**).

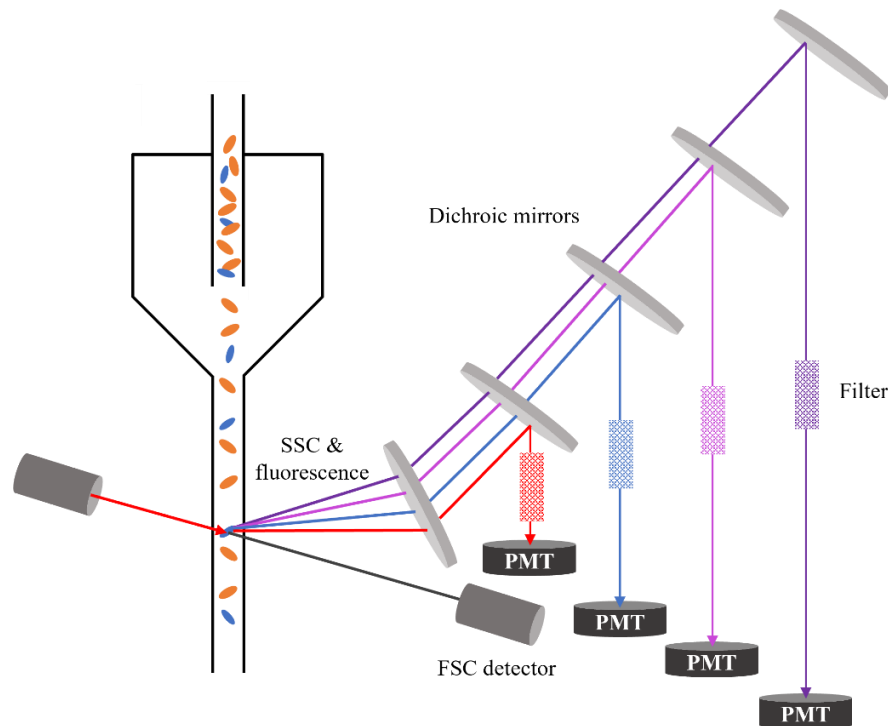


**Figure 1.6:** Schematic of multiple colour flow cytometry, showing how dichroic mirror filters separate specific wavelengths to capture the fluorescence emitted from cells at specific wavelengths, before they are directed towards photomultiplier tubes, which can also detect side scatter. A separate detector detects forward scatter.

In the final step, the signals generated *via* light scattering or fluorescence are converted into electrical current by photodetectors. For that purpose, photodiodes and photomultiplier tubes are commonly used. FSC produces a stronger signal which can

be detected by photodiodes. SSC and fluorescence, however, produce a weaker signal, which can be recorded by photomultiplier tubes (PMTs) as they have a higher sensitivity compared to photodiodes. However, it is worth mentioning that PMTs can only detect fluorescence at a specific wavelength. Therefore, multiple PMTs are required in the setup of a multicolour FCM.

The electric current (analog signal) produced by the photodetectors is finally converted into a digital signal for further computation and analysis [50].

Using this technique, a large amount of information about the singular cells (e.g., cell size, membrane integrity, granularity, or fluorescence features from antibodies or dyes, etc.) can be obtained and associated with specific cell types and cellular components, which makes FCM a popular method in cell function analysis [50]. In TE for example, the activation and phenotype of immune cells (e.g., macrophages) after they were exposed to the scaffold, can be studied [49].

### 1.2.3. Mechanical biocompatibility assessments

In the development of bone TE scaffolds, it is important to consider the mechanical properties of the implant to ensure that it can withstand the forces experienced at the implant site without fracturing [51]. On the other hand, excessive mechanical properties *can cause stress shielding upon implantation which can lead to bone loss and osteoporosis at the damaged site* [32]. In the following sections, common destructive and non-destructive methods for the mechanical assessment of scaffolds are presented.

#### (1) Tensile strength testing

In tensile testing, planar samples, which are gripped at both ends are fractured by applying pulling forces along the longitudinal axis (**Figure 1.7A**). Thereby, information can be provided about the stress-strain behaviour. Typical stress-strain curves for ceramics, metals and polymers are displayed in **Figure 1.7B** [52].

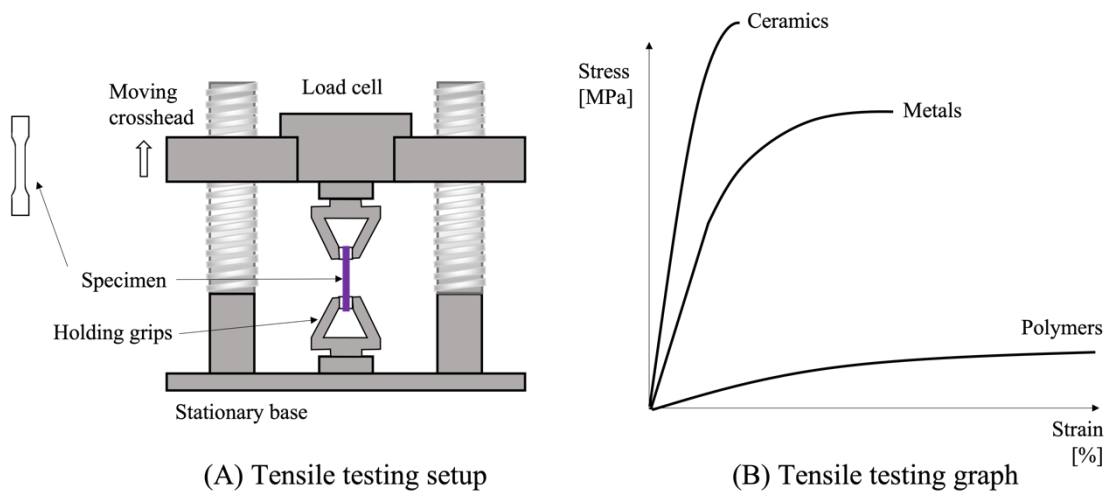


**Figure 1.7:** Schematic of tensile strength testing, showing a sample clamped between two holding grips and pulled at a specific force until fracture occurs. (B) Typical stress-strain curves for three classes of materials.

This technique can also be used to measure the force that is required to break a sample as well as to what extent it can be stretched before fracturing occurs [53].

## (2) Compression strength examination

In compression testing, a cylindrical or rectangular specimen is compressed between two parallel plates in an axial manner (**Figure 1.8**). Thereby, the compressive yield strength as well as the modulus of the specimen can be determined [54].

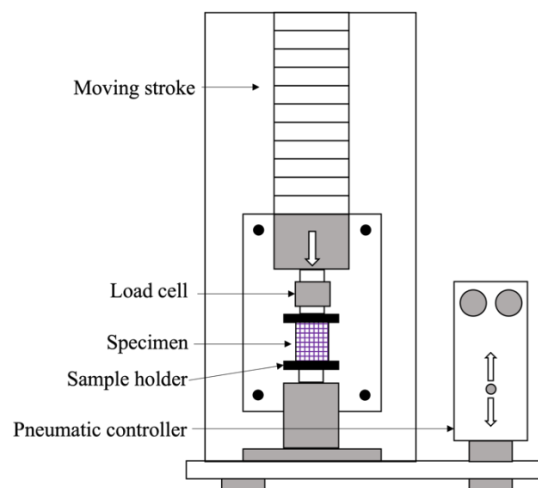


**Figure 1.8:** Schematic of compression strength testing wherein a rectangular or cylindrical sample is compressed between two parallel plates in an axial manner.

In bone TE, compression tests are usually conducted to establish whether the scaffolds compressive strength agrees with the one observed in human bone [51].

Tensile and compressive strength tests are commonly used methods to assess the mechanical strength bone TE scaffold. This is a paramount step in the development of bone TE, as inadequate implant properties can lead to stress shielding of bone tissue surrounding the implant, whilst implants with insufficient tensile and compressive strength can undergo fracture in load bearing regions.

### (3) Nanoindentation

Via nanoindentation, the hardness, elastic modulus, mechanical strength, creep behaviour and fracture toughness of nano- and microscale samples can be evaluated. In this method, a pyramidal or spherical diamond probe indents the sample under a continuously increasing load ( $P$ ), up to a predetermined level ( $h_{max}$ ) (**Figure 1.9**).

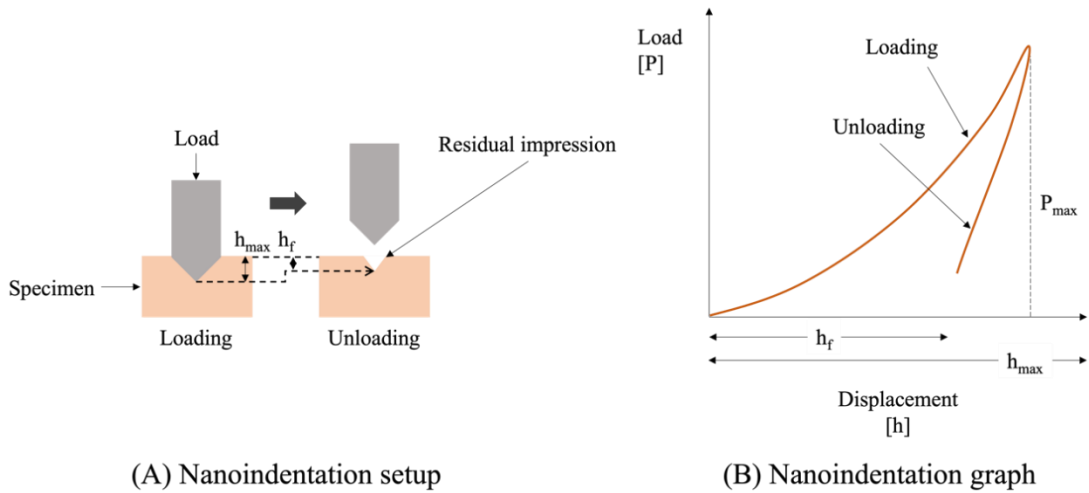


**Figure 1.9:** Schematic of nanoindentation, where a pyramidal or spherical probe is indented under a continuously increased load ( $P$ ), until a predetermined level is reached ( $h_{max}$ ). Once the probe is removed, a residual impression ( $h_f$ ) remains on the sample surface. (B) The nanoindentation graph is comprised of a displacement axis (x-axis) which represents the probe displacement over the course of sample penetration. The y-axis displays the load applied on probe, which increases as the sample is penetrated.

After a consistent predetermined load is applied for a distinct time, the probe is removed from the sample surface. To obtain significant results that can give an insight on material properties, the load parameters shall achieve plastic deformation in the sample of interest, so that after probe removal a mark of a certain depth ( $h_f$ ) can be measured in the area where the load was applied. The resulting displacement-load curve (**Figure 1.9B**) is used to assess the materials' mechanical properties [55]. The sample hardness can be determined by dividing the maximum load ( $P_{max}$ ) by the probe contact area. The obtained value indicates the materials' resistance to plastic deformation. By calculating

the slope from the linear portion of the loading curve, the elastic modulus of the sample can be assessed. The slopes of the loading and unloading curves represent the materials' resistance to deformation and indicate its stiffness [56].

The loading-displacement curve obtained from nanoindentation experiments represents the elastic deformation, occurring in linear to near-linear regions and plastic deformation, occurring after the elastic deformation, in the non-linear region. The curve reaches its peak once the maximum penetration depth ( $h_{max}$ ) is reached. The unloading curve gives an insight about the relationship between the probe displacement and the applied load as the probe is lifted from the sample. By assessing the residual displacement at the end of the unloading curve, the depth ( $h_f$ ) of the mark left by the probe can be determined.

Nanoindentation is a useful tool to measure mechanical properties at small scales and has become an integral analysis method in thin-film development. It is widely adopted to investigate elastoplastic behaviour of metals, polymers, metals, and ceramics. Furthermore, this technique can be applied to gain an understanding of the mechanical properties of regenerating bones at different maturity stages [57][58][59].

#### (4) Dynamic mechanical analysis (DMA)

DMA is a non-destructive, highly sensitive method that is used to study a mechanical and viscoelastic properties of polymers, by applying oscillating stress and measuring the samples strain response at varying temperatures, oscillation cycle duration and frequencies [60] [61]. This allows the operator to test different ranges of temperatures, frequencies or shear rates and assess the modulus for each sequence. Whilst the phase lag between measures strain at specific stress loads reflects the material's tendency to flow (viscosity), the samples' ability to recover from the applied stress load reflects its stiffness (modulus) [62].

**Figure 1.10** depicts the method setup, where a sample is positioned onto a stationary base.

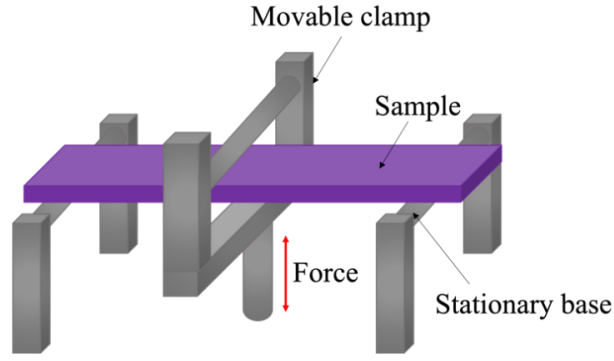


**Figure 1.10:** Schematic of dynamic mechanical analysis, where a sample is positioned onto a stationary base as a force is applied to a moveable clamp, that applies a controlled strain.

When investigating the effect of temperature, samples are mounted in a temperature-controlled chamber. The clamp and sample geometry are adjusted depending on the testing mode. Usually, DMA is used to analyse solid materials, such as films, rods, and scaffolds.

Common frequencies at which DMA system operate between 0.01 and 100 Hz, whereas temperature regions vary between  $-150^{\circ}\text{C}$  and  $300^{\circ}\text{C}$  [62]. A force resolution of 0.0001 N contributes to the methods sensitivity [61].

The applied stress  $\sigma$  is defined as

$$\sigma = \sigma_0 \sin(t\omega + \delta),$$

where  $\omega$  is the frequency of the oscillatory stress,  $t$  is the time and  $\tan \delta \left(\frac{E''}{E'}\right)$  is the phase angle between stress and strain. The strain  $\varepsilon$  is defined as

$$\varepsilon = \varepsilon_0 \sin(t\omega)$$

By defining stress and strain, DMA can provide information about the materials':

- Elastic/storage modulus (the samples' ability to storge and return energy,  $E'$ )

$$E' = \frac{\sigma_0}{\varepsilon_0} \cos \delta$$

- Loss modulus (the samples tendency towards viscous energy loss,  $E''$ )

$$E'' = \frac{\sigma_0}{\varepsilon_0} \sin \delta$$

- And dynamic modulus (the samples' resistance to deformation,  $E^*$ )

$$E^* = E' + iE'' = \sqrt{E'^2 + E''^2} \quad [63]$$

The amplitude of the phase angle and DMA signal (**Figure 1.11** (right)) are used to calculate these values. These values relate to each other as shown in (**Figure 1.11** (left)).

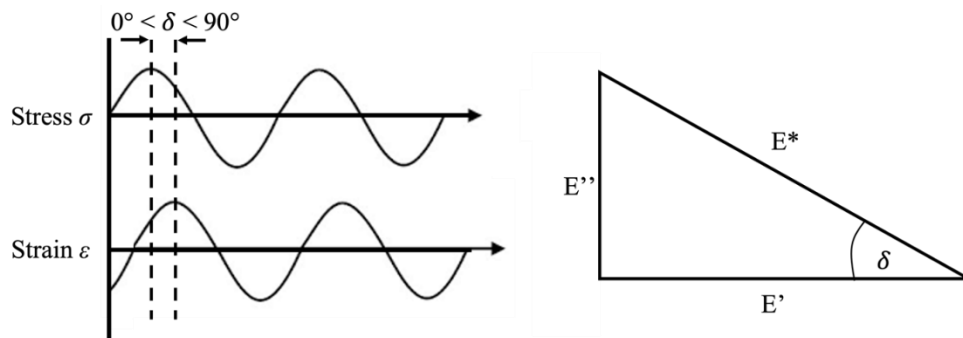


**Figure 1.11:** Relationship between storage modulus ( $E'$ ), loss modulus ( $E''$ ) and dynamic modulus ( $E^*$ ), modified from [64]

Other values that can be retrieved from DMA analysis include:

- Complex shear modulus (samples' resistance to deformation/stiffness,  $G^*$ )

$$G^* = \frac{E^*}{2(1 + \nu)}$$

- Complex viscosity (the samples' dependent viscosity function under oscillating shear stress,  $\eta^*$ )

$$\eta^* = \frac{E^*}{\omega} = \frac{3G^*}{\omega} = \eta' - i\eta''$$

- And complex compliance (also known as inverse modulus, which gives an insight on the samples' willingness to deform,  $J^*$ ) [65]

$$J^* = \frac{1}{G^*}$$

A sinusoidal stress is applied to a moveable clamp at a specific frequency. The resulting strain is calculated for complex modulus ( $G^*$ ) analysis.

If the sample of interest is purely elastic, stress and strain will be in phase. If the sample is purely viscous, the phase angle  $\tan \delta$  will be  $90^\circ$  [63].

Furthermore, transition temperatures, such as glass transition temperature ( $T_g$ ) can be measured *via* DMA through the determination of changes in mechanical properties whilst conducting tests at a set temperature range to obtain a modulus-temperature curve. Herein,  $T_g$  can be recognized as a significant decrease in storage modulus  $E'$  and a significant increase in the loss modulus  $E''$  [63].

In the development of bone scaffolds, an appropriate and stable implant stiffness needs to be accounted for. Ideally these properties shall increase the velocity of cell migration and support the formation of callus.

DMA can be used to assess the samples' mechanical strain and stress response to tensile and compressive forces. Based on the results, the samples' stiffness, compressive and tensile strength can be determined. Herein, the compressive and tensile strength give an insight on the maximum force that can be applied to the material before scaffold breakage occurs. Furthermore, this method can be used to assess stiffness changes occurring over time in gradually mineralizing materials [61].

### **1.3. State-of-the-art bone tissue engineering**

In recent years, major findings have been made in the research of stem cells, cell growth and differentiation, biomaterials, and tissue microenvironments, which have enabled the fabrication of tissue like material *via* TE strategies. TE shows great potential in the field of regenerative medicine by integrating biology with engineering, to develop biological substitutes that can repair or replace organs or tissues [66].

A common approach investigated in bone TE is to seed cells and other biological components, e.g., growth factors, into so-called scaffolds. The fabricated scaffolds act as mechanical support material that templates tissue formation. Seeded cells can be obtained from different sources, such as established cell lines, stem cells or primary cells (autologous, allogeneic, or xenogeneic). The biomaterials used to produce the scaffold should ideally enable cell adhesion and migration, vascularization, diffusion of cell nutrients and support biological functions. After the biological components are seeded into the scaffold, cellular interactions can be triggered by exposing the scaffold to appropriate stimuli. This can be done in a bioreactor system or by implementing other *in vitro* cell culturing techniques [67]. Like this, cell-cell or cell-scaffold interactions, such as cell proliferation and differentiation, or osteogenesis can be achieved [68][69]. Ideally, the formed tissue can be inserted into the patient's damaged site and provide a porous and stable environment that enables bone ingrowth from the damaged site into the scaffold whilst withstanding external forces (**Figure 1.12**).

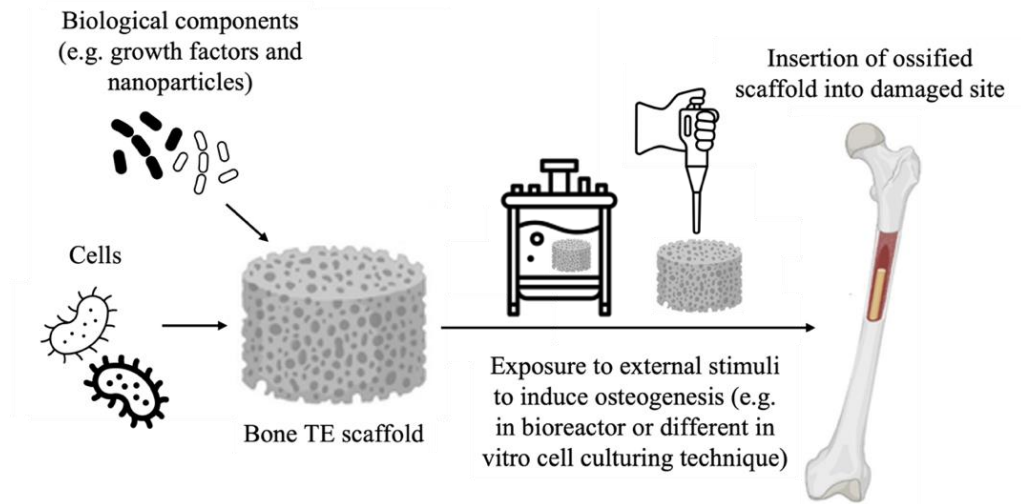


**Figure 1.12:** Bone TE approach schematic, showing how cells and biological components are seeded into a bone TE scaffold before it is exposed to external stimuli that induce osteogenesis in a bioreactor or using a different cell culturing technique. Thereafter, the ossified scaffold is inserted into the damaged site to achieve recovery.

Scaffolds used in bone TE must fulfil certain requirements to support tissue formation, such as to provide:

- Biocompatibility, to avoid cyto- or genotoxicity.
- Interconnected porosity, to allow vascularization of the scaffold, removal of metabolic waste and diffusion of nutrients. For bone TE, the ideal pore size lies between 200 - 900  $\mu\text{m}$ .
- Surface properties that chemically and topographically enable cell adhesion, differentiation, and proliferation.
- Osteoconductivity to achieve bone new formation.
- Preferably a scaffold biodegradability rate that matches the new bone formation rate [68].
- Mechanical properties that can withstand the forces exerted throughout the treatment and can support the scaffolds' own weight, i.e., compressive strength  $\sim 2 - 12 \text{ MPa}$  and Youngs' modulus  $\sim 0.1 - 5 \text{ GPa}$  [36].

Choosing a suitable biomaterial and manufacturing technique for the desired bone TE application is crucial to achieve satisfactory mechanical and biological performance of the scaffold design [70].

In the following, bone TE scaffold manufacturing techniques as well as suitable materials and their limitations are presented.

### 1.3.1. Conventional bone tissue engineering scaffold fabrication methods

Herein, conventional techniques that are used to fabricate 3D TE scaffolds are described.

#### 1.3.1.1. Solvent casting and particulate leaching (SCPL)

In SCPL, a polymer is dissolved in a volatile solvent to synthesize a polymeric solution. Thereafter, a porogen is uniformly distributed within the polymeric solution. Commonly used porogen materials include water-soluble salts, such as NaCl, or organic compounds such (i.e., gelatin or collagen). Thereafter, the solvent is evaporated, resulting in the formation of a polymeric matrix with entrapped porogen. In the final step, the polymeric matrix is submerged in a suitable porogen solvent, causing the porogen to leach out and enabling the formation of a porous network (**Figure 1.13**).

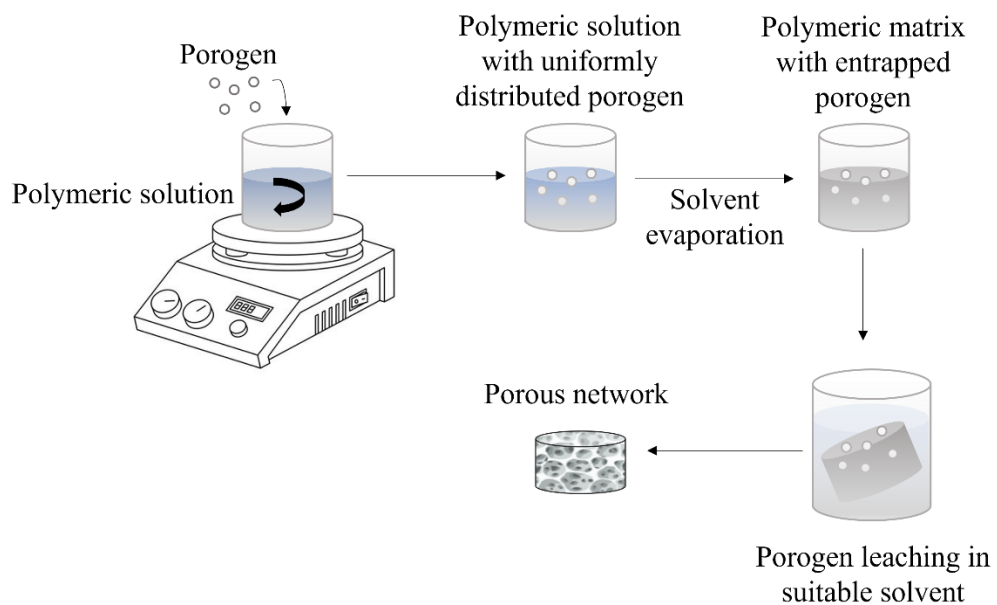


**Figure 1.13:** Schematic of SCPL, wherein porogen is dispersed in a polymer-solvent solution. After the solvent is evaporated, the resulting matrix is immersed in a suitable porogen solvent, leading to porogen leaching and forming a porous network. Modified from [2].

Using this technique, a porosity 88-% - 90% can be achieved at a pore size of approx. 30-300  $\mu\text{m}$ . The pore size can be tuned through modifications of the porogen size or shape as well as variation of the salt/polymer ratio. However, limitations associated with this technique include limited mechanical properties, low controllability of the spatial pore geometry, as well as their interconnectivity, and restricted complexity of the fabricated scaffold geometry. Moreover, the occurrence of cytotoxic solvent residuals and porogen cannot be ruled out [70] [2] [71] [72].

### 1.3.1.2. Thermally induced phase separation (TIPS)

In this technique, a polymer of choice is dissolved in an organic solvent to form a stable, homogenous polymer solution. Thereafter, thermodynamic instability is induced by exposing the solution to low temperatures, triggering phase separation of the solution into a polymer-rich and a solvent-rich/polymer-deficit phase.

The solvent is then evaporated *via* i.e., freeze drying, sublimation or extraction. During this process, the polymer-rich phase forms the resulting scaffold matrix, whilst the solvent-rich/polymer-deficit phase contributes to the formation of pores within the matrix. A process schematic is depicted in **Figure 1.14**.

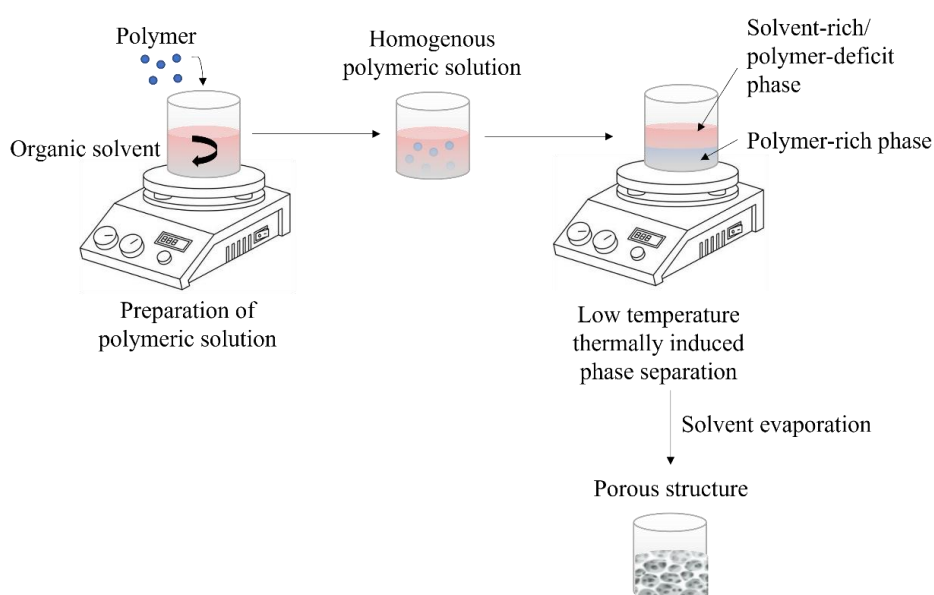


**Figure 1.14:** Schematic of temperature induced phase separation, wherein an initially stable polymeric solution is separated into a polymer-rich and a polymer-deficit phase *via* low temperature thermally induced phase separation. The fabrication of a porous structure is achieved through solvent evaporation. Modified from [2]

Using this inexpensive technique, a large volume of pores (>97%) with high interconnectivity can be produced. The fabricated pores can be controlled in size (>200  $\mu\text{m}$ ). Furthermore, the scaffolds' morphological properties can be tuned by means of process parameter manipulation, such as choice of polymer type and concentration, temperature rate, solvent/non-solvent ratio, as well as presence of surfactant. This method is suitable for organic solvents and polymers with low melting temperatures. However, the use of organic solvents imposes a risk of residues in the final scaffold [70] [2] [73].

### 1.3.1.3. Freeze-drying

Freeze-drying, also known as lyophilization, is, like the previously introduced TIPS method, a phase-separation-based technique.

Herein, a polymer is firstly dissolved to prepare a polymer solution/dispersion. The solvent chosen for polymer dissolution is dependent on the later applied freeze-drying method. For non-emulsion-based freeze-drying, organic solvent alone is used, whereas an emulsion of water and organic solvent is used for emulsion-based methods.

Subsequently, the solution/dispersion is mould-casted and thereafter freeze-dried *via* liquid nitrogen below its triple point, at which all the states of solvent matter (liquid, gas and solid) co-exist. This step enables the sublimation of ice crystals, meaning that solid crystals transform into gas. In a second freeze-drying step, unfrozen components can be removed *via* evaporation. As a result, pores form where ice crystals were previously present, forming a porous, interconnected polymer network [71][74].

**Figure 1.15** shows a schematic for emulsion-based freeze-drying scaffold fabrication.

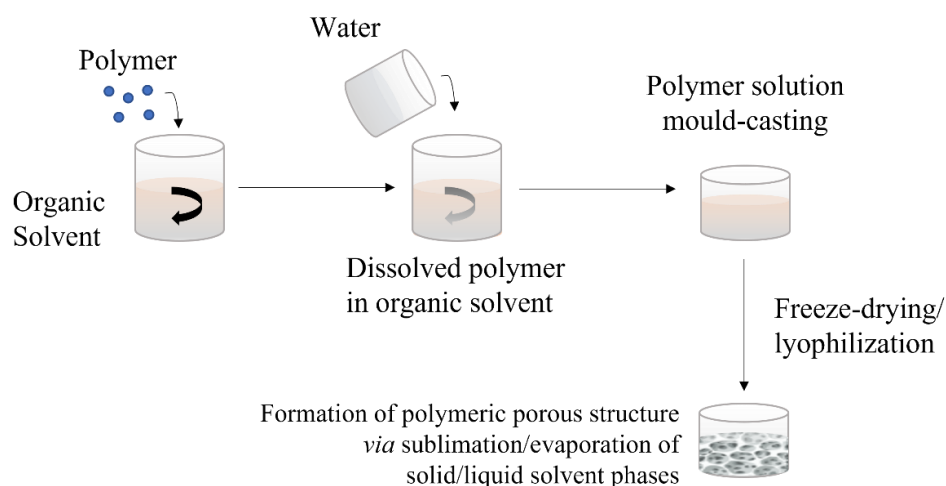


**Figure 1.15:** Schematic of freeze drying, wherein an emulsion of water and polymer solution is mould-casted and thereafter freeze-dried to enable sublimation/evaporation of solid/liquid solvent phases to form a polymeric porous structure.

Using this technique, a porosity of  $> 90\%$  with pore sizes between  $20 - 400 \mu\text{m}$  can be achieved. This method can be applied for natural polymers and molecules, as it does not require elevated temperatures. However, this technique bears a risk of solvent residuals and irregular pore sizes [70][2].

#### 1.3.1.4. Sol-Gel Method

Sol-Gel scaffold fabrication is a physical-chemical method which operates at low temperatures to obtain dense or homogenous constructs. This method is commonly used for processing bioactive glasses and bioceramics [71][75]. **Figure 1.16** depicts the fabrication process.

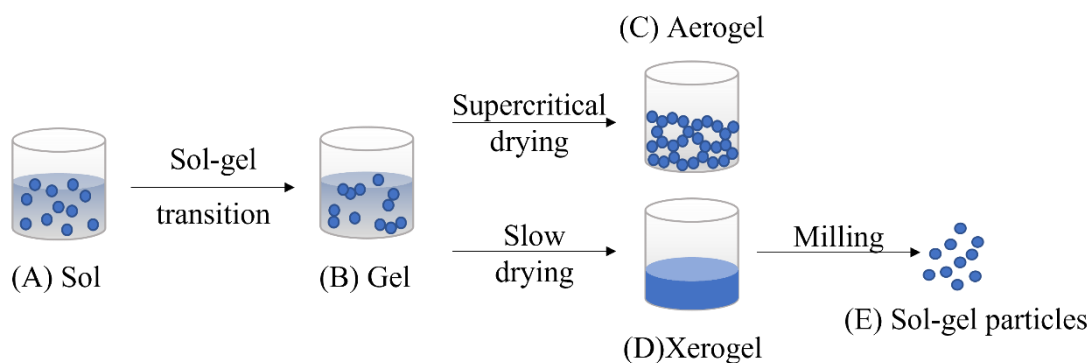


**Figure 1.16:** Schematic of sol-gel fabrication method, wherein (A) a sol is synthesized which forms a (B) gel through hydrolysis and condensation reactions. Depending on the desired final morphology, supercritical drying can be applied to achieve the formation of an (C) aerogel. Alternatively, slow evaporation can achieve the formation of a (D) xerogel, which can be processed to obtain sol-gel particles.

In the first stage of this process, molecular precursor compounds (usually metal alkoxide) are mixed with catalysts, water, and if required, a co-solvent. Thereby, a colloidal solution is created, in which hydrolysis and condensation reactions occur (**Figure 1.16A**). After hydrolysis is initiated, partially hydrolyzed molecules undergo condensation, which leads to polymerization and thereby the formation of larger molecules. Randomly interconnected large molecules form a 3D structure, initiating the second stage of the process.

At this point, the stable porous structure has a solid conformation and is immersed in a liquid medium, that fills internal pores of the 3D construct. The viscosity of the solution exponentially increases as the sol-gel transition occurs (**Figure 1.16B**).

In the third stage, a drying process is conducted to remove the liquid phases in the gel and obtain a solid vitreous or ceramic material. This stage determines the structure of the final solid material. If a supercritical drying process is conducted, an aerogel can be produced, which is mainly composed of air and has a solid volume fraction of approx. 1% (**Figure 1.16C**). If a slow evaporation process is applied, a fragile xerogel is obtained (**Figure 1.16D**), which can be milled to form sol-gel particles (**Figure 1.16E**) [75].

Alternatively, sol-gel foam scaffolds can be fabricated through process modifications, as shown in **Figure 1.17**.

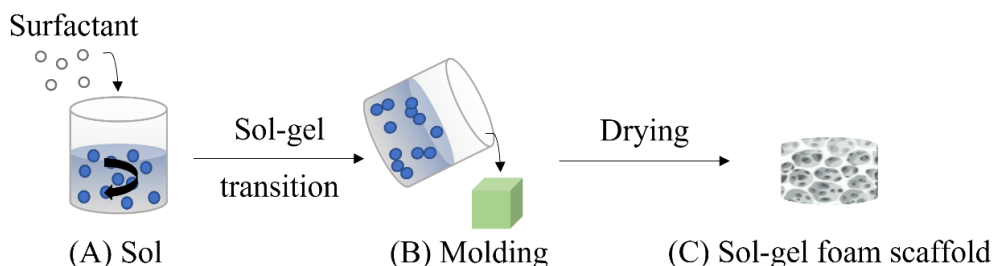


**Figure 1.17:** Schematic of sol-gel fabrication method for sol-gel foam scaffolds, wherein (A) a surfactant is added to the synthesized sol. (B) As the solution undergoes the sol-gel transition, it is poured into a mold that possesses the desired scaffold morphology. (C) By drying the molded structure, a solid scaffold can be obtained.

Herein, surfactant is added in the sol synthesis stage. Thereafter, vigorous agitation of the initial sol prior to gelation is conducted (**Figure 1.17A**). Subsequently, before the sol-gel transition is completed, the solution is poured into a mold that possesses the desired scaffold morphology (**Figure 1.17B**). After drying the structure, a solid 3D scaffold can thereby be produced (**Figure 1.17C**) [75].

#### 1.3.1.5. Gas foaming

In this method, polymer discs are saturated with inert gas, such as CO<sub>2</sub>, creating foams composed of gas and polymer. This causes the pressure in the discs to drop to ambient levels, which induces separation of the gas phase and thereby the nucleation of bubbles. As the gas diffuses over time, pore growth occurs (**Figure 1.18**).

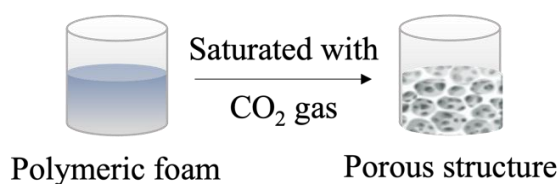


**Figure 1.18:** Schematic of gas foaming, wherein polymer discs are subjected to high-pressure *via* saturation with inert gas, causing the formation of foam. As the pressure drops, phase separation is induced, resulting in a porous structure.

With this technique, a porosity of >93% at pore sizes of 40 – 800 μm can be achieved. Despite the simplicity of the process, lacking interconnectivity of the pores imposes a challenge in the fabrication of bone TE scaffolds [70].

### 1.3.1.6. *Electrospinning*

Using electrostatic forces, fine polymer fibers, which can range from micrometers to nanometers, are created during electrospinning and are accumulated on a fiber collector. The polymer is fed to the capillary tube as a high voltage is used to induce polarity to accelerate polymer filaments from the tip of a syringe to direct them towards a fibre collector, which is either neutral or of opposite polarity to the polymer (**Figure 1.19**).

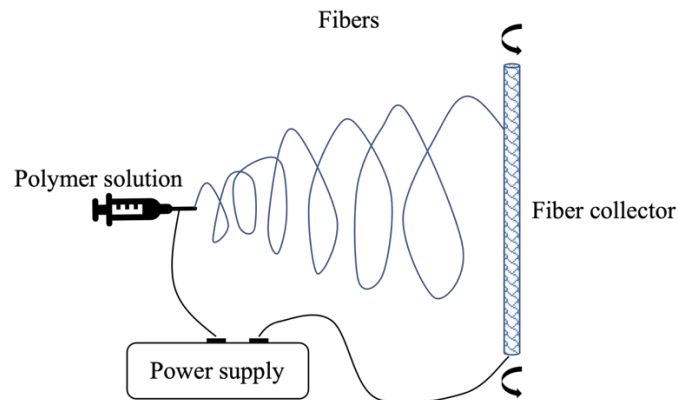


**Figure 1.19:** Schematic of electrospinning, wherein polymer solution is fed through a capillary tube, as high voltage is used to induce polarity to accelerate polymer filaments from the tip of a syringe to direct them towards a fibre collector.

Parameters of interest in this process include the type of polymer that is electrospun, the polymer feed rate, temperature, humidity, as well as the distance between the feeding syringe and the fiber collector. By using this technique, high surface area structures can be produced which mimic natural extra cellular matrix tissue. However, the fibers lack mechanical strength [70].

In **Table 1.4**, advantages, and disadvantages of the herein presented conventional scaffold fabrication techniques are summarized.

<b>Technique</b>	<b>Pore size [<math>\mu\text{m}</math>]</b>	<b>Porosity [%]</b>	<b>Advantages</b>	<b>Disadvantages</b>
Solvent casting and particulate leaching (SCPL)	30 – 300 $\mu\text{m}$	88% - 90%	Low cost, Simple method, controlled and adjustable pore size and porosity [73]	Low control on spatial pore geometry and interconnectivity [70], risk of (toxic) residual solvent/particles, mechanical integrity insufficient for load-bearing applications [73]
Thermally induced phase separation (TIPS)	5 – 600 $\mu\text{m}$	>97%	Inexpensive method, high pore interconnectivity [73]	Only suitable for materials with low melting points [70], risk of solvent residuals, lengthy process [73]
Freeze drying	15 – 35 $\mu\text{m}$	>90%	No need for elevated temperatures [70], high pore interconnectivity [73]	Risk of irregular pore sizes and solvent residuals [70], inadequate mechanical strength in load-bearing applications [73]
Sol-Gel method	>600 $\mu\text{m}$	>70%	Can achieve architecture resembling dry human trabecular bone, fabrication of high surface area structures [73]	Inadequate mechanical strength in load-bearing applications, possibility of solvent residuals [73]
Goas foaming	40 – 800 $\mu\text{m}$	>93%	Simple method [39], no use of toxic solvents, controllable porosity [73]	Inadequate interconnectivity between pores [70], inadequate mechanical strength in load-bearing applications, risk of closing pore structures [73]
Electrospinning	<1 – 10 $\mu\text{m}$	90%	Fabrication of high surface area structures, possibility to mimic ECM tissue [70], high interconnected porosity [73]	Produced fibers have inadequate mechanical strength in load-bearing applications [70], limited sample thickness, possibility of solvent residuals [73]

**Table 1.4:** Advantages and disadvantage of conventional bone tissue engineering scaffold fabrication techniques

In summary, the presented conventional scaffold fabrication methods have limitations with regards to the control over the microstructure, including parameters such as porosity, pore size and geometry and the connection between pores [68]. Furthermore, challenges regarding their mechanical properties are often encountered [70] [72] [73].

Due to tight structural control and the ability to fabricate highly complex structures at high resolutions, Additive Manufacturing (AM) has gained popularity in scaffold fabrication [76].

### 1.3.2. Additive Manufacturing techniques for bone tissue engineering

AM has found numerous fields of application over the past decades, ranging from aeronautics to the food industry. It is particularly useful in product development and rapid prototyping, as it can reduce development costs drastically, whilst diminishing cycle time. To manufacture a 3D-model, a 3D CAD (computer aided design) model is needed. The CAD model is exported to an stl.file, which slices it into thin two-dimensional (2D) cross-sections. The 3D-printer program then generates a g-code.file which determines the print head movement in x-, y- and z- direction to create a physical model in a layer -by-layer fashion.

For the most part, AM is used in engineering and material sciences. The second biggest 3D-printing application area comprises medicine, dentistry, and biotechnology. The pie chart in **Figure 1.20** shows the contribution of AM to different industries and fields of research [77].

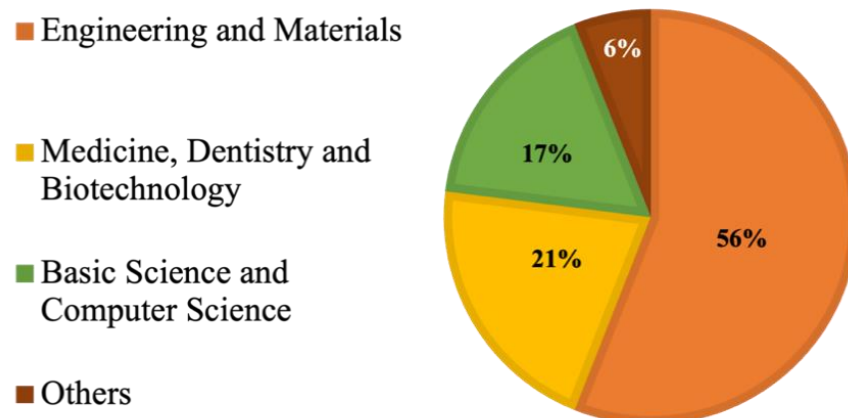


**Figure 1.20:** Pie chart depicting the contribution of AM to different industries and fields of research [77].

The currently available AM technologies can be classified into the following seven categories: VAT polymerization/stereolithography (SLA), material jetting, binder jetting, material extrusion, powder bed fusion, sheet lamination and direct energy deposition [78]. In bone TE, the selection of an appropriate biomaterial and a suitable AM method is crucial to successfully fabricate 3D scaffolds [31].

In the following, AM technologies are described which are commonly used for the fabrication of TE scaffolds. Furthermore, their performance in this field of interest is briefly evaluated.

#### 1.3.2.1. VAT polymerization (SLA-printing)

In SLA-printing, a vat is filled with photopolymer resin. This photo-sensitive material is exposed to UV light in a controlled manner, leading to the formation of polymerized layers of material. After each layer, the building plate of the system is moved upwards, or downwards, depending on the selected system, to form a subsequent layer of polymerized material that adheres to the previously polymerized material, thereby forming a 3D-object (**Figure 1.21**). This method requires post-processing of the manufactured part in the form of drying, post-curing and the removal of sacrificial support structures [79].

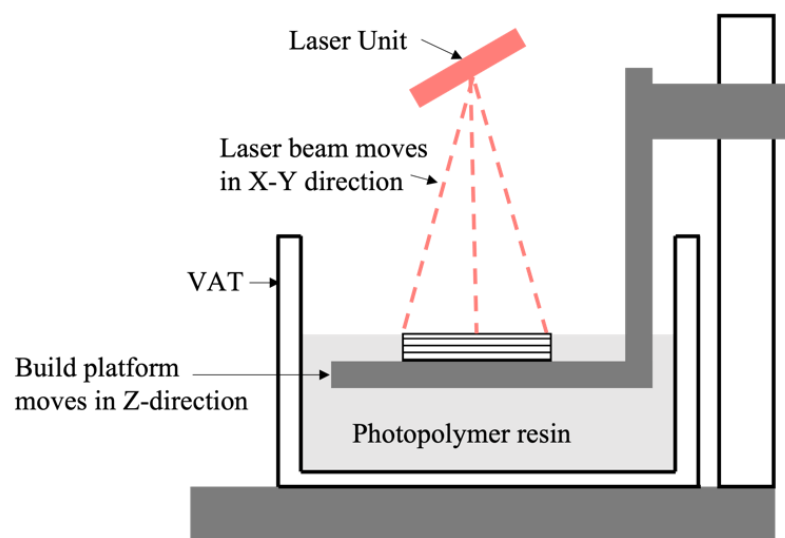


**Figure 1.21:** VAT polymerization printing schematic, showing laser beams curing photo polymeric resin in a VAT in a layer-by-layer fashion as the build platform moves in z-direction after each material layer is cured.

Due to its high resolution and low cost, SLA-printing has emerged as a popular technique in bone TE. Additionally, SLA-printing enables 3D-printing of scaffolds onto which cells can be seeded, and allows direct bioprinting of cell infused resins to produce cell-laden tissue constructs [80]. It has been shown that the ability to integrate osteogenesis inducing growth factors into the resin can improve cell differentiation [81]. However, a risk of unpolymerized monomers remains despite extended curing procedures post-processing, which can induce toxicity and thereby make SLA printed implants unsuitable for TE purposes [82][83].

### 1.3.2.2. *Material jetting*

Material jetting, also known as inkjet 3D-printing, utilizes digitally controlled actuation mechanisms, such as piezoelectric elements, to deposit low viscosity UV curable photopolymers with high accuracy. A schematic of the printing process is depicted in **Figure 1.22**.

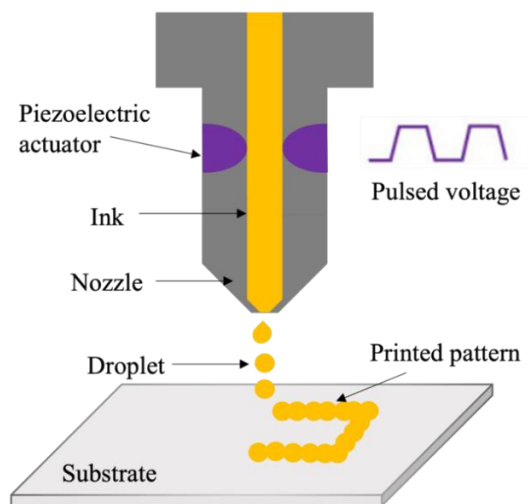


**Figure 1.22:** Schematic of a regular inkjet printing system, wherein a piezoelectric actuator generates a pressure pulse to eject fluid droplets in a controlled manner onto a substrate. *Via* coordination between the motion system and actuator electronics, deposition of custom printed patterns can be achieved [84].

To support overhanging structures, sacrificial support materials, e.g., water soluble resins, are deposited together with the photopolymers and removed during post-processing. In advanced printhead systems, line widths of 20–100  $\mu\text{m}$  can be produced with high accuracy. This technique is widely employed for different applications, such as wearable lifestyle devices, custom anatomical models as well as tissue engineering scaffolds [84].

Despite its advantages, some challenges are associated with this printing technique. These challenges particularly include formulation and optimization of suitable inks and the establishment of appropriate printing parameters and curing procedures. These parameters strongly affect the physical and mechanical properties of the printed constructs. Furthermore, improvements need to be made with regards to the edge and surface quality of printed structures. More limitations that concern inkjet printing include the exposure of cell-loaden material to non-uniform droplet size, mechanical and thermal stress as well as the potential of nozzle clogging, which is a frequently encountered issue in material jetting. [85]

With regards to bone TE, research has shown that inkjet printing of bone tissue scaffold can reach the compressive strength of trabecular bone (1.5 – 38 MPa). However, this compressive strength is not sufficient for the fabrication of cortical bone, which can reach compressive strengths up to 200 MPa [86].

### 1.3.2.3. Binder jetting

Binder Jetting can be used to additively manufacture a variety of powdered materials, such as ceramics, polymers, or metals. Due to the ability to rapidly produce complex structures with isotropic properties, binder jetting is a promising AM technology [87]. In this process, liquid binder is jetted onto layers of powdered material *via* material jetting to selectively join the powder which is then densified (**Figure 1.23**) [88].

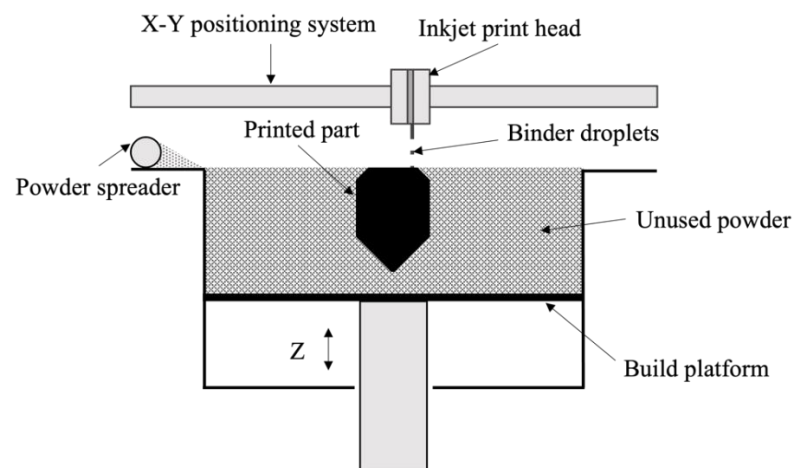


**Figure 1.23:** Schematic of binder jetting 3D printing, showing a powder spreader distributing the material of choice across the powder build platform in an even manner. Thereafter, an inkjet printhead deposits binder droplets into distinct positions in a bed of powdered material to fuse the desired part. The print head is led by a X-Y positioning system, whilst the three-dimensionality of the fabricated part is achieved through movement of the build platform in Z-direction, modified from [88].

Important parameters that need to be considered in this technology include powder characteristics, such as powder morphology, particle size and particle distribution. With regards to the printing process, print orientation and speed, layer thickness, and binder saturation need to be optimized to successfully print parts. Furthermore, drying time in between the layers and post-processing needs to be considered [88]. The main challenges in binder jetting are the high porosity of the final part as well as the shrinkage post-densification and -drying, which is a parameter that is difficult to predict [89]. Binder jetting is a popular 3D-printing technique choice in the fabrication of composite powders to achieve the fabrication of e.g. Hydroxyapatite-based or bioactive glass scaffolds for bone TE [90]. The challenging aspect in binder jetting of HAp scaffolds is the selection of a suitable binder material (amount), that can achieve satisfactory scaffold resolution and strength. Other factors that can influence print quality are the powder particle size and shape, which affect powder flowability, as small particles may enhance the packaging density of the powder bed but can also cause powder agglomeration, leading to decreased flowability [90]. Furthermore, high resolution printing of HAp scaffolds requires the utilization of sacrificial materials [91].

#### 1.3.2.4. Powder bed fusion

In powder bed fusion (PBF), a powder roller spreads a layer of metal powder onto a powder reservoir with a substrate plate in an even manner. *Via* thermal energy, e.g., a laser beam, traces the 2D-geometry of an individual layer of the desired 3D-model is on the powder bed surface. This process is repeated until the 3D-part is produced. Loose powder acts as a supporting material for overhanging structures (**Figure 1.24**) [92].

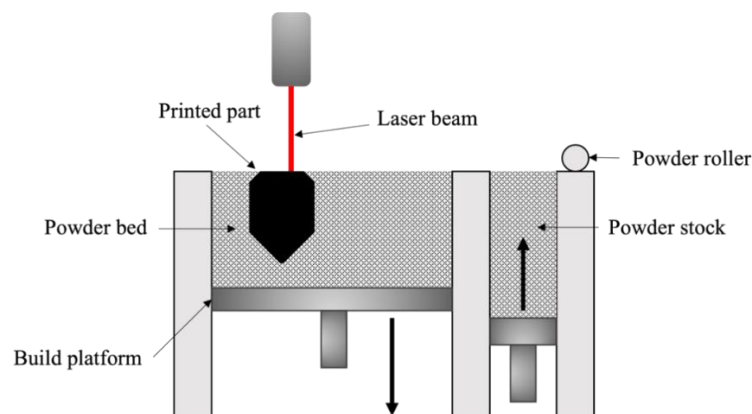


**Figure 1.24:** Schematic of PBF, wherein a powder roller evenly spreads loose powder material from the powder stock onto the powder bed. A thermal source, repeatedly traces the 2D-geometry of an individual layer of the desired 3D-model, forming the 3D-part in a layer-by-layer fashion [92].

A popular biomaterial that can be used in PBF for bone tissue engineering, is titanium (Ti) alloy, as it displays preferable material properties, such as lightweight, corrosion resistance, biocompatibility and high strength [93]. However, disadvantages of this material have been registered in previous research, wherein weak osteoconductivity was observed, which can negatively affect bone regeneration by inducing the formation of fibrous tissue at the interface between bone and metal. Furthermore, the use of Ti in bone scaffolds imposes a risk of osteolysis caused by bone resorption which stems from the Young's Modulus of Ti that is higher than in human bone tissue, causing stress shielding. In addition to that, metal debris can cause inflammation and necrosis *in vivo* [93].

#### 1.3.2.5. Material extrusion

Material extrusion-based AM techniques can be classified into three mechanisms, i.e., plunger-, filament- and screw-based extrusion (**Figure 1.25A, B, C**, respectively).

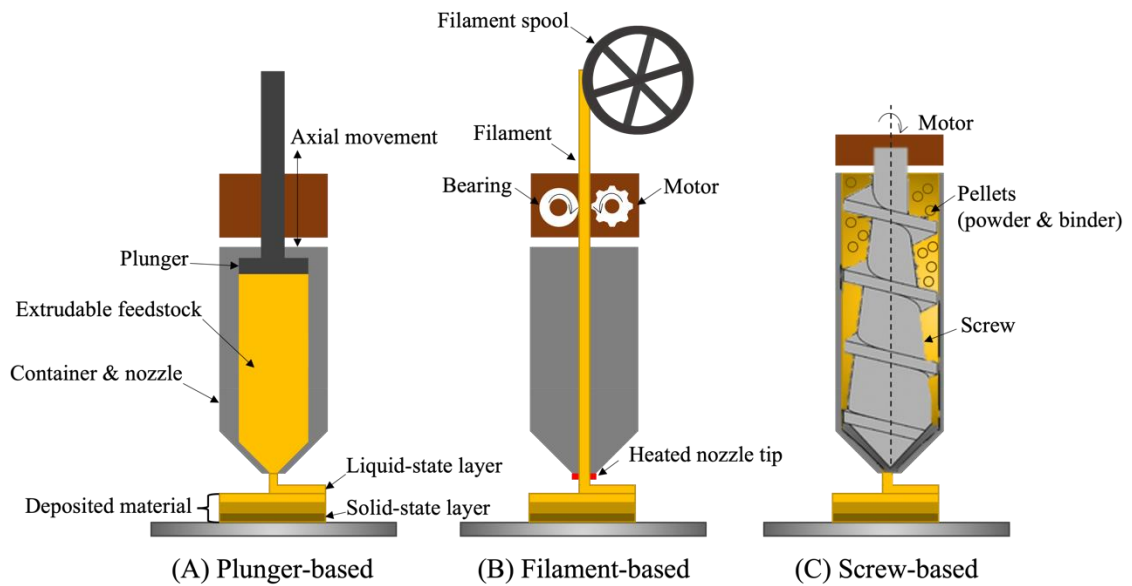


**Figure 1.25:** Schematic of (A) plunger-based material extrusion: A plunger pushes extrudable feedstock through a nozzle through axial movement in Z-direction. (B) Filament-based material extrusion: a motor and bearing wheel rotate in opposite directions to push a filament through the container and a heated nozzle to melt the feedstock. (C) Screw-based material extrusion: A screw, driven by a motor, rotates around its own axis to feed pellets to the nozzle tip. In all processes, the material is in a liquid state when it exits the nozzle and transforms to a solid state once it is deposited onto the substrate to allow layer-by-layer fabrication [94].

In material extrusion (ME), constant input pressure is exerted onto the feedstock to allow continuous feeding of the printing material of interest (e.g., filament, wire, pellets, or viscous pastes/gels) through a nozzle.

Depending on the technique, the contained material is pushed through the nozzle using different mechanisms. Whilst in a plunger system, axial movement achieves material extrusion (**Figure 1.25A**), a motor and bearing that rotate into opposite directions guide a filament through the container in filament-based extrusion (**Figure 1.25B**). Thereafter, the material is heated and melted at the nozzle tip to enable shapely deposition onto the substrate. In a screw-based system, a motor rotates the centered screw around its own axis to transport pellets to the tip of the nozzle (**Figure 1.25C**) [94]. Ideally, the extruded material is in a liquid state at the point of extrusion and solidifies once it is deposited onto the substrate, forming an individual cross-sectional layer of the 3D-printed part. Solidification post-extrusion enables the deposition of a subsequent material layer and thereby AM [95].

The nozzle tip selection is a crucial part of the printing optimization process, as the nozzle inner diameter, length, geometry, and material impact printing parameters, such as printing speed, pressure, extrudability and shape accuracy and fidelity [96] [97] [98]. Generally, material extrudability can be increased *via* selection of a larger and/or shorter nozzle. Conical nozzles improve extrudability compared to cylindrical nozzles. On the other hand, shape accuracy and fidelity can be enhanced *via* selection of a nozzle with a smaller inner diameter. This can however introduce a risk of partial or full nozzle clogging which can negatively impact print accuracy, or fully impede extrudability [98].

A major challenge in material extrusion is the formulation of an extrudable ink. ME is strongly influenced by the rheology of the ink in question [99].

By definition, rheology is the '*study of the physical principles that regulate the flow and deformation of matter subjected to forces*'. In ME, the extruded material of interest is exposed to external forces and undergoes recovery/rest stages. The materials' rheological properties hence strongly impact its extrudability as well as its behaviour throughout the printing process [100].

Before extrusion is initiated, the material is in a resting state. Once an appropriate force is applied, the material undergoes deformation and flows under shear conditions as it moves through the nozzle walls. To initiate extrusion and counteract the resistance to

movement, the applied force is required to be greater than the materials' yield stress. In the centre of the nozzle, increased velocity is experienced compared to the nozzle walls. In contrary, higher shear stresses are experienced at the nozzle walls compared to its centre. Once the material is extruded onto the substrate of choice, it ideally recovers its viscoelastic behaviour after it underwent shear stress induced deformation. Thereby, layer-by-layer constructs with appropriate shape fidelity can be manufactured (**Figure 1.26**) [98].

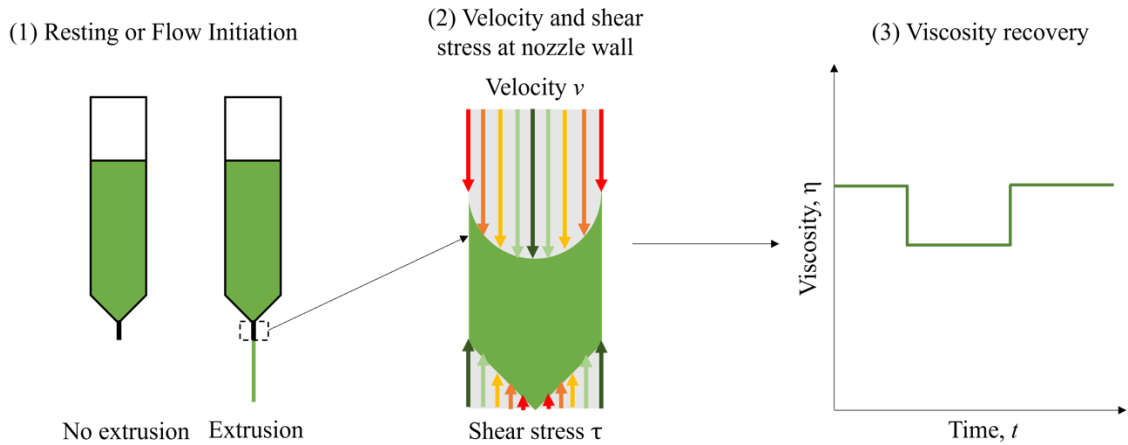


**Figure 1.26:** Depiction of transition stages experienced during ME. (1) After extrusion is induced by applying appropriate forces onto the material stored in a cartridge (2) different velocities and shear stresses are exhibited onto the material as it passes through the nozzle. (3) Thereafter, the material undergoes recovery to achieve the fabrication of 3D constructs.

Rheological properties which strongly contribute to these transitions are the materials' viscosity, its viscoelastic shear moduli, its viscosity recovery behaviour as well as the experienced shear stress. These parameters can be correlated with the materials performance before (**Figure 1.26** (1)), during (**Figure 1.26** (2)) and after (**Figure 1.26** (3)) extrusion [98].

Viscosity is defined as a mediums' resistance to gradual deformation under the impact of shear stress [101]. Whilst the materials' viscosity impacts its flow through the nozzle and how well it will maintain its shape after extrusion, the materials' elasticity determines its response to strain and stress. Consequently, it is crucial to gain an understanding of the materials' gelling mechanism as well as its shear thinning behaviour, viscoelasticity and thixotropy, to optimize the printing parameters and achieve the desired quality and accuracy of performed prints.

Fluids are commonly classified based on how they respond to externally imposed shear stress. The rheological classification is depicted in **Figure 1.27**,

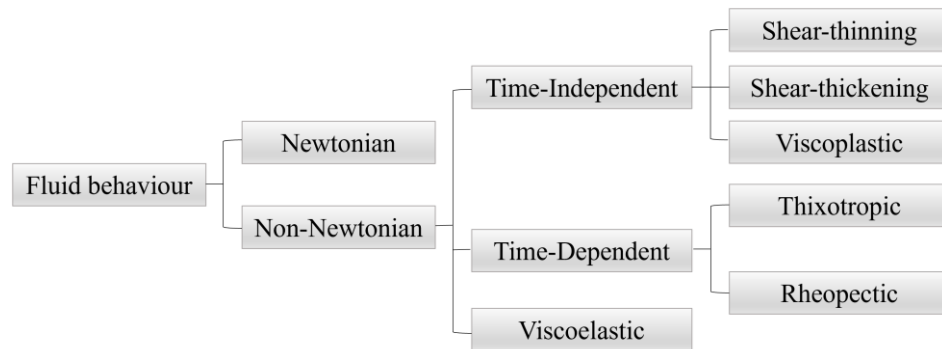


**Figure 1.27:** Flow chart depicting the categorization of fluid behaviour into Newtonian and Non-Newtonian.

Whilst the viscosity of Newtonian materials is independent from the shear strain-rate and time [101], non-Newtonian fluids can be:

1. Time-independent, meaning that the shear stress solely depends on the shear rate applied at a given time point.
2. Time-dependent, meaning that the duration of the applied shear stress and the fluid kinetics impact the correlation between shear stress and shear rate.
3. Viscoelastic, meaning that the material displays partial elastic recovery post-deformation.

The subcategories of non-Newtonian fluids are elaborated on in the following.

#### *Non-Newtonian time-independent fluids*

Shear-thinning fluids are the most common non-Newtonian, time-independent fluids. These viscosity of these materials decreases as the shear rate increases [100]. Shear-thinning behaviour can for example be observed in shower gel, paints, and glues, where the viscosity decreases as the shear rate is increased [101].

Examples of shear-thickening, also known as dilatant materials, are wet sand or starch dispersions, which display an increase in viscosity as shear stress increases [101].

Viscoplastic fluids possess a yield point  $\tau_0$  that needs to be exceeded to initiate fluid flow and deformation. Such materials display a rigid three-dimensional structure

in a state of rest, which can withstand external forces  $< \tau_o$  and display elastic deformation. Once  $\tau_o$  is exceeded, the material behaves like a fluid as its 3D-structure breaks down. If a linear relationship between shear rate and shear stress is exhibited, the fluid is classified as a Bingham plastic. If this relationship is non-linear, it is classified as a Bingham pseudoplastic.

In most viscoplastic materials, the transition from a solid- to a liquid like fluid is reversible. The recovery capacity is material dependent. Examples of materials which exhibit viscoplastic behaviour include jam, egg white or toothpaste [100].

#### *Non-Newtonian time-dependent fluids*

In such fluids, the shear rate magnitude, and its duration, as well as the time lapse between the consecutive applications of those, determine the shear stress. Once the shear stress is no longer applied, the materials apparent viscosity recovers.

Time dependent fluids can be divided into two main categories (1) thixotropic fluids and (2) rheopectic (antithixotropic) fluids. Whilst thixotropic fluids display a viscosity decrease over time when subjected to a constant shear rate (at a fixed temperature), the opposite is the case in antithixotropic fluids (**Figure 1.28**) [100].

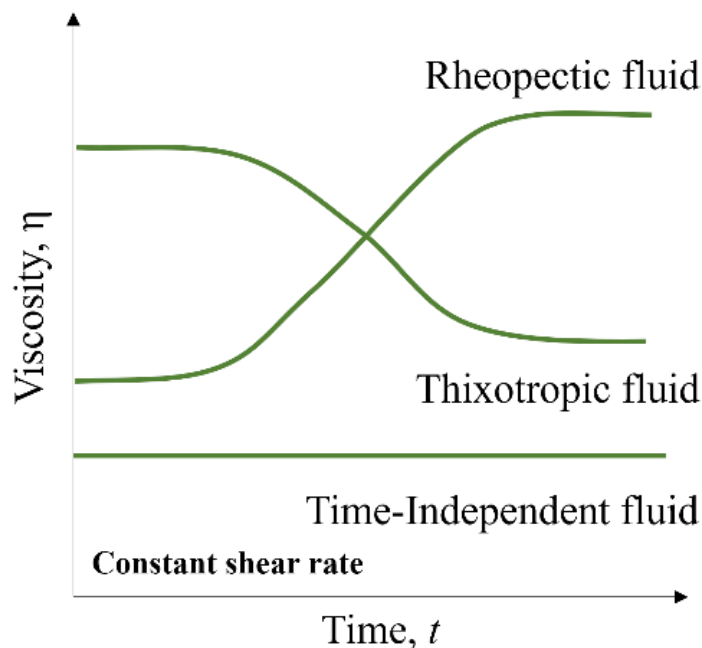


**Figure 1.28:** Graph showing how the viscosity of non-Newtonian time-dependent fluids changes over time under application of a constant shear rate, whereas the viscosity of non-Newtonian time-independent fluids remains constant under such conditions.

### Viscoelastic fluids

The properties of these fluids lie between those of purely viscous and elastic fluids. Such complex materials are often studied *via* dynamic oscillatory shear tests.

In these tests, the material of interest is subjected to deformation in sinusoidal manner, whilst its mechanical response is recorded over time. Depending on the materials' mechanical properties, the recorded sinusoidal curves display a distinct behaviour and relationship between stress and strain (**Figure 1.31**) [100].

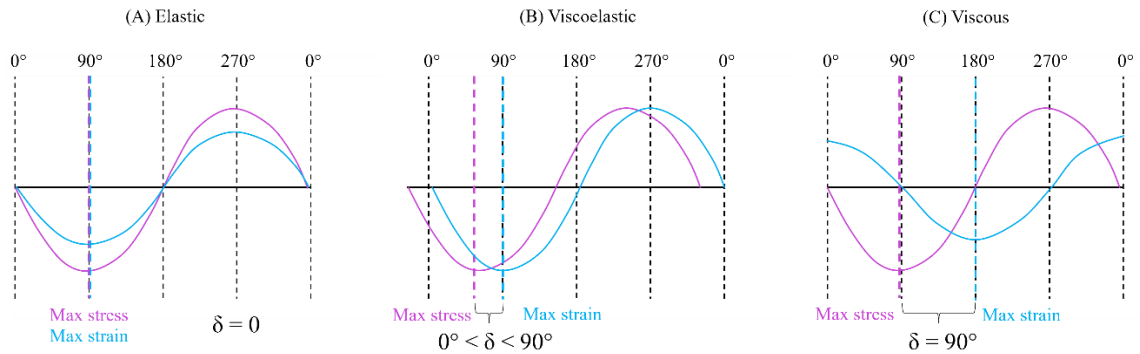


**Figure 1.29:** Stress and strain wave relationships for purely (A) elastic, (B) viscoelastic and (C) viscous material.

The maximum stress and strain coincide in the case of purely elastic material. Furthermore, both stress and strain are in phase, resulting in a phase angle  $\delta = 0^\circ$ . In purely viscous materials however, maximum stress occurs when maximum strain is peaking. This results in a phase shift of  $90^\circ$  between stress and strain. Most commonly, samples display viscoelastic behaviour. Herein, the phase shift between stress and strain lies between these extremes, resulting in  $0^\circ < \delta < 90^\circ$  [100].

In the following figure, the relationships between shear stress and shear rate (**Figure 1.30A**), and between viscosity and shear rate (**Figure 1.30B**) of the herein presented materials are presented.

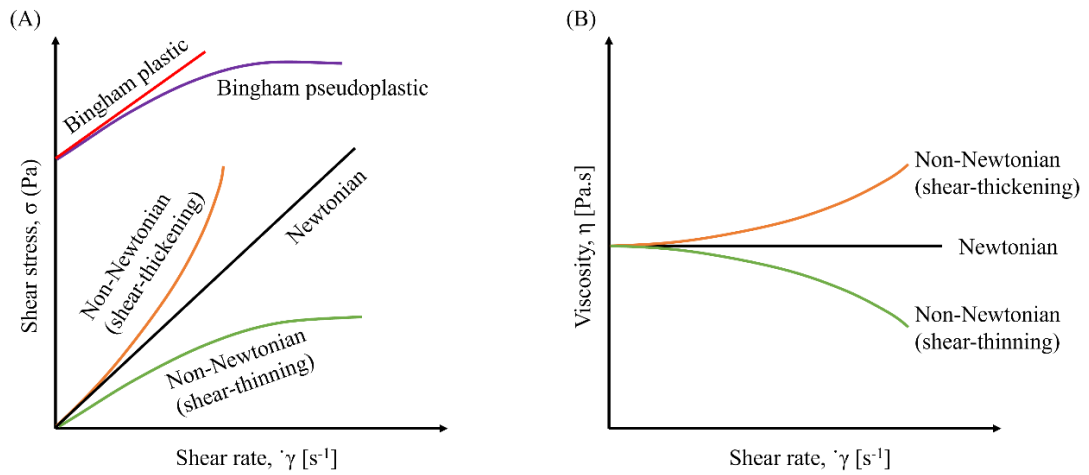


**Figure 1.30:** Graph showing the relationship between viscosity and shear rate in different types of fluids (Newtonian and non-Newtonian) [102].

Viscosity ( $\eta$ ) is an indicator of how much force is needed to maintain a certain rate of flow in a fluid and can be defined by Newton’s law of viscosity:

$$\tau = \eta \frac{du}{dy}$$

where shear stress [ $\tau$ ] acts to deform the material in the flow direction, and  $[\frac{du}{dy}]$  represents the fluids’ velocity gradient that is perpendicular to the flow. Hence, materials with a higher viscosity show stronger resistance to flow (e.g. honey), whereas lower viscosity materials flow more easily (e.g. water) [102].

The rheological properties majorly impact the printability of an ink at three stages, of which each plays an important role in the printing process. The stages are represented in **Figure 1.31**.

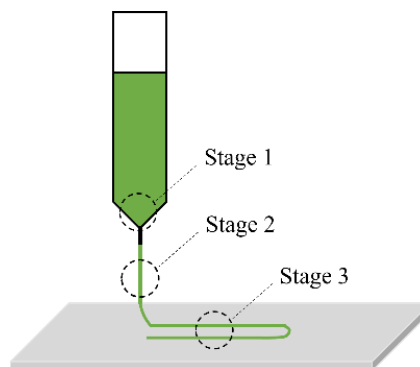


**Figure 1.31:** Three different stages of rheological bio ink evaluation (1) flow initiation (2) study of viscoelastic and thixotropic behaviour, (3) post-printing recovery assesses the materials viscosity recovery time.

- (1) The first critical stage occurs at the nozzle, before ME occurs. Ideally, the viscosity of the material of interest should rapidly decrease as soon as an external force is applied to the resting material. This shall allow for easy ME through the nozzle. Simultaneously, the materials' viscosity shall sufficiently recover once the force is removed, to avoid deposition of material during print head movement. Consequently, well performing inks should exhibit pseudoplastic behaviour by showing a decrease in viscosity under shear stress and possessing a yield point  $\tau_0$  that needs to be exceeded to initiate fluid flow and deformation.
- (2) Once the material exists the nozzle, it needs to recover a higher degree of viscosity and exhibit mechanical resistance to minimize deformation and enable uniform material flow. At this stage, the material's viscoelastic properties determine whether the material mainly exhibits elastic or viscous behaviour. This property impacts both the filament shape and shape fidelity of the printed construct. Herein, the thixotropic properties of the material greatly contribute to its viscosity recovery ability. Rapid thixotropic behaviour enables shape integrity and maintenance of extruded material. Furthermore, it allows to control material flow and enables deposited material to retain its shape post-deposition.
- (3) The layer-by-layer construction represents the third critical stage. The performance of this stage is also impacted by the materials' viscosity recovery time and the filaments' internal structure after undergoing stress induced deformation. At this stage, the material shall ideally develop self-supporting capacity in a timely manner to be able to be exposed to the weight of material layers deposited subsequently, without losing its integrity by deforming under the impact of gravity of the merging of consecutive layers [100].

By adjusting the material formulation, its rheological properties can be optimized. Parameters that can be altered are, e.g., type and concentration of materials, additives, or cells and their concentration. Once the velocity of the material flow is determined, a window of printability needs to be determined, which defines at which printing settings structures can be produced which provide satisfactory print quality [103].

ME is a popular technique in TE and it allows processing of temperature sensitive materials [104]. Despite the comparatively high control over the structural arrangement of scaffolds, extrusion 3D-printing in bone TE is still facing numerous limitations. These include poor mechanical strength, shape complexity and issues with neovascularization, inappropriate degradation rate, cell attachment and immune response. Furthermore, the viability of cells and growth factors throughout the printing process remains a major challenge [105]. Hence, research in the development of appropriate printable materials and suitable printing parameters is still ongoing [27] [106].

**Table 1.5** summarizes the advantages and disadvantages of herein presented AM techniques.

<b>AM method</b>	<b>Advantages</b>	<b>Disadvantages</b>
Stereolithography	Minimal waste, ability to recycle unused resin, high resolution [83]	Requires post-processing, risk of residual (toxic) monomers, costly, excessive curing can cause warping [83]
Material Jetting	Particularly high accuracy, broad scope of applications [84]	Difficult establishment of appropriate printing parameters and curing procedures, limited edge and surface quality, non-uniform droplet size, mechanical and thermal stress exhibition on printing material, prone to printer head clogging [85]
Binder Jetting	Suitable for ceramics and glass [90]	Low surface resolution, requires post-processing, high porosity, hard to predict shrinkage after post-processing [89]
Powder bed fusion	Minimal waste, ability to recycle unused powder, high resolution [83]	Costly, high operating temperatures [83]
Material Extrusion	Enables low-temperature deposition, low cost, enables direct integration of cells [83]	Poor mechanical strength, limited shape complexity resulting in issues with neovascularization, limitations in application to biodegradable polymers, resulting in inappropriate degradation rate, limited cell attachment [105] and [83]

**Table 1.5:** Summary of advantages and disadvantage of AM bone TE scaffold fabrication techniques.

### 1.3.3. Common materials in tissue engineering scaffold fabrication

Different materials have been explored to meet biological, structural, and mechanical requirements of bone TE scaffolds. Most commonly, metals, ceramics, and polymers, as well as their composites have been studied towards their ability to support and promote osteogenesis [36].

#### 1.3.3.1. *Metals in bone tissue engineering scaffold fabrication*

Historically, metals (e.g., Titanium (Ti-6Al-4V), stainless steel 316 L, Cobalt based alloys or Magnesium) have been used for plates, screws and prostheses [107].

Their mechanical strength provides structural stability in load-bearing applications – properties, which have drawn attention to their use in the fabrication of porous bone scaffolds. However, metals generally exhibit a higher elastic modulus than human bone. Upon implantation, this can cause unfavoured consequences, such as stress shielding and resorption of surrounding bone tissue. Furthermore, metallic implants can release of toxic metallic ions/particles upon wear or corrosion, which may lead to inflammation or allergic reactions and thereby negatively impact biocompatibility, which can lead to tissue necrosis. Further drawbacks include properties, such as non-degradability and fatigue [5][36].

In addition to that, as mentioned in *chapter 1.2.1*, metals often fall into the category of bioinert biomaterials, meaning that implants do not interact with biological tissue or fluids. This property imposes a disadvantage due to lack of biological implant recognition on its surface. [31][5].

The mechanical properties of different metals define their suitability for the fabrication of porous structures. For instance, some metals possess insufficient mechanical properties to obtain their structural integrity in a porous construct, whilst other metals are too stiff to manufacture scaffolds for load bearing applications, as they could easily fracture. Furthermore, the processibility is varies amongst metals [5].

Metallic scaffolds can commonly be fabricated *via* the sol-gel method, powder bed fusion (PBF) or sintering based methods, as well as binder jetting [108].

The following section provides an overview of the benefits and drawbacks of commonly studied metals for bone TE scaffold fabrication.

### *Titanium and Titanium alloys*

In general, Titanium-Aluminium-Vanadium alloys, e.g. Ti6Al4V, possess more suitable mechanical properties than pure titanium [5].

Titanium (Ti) and its alloys are nearly bioinert in a human body environment, resulting better biocompatibility than stainless steel or chromium-cobalt alloys. Furthermore, Ti forms a stable TiO<sub>2</sub> film on its surface which enhances biocompatibility and enables strong corrosion resistance.

However, the excessive mechanical properties of Ti6Al4V alloy can cause stress-shielding upon implantation. In addition to that, the material lacks bioactivity and therefore profits from surface modification *via* e.g., bioactive coating.

Furthermore, the presence of vanadium in Ti-6Al-4V has raised concerns, as this element is toxic in its elemental state. Therefore, new Titanium alloys are being investigated in which toxic elements are substituted for alloying non-toxic elements such as Tantalum (Ta) [5][109].

### *Tantalum*

Tantalum (Ta) is a bioactive metal that displays both, good biocompatibility, and resistance to corrosion. Using this material, highly porous (>80%), interconnected scaffold can be manufactured which enable reliable bone ingrowth. Moreover, porous structures based on Ta show sufficient mechanical strength to display structural integrity in load-bearing applications.

However, its large elasticity modulus and weight, limits Tantalum in its suitability for clinical applications. Therefore, as previously mentioned, Ta is often used in Titanium alloys, such as Ti-Ta-Nb-Zr alloys, to achieve the generation of porous structures with reduced weight and elasticity modulus, compared to pure Ta scaffolds [5][109].

### *Magnesium and Magnesium alloys*

Magnesium (Mg) and its alloys have displayed great potential for surgical applications, as they do not induce inflammation, are osteoconductive, support cell attachment and have been shown to be bioresorbable, thereby reducing the risk or need for secondary scaffold removal surgery. Furthermore, the materials' mechanical properties strongly resemble that of human bone, qualifying it for load-bearing applications.

However, even though dissolved pure Mg can be removed by the body *via* urine, its ability to be resorbed by the body has raised toxicity concerns as the risk of hypermagnesemia, which can cause general unwell being in patient, remains due to the materials rapid dissolution rate [5].

#### *Nickel-titanium alloys (Nitinol)*

Apart from showing enhanced biocompatibility, compared to stainless steel, porous Nitinol possesses novel properties, including superplasticity, high damping properties and shape memory effect (SME), meaning that post-implantation, shape change can be initiated as the scaffold is imposed to human body temperature. Furthermore, the elastic modulus and compressive strength of Nitinol foams resemble that of the bone.

However, the toxicity and potential carcinogenicity associated with the release of Ni ions has raised concerns in the development of Nitinol [5].

#### *1.3.3.2. Ceramics in bone tissue engineering scaffold fabrication*

Hydroxyapatite (HAp), Calcium Phosphates (CaP) and Tricalcium Phosphates (TCP) are popular and versatile bone substitute materials which show a similar composition to bone mineral, have a tailorable biodegradability compared to other ceramics, and show excellent biocompatibility with no risk of immunogenicity. Furthermore, the compressive strength is comparable to that of trabecular bone.

It has been observed that osteogenesis related cells, such as osteoprogenitor cells and osteoblasts, are more prone to attach to rough, mineralized surfaces. These materials enable the fabrication of highly interconnected porous scaffolds and can thereby promote bone ingrowth as well as vascularization. Furthermore, cell differentiation towards an osteoblastic phenotype is more likely to occur when the mechanical properties of the inserted scaffold match those of naturally biomineralized material [61]. In the pursuit of bone regeneration scaffold enhancement, biomineralized materials, that grow or incorporate HAp into bone scaffolds, have shown better performance than non-biomineralized materials. One of the reasons for this improved performance is the release of calcium and phosphate ions occurring upon HAp degradation, which trigger an osteogenic response and thereby improve scaffold osteoinductivity [36] [61].

However, the use of ceramic-based scaffolds is limited due to their high brittleness, which makes them unsuitable for load-bearing application. This limitation can be

overcome through the synthesis of composite ceramic-polymer materials, which profit from the durability of polymers, whilst exhibiting excellent biocompatibility properties.

The most popular AM technique that is used in ceramic scaffold printing is binder jetting, whilst the sol-gel manufacturing technique is a commonly used conventional technique [36].

#### *1.3.3.3. Polymers in bone tissue engineering scaffold fabrication*

Due to their versatile properties and excellent tunability, polymers have emerged as promising candidate in bone TE. A broad range of fabrication techniques can be applied in the generation of polymeric scaffolds, including solvent casting, freeze drying, gas foaming, phase separation, electrospinning, FDM, ME, SLA (for photosensitive polymers) etc. They can be divided into two main groups natural polymers and synthetic polymers. Biodegradable polymers are of particular interest in this field, as they have the potential to support tissue regeneration prior to being resorbed by the body. The advantages and drawbacks of natural and synthetic polymers are presented in the following sections [36].

##### *Natural polymers*

Due to their excellent biocompatibility and confirmed ability to facilitate cell growth, natural polymers are of particular interest for bone TE. Natural polymers commonly used in this field include silk fibroin, chitosan, collagen, hyaluronic acid, as well as alginate. Properties of natural polymer scaffolds (e.g., porosity, mechanical properties, etc.) can be tuned by varying their concentration or the applied fabrication technique.

Furthermore, natural polymer scaffolds show a unique ability to improve tissue regeneration through the incorporation of ECM binding domains. Another advantage of natural polymers is the ability to fabricate 3D hydrogel networks. These constructs have a high water content (>90%), show structural stability, and enable homogenous cell encapsulation, making them promising candidates for the fabrication of biocompatible TE scaffolds.

However, the degradation rate of natural polymers is difficult to control. Furthermore, they can display insufficient mechanical properties in load-bearing applications [36].

### *Synthetic polymers*

The main advantage of scaffolds fabricated from synthetic polymers is the ability to tune the polymers' properties, resulting in controllable degradation rates as well as adjustable mechanical properties. Furthermore, synthetic polymers can be sourced more reliably than natural polymers. Through the synthesis of composite materials, bioactivity properties can be enhanced. However, in contrast to naturally sourced polymers, the organic synthesis of polymers limits tissue-scaffold interactions due to the lack of bioactivity and introduces a risk of toxic degradation byproducts.

Amongst others, common synthetic polymers used in bone TE include Poly(lactic acid), Polycaprolactone, Poly(glycolic acid) and Poly(DL-lactic–glycolic acid) (PLGA) [36].

**Table 1.6** summarizes the advantages and disadvantages of commonly used materials in bone TE.

<b>Materials</b>	<b>Examples</b>	<b>Advantages</b>	<b>Disadvantages</b>
Metals	Tantalum, Magnesium, Titanium (alloys), Nickel-titanium alloy (nitinol)	Strong mechanical properties, structural stability in load-bearing applications	Higher elastic modulus than bone, risk of stress shielding and bone resorption, ion release, fatigue, limited integration, fibrous tissue formation
Ceramics	Hydroxyapatite, Calcium phosphate, Tricalcium phosphate/, bioactive glasses, Calcium sulfate	Biocompatible, can be biodegradable, versatile, osteoconductive, osteoinductive, enable neovascularization, similar mechanical properties, and mineral composition to human bone	Brittle, prone to fracture/fatigue
Natural polymers	Silk fibroin, chitosan, collagen, hyaluronic acid, alginate, collagen, gelatin	Biocompatible, biodegradable, osteogenic	Lack of mechanical properties for load bearing applications, difficult to control degradation rate
Synthetic polymers	Poly(lactic acid), polycaprolactone, poly(glycolic acid), poly(DL-lactic–glycolic acid) (PLGA), poly(ethylene oxide), poly(propylene fumarate)	Tunable properties, reliably sourced	Unfavourable degradation byproducts, lack of bioactivity

**Table 1.6:** Advantages, disadvantage and suitable fabrication methods for conventionally used bone tissue engineering scaffold fabrication materials [36] [1].

As previously mentioned, the development of hybrid or composite biomaterials, which combine multiple materials into a superior matrix, synergizes beneficial properties of each constituent. For example, combining polymers with other materials provides the ability to tune the composites' mechanical properties and degradation kinetics, which can positively impact cellular interactions and encourage host tissue integration.

As previously highlighted, scaffold integration into the host tissue can be enhanced using biomineralized biomaterials.

In nature, biomineralization is guided by living organisms and defined as the formation of hierarchically structured organic–inorganic materials. Examples of biomineralization include bone, teeth, and shells [110]. For bone regeneration, the main aim is to generate the biomineralization of material similar to HAp, which is found in natural bone. HAp is mainly formed of calcium and phosphate and has a Ca/P ratio of approximately 1.67 [36].

Conclusively, particular attention has been drawn to the development of ceramic-polymer hybrid materials. The addition of ceramics to a polymeric scaffold can enhance osteoconductivity and enables improved bone-bonding potential through the introduction of an inorganic phase. Thus, a bioactive scaffold can be generated that enhances tissue formation and provides improved structural scaffold integrity, compared to pure ceramic scaffolds [111].

Despite these advances, further development is required to improve the performance of these composites. Unsatisfactory mechanical behaviour and poor dispersion of polymers limit their use in the synthesis of composite materials. Additionally, poor interfacial bonding can result in undesired mechanical properties with insufficient structural uniformity [112].

As few biomaterials possess all the necessary characteristics desired in TE, expanding the toolbox of materials has become a crucial aspect in this research field [113].

Peptides do not only play an essential role in fundamental physiological processes, but they have also been found to play a crucial role in the biomineralization process [114]. Additionally, several peptides can contribute to osteogenic differentiation, mediate angiogenesis and facilitate cell adhesion, which has drawn attention to their potential for bone TE. Furthermore, they provide a viable alternative to growth factors, as they are less costly and easier to synthesize [115].

In previous work, elastin like polypeptides (ELPs) were used to propose an innovative platform for hard tissue repair.

Whilst peptides are short strings of 2 to 50 amino acids, joined together *via* covalent bonds [116], polypeptides, also known as protein molecules, are made up of multiple amino acid chains, that are linked to one another *via* covalent peptide bonds [117].

Flexible tissues, such as blood vessels and ligaments, owe their elastic properties to the peptide elastin. Elastin is composed of hierarchically assembled tropoelastin monomers, which are flexible enough to undergo self-assembly without negatively impacting tissue. This property has drawn attention to modified tropoelastin sequences in the field of TE [118][119].

Through peptide functionalization *via* chemical (e.g., hydrolysis, oxidation, etc.) or physical methods (e.g., entrapment, self-assembled monolayer formation, etc.) its functionality can be expanded. The peptides' chemical composition and its amino acid sequence dictate suitable functionalization methods [113].

#### **1.4. Elastin like polypeptides in tissue engineering applications**

ELPs are genetically engineered polypeptides that are inspired by tropoelastin and are highly biocompatible. They are produced by applying DNA technologies that enable the preparation of block-copolymers with individual blocks of specific amino acid sequences. These sequences can be tailored to exhibit certain biological, physical, and mechanical properties for specific applications.

ELPs are composed of the following repeating pentapeptide sequence:

***V (Valine) - P (Proline) - G (Glycine) - X (Guest residue) - G***

where **X** can be any amino acid, except proline.

For example, a lysine (**K**) guest residue can enable site-specific cross-linking, *via* covalent bonds through reaction with the primary amine [120]. Other possible stimuli include light responsiveness, protein concentration and size, pH and presence of salt [121]. The tuneable stimuli responsiveness of ELPs has found applications in medical fields, such as drug delivery and TE, through the synthesis of self-assembling nanoparticles and hydrogels [122][123].

Cross-linked ELP hydrogels are of particular interest for TE applications. However, physical as well as chemical cross-linking strategies impose challenges in the synthesis of such hydrogels.

Physically cross-linked ELP hydrogels often show insufficient mechanical integrity. By forming covalent cross-links between ELP chains through the integration of lysine into the amino acid sequence, the stiffness of ELP hydrogels can be increased. However, many chemical cross-linking agents (CLAs) are toxic and/or require dissolution in non-biocompatible organic solvents [124].

Furthermore, these polypeptides demonstrate reversible lower critical solution temperature (LCST) behaviour, meaning that below their characteristic transition temperature ( $T_t$ ), ELPs are soluble, whilst above  $T_t$ , they undergo supramolecular self-assembly to form insoluble macromolecules. As previously mentioned, triggering stimuli can be tailored to the desired application through amino acid sequence modification [122].

In the following, drivers of supramolecular self-assembly are elaborated on.

#### 1.4.1. Supramolecular self-assembly

In nature, supramolecular assemblies can for example be observed in the formation of phospholipids in cellular membranes. Biological processes, such as molecular transport and release or cell-extracellular interactions are also guided *via* supramolecular assembly. The ability to synthesize biomaterials, such as hydrogels, nanoparticles, capsules or coating films, that can undergo supramolecular assembly has opened a variety of new routes in disease treatment and diagnosis [125]. Generally, self-assembly is the result of an interplay of non-covalent interactions, which include hydrophobic interactions, hydrogen and ionic bonding, and  $\pi$ -stacking [126].

Hydrophobic interactions are a key component in protein self-assembly. They are defined by the proneness of nonpolar groups or molecules to accumulate in water and thereby exclude water molecules. One example of hydrophobic interactions is the assembly of micelles, which are composed of amphiphilic peptide building blocks, that mimic surfactant molecules. They are composed of a polar hydrophilic head and a non-polar hydrophobic tail [126] (**Figure 1.32**).

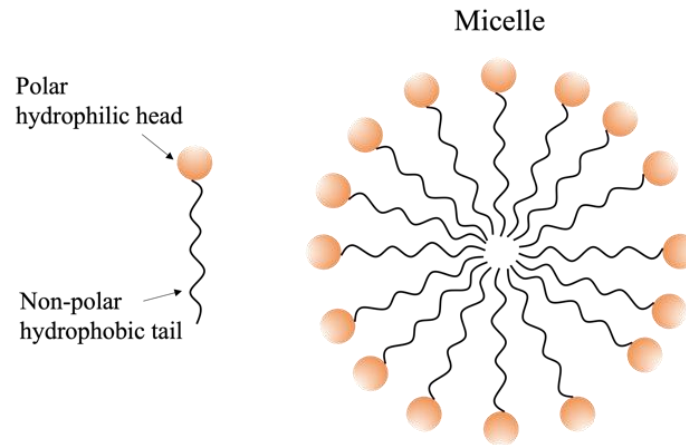


**Figure 1.32:** Structural composition of a micelle, consisting of surfactant molecules with a hydrophilic head and a hydrophobic tail.

Higher hierarchical organization of protein nanostructures are supported through ionizable residue sidechains, which can undergo ionic bonding. Ionic bonding involves electrostatic interactions between ions of opposite charge or between two atoms with sharply different electronegativities [127]. Ionic bonds are formed *via* the transfer of one or more electrons between two or more atoms [128]. **Figure 1.33** depicts ionic bonding using the example of sodium chloride, wherein a Sodium (Na) atom donates an electron to Chlorine (Cl). This results in a positively charged ion, also called cation, ( $\text{Na}^+$ ) and a negatively charged ion, also called anion ( $\text{Cl}^-$ ), forming a stable ionic bond.

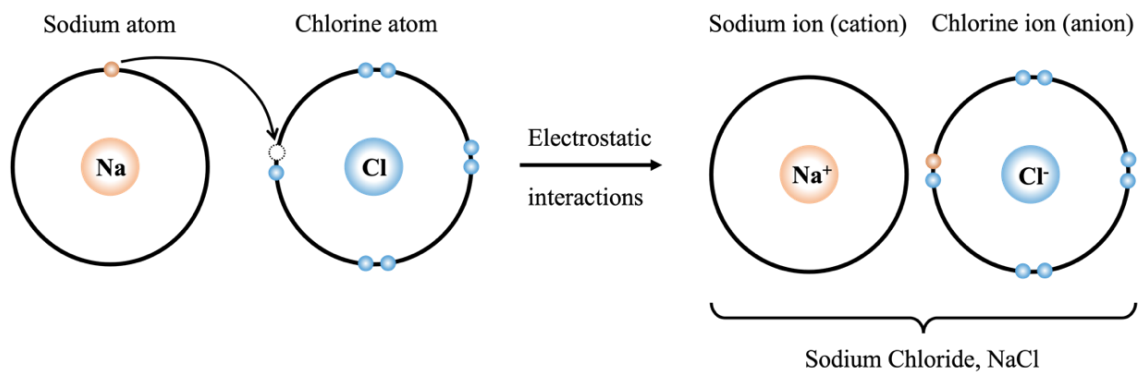


**Figure 1.33:** Ionic bonding in sodium chloride, wherein the donation of a sodium (Na) electron to chlorine (Cl) results in a positive  $\text{Na}^+$  cation and a negative  $\text{Cl}^-$  anion, forming a stable ionic bond.

In protein assemblies,  $\pi$ -stacking refers to interactions between cations and neighbouring aromatic rings (cation- $\pi$ ), or between neighbouring aromatic rings ( $\pi$ - $\pi$ ). These interactions are increasingly considered to be important in the structural formation of proteins and their underlying functionalities [126].

The formation of hydrogen bonds often contributes to directionality in protein folding and therefore is crucial in assembly of the protein secondary structures [126]. Hydrogen bonding is a strong intermolecular interaction between a Hydrogen (H) atom and a more electronegative atom or group, e.g., Oxygen (O). **Figure 1.34** depicts H-bonding in water ( $\text{H}_2\text{O}$ ).

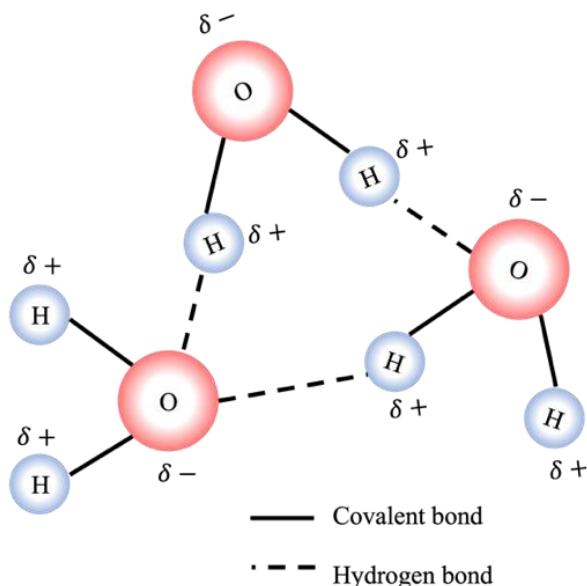


**Figure 1.34:** Hydrogen bonding caused by intermolecular interactions between hydrogen (H) and oxygen (O), forming water ( $\text{H}_2\text{O}$ ).

As previously mentioned, the self-assembly in ELPs can be tailored through amino acid sequence modification. Whilst the unmodified amino acid sequence represents the primary protein structure, modifications (i.e., stretches) of the polypeptide chain form  $\alpha$  helices and  $\beta$  sheets, constituting the protein secondary structure [117].

#### 1.4.1.1. Protein secondary structure

Protein secondary structure is mainly composed of  $\alpha$ -helix and  $\beta$ -strand motifs ( $\beta$ -pleated sheets and  $\beta$ -turns), which are stabilized by H-bonds between amide hydrogens and carbonyl oxygens of the peptide backbone [129]. Another relevant region of proteins which does not fall under the mentioned categories are random coils, which are unstructured regions [130].

### *$\alpha$ -helices*

In  $\alpha$ -helical structures, the backbone of the polypeptide is wound around the long axis of the molecule, whilst the amino side chains (R) stand out from the helical backbone (**Figure 1.35**). Each carbonyl oxygen (residue,  $n$ ) of the  $\alpha$ -helix polypeptide backbone is interconnected to the backbone amine hydrogen of the fourth residue further towards (residue,  $n + 4$ ) the C-terminus *via* a H-bond. These intermolecular H-bonds run almost parallelly to the helices' long axis [129].

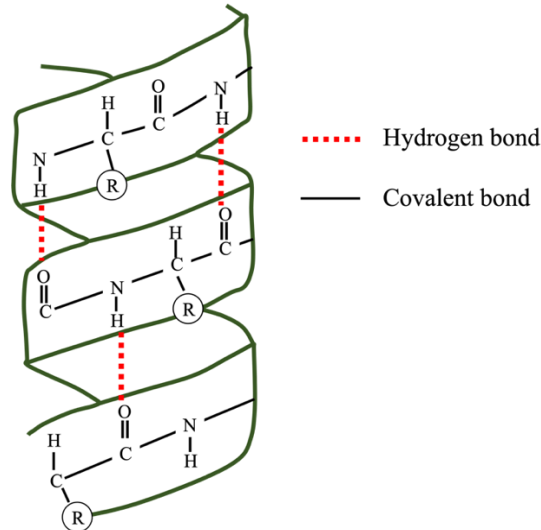


**Figure 1.35:** Structural organization of a typical  $\alpha$ -helix, wherein in the hydrogen bonds are represented as dotted lines between the residues  $n$  and  $n+4$ .

### *$\beta$ -pleated sheets and $\beta$ -turns*

$\beta$ -pleated sheet, also known as  $\beta$ -sheets, involve two or more polypeptide chains, which are called  $\beta$ -strands. In this motif, H-bonds form between residues of different polypeptide chains. As a result, the H-bonds that connect the  $\beta$ -strands are oriented perpendicularly to the polypeptide backbones (**Figure 1.36**) [130].

The  $\beta$ -strands in the  $\beta$ -sheets can run parallelly or antiparallely. In a parallel orientation, the  $\beta$ -strands run in the same N- to C-terminal (**Figure 1.37B**), whereas they run in opposite N- to C-terminal directions in antiparallel orientations (**Figure 1.37 A**).

$\beta$ -turns are composed of four polypeptide chains and often connect antiparallely, causing the polypeptide chains to turn back onto themselves [129].

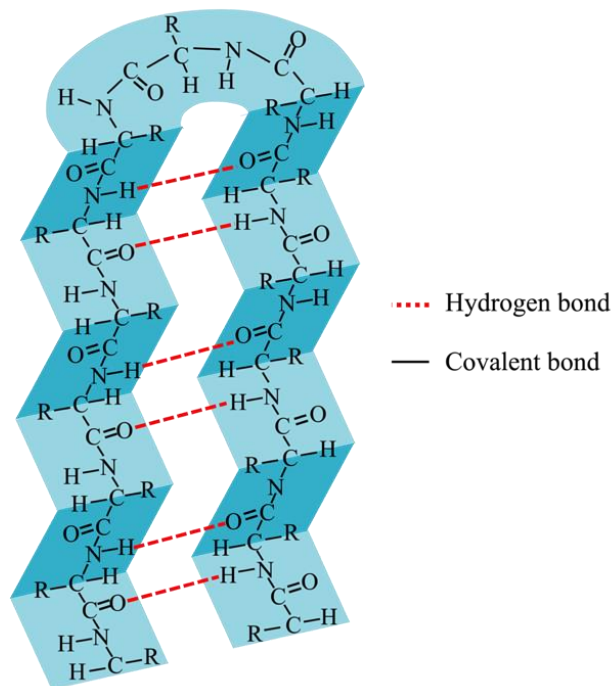


**Figure 1.36:** Structural organization of  $\beta$ -pleated sheets, wherein H-bonds connect two or more polypeptide chains ( $\beta$ -strands). H-bonds are oriented perpendicularly to the polypeptide backbones.

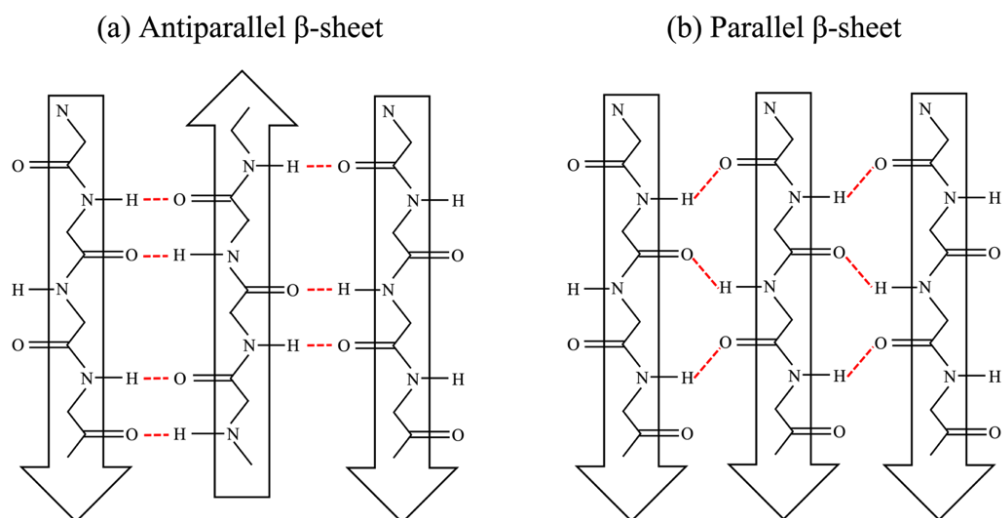


**Figure 1.37:** Depiction of parallel vs. antiparallel orientation  $\beta$ -strands. (a) Parallel orientation:  $\beta$ -strands run in the same N- to C-terminal, as indicated by the arrows. (b) Antiparallel orientation:  $\beta$ -strands run in opposite N- to C-terminal direction, as indicated by the arrows.

Common techniques that can be used to analyse the protein secondary structure are Raman spectroscopy, circular dichroism (CD) spectroscopy and Fourier transform infrared (FTIR) spectroscopy [131].

#### 1.4.1.2. Protein secondary structure analysis

##### Fourier transform infrared spectroscopy

FTIR analysis a useful technique for chemical identification which can identify a material *via* infrared (IR) light scanning. An IR spectrum is created through absorption or emission of liquid, gas or solid. This can be useful to characterize (in)organic and polymeric materials [132] [133]. In FTIR spectroscopy, IR light is passed through the sample of interest, causing molecules in the sample to vibrate. The amount of absorbed IR light at specific wavelengths and its intensity is measured [134]. The signal that is obtained post absorption represents the materials' molecular fingerprint, which is unique to every molecule [132] (**Figure 1.38**).

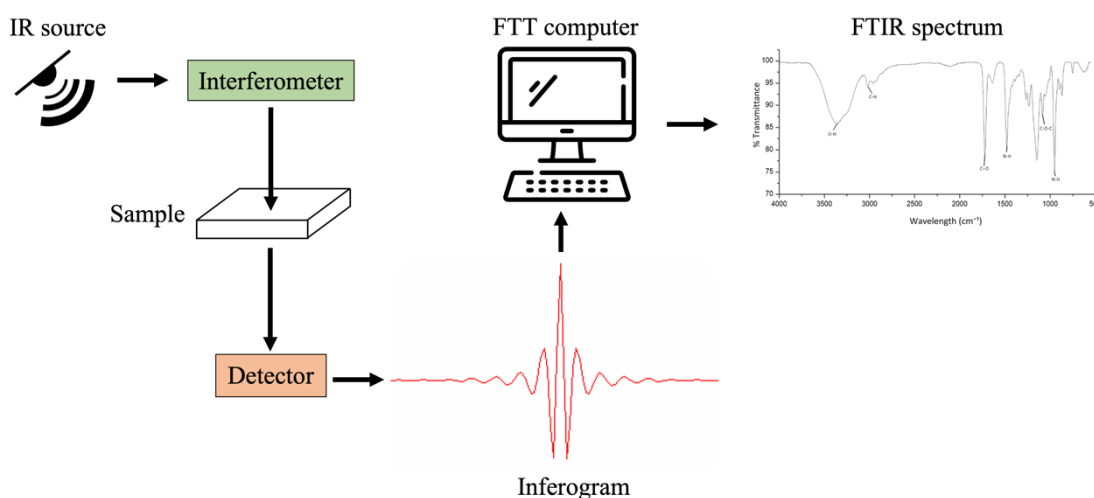


**Figure 1.38:** Schematic of FTIR spectroscopy, wherein IR light is passed through the sample of interest, which causes molecules in the sample to vibrate. The amount of absorbed IR light at specific wavelengths is measured to create a spectral fingerprint of the sample which is represented in the FTIR spectrum.

The wavenumbers [cm<sup>-1</sup>] is represented on the X-axis of the spectral FTIR graph. The wavenumber corresponds to the wavelength and is the standard unit used in FTIR spectroscopy. The Y-axis in FTIR spectra, depending on the selected settings, represents the light absorbance, which is measured in absorbance units [AU] or the light transmission [%] at each specific IR wavelength that is passed through the sample. Whilst transmittance measures the amount of light passed through the sample of interest and sets it into relation to the incident light, absorbance measures the amount of light absorbed.

Each peak in an FTIR spectrum stands for the specific vibrational modes of different functional groups in the sample and is associated with a particular bond or group in the molecule. Commonly represented functional group peaks include C-H stretches (3000 – 2800  $\text{cm}^{-1}$ ), O-H stretches (3600 – 3200  $\text{cm}^{-1}$ ), C=O stretches (carbonyl groups) (1750 – 1650  $\text{cm}^{-1}$ ), N-H stretches (3300 – 3500  $\text{cm}^{-1}$ ) and C-O stretches (1300 – 1000  $\text{cm}^{-1}$ ). Strong peaks indicate a high relative amount of functional group presence [135].

FTIR spectroscopy can also be used to determine the secondary structure in proteins and polypeptides [134]. Polypeptide and protein molecules display many vibrational frequencies. These characteristic group frequencies [ $\text{cm}^{-1}$ ] are identified and categorized as follows: amide A (~3,300  $\text{cm}^{-1}$ ), amide B (~3,100  $\text{cm}^{-1}$ ), amide I (~1,650  $\text{cm}^{-1}$ ), amide II (~1,550  $\text{cm}^{-1}$ ), amide III (~1,300  $\text{cm}^{-1}$ ), amide IV (~735  $\text{cm}^{-1}$ ), amide V (~635  $\text{cm}^{-1}$ ), amide VI (~600  $\text{cm}^{-1}$ ) and amide VII (~200  $\text{cm}^{-1}$ ). These vibrational amide bands can be traced in terms of in-plane and out-of-plane displacement. Herein, C=O stretching, C-N stretching, N-H stretching, OCN bending, and CNH bending are in-plane, whereas C-N torsion, C=O and N-H bending and out-of-plane. Differential patterns in geometrical orientation and H-bonding of amine bonds are assigned to  $\alpha$ -helices,  $\beta$ -sheets,  $\beta$ -turns, and random coils. This allows different frequencies to be assigned to secondary structural folding. Usually, amide absorbance is represented as a single band. Therefore, deconvolution of the overlapping bands is required *via* contour, band-narrowing methods and curve fitting [134].

#### Raman spectroscopy

Raman spectroscopy is a noninvasive and inexpensive method that can be used to quantitatively characterize modified proteins and amino acids. The method does not require extensive sample preparation and proteins be studied *in situ* as the method water insensitive [136][137].

In this method, like in FTIR analysis, the generated spectrum is dependent on the protein secondary structure and the vibrations of the amide groups in the peptide bonds [137]. The difference between the incident and the scattered radiation frequencies that are passed through the sample of interest are reported as the Raman spectra. Conclusively, the types of peptide bonds and their modes of vibration determine the scattered radiation frequencies. Thereby, the supramolecular protein building blocks can be detected [137][138].

As previously mentioned, FTIR results are based on the absorption energy of vibrating chemical bonds, such as stretching and bending motions. Raman spectroscopy can provide information on the same types of transitions.

In Raman spectroscopy, the characteristic group frequencies [ $\text{cm}^{-1}$ ] are characterized as previously specified for FTIR analysis. The two techniques can provide complementary information as they amplify obtained frequencies at different intensities, so that weak peaks in FTIR may be more prominent in Raman and *vice versa* [138].

### Circular dichroism

Light is defined as an electromagnetic wave. It can be characterized by its travel direction and the electric and magnetic fields which are perpendicular to each other. Whilst in linearly polarized light, the vector of the electric field oscillates in one plane, as shown in **Figure 1.39A**, circularly polarized light rotates around the axis of propagation at a constant amplitude, as depicted in **Figure 1.39B**.

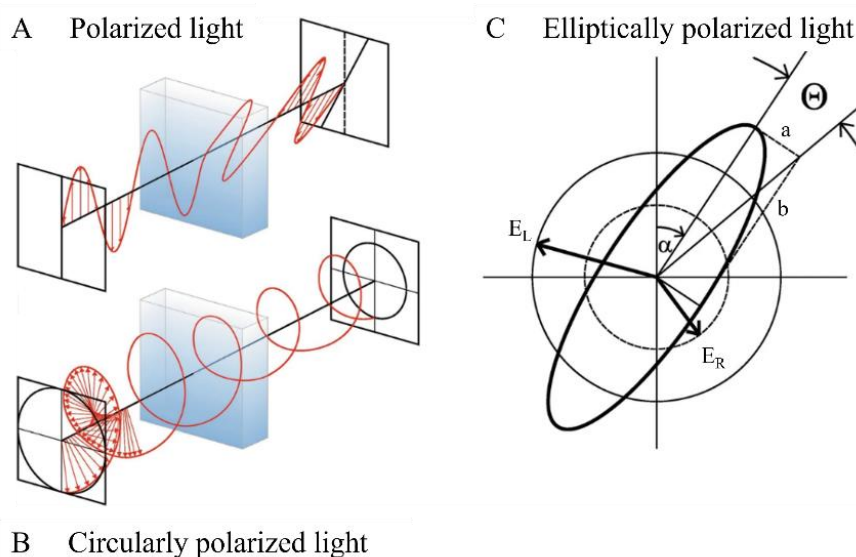


**Figure 1.39:** (A) Depiction of polarized light, wherein the vector of polarized light rotates in one plane as it passes through the sample. (B) Depiction of circularly polarized light which propagates at a constant amplitude whilst penetrating the sample. (C) Electric field vector of circularly polarized light, rotating clockwise ( $E_R$ ) and counter clockwise ( $E_L$ ) at different amplitudes and thereby creating elliptically polarized light, wherein angle alpha represents the optical rotation of the plane of polarization as light interacts with material with chiral properties. Modified from below [139]

As light travels towards the observer, the electric field vector rotates clockwise and counterclockwise respectively, representing the right ( $E_R$ ) and left ( $E_L$ ) circularly polarized lights, as highlighted in **Figure 1.39C**.

If the amplitudes of left and right circularly polarized light are equal, their summation results in linear polarized light (**Figure 1.39A**), whereas unequal amplitudes of left and right circularly polarized result in elliptically polarized light (**Figure 1.39C**). Angle  $\alpha$  in **Figure 1.39C** represents the optical rotation of the plane of polarization as light interacts with optical active material with chiral properties in a polarization dependent manner. This angle corresponds to the differential absorption between right and left circularly polarized light in circular dichroism (CD) [139].

Protein secondary structure *via* CD is based on this phenomenon, as electronic transitions of peptide bonds contribute to the CD spectrum of proteins in the far-UV region between 170 and 250 nm. Distinct, characteristic spectral profiles can be exhibited by polypeptide chains with different conformations. Thereby, proteins of distinct architecture, such as  $\alpha$ -helices (negative band near 222 and 208 nm, and positive band near 192 nm), parallel and antiparallel  $\beta$ -sheets (negative band near 216 and near 175 nm, and a positive band between 195 and 200 nm), as well as disordered regions (negative band near 200 nm) can exhibit characteristic spectral shapes in CD and hence enable the determination of the secondary protein structure.

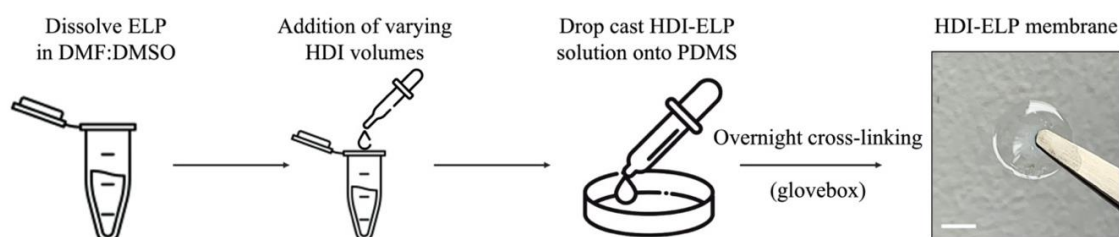
However, the position and magnitude of the mentioned bands can vary, which limits the accuracy of predicting  $\alpha$ -helices and  $\beta$ -sheets in this method [138][139].

#### 1.4.2. SN<sub>A</sub>15 elastin like polypeptides in hard tissue engineering applications

Previously published work has proposed the use of SN<sub>A</sub>15 ELP molecules for the fabrication of biomineralizing membranes as a novel strategy for hard tissue repair [140]. The SN<sub>A</sub>15 ELP molecule is derived from the HAp recognition domain of the biomineralization protein statherin [140][141]. Statherin is a Calcium binding protein that is present in saliva. Through it, saliva is supersaturated with Calcium and Phosphate (CaP). This inhibits precipitation of HAp and other CaP salts from saliva and thereby provides a protective and reparative environment for teeth by avoiding surficial mineral accretions [142][143][144]. In this ELP sequence, a lysine guest residue enables covalent cross-linking through reaction with the primary amine [120].

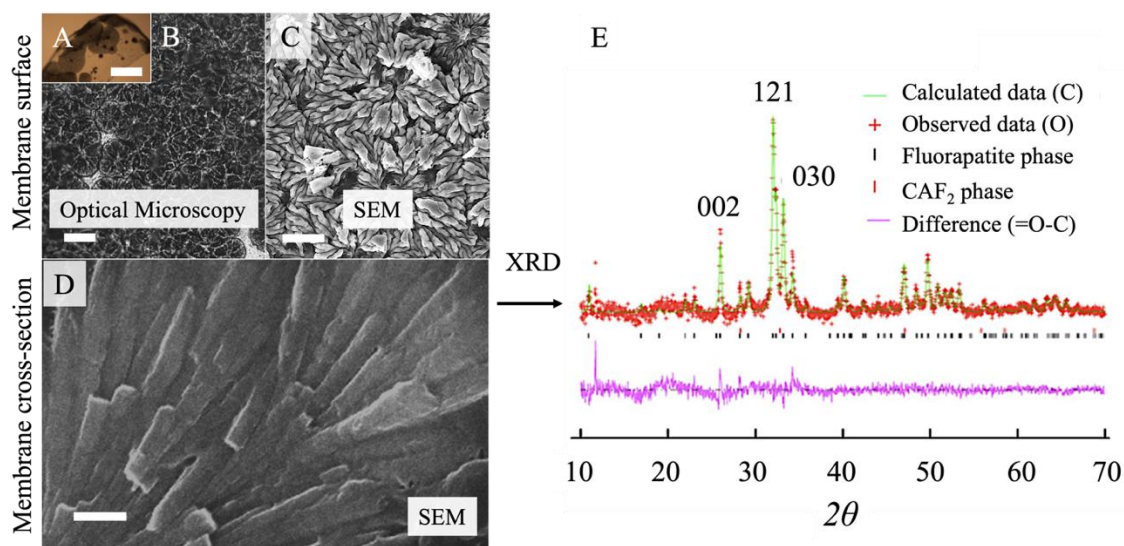
The referenced work proposed that the intrinsic ability of the processed ELPs to form supramolecular matrices, composed of distinct protein secondary structures, provide an organic template that can guide hierarchical biomineralization of the synthesized gel-like membranes.

Herein, SN<sub>A</sub>15 ELP molecules were dissolved in an organic solvent mixture of Dimethylformamide (DMF) and Dimethyl sulfoxide (DMSO) at a 9:1 ratio and cross-linked with the Hexamethylene diisocyanate (HDI). Thereafter, the ELP-HDI solution was drop casted onto Polydimethylsiloxane (PDMS) substrate and left to cross-link over-night in a low humidity (< 20%) glovebox, resulting in the formation of flexible, transparent ELP based membranes (**Figure 1.40**).



**Figure 1.40:** HDI-ELP membrane fabrication method, where ELP was dissolved in solvent mixture and subsequently HDI was added *via* pipetting before drop casting the HDI-ELP solution on PDMS. The far-right image shows a transparent, flexible HDI-ELP membrane that formed after overnight cross-linking in a low humidity glovebox environment. Scale bar: 500  $\mu$ m.

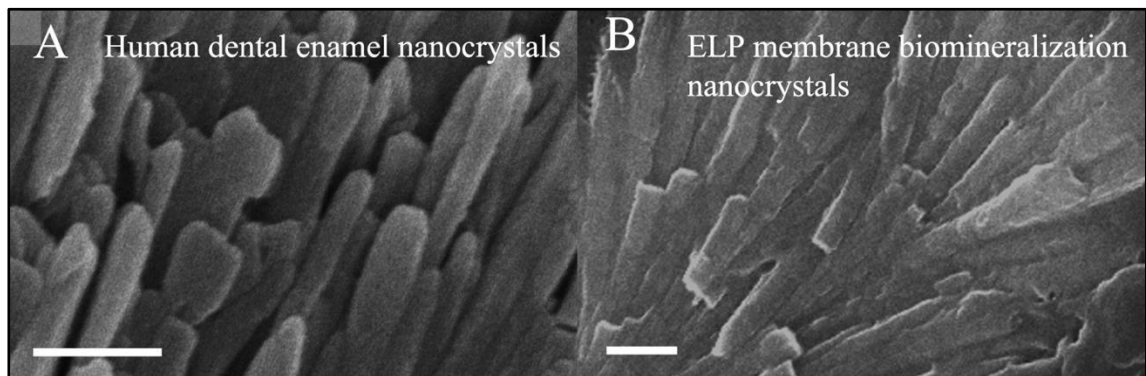
HDI-ELP membranes were immersed in Ca<sub>3</sub>(PO<sub>4</sub>)<sub>2</sub> biomineralization solution (pH = 6) and incubated at 38 °C for 8 days. Thereafter, the membranes displayed full biomineralization (**Figure 1.41A, B, C**). X-Ray diffraction results showed that the biomineralization was composed of Fluorapatite (FAP) nanocrystals (**Figure 1.41D, E**).



**Figure 1.41:** (A) Biomaterialized HDI-ELP membrane (B) Optical microscopy image and (C) SEM image of biomaterialized structures on the membrane surface. (D) SEM image of fluorapatite (FAP) nanocrystals in the membrane cross-section. (E) XRD results showing peak regions overlap with FAP control group (modified from [140]). Scale bars: (A): 500  $\mu$ m, (B): 20  $\mu$ m, (C): 5  $\mu$ m, (D): 250 nm.

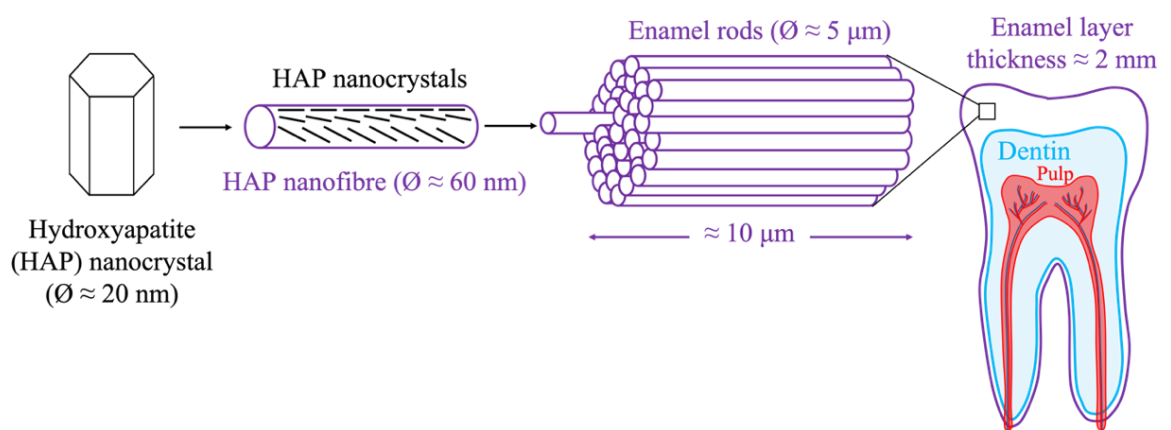
FAp and HAp have the same crystallographic profile [145]. The difference is that the CaP in FAp is associated with Fluoride groups, whereas in HAp, it is associated with Hydroxide groups [146]. Compared to HAp, FAp is less soluble in acidic conditions, providing corrosion resistance in e.g., enamel [147] and making it a popular material for bone regeneration therapy.

Close-up SEM images showed that the biomineralized structures were composed of aligned nanocrystals (**Figure 1.42B**), similar to those observed in human dental enamel (**Figure 1.42A**).



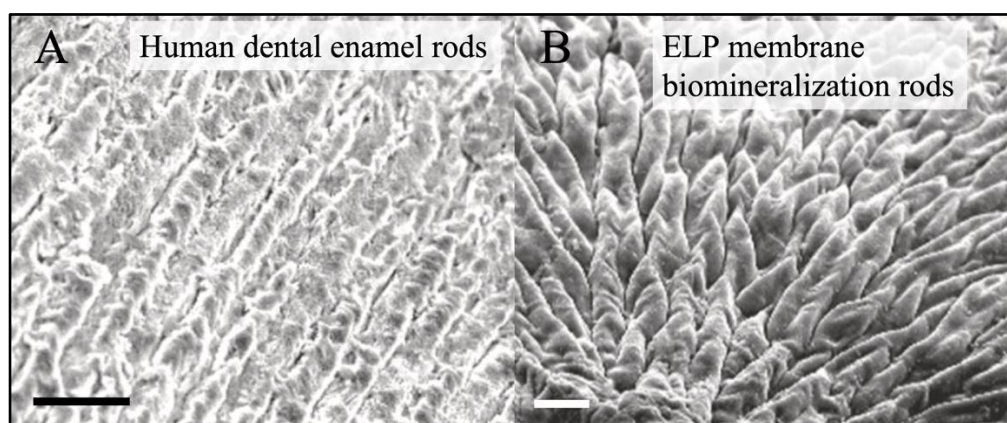
**Figure 1.42:** SEM images depicting the resemblance between (A) nanocrystals present in enamel (image modified from [148]) and (B) nanocrystals in biomineralized ELP membranes. Scale bars: 250 nm.

**Figure 1.43** depicts the inherent hierarchy in human dental enamel, wherein HAp nanocrystals form bundles *via* protein interface bonding, to form HAp nanofibers. These nanofibers accumulate to enamel rods to make up a 2 mm thick enamel layer [148].



**Figure 1.43:** Illustration of the hierarchical structure of human dental enamel, wherein hydroxyapatite (HAP) nanocrystals bundle *via* proteins to form nanofibers that assemble to enamel rods. The 2 mm thick enamel layer is composed of multiple enamel rods. This hierarchical structure enables the strong mechanical properties in enamel [149].

Enamel consists of approximately 95% substituted HAp, 2 – 4% water and 1 – 2% organic material/proteins [150]. When enamel matures, its characteristic hardness develops as the aligned enamel rods (**Figure 1.44A**) expand in width and thickness. This hierarchical structure enables the formation of the hardest and most mineralized tissue in the human body [151]. Rod formation was also observed in biomineralized ELP membranes (**Figure 1.44B**) [140].

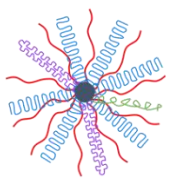
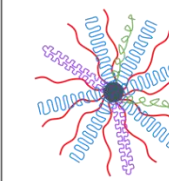
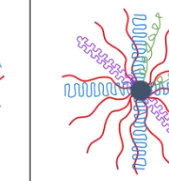


**Figure 1.44:** Macroscale SEM images of (A) characteristic enamel rods, that are composed of nanocrystals. The shown SEM image was modified from [148]. (B) The formation of rods composed of nanocrystals was equally observed in biomineralized HDI-ELP membranes. Scale bars: 20  $\mu\text{m}$ .

In the referenced work, different amounts of cross-linker were integrated into the material formulation, which were referred to as ratio 1, ratio 4 and ratio 12. These ratios relate to lysine cross-linking site saturation, where ratio 1 was calculated to saturate all cross-linking sites, and ratio 4 and 12 imply a four and twelve fold saturation.

The membranes' underlying self-assembled protein secondary structure was assessed *via* FTIR spectroscopy. Results showed that the integration of various CLA concentrations affected the order-disorder ratio in the protein secondary structure. With an increase in cross-linker ratio, a decrease in protein order was observed (**Table 1.7A**).

Nanoindentation studies showed that the mechanical properties of these mineralized structures could exhibit the same mechanical properties as bone and dentine (**Table 1.7C, D** and **Figure 1.45**).

Cross-linker ratio	Ratio 1	Ratio 4	Ratio 12
(A) Supramolecular matrix visualization			
(B) Biomineralized structure morphology			
(C) Stiffness	$33 \pm 20.1$ GPa	$17.7 \pm 11.3$ GPa	$8.2 \pm 1.4$ GPa
(D) Hardness	$1.08 \pm 0.81$ GPa	$0.75 \pm 0.25$ GPa	$0.57 \pm 0.12$ GPa



**Table 1.7:** Order-disorder interplay of protein secondary structure in ELP based membranes, (A) determining the morphology of mineralized structures and their mechanical properties. An increase of cross-linker caused an increase in disorder (random coils) in the protein secondary structure (B), which resulted in more defined biomineralized structures. (C, D) As disorder was increased, the mechanical hardness and stiffness was decreased. Images modified from [140].

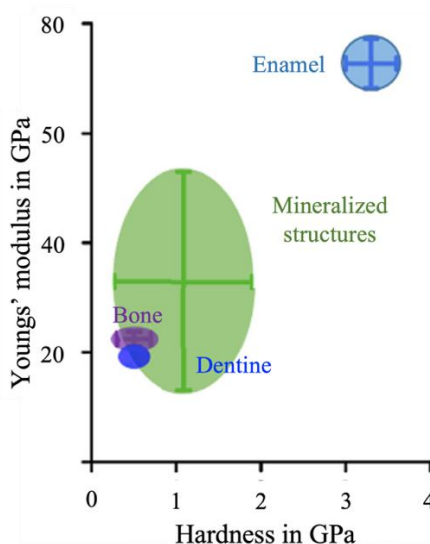


**Figure 1.45:** Mechanical properties (hardness and young's modulus) of mineralized structures in HDI-ELP membranes in comparison with mineralized tissue in the human body.

Hence, it was proposed that by integrating different CLA concentrations into the formulation, the order-disorder interplay of the formed protein secondary structure was modified to guide the emergence of biomineralized structures with varying morphologies (**Table 1.7B**) and mechanical properties(**Table 1.7C, D**) [140].

Furthermore, a mechanism for the emergence of biomineralized structures was proposed. Polarized light microscopy (PLM) of unmineralized ELP-membranes showed the presence of Maltese cross-patterned structures, which were referred to as organic spherulites (**Figure 1.46**). These spherulites were assumed to visually indicate self-assembled ELP polypeptides.



**Figure 1.46:** Polarized light microscopy image of unmineralized HDI-ELP membrane, showing the presence of cross-patterned structures (organic spherulites). Scale bar: 3  $\mu\text{m}$ . Modified from [140]

It was suggested that these organic spherulites functioned as nucleic sites in biomineralization, out of which so called biomineralizing ‘volcanoes’ emerged and rose to the membrane surface to spread in a circular manner (**Figure 1.47**) [140].

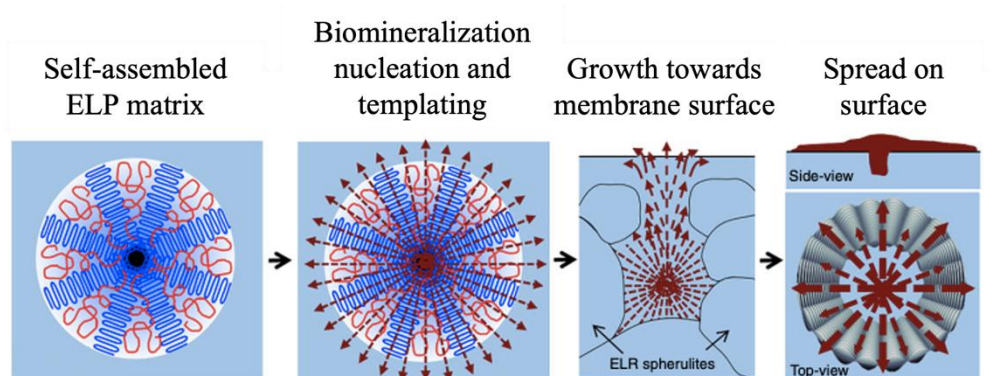
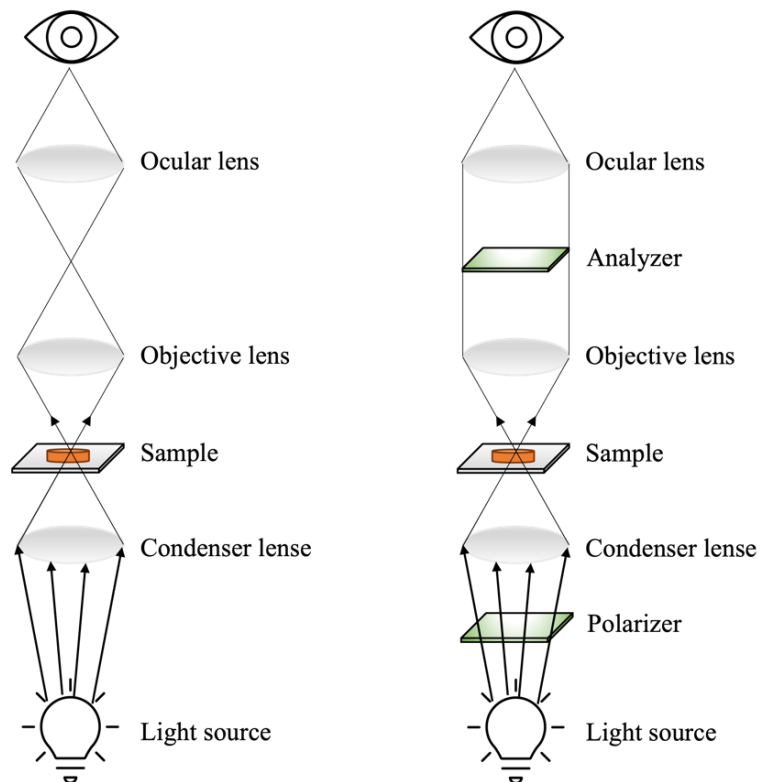


**Figure 1.47:** Visualization of biomineralization mechanism in HDI-ELP membranes, proposing that organic spherulites, function as nuclei sites in the formation of biomineralized structures that emerge to the membrane surface and spread horizontally, in a circular manner. Image modified from [140].

In the following, techniques that were used to analyse ELP based membranes are elaborated on.

### 1.4.2.1. Optical and polarized light microscopy

Optical microscopy is a commonly used technique to observe samples at microscopic scale *via* optical light. Herein, light from a light source is passed through a condenser lens to be converged and illuminate the sample. Above the sample, an objective lens is positioned which collects the light that priorly interacted with the sample. *Via* the objective lens, a magnified real image is formed which is further magnified by the ocular lens. The magnified image is then directed to the eye piece, which forms a virtual image that can be viewed by the operator (**Figure 1.48A**). By adapting different objective lenses with different magnification and adjusting the focus, various details of the sample can be observed by the operator [152].



**(A) Optical Light Microscopy (B) Polarized Light Microscopy**

**Figure 1.48:** Schematics of (A) optical light microscopy: light is passed through condenser lens to illuminate a sample and form an image that is transmitted through the objective lens. The objective lens can have different magnifications. The formed magnified imaged is passed through the ocular lens and can then be viewed by the operator; and (B) polarized light microscopy: the setup in PLM is similar to conventional optical microscopy. However, the additional components are added. (1) Polarizer: only allows light waves to pass through which vibrate into a specific direction. (2) Analyzer: only allows light waves which vibrate at the perpendicular direction to the light transmitted by the polarizer.

In PLM, polarized light is used to observe specific structural details and optical properties of the sample of interest. The characteristics of polarized light were further elaborated on in *chapter 1.4.1.2*. This technique is particularly useful when observing birefringent materials. If a material is birefringent; it exhibits different refractive indices in different directions. By passing polarized light through the sample, the light is split into two components which are oriented orthogonally to one another and have different refractive indices. In this case, both components vibrate perpendicularly to each other. **Figure 1.48B** shows the schematic of PLM, which strongly resembles conventional optical light microscopy. However, a polarizer is situated below the sample, which only allows light waves to pass through which vibrate into a specific direction, the polarization direction. Light waves that vibrate in other directions are blocked by the polarizer. The second component, which is placed above the sample, is the analyzer filter. The analyzer polarizes light in a perpendicular direction to the first one [153].

#### *1.4.2.2. Scanning electron microscopy*

In scanning electron microscopy (SEM), images are produced by scanning the sample surface with a focused high energy beam of electrons, causing the electrons to interact with the atoms in the sample. Thereby, signals are produced which are detected by a detector and amplified to image the sample. This technique is used in numerous scientific fields, such as material science, biology, geology and nanotechnology [154].

**Figure 1.49** depicts a schematic of the SEM imaging technique. The electron source, which is located at the top of the setup, generates an electron beam of high energy electrons. This source is usually a heated tungsten filament or a field emission electron gun. In the next step, the electron beam is passed through a series of electromagnetic lenses and an objective aperture which are used to condense the path of the electron beam path to achieve focus onto the sample. Thereafter, the scanning coil deflects the previously focused electron beam across the surface. The sample is scanned line by line, triggering the emitted electrons to interact with the atoms in the sample. The electrons that are backscattered from the sample are collected by a detector and converted into electrical signals which are amplified and processed by the electronical computer system to form an image [155].

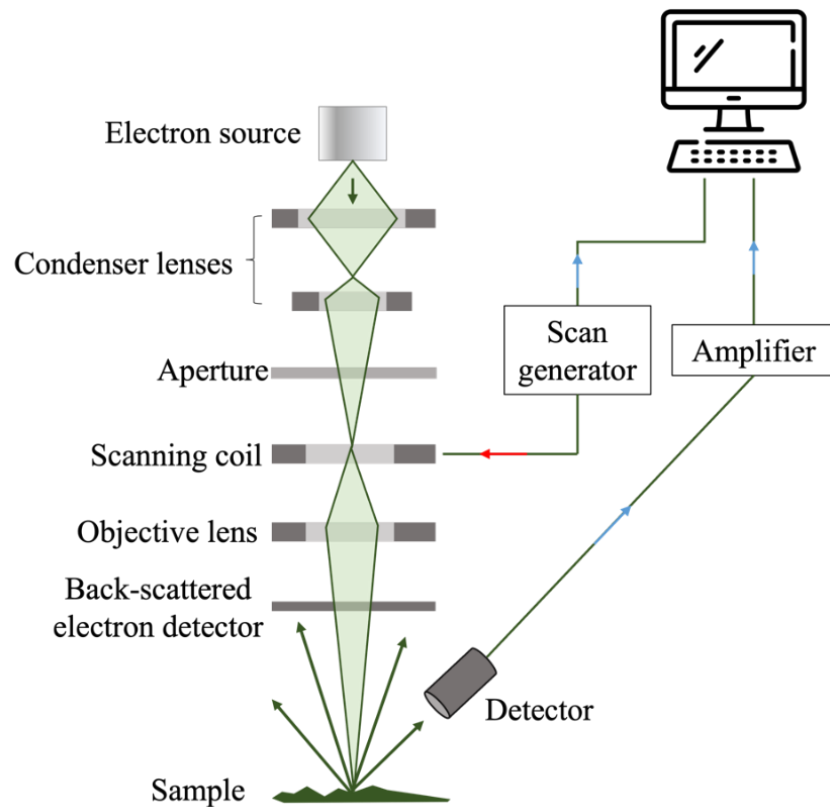


**Figure 1.49:** Schematic of scanning electron microscopy principle, where an electron source passes an electron beam through condenser lenses and an aperture, which condense the beam, before it is deflected onto the sample surface by a scanning coil. The electrons that are backscattered from the sample are collected by a back-scattered electron detector, amplified, and processed by a computer system to form a high-resolution image [155].

#### 1.4.2.3. X Ray Diffraction

X-Ray diffraction (XRD) is a vastly used tool to obtain information about the crystallographic profile of solid, crystalline samples. X-Rays are emitted from an X-Ray source onto the sample. The crystalline lattice in the sample then causes the X-Rays to diffract in certain directions at the angle  $2\theta$ , thereby creating a pattern of scattered X-Rays (**Figure 1.50**). Diffraction is quantified by measuring its angles and intensities.

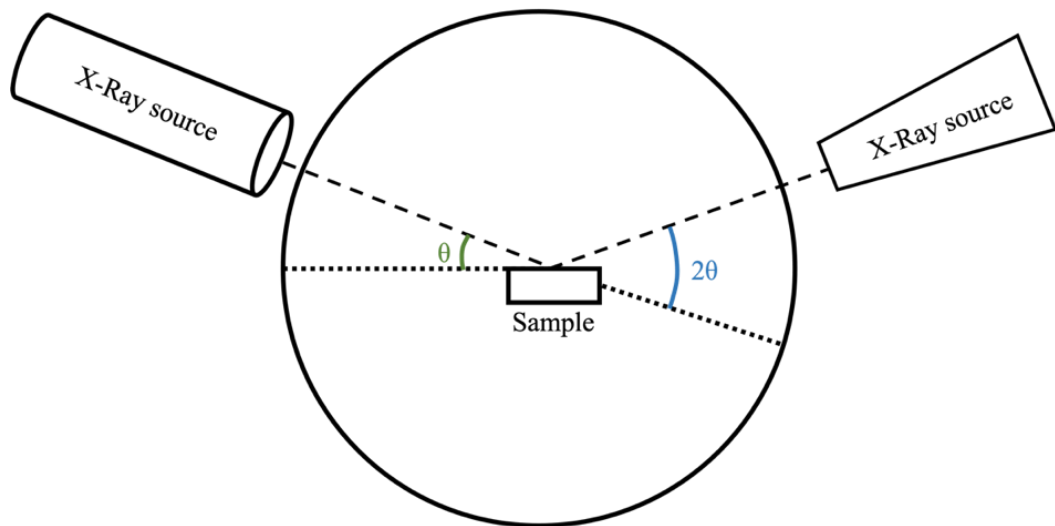


**Figure 1.50:** Schematic of X-Ray diffraction technique, wherein X-Rays are emitted from an X-Ray source onto a crystalline sample, which diffracts the X-Rays at angle  $2\theta$ .

The resulting X-Ray pattern gives information about the atoms in the analysed crystal lattices as well as the distance and angle between them to produce a crystallographic profile [156].

## **1.5. Aims and objectives**

In the herein presented literature review, it has been established that TE has opened a promising path to tackle challenges faced in bone defect repair. Despite advances in the development of biomaterials as well as TE scaffold fabrication methods, there remains a need for the development materials that can display biocompatibility and can simultaneously be used to fabricate scaffolds that can provide appropriate structural integrity in load-bearing defect sites.

Bone TE scaffolds based on pure biomineralized material, such as HAp, have displayed satisfactory material properties with regards to biocompatibility and osteoinductivity, but are unsuitable for load bearing applications due to their excessive brittleness. The development of composite materials that integrate inorganic HAp, and organic polymer phases has found to significantly improve the mechanical properties of such composite scaffolds. However, issues with interfacial bonding between the phases remain in such composites.

Previous research has proposed a fabrication method for ELP based membranes, which can gradually undergo stimuli triggered biomineralization. Biomineralized membranes were composed of FAp nanocrystals and exhibited mechanical properties similar to bone. It was suggested that the inherent underlying protein secondary structures of the synthesized templates provided an organic template for hierarchically structured biomineralization. However, environmental triggers that induce protein secondary structure formation were not identified in this work. Additionally, the proposed fabrication method was restricted to the synthesis of 2D membranes and therefore unsuitable in the fabrication of 3D bone TE scaffolds.

The aim of this project is to extend this proposed platform by synthesizing ELP-based materials that can be integrated into AM to produce shapely constructs that can undergo biomineralization.

This shall be achieved by delivering the following objectives:

1. Development a novel chemically cross-linked ELP-gel formulation

The development of a structurally stable gel that can be analysed towards its protein secondary structure over time shall open the opportunity to investigate environmental triggers that induce protein secondary structure formation/supramolecular self-assembly.

Chemical cross-linking is preferred over a physical cross-linking method, as, according to literature, physically cross-linked polypeptide gels often show insufficient mechanical integrity, whilst chemical cross-links can enhance gel stiffness.

2. Biomineralization of extruded ELP-based filaments

The ability to extrude ELP-based filaments which maintain their shape post-extrusion shall lay the foundation for fabrication integration into AM. By fabricating filaments that can undergo biomineralization, challenges faced in previous research that concern interfacial bonding between organic and inorganic phases are tackled, as inorganic phases shall gradually emerge within the organic matter.

3. Proposal for biomineralization mechanism in newly ELP-based formulations

Understanding the biomineralization mechanism in novel ELP-based formulations is considered crucial to propose strategies that can achieve structurally biomineralization.

4. Fabrication of ELP-based constructs *via* Material Extrusion

Material Extrusion was selected as AM method, as this technique that does not require high temperatures. Thereby, protein degradation can be avoided. Furthermore, compared to binder jetting, which is commonly used for the fabrication of HAp scaffolds, structures with higher resolution can be manufactured *via* ME. This is considered favourable for the desired application.

## 2. Materials and Methods

### 2.1. Materials

#### 2.1.1. SN<sub>A</sub>15 ELP sequence

The SN<sub>A</sub>15 ELP molecule used in this study was provided and synthesized by Technical Proteins Nanobiotechnology, S. L. in Valladolid, Spain. The molecule is composed of a hydrophobic framework (VPGIG), a positively charged segment (VPGKG) and a statherin-derived amino acid sequence (DDDEEKFLRRIGRFG), resulting in the following sequence

*MESLLP-(((VPGIG)<sub>2</sub>VPGKG(VPGIG)<sub>2</sub>)<sub>2</sub>-DDDEEKFLRRIGRFG-((VPGIG)<sub>2</sub>VPGKG(VPGIG)<sub>2</sub>)<sub>3</sub>-V*  
Lysine (**K**) (**Figure 2.1**) in the positively charged segment serves as a cross-linking site by providing a primary amine group (NH<sub>2</sub>).

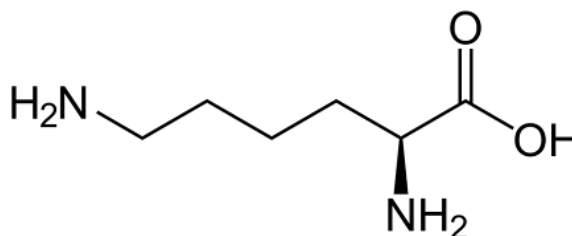


**Figure 2.1:** Chemical structure of lysine with a primary amine group (NH<sub>2</sub>).

To process the ELP sequence of interest, the solid, white ELP fiber material was dissolved in organic solvents, specified in the following section.

#### 2.1.2. Organic solvents

*Dimethyl formamide (DMF) and Dimethyl sulfoxide (DMSO)*

DMF (anhydrous, 99.8%, CAS No. 68-18-2) (**Figure 2.2**) and DMSO (99.7%, CAS No. 67-68-5) (**Figure 2.3**) were purchased from Sigma Aldrich UK. In all tested formulations, a solvent mixture at a 9:1 ratio (DMF:DMSO) was utilized.

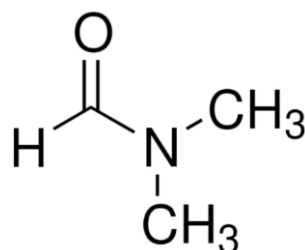


**Figure 2.2:** Chemical structure of Dimethyl formamide (C<sub>3</sub>H<sub>7</sub>NO)

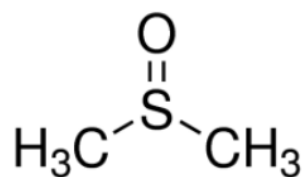


**Figure 2.3:** Chemical structure of Dimethyl sulfoxide (CH<sub>3</sub>)<sub>2</sub>SO

### 2.1.3. Cross-linking agents

*Hexamethylene diisocyanate (HDI) ≥ 99.0%*

HDI (**Figure 2.4**) is a hygroscopic, linear isocyanate with a molecular weight of 168.19 g mol<sup>-1</sup> and a density of 1.047 g/mL. It was purchased from Sigma Aldrich UK (CAS No. 822-06-0).

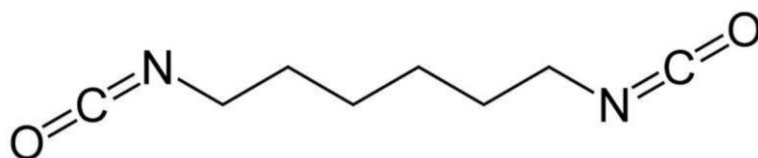


**Figure 2.4:** Chemical structure of hexamethylene diisocyanate, OCN(CH<sub>2</sub>)<sub>6</sub>NCO<sub>2</sub>

*Polymeric diphenylmethane diisocyanate (PMDI)*

PMDI (**Figure 2.5**) is a hygroscopic, polymeric isocyanate with a reported monomeric molecular weight of 149.15 g mol<sup>-1</sup>. It has a comparatively high viscosity (180 cP), at a density of 1.2 g/mL. It was purchased from Sigma Aldrich UK (CAS No. 9016-87-9). Herein, PMDI with a M<sub>n</sub> ~340 was utilized.

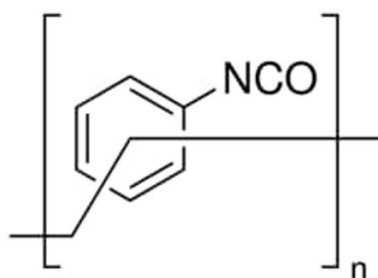


**Figure 2.5:** Chemical structure of Polymeric diphenylmethane diisocyanate [C<sub>6</sub>H<sub>3</sub>(NCO)CH<sub>2</sub>]<sub>n</sub>

*Genipin ≥ 98.0%*

Genipin (**Figure 2.6**) is an aglycone that is naturally derived from geniposide, which is an iridoid glycoside that can be found in the fruit of *Gardenia jasminoides* [157]. Upon

oxidation of reaction with amino acids, it produces dark blue pigments, making it a popular protein in food dye fabrication [158].

The cross-linking agent has a molecular weight of 226.23 g mol<sup>-1</sup>, and is soluble in DMSO (50 mg/ml), DMF (25 mg/ml) and 100% ethanol (5 mg/ml) [159]. Genipin was purchased from Sigma Aldrich UK (CAS No. 6902-77-8).

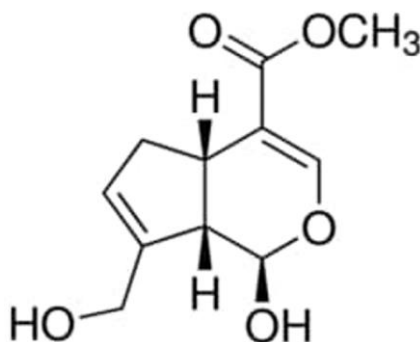


**Figure 2.6:** Chemical structure of genipin, C<sub>11</sub>H<sub>14</sub>O<sub>5</sub>

## 2.2. Methods

### 2.2.1. Fourier transform infrared spectroscopy

In this study, FTIR spectra were acquired using an FTIR spectrometer (Cary 630, Agilent Technologies, Santa Clara, California, USA). The absorbance of synthesised samples was acquired at a spectral range of 650 – 4000 cm<sup>-1</sup>. The MicroLab FTIR Software (Agilent Technologies) was set to acquire 100 sample scans at a resolution of 2 cm<sup>-1</sup>. Using the OriginPro software (OriginLab Corporation, Northampton, Massachusetts, USA), the amide III region (1350 – 1200 cm<sup>-1</sup>) of the obtained spectra were deconvoluted and the formed protein secondary structure was determined under consideration of the following spectral bands: 1220 – 1250 cm<sup>-1</sup> for β-sheets, 1250 – 1270 cm<sup>-1</sup> for random coils, 1270 – 1295 cm<sup>-1</sup> for β-turns, and 1295 – 1330<sup>-1</sup> cm for α-helix [160] [161].

**Figure 2.7** shows an example of a deconvoluted amide III region from FTIR spectra of an analyzed ELP-based membrane sample.

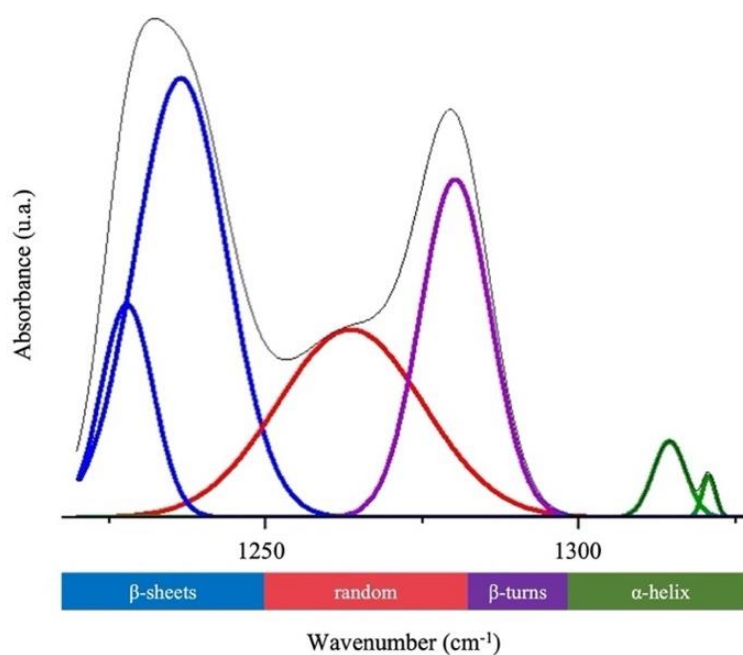


**Figure 2.7:** Example of a deconvoluted FTIR spectra, showing the spectral bands of the protein secondary structure in accordance with the specified spectral bands (blue =  $\beta$ -sheets, red = random coils, purple =  $\beta$ -turns, green =  $\alpha$ -helices).

The principle of protein secondary structure analysis *via* FTIR was further elaborated on in *chapter 1.4.1.2*.

### 2.2.2. Assessment of sample shrinkage/swelling

To calculate the capacity of samples to swell/shrink, the following formula was applied [162]:

$$\text{Shrink/Swell capacity (\%)} = \frac{(w_s - w_d)}{w_d} \times 100$$

Where  $w_s$  is represents the weight of the swollen sample and  $w_d$  represents the non-swollen/dried sample weight. Samples were weighed, using a microscale (Analytical Balance XS205DU, Mettler Toledo, Columbus, Ohio, USA).

The obtained quantitative results are expressed as mean  $\pm$  standard deviation. Statistical significance, in accordance with the two-sample t-test, was indicated in the graphs and elaborated on in the respective sections. The software GraphPad Prism (GraphPad Software, San Diego, USA) was used to plot graphs.

### 2.2.3. Preparation of biomineralization solution

The  $\text{Ca}_3(\text{PO}_4)_2$  biomineralization solution was prepared as described by Chen et. al [163]. 2 mM HAp powder (Sigma Aldrich, UK, CAS No. 1306-06-5) and 2 mM Sodium Fluoride (Na) (Sigma Aldrich, UK, CAS No. 7681-49-9) were mixed into ultra-pure water to synthesise a supersaturated FAp solution [140]. Using a magnetic bar, the solution was continuously stirred on a hotplate (Cole-Parmer Stuart ® US152), at room temperature. After calibration, a pH meter (FiveEasy™, Mettler Toledo, Columbus, Ohio, USA) was used to measure the pH of the solution. Nitric Acid ( $\text{HNO}_3$ ) (Sigma Aldrich, UK, CAS No. 7697-37-2) was added in a drop wise manner until the powders were fully dissolved. Thereafter, the pH was adjusted to 2.4. To reach a physiological pH of 6, Ammonium Hydroxide ( $\text{NH}_4\text{OH}$ ) (Sigma Aldrich, UK, CAS No. 1336-12-6) was gradually added to the solution.

### 2.2.4. Optical light microscopy and polarized light microscopy

Samples were optically observed under the Zeiss Axioplan Microscope (Zeiss, Jena, Germany).

This microscope was also used to conduct polarized light microscopy (PLM). To obtain qualitative PLM images, a polarizing lens was introduced into the system and the exposure in the camera setting was set to 600-1000 ms using the bright field setting. The used microscope had a maximum magnification of 40x. Obtained images were analyzed *via* the ImageJ software (National Institutes of Health).

### 2.2.5. Scanning electron microscopy

In this study, the samples of interest were dried at room temperature and thereafter mounted onto aluminum stubs. To adhere samples to the mounting stub, they were fixated with self-adhesive double sided carbon tape. To assess sample surfaces, they were mounted onto the tape in a flat manner, whereas the bulk regions were assessed by breaking the samples using tweezers and perpendicularly mounting them onto the stub. Sputter coating was required to induce sample conductivity and thereby obtain high quality SEM images. Using coating the iridium coating machine Q150T ES (Quorum Technologies, Sussex, UK), the samples were coated with an 10nm thin iridium layer.

To enhance image quality, the SEM equipment JOEL JSM-7000f 7000f (Oxford Instruments, Abingdon, UK) was operated at 15 kV at working distance of 10 mm. Images from different sample locations were attained whilst adjusting the focus, contrast and brightness setting as required.

#### 2.2.6. X-Ray diffraction

In this project, samples were mounted onto the XRD Bruker D8 Advance system with a Da Vinci LYNXEYE 1D detector (Bruker, Billerica, Massachusetts, USA), using designated holder plates and cellar tape. XRD patterns were obtained using Cu K $\alpha$ 1 radiation ( $\lambda=1.5406\text{\AA}$ ) at 40kV and 40 mA. The  $2\theta$  range of the diffraction pattern was set at a range from  $5^\circ$  -  $90^\circ$  with a step size  $0.05^\circ$  and a step time of 22s.

#### 2.2.7. Plunger-based material extrusion

In this study, pneumatic plunger-based extrusion 3D-printing system (Cellink Incredible bioprinter (Bico, Gothenburg, Sweden), **Figure 2.8**) was used.



**Figure 2.8:** Cellink Incredible bioprinter

The principle of this 3D-printing technique is elaborated on in *chapter 1.3.2.2*.

Printing speed and nozzle travel direction were controlled *via* a g-code.file, which was programmed using the operating software ‘Cellink Heartware’. The pneumatic pressure applied to the plunger inside the printing cartridge was adjusted manually, using the integrated control knobs on the printing system.

### 3. Novel material formulations for SN<sub>A</sub>15 ELP based samples

In this chapter, the molecularly distinct CLAs (a) polymeric diphenylmethane diisocyanate (PMDI) and (b) genipin were tested to develop two novel ELP based formulations, with the aim to substitute the volatile, monomeric isocyanate CLA HDI, that was used in the sample preparation method previously published [140]. Thus, in this study, HDI-ELP membranes served as a control group.

PMDI was selected as a less volatile, polymeric substitute CLA with the aim to reduce overall toxicity in the system. Previous studies have shown that unpolymerized monomers, such as HDI, can exhibit toxic effects *in vitro*, such as genetic mutations or functional and structural damage, by interacting with cells [164]. With regards to unpolymerized monomers in bone tissue environments, studies have shown that osteoblastic cell proliferation and therefore mineralized tissue formation can be inhibited [165]. The integration of the isocyanate HDI was herein considered a risk, as mineralized HDI-ELP samples may contain unpolymerized HDI monomers that could leach into the environment and cause cytotoxic reactions.

Genipin was chosen as a second CLA of interest because it is known to react with nucleophilic groups, such as primary amino groups [166]. As lysine, which incorporates a primary amino group, functions as a cross-linking site in ELP sequence of interest, genipin was identified as a promising CLA substitute. Furthermore, due to its biocompatibility and low toxicity [167], genipin has increasingly gained popularity in bone and cartilage TE [168][169][170].

### 3.1. Protein secondary structure formation in PMDI-ELP gels

In this section, structurally integral ELP gels shall be formulated and used to study the underlying protein secondary structure formation sequence *via* deconvolution of FTIR spectra obtained from the samples of interest. The method applied for FTIR spectroscopy and spectra evaluation with regards to protein secondary structure analysis is specified in *chapter 2.2.1*.

The aim was to identify external stimuli that triggered supramolecular self-assembly. The identification of triggers shall allow the proposal of modification tools that can alter the protein secondary structure configuration.

#### 3.1.1. PMDI-ELP gel synthesis

4% SN<sub>A</sub>15 ELP were dissolved in 50% of the total solvent mixture volume (1 mL). The remaining 50% of the solvent mixture were mixed with 0.3 wt% PMDI. Thereafter, the two solutions were mixed, using a vortex. The constituents were separately processed to enhance uniform distribution of the highly viscous CLA. The PMDI concentration was determined by weight as its viscosity impeded material transfer *via* pipetting.

The process was conducted at room temperature, in a fume hood. Immediate (< 3 seconds) gel formation was observed as the two constituents were mixed (**Figure 3.1**). The synthesized gel was removed from the Eppendorf tube using a pipette tip to avoid gel breakage (**Figure 3.1B**).

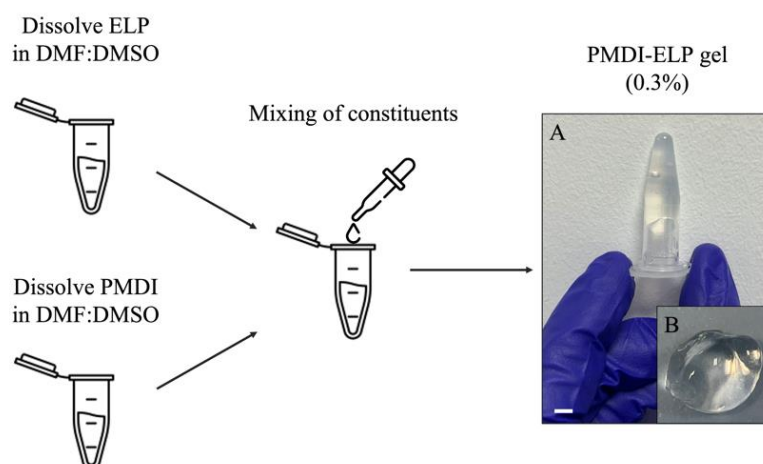


**Figure 3.1:** Fabrication method PMDI-ELP gels where ELP and PMDI were dissolved separately before mixing the constituents. The image shows the formed PMDI-ELP gel in an Eppendorf tube (A) and after removal from the tube (B). Scale bar: 2.5 mm.

### *Understanding the gelation mechanism in PMDI-ELP gels*

Preliminary studies were conducted, wherein different PMDI concentrations (0.1 wt%, 0.2 wt%, 0.3 wt%) were integrated into the formulation, to determine whether a certain PMDI threshold concentration was required to induce instant gelation (**Figure 3.2**).

Whilst the PMDI-ELP mixture remained liquid at CLA concentrations of 0.1 wt% and 0.2 wt%, material gelation occurred within < 3 seconds at a PMDI concentration of 0.3 wt%. It was concluded that the threshold for instant material gelation was likely to lay between 0.2 wt% and 0.3 wt% PMDI.

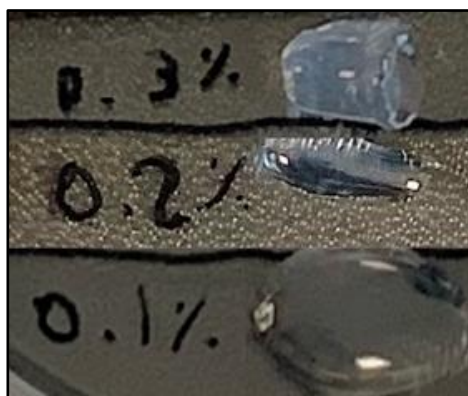


**Figure 3.2:** Integration of 0.1 wt%, 0.2 wt% and 0.3 wt% PMDI were integrated into 4% ELP solution. At 0.1 wt% and 0.2 wt% PMDI, the solution remained liquid. At 0.3 wt% PMDI, material gelation occurred within 3 seconds.

To test this hypothesis, PMDI concentrations of 0.23 wt%, 0.24 wt% and 0.25 wt% were tested (**Figure 3.3**). A cloudy solution was synthesized at a PMDI concentration of 0.24 wt%. At a 0.25 wt% PMDI concentration, a partially gelled material was synthesised. However, the synthesised material lacked structural integrity, causing it to spread across the PDMS substrate, whilst in contrast, at a PMDI concentration of 0.3 wt%, the synthesised gel maintained its three-dimensional shape (**Figure 3.2**).



**Figure 3.3:** Threshold determination for PMDI-ELP gel formation. Examining PMDI concentrations of 0.23 wt%, 0.24 wt% and 0.25 wt% PMDI showed that the threshold lay at approximately 0.25 wt%.

Conclusively, the threshold for the synthesis of a 3D PMDI-ELP gel was assumed to lay between 0.25 wt% - 0.3 wt% PMDI when mixed with 4% ELP in a 1 mL solvent mixture. To further investigate the formulation gelation threshold, the chemical cross-linking mechanism between PMDI and the SN<sub>A</sub>15 ELP sequence was examined.

**Figure 3.4** shows how the functional isocyanate groups form a cross-link with the primary amine of the lysine cross-linking site to form an isourea bond [171].

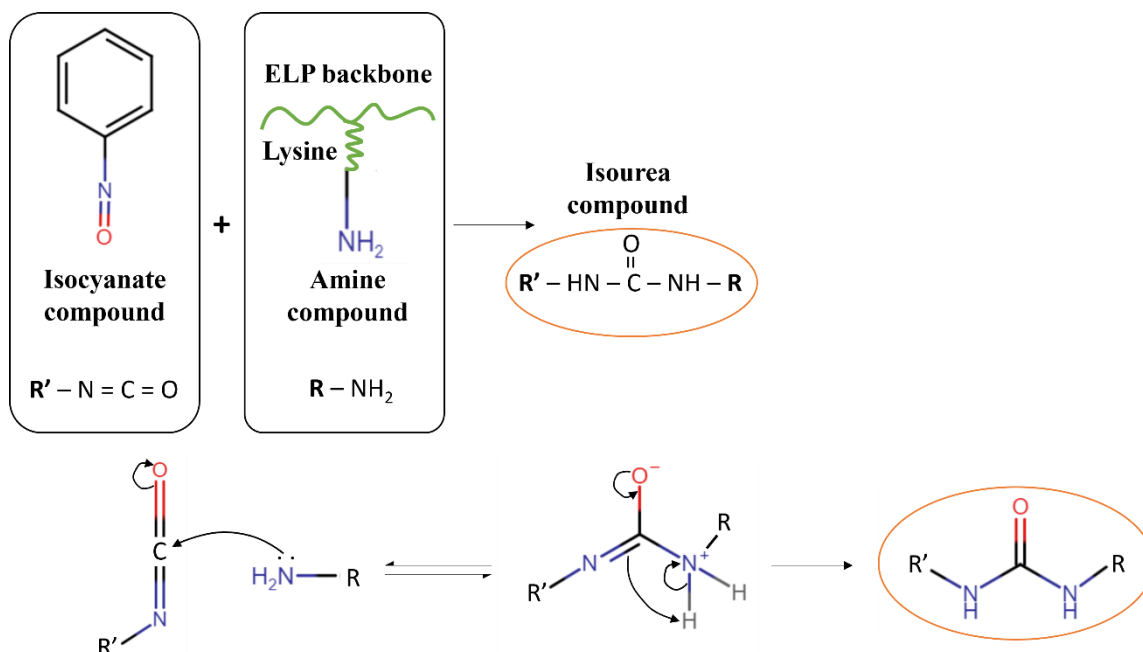


**Figure 3.4:** PMDI-ELP cross-linking mechanism illustration, wherein the cross-linking interactions between the functional isocyanate compound of PMDI and the cross-linking specific primary amine of lysine form an isourea compound [171].

In the following, the theoretical volume of PMDI required to saturate 100 mg of SN<sub>A</sub>15 ELP was calculated. These theoretical calculations considered the ELP sequence, provided by the supplier, stating the presence of 15 lysine (**K**) cross-linking sites.

*MESLLP-(((VPGIG)<sub>2</sub>VPGKG(VPGIG)<sub>2</sub>)<sub>2</sub>-DDDEEKFLRRIGRFG-((VPGIG)<sub>2</sub>VPGKG(VPGIG)<sub>2</sub>)<sub>2</sub>)<sub>3</sub>-V*  
 According to the supplier, the sequence has a molecular weight of 31,877 g mol<sup>-1</sup>.

The  $M_{wt}$  stated by the supplier, states that  $3,137e^{-06}$  molecules are present in 100 mg of SN<sub>A</sub>15 ELP (equation (1)), concluding a total of  $4,706e^{-05}$  lysine cross-linking sites (equation (2)). Consequently, considering the chain length of PMDI ( $M_n \sim 340$ ),  $1,384e^{-07}$  molecules of PMDI are required to saturate the lysine primary amine cross-linking sites in 100 mg of SN<sub>A</sub>15 ELP (equation (3)).

$$(1) \quad \frac{0.1 \text{ g}}{31,877 \frac{\text{g}}{\text{mol}}} = 3,137e^{-06} \text{ mol in 100 mg SN}_{A15} \text{ ELP}$$

$$(2) \quad 3,137e^{-06} \text{ mol} \times 15 = 4,707e^{-05} \text{ mol lysine in in 100 mg SN}_{A15} \text{ ELP}$$

$$(3) \quad \frac{4,707e^{-05} \text{ mol}}{340} = 1,384e^{-07} \text{ mol PMDI saturates } 4,707e^{-05} \text{ mol lysine}$$

Considering the number of molecules in a unit mass of PMDI ( $M_n \sim 340$ ) and the weight of a single molecule as provided by the supplier ( $149.15 \text{ g mol}^{-1}$ ), a molecular weight of  $50,707 \text{ g mol}^{-1}$  per polymer chain was assumed (equation (4)).

Thus, 7.02 mg would be needed to saturate the lysine primary amine cross-linking sites in 100 mg (100%) of SN<sub>A15</sub> ELP (equation (5)).

$$(4) \quad 340 \times 149.15 \frac{\text{g}}{\text{mol}} = 50,707 \frac{\text{g}}{\text{mol}} = M_w \text{ of } M_n \sim 340 \text{ PMDI chain}$$

$$(5) \quad 1,384e^{-07} \text{ mol} \times 50,707 \frac{\text{g}}{\text{mol}} = 0.00702 \text{ g} = 7.02 \text{ mg} \quad \text{of PMDI required to cross-link 100 mg SN}_{A15} \text{ ELP}$$

$$(6) \quad \frac{7.02 \text{ mg}}{100} \times 4 = 0.28 \text{ mg of PMDI required to cross-link 4 mg SN}_{A15} \text{ ELP}$$

According to these calculations, all lysine cross-linking sites in 4% SN<sub>A15</sub> ELP can in theory be saturated with 0.28 mg (0.28 wt% in 1 mL solvent) PMDI (equation (6)).

Based on these results, it is herein hypothesized that by surpassing the lysine saturation threshold in a PMDI-SN<sub>A15</sub> ELP formulation, intramolecular polymerization amongst excess highly reactive isocyanate groups in the cross-linking agent achieves the synthesis of a gel-like material.

This hypothesis is considered to be in good agreement with the executed practical experimental results. As demonstrated above, at a PMDI concentration of 0.3 wt%, a shapely gel was synthesized, which maintained its integrity after it was deposited onto PDMS substrate (**Figure 3.2**). In contrast, the slightly gelled material synthesized at a PMDI concentration of 0.25 wt% lacked integrity and spread across PDMS substrate (**Figure 3.3**).

At a PMDI concentration that lies slightly below the calculated lysine saturation threshold (0.25 wt%), it is therefore suggested that not all lysine cross-linking sites are saturated. Due to the high reactivity of PMDI, a low degree of intramolecular polymerization between functional isocyanate groups was assumed to occur, inducing partial gelation. At a cross-linker concentration that lies above the calculated lysine saturation threshold (0.3 wt%), all lysine cross-linking sites are assumed to be saturated, allowing for more extensive intramolecular polymerization between functional

isocyanate groups and thereby enabling the synthesis of a shapely 3D gel. It is therefore assumed that the gel-integrity can be modified by altering the PMDI concentration.

It needs to be taken into consideration that the cross-linking agent as well as the ELP sequence are synthetically synthesized. Therefore, the polymer chain length of PMDI and the molecular weight of the ELP sequence considered in theoretical calculations are based on averages and may vary in practice. Therefore, interactions between the cross-linker and the ELP can vary in practical experiments and from batch to batch. Additionally, PMDI is hygroscopic, which may cause altered reactivity depending on environmental factors, such as room humidity.

When the isocyanate groups in PMDI react with water, the intermediate compound carbamic acid is formed (**Figure 3.5**).

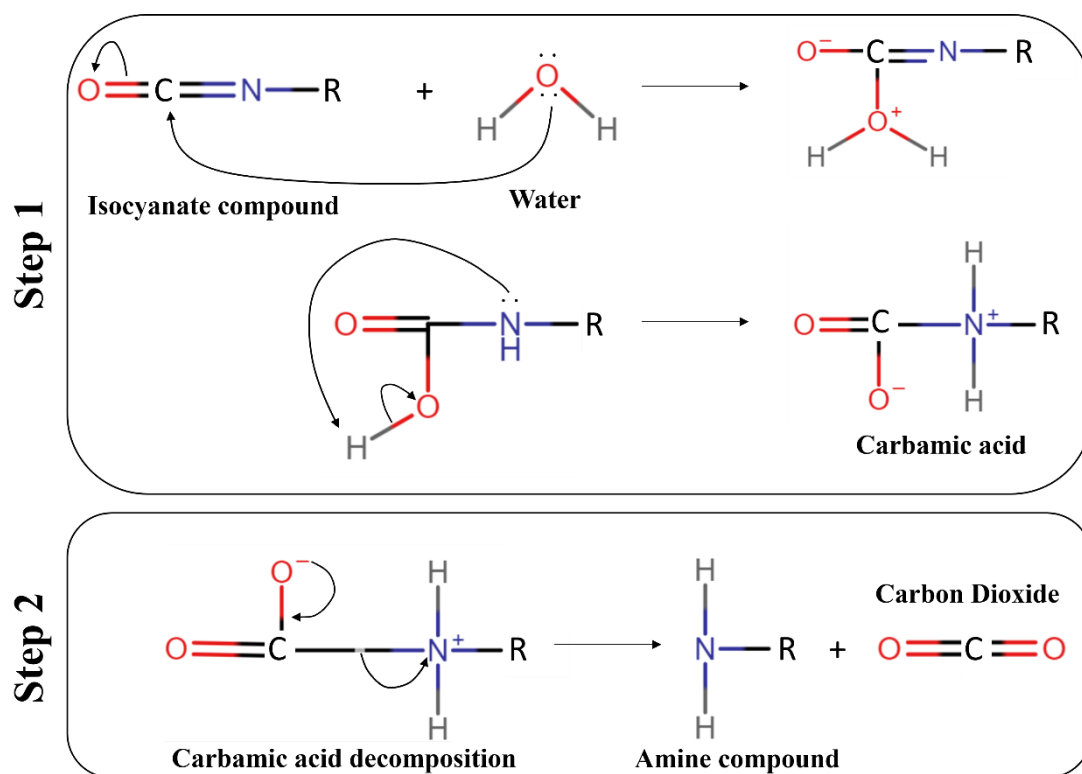


**Figure 3.5:** Interaction between functional isocyanate groups and water, leading to the formation of an intermediate carbamic acid and potential decomposition to an amine compound under the release of  $\text{CO}_2$  gas [172].

In the case of extended PMDI exposure to water, this unstable intermediate decomposes to an amine compound whilst  $\text{CO}_2$  gas is released [172]. Remaining functional

isocyanate groups can thereafter react with the resulting amine group to form an isourea compound [171] as shown in **Figure 3.4**.

In the case of comparatively less exposure to water, such as on a bench top in a non-humidity-controlled environment, it is assumed that the carbamic acid does not significantly decompose and the compound mostly remains in an intermediate state. Nonetheless, this interaction is assumed to interfere with cross-linking interactions between available functional isocyanate groups and lysine cross-linking sites, conclusively increasing the PMDI concentration threshold for lysine saturation.

### 3.1.2. Identification of supramolecular protein secondary structure formation triggers in PMDI-ELP gels

To identify environmental triggers that induce protein secondary structure formation, synthesised PMDI-ELP gels were retained in a sealed Eppendorf tube and subjected to FTIR analysis daily for four days. This was done to understand whether the mere integration of cross-linker was sufficient to trigger the formation of an ordered protein secondary structure structure ( $\beta$ -sheets,  $\beta$ -turns or  $\alpha$ -helices).

ELP-solution was synthesized by dissolving 4% ELP 20  $\mu$ l solvent mixture ( $n = 2$ ). These solutions were FTIR analysed towards the underlying protein secondary structure to provide a CLA-free control group.

In the next step, synthesized PMDI-ELP gels were removed from the vial they were fabricated in and left to cross-link at room temperature in different environments, i.e., in a fume hood, glovebox and vacuum oven, or submerged in deionised (DI) water. This was done to introduce different environmental parameters, such as pressure, solvent evaporation time span and environmental humidity, with the aim to correlate secondary structure formation with environmental triggers.

Allowing PMDI-ELP gels to cross-link in the open air caused the samples to lose their gel-like state, turning into solid, brittle structures instead. The time frame for solidification depended on the gel volume. On the other hand, PMDI-ELP gel samples that were contained in DI water remained flexible but shrank in size.

In the following data evaluation sections, numerical values relating to the secondary structures, have been translated into visual illustrations of the protein secondary

structure (**Figure 3.7**, **Figure 3.9** and **Figure 3.13**). In those visualizations, one protein strand represents 5% of the total protein secondary structure configuration, resulting in a total of 20 strands per protein secondary structure configuration. When less than 2% of a specific protein coil was present within the protein secondary structure configuration, it was not represented in the respective illustrations. Graphs of deconvoluted FTIR spectra of the tested samples can be found in Appendix B.

### 3.1.2.1. Protein secondary structure in contained PMDI-ELP gel

In PMDI-ELP gels that were contained in a closed vial, FTIR spectra deconvolution displayed a static, predominantly disordered ( $\approx 95\%$  random coils) protein secondary structure configuration (**Table 3.1**).

**Table 3.1:** Numerical values [%] obtained through the deconvolution of FTIR spectra of PMDI-ELP gel in a sealed container (Day 0 – Day 4), showing static disorder (random coils) in the ELP protein secondary structure over time. Corresponding FTIR spectra can be found in Appendix B.

	Day 0	Day 1	Day 2	Day 3	Day 4	Mean	St.Dev.
$\beta$ -sheets	-	-	-	-	-	-	-
random coils	<b>92.84</b>	<b>96.13</b>	<b>93.71</b>	<b>95.67</b>	<b>95.81</b>	<b>94.83</b>	1.46
$\beta$ -turns	1.62	1.53	2.85	1.58	1.57	1.83	0.57
$\alpha$ -helix	2.54	2.37	3.44	2.75	2.62	2.74	0.41

### Assessment of protein secondary structure of ELP in solvent (control)

FTIR spectra obtained from the CLA-free ELP solution showed that the underlying protein secondary structure was mostly disordered ( $\approx 73\%$  random coils), whilst approximately 20% of the protein secondary structure was composed of  $\beta$ -sheets (**Table 3.2**). It was assumed that the observed structural order was achieved through the peptides' intrinsic ability to undergo self-assembly.

**Table 3.2:** Numerical values [%] of the underlying protein secondary structure of CLA-free ELP-solution, displaying a predominant presence of random coils. Approx. 20%  $\beta$ -sheets were detected. Corresponding FTIR spectra can be found in Appendix B.

	Sample 1	Sample 2	Mean	St.Dev.
$\beta$ -sheets	21.72	19.06	20.39	1.88
random coils	72.49	75.41	73.95	2.06
$\beta$ -turns	3.54	3.33	3.44	0.15
$\alpha$ -helix	2.25	2.18	2.22	0.05

In conclusion, the addition of CLA was shown to induce a higher degree of disorder to the protein secondary structure, compared to that of ELP in solvent.

These results suggested that the integration of cross-linker alone was not sufficient to trigger protein secondary structure formation.

It was proposed that this occurred due to the lysine cross-linking sites in ELP being occupied by CLA, thereby suppressing the peptides' intrinsic ability to self-assemble.

### 3.1.2.2. Protein secondary structure in cross-linked PMDI-ELP gels

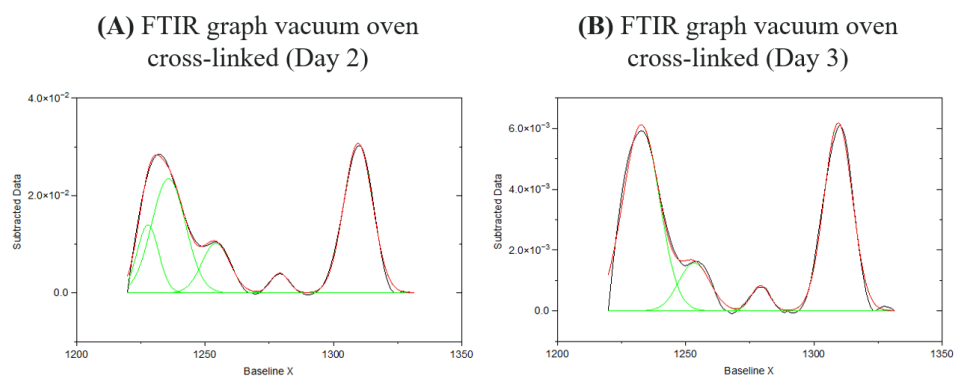
It was observed that PMDI-ELP gels shrunk and solidified to form brittle structures after cross-linking at in a fume hood for 3 days. **Table 3.3** contains the secondary structure values acquired on respective FTIR scan days as the sample was cross-linked in a fume hood.

**Table 3.3:** Numerical values [%] of FTIR spectra deconvolution from PMDI gel that was cross-linked in a fume hood (Day 1 – Day 3). Results revealed a sequential order in protein secondary structure formation, wherein on the first day, proteins were mainly randomly ordered, and then reached ordered conformations *via* the formation of  $\alpha$ -helices (Day 2),  $\beta$ -sheets and  $\beta$ -turns (Day 3). Corresponding FTIR spectra can be found in Appendix B.

	Day 1	Day 2	Day 3
$\beta$ -sheets	-	35.58	<b>63.62</b>
random coils	<b>95.59</b>	0.9	-
$\beta$ -turns	-	-	<b>5.1</b>
$\alpha$ -helix	4.41	<b>63.52</b>	31.28

The results showed that over time, the gels underlying protein secondary structure sequentially transformed from being mostly unordered to being ordered.

Once the samples had solidified; their secondary structure remained stable. The following graphs show FTIR spectra obtained from a solidified PMDI gel dried in a vacuum oven, at room temperature, showing no significant changes in secondary structure between the day the sample had solidified (**Figure 3.6A**, Day 2) and the subsequent day (**Figure 3.6B**, Day 3).



	Protein secondary structure composition (Day 2)	Protein secondary structure composition (Day 3)
$\beta$ -sheets	46.4	47.4
random coils	12.3	10.8
$\beta$ -turns	3.1	3.3
$\alpha$ -helix	38.1	38.6

**Figure 3.6:** FTIR spectra deconvolution of PMDI-ELP gel showing that the secondary structure showed no significant changes between the day the sample solidified (A) and the day after (B).

The cross-linking capability of the ELP sample was therefore considered to be exhausted at the point of solidification.

It was herein hypothesized that in the solidified state, the molecular entropy of the processed sample was lost, causing the polypeptide secondary structure to remain.

Based on these results the following protein secondary structure formation sequence was proposed:

**Random coils  $\rightarrow$   $\alpha$ -helix  $\rightarrow$   $\beta$ -sheets  $\rightarrow$   $\beta$ -turns**

These findings correspond with literature research, which states that in  $\alpha$ -helices are stabilized by intramolecular hydrogen bonding within the polypeptide [173]. Meanwhile, in  $\beta$ -pleated sheet, H-bonds form intermolecular bonds between residues of different polypeptide chains [174]. Hence, it is proposed that amino side chains (R), form the basis for the subsequent formation of  $\beta$ -pleated sheets, including both  $\beta$ -sheets and  $\beta$ -turns.

Furthermore, literature research showed that in  $\beta$ -turns, polypeptide chains often connect antiparallely [129]. In the proposed PMDI-ELP cross-linking mechanism illustration shown in *chapter 3.1.1*, it was shown that cross-linking bonds between the lysine primary amine and the ELP backbone run parallelly, in line with the CLAs linear

isocyanate N=C=O functional groups. It is assumed that the proneness in PMDI-ELP formulations to form  $\beta$ -sheets, stems from the parallel alignment of ELP backbones. Lastly,  $\beta$ -sheets are often associated with  $\beta$ -turns as part of  $\beta$ -links [175]. Consequently, the prior formation of  $\beta$ -beta sheets was proposed to have led to the formation of  $\beta$ -links to initiate  $\beta$ -turn formation.

This hypothesis was further supported by results obtained through the daily deconvolution of FTIR spectra from glovebox and vacuum oven cross-linked PMDI-ELP gels. The numerical values [%] of protein secondary structures analyzed on respective days of cross-linking are stated in **Figure 3.7**. Corresponding FTIR spectra can be found in Appendix B.

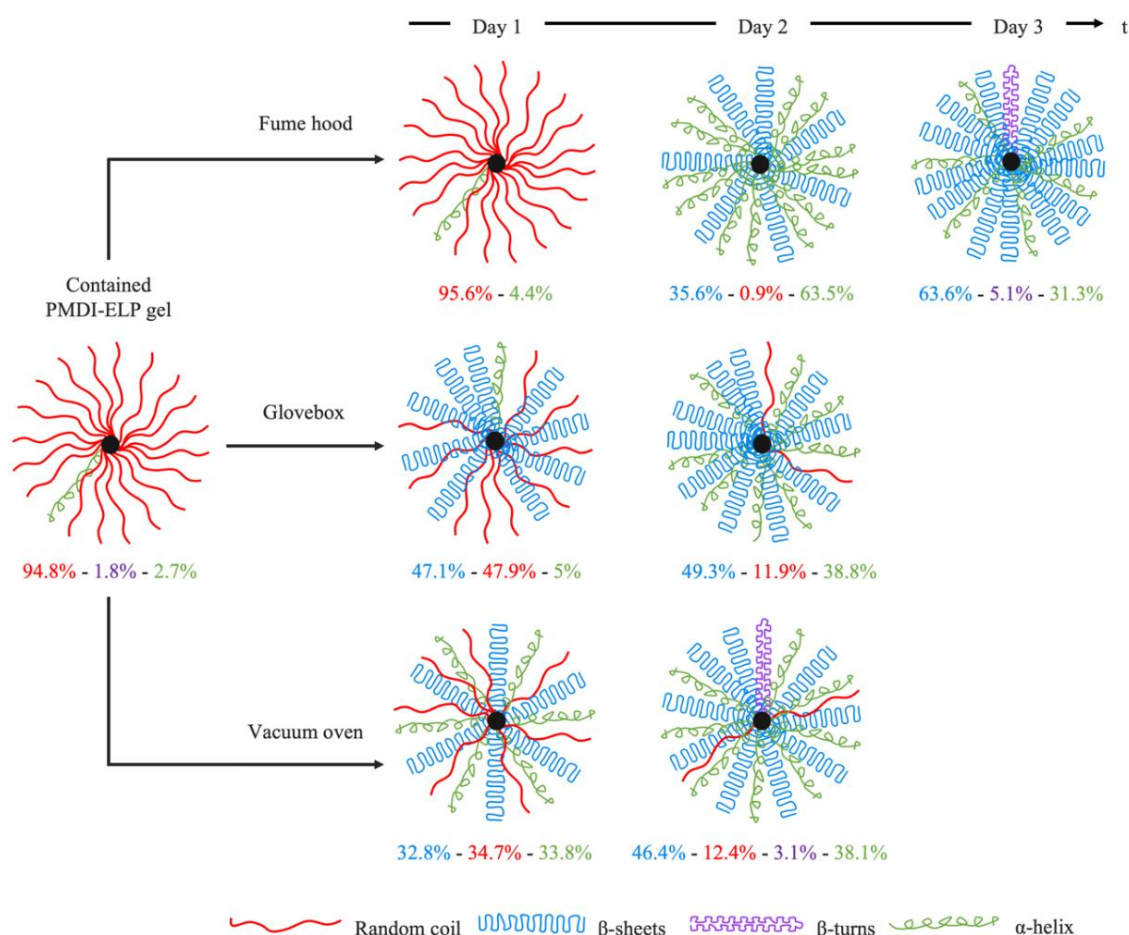


**Figure 3.7:** Visualization of changes in secondary structure in PMDI-ELP gels over time in different cross-linking environments, depicting how accelerated PMDI-ELP gel solidification sped up protein secondary formation but also decreased molecular order in the final protein secondary structure conformation.

In a glovebox and in a vacuum oven, gel cross-linking was observed to be accelerated. It was assumed that this occurred due to the comparatively lower humidity, which accelerated solvent evaporation [176] and thereby sample solidification and loss of molecular entropy. Samples cross-linked in these environments displayed higher molecular disorder (random coils), more  $\alpha$ -helices and significantly less of  $\beta$ -sheets and  $\beta$ -turns, than samples cross-linked in a fume hood.

To further test the hypothesis, ELP molecules were dissolved in solvent mixture (with no addition of CLA), drop casted onto PDMS substrate and dried in a fume hood and in a glovebox. Overnight, brittle, thin membranes were formed. Numerical values related to the protein secondary structure obtained from FTIR spectra deconvolution carried out on these membranes ( $n = 1$ ) are stated in **Table 3.4**.

**Table 3.4:** Numerical values [%] of FTIR spectra deconvolution from ELP in solvent, dried on PDMS substrate in a fume hood (left column) and in a glovebox (right column). The results showed higher molecular disorder (more random coils) in glovebox dried, non-cross-linked ELP membranes. Corresponding FTIR spectra can be found in Appendix B.

	Fume hood	Glovebox
$\beta$ -sheets	59.78	56.28
random coils	<b>8.9</b>	<b>14.45</b>
$\beta$ -turns	5.38	5.45
$\alpha$ -helix	25.84	23.83

Results showed a higher degree of disorder in glovebox cross-linked membranes. As membrane formation was observed to be accelerated in low-humidity environments, this result agrees with the previously proposed hypothesis stating that supramolecular self-assembly was sequential and time dependent.

To assess whether protein secondary structure formation could solely be achieved in a dry environment, PMDI-ELP gel was submerged in DI water post synthesis. Immediate solvent leaching was observed, which led to sample shrinkage/solidification.

As previously mentioned, the gelation of PMDI-ELP was hypothesized to occur due to the saturation of lysine cross-linking sites in the polypeptide of interest and excess isocyanate cross-linking sites in the CLA undergoing polymerization. FTIR analysis synthesized gels showed that the underlying protein secondary structure in such samples is mainly composed of an unstable network of disordered coils (> 90%). It is therefore

assumed that the solvent incorporated in this formulation is entrapped in this network of random coils.

To understand why leaching of the solvents into the aqueous solution occurs, literature research was undertaken to understand interactions between water and the solvents of interest, DMF and DMSO.

Both DMF and DMSO are polar aprotic solvents that can form hydrogen bonds. Water molecules can equally form hydrogen bonds due to their inherent polar covalent bonds [177]. As a result, these organic solvents interact with water, hydrogen bonds form between the respective polar groups, leading to the dispersion of solvent molecules in water, and *vice versa* [178][179].

In addition to that, DMF, which is the main component of the solvent mixture, is not stable in water over a long period of time as degrades to the secondary amine dimethylamine (DMA) and the carboxylic acid, formic acid (FA) (**Figure 3.8**) [180].

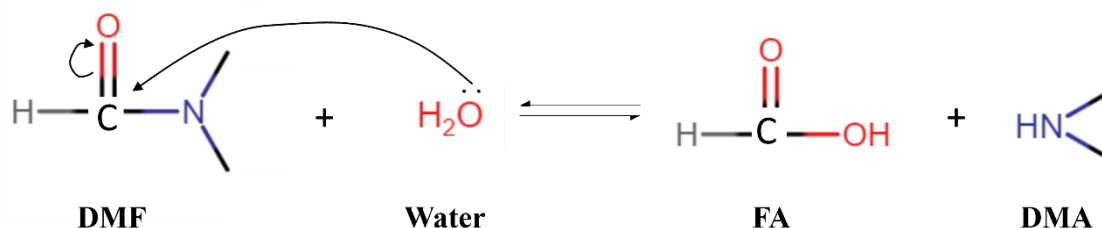


**Figure 3.8:** Schematic of DMF hydrolysis to dimethylamine (DMA) and formic acid (FA) [181]

**Figure 3.9** illustrates the secondary structure translation after 3h immersion in DI water and states the numerical values [%] obtained upon FTIR spectra deconvolution.

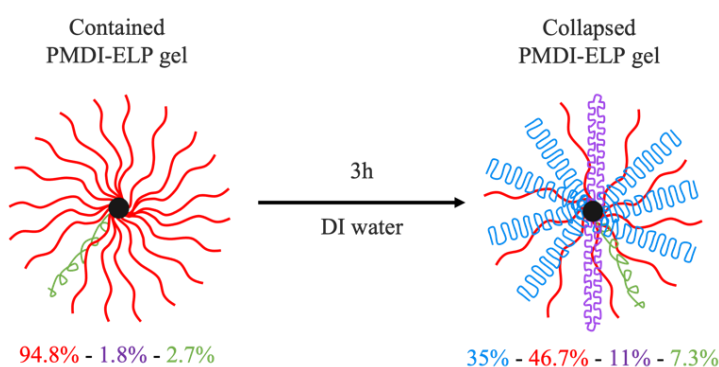


**Figure 3.9:** Visualization of changes in secondary structure in PMDI-ELP gels after immersion in DI water, showing the translation from a highly disordered protein secondary structure to a mostly ordered configuration. Corresponding FTIR spectra can be found in Appendix B.

Results obtained from samples which underwent solvent leaching showed that the formation of ordered protein coils was compromised in a wet environment compared to a dry cross-linking environment (**Figure 3.7**), but could be achieved, nonetheless.

The relatively increased disorder, compared to samples that were cross-linked at the open air, was suggested to be rooted in the accelerated sample solidification, leading to the accelerated the loss of molecular entropy. Furthermore, as previously established, long-time humidity exposure of the CLA PMDI reportedly leads to decomposition of functional isocyanate groups (**Figure 3.5**) [172], which was herein assumed to diminish the CLA's reactivity capacity to form cross-links with the ELPs' lysine cross-linking sites.

Based on these results, it was suggested that secondary structure formation was not only time dependent, but also relied on sample solidification, which could be achieved in dry and wet environments.

### *3.1.2.3. Investigation of gel shrink capacity*

In the above, it was suggested that sample shrinkage plays a role in the formation of an ordered protein secondary structure in ELP-based gels. Under consideration of the aim to integrate the fabrication process into AM, gel shrinkage was assessed to gain an understanding of the sample dimensional behaviour post cross-linking. It is essential to understand the materials' shrinkage behaviour to generate print files which account for the material shrinkage. For example, if material shrinkage of 50% post cross-linking is observed, print files shall be generated at 150% of the desired size to achieve the desired sample size post cross-linking.

In this section, shrinkage of PMDI-ELP gels after three days in different cross-linking environments (i.e. in a fume hood (FH), a glovebox (GB), a vacuum oven (VO) and DI water) was quantified in accordance with the method specified in *chapter 2.2.2*. Obtained numerical values are attached in Appendix A.

Test samples were run in duplicate to account for sample-to-sample variability. The quantitative data is expressed as mean  $\pm$  standard deviation (**Figure 3.10**).

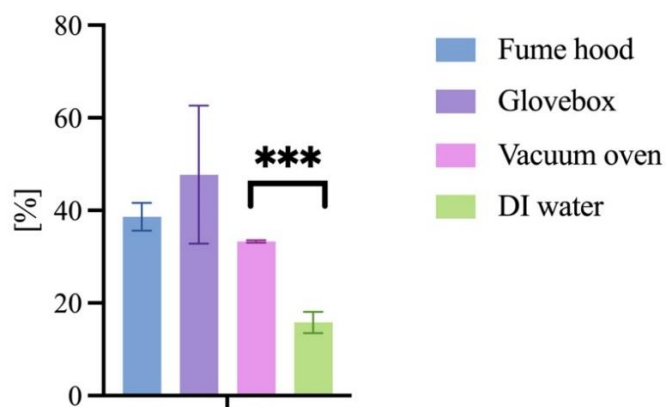


**Figure 3.10:** PMDI-ELP gels shrinkage bar chart, showing significantly less shrinkage in DI water. Mean values: fume hood 38.6 %, glovebox 47.7 %, vacuum oven 33.3 %, DI water 15.8 %.

The differences in shrinkage between gels which were cross-linked in a dry environment were not found to be statistically significant. However, gels submerged in DI water showed statistically significantly ( $P = .0087$ ) less shrinkage, compared to dried samples.

This difference was attributed to the fact that these samples did not only shrink due to solvent leaching, but also absorbed water, which was not removed before sample weighing. It is assumed that  $\text{CO}_2$  gas bubbles, which can as mentioned form during the decomposition of PMDI upon hydrolysis (**Figure 3.5**) additionally enabled the entrapment of water.

Strong vertical collapse was experienced post cross-linking in a dry environment. However, the samples did not fully collapse into 2D membranes (**Figure 3.11**).

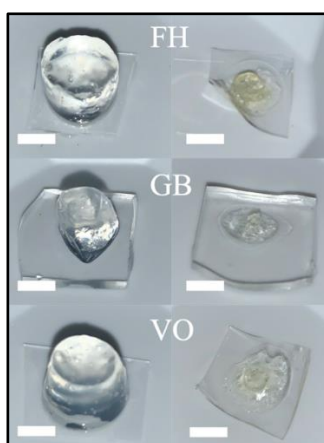


**Figure 3.11:** PMDI-ELP gels before (left) and after shrinkage (right), depicting vertical sample collapse after cross-linking in different dry environments. Scale bars: 5 mm.

### 3.2. Protein secondary structure formation in genipin-ELP gels

To fabricate genipin-ELP gel, 0.5 wt% genipin and 4% SN<sub>A</sub>15 ELP molecules were separately dissolved in solvent mixture at a 1:1 ratio at room temperature, before the constituents were mixed *via* vortex. The constituents were dissolved separately with the aim to homogeneously disperse the powdered CLA. Incubation of the genipin-ELP solution in a sealed Eppendorf tube resulted in the formation of a homogenous gel after approximately 5 – 7 days (**Figure 3.12**). The gelation speed was dependent on the solvent mixture volume. An increase in solvent volume resulted in extended incubation periods. It was assumed that the gelation was based on ELP reticulation, meaning that a disordered but stable protein secondary structure was formed [182].

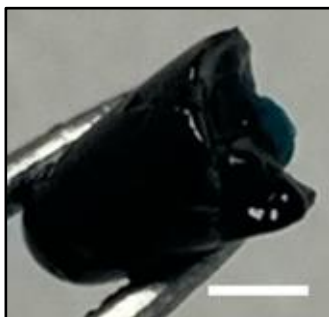


**Figure 3.12:** 0.5 wt% genipin-ELP gel (200  $\mu$ m) that formed after 6 days of incubation. Scale bar: 5 mm.

#### 3.2.1. Identification of protein secondary structure formation triggers in genipin-ELP gels

To understand which stimuli triggered self-assembly in this formulation, the genipin-ELP gel was FTIR analyzed daily for seven days, as it remained contained in a sealed Eppendorf tube. Consequently, the formulation was tested in a liquid state (Day 0 – 5) and a gel state (Day 5 – 7).

Thereafter, the gels were cross-linked in different environments, i.e., in a fume hood, a glovebox and in a vacuum oven (at room temperature). Cross-linking gel samples were FTIR scanned daily until they attained a solid configuration. FTIR spectra were deconvoluted in accordance with the methods described in *chapter 2.2.1*.

### 3.2.1.1. Protein secondary structure in contained genipin-ELP gel

A highly disordered protein secondary structure ( $\approx 96\%$  random coils) was observed in the genipin-ELP solution from Day 1 – 4, as well as in gel configuration (Day 5 – 7) (**Table 3.5**).

**Table 3.5:** Numerical values [%] obtained through the deconvolution of FTIR spectra of genipin-ELP solution (Day 0 – 4) and the thereafter forming gel (Day 5 – 7), showing a static predominantly disordered protein secondary structure over time. Corresponding FTIR spectra can be found in Appendix B.

	Day 0	Day 1	Day 2	Day 3	Day 4	Day 5	Day 6	Day 7	Mean	St.Dev.
$\beta$ -sheets	-	-	-	-	-	-	-	-	-	-
random coils	95.95	95.53	95.76	97.32	95.94	95.83	96.08	97.48	96.24	0.69
$\beta$ -turns	1.85	2.32	1.73	-	1.83	1.8	1.59	-	1.39	0.83
$\alpha$ -helix	2.2	2.15	2.62	2.68	2.23	2.37	2.34	2.52	2.39	0.19

These results coincided with the findings made in PMDI-ELP gel secondary structure analysis. As observed in PMDI-ELP formulations, the addition of genipin to ELP in solution alone did not suffice to trigger the formation of an ordered protein secondary structure. Furthermore, these results coincide with the above made hypothesis, wherein it was suggested that the gelation mechanism was based on reticulation of a disordered but stable protein secondary structure. ELP reticulation was herein assumed to avoid chemical cross-linking interactions between the lysine cross-linking sites in the ELP and the genipin cross-linking agent.

A similar genipin-molecule interaction has been described in a previous study, wherein gradual gelation was observed in binding genipin to primary amines in lactose modified chitosan. This phenomenon was also attributed to protein reticulation [183].

Conclusively, within the scope of this work, time was not a parameter that was considered within this experimental setup as this parameter was not found to be a significantly relevant factor in the formation of an ordered supramolecular network in contained genipin-ELP solution/gel.

In the following section, genipin-ELP gels were dried in different environments, i.e., fume hood, glovebox, and vacuum oven, and FTIR scanned daily to gain an understanding of the protein secondary structure formation.

### 3.2.1.2. Protein secondary structure in cross-linked genipin-ELP gels

**Figure 3.13** visualizes FTIR spectra deconvolution results obtained from genipin-ELP gels over time in the respective environments. Corresponding FTIR spectra can be found in Appendix B.

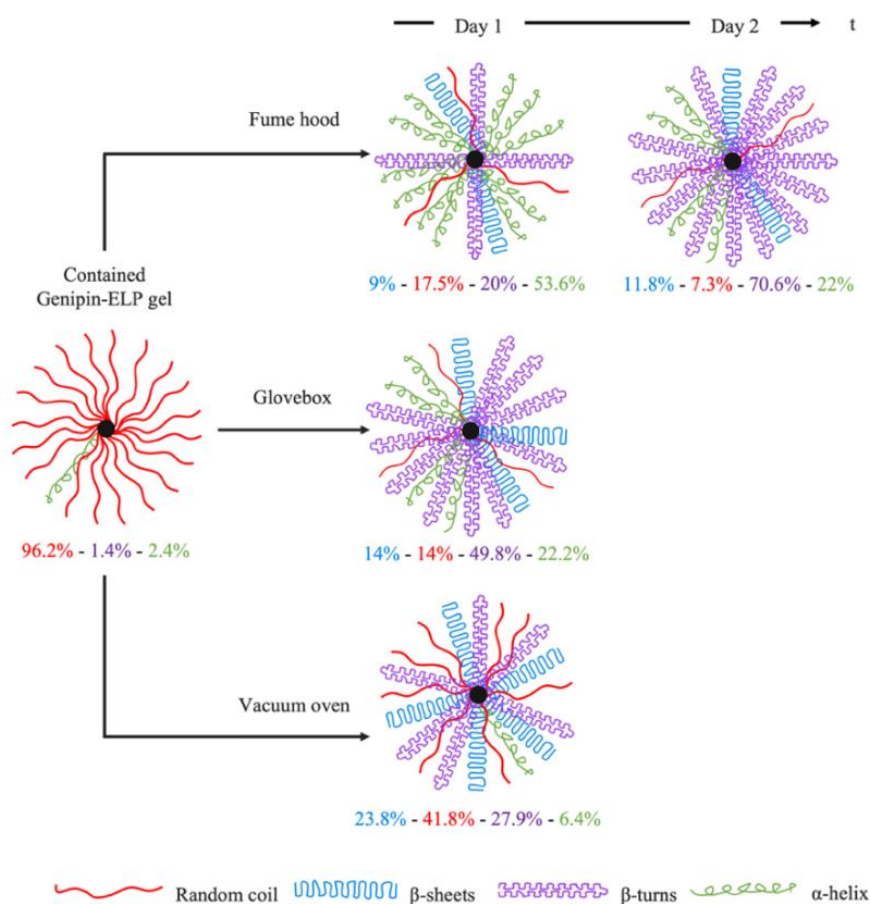


**Figure 3.13:** Visualization of changes in secondary structure in genipin-ELP gels over time in different cross-linking environments, depicting how accelerated sample solidification sped up protein secondary formation but also caused higher disorder in the final protein secondary structure configuration.

The highest degree of protein secondary structure order in solidified genipin-ELP gels was achieved *via* fume hood cross-linking. Based on previously drawn hypotheses in the assessment of protein secondary structure formation in PMDI-ELP gels, this was attributed to the decelerated sample solidification speed in a comparatively high atmospheric pressure environment, resulting in a cross-linking time span of two days. By comparison, the glovebox cross-linked gel showed intermediate levels of protein secondary structure order, and the vacuum oven cross-linked gel showed the lowest level of protein secondary structure order, in line with an accelerated cross-linking time span of one day.

Based on these results, it was suggested that supramolecular order was increased, when the environmental factors allowed for an extended sample solidification period. The drying time was extended in environments with a comparatively higher atmospheric pressure, i.e., the fume hood. In environments with lowered atmospheric pressure, i.e., glove box or vacuum oven, the drying period was shortened in comparison to the fume hood. Lowering atmospheric pressure is often employed to accelerate drying processes, as it accelerates solvent evaporation [184][185].

FTIR spectra deconvolution results suggested that protein secondary structure formation in genipin-ELP gels was time dependent and formed in a sequential manner. Based on these results, the following sequential formation was proposed:

**Random coils  $\rightarrow$   $\alpha$ -helix  $\rightarrow$   $\beta$ -turns  $\rightarrow$   $\beta$ -sheets.**

These findings correspond with literature research, which states that in  $\alpha$ -helices are stabilized by intramolecular hydrogen bonding within the polypeptide [173]. Meanwhile, in  $\beta$ -pleated sheet, H-bonds form intermolecular bonds between residues of different polypeptide chains [174]. Hence, it is proposed that amino side chains (R), form the basis for the subsequent formation of  $\beta$ -pleated sheets, including both  $\beta$ -sheets and  $\beta$ -turns. Furthermore, literature research showed that in  $\beta$ -turns, polypeptide chains often connect antiparallely [129].

In *chapter 3.1.2.2.*, it was hypothesized that the change in sequence of protein secondary structure formation was determined by the CLAs' chemical structure which enables cross-linking between the functional isocyanate groups and the primary amine groups of lysine, in a parallelly aligned manner. Whilst this the linear alignment of functional isocyanate groups in PMDI was assumed to primarily cause parallel  $\beta$ -sheet alignment prior to  $\beta$ -turns regarding the sequential secondary protein structure formation, a different mechanism was assumed for genipin cross-linking. The assumed cross-linking mechanism is described in the following.

Genipin provides two cross-linking sites for interactions with lysine primary amines (**Figure 3.14**) [186]. Therefore, two possible cross-linking routes need to be considered [187], wherein (1) two primary amine groups that stem from the same ELP backbone form cross-links with the same genipin molecule, or (2) two primary amine groups that stem from two separate ELP backbones form cross-links with the same genipin molecule.

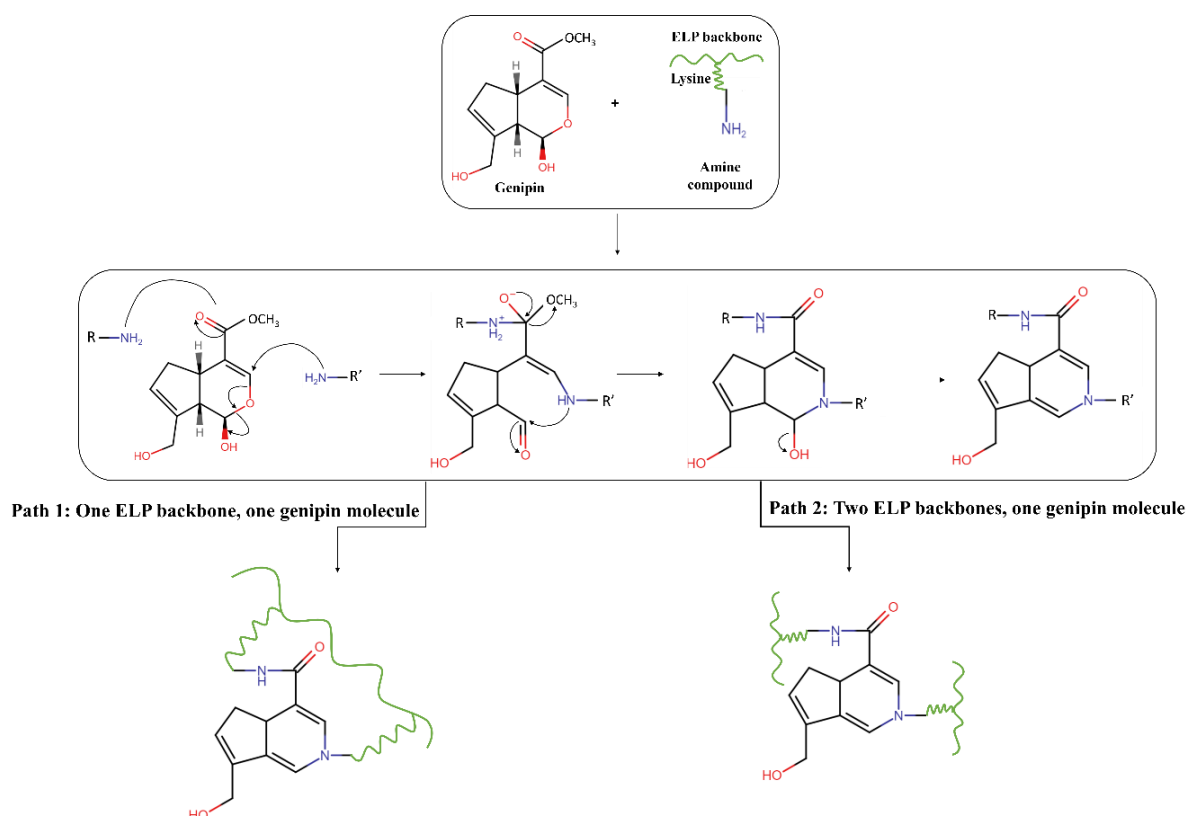


**Figure 3.14:** Genipin-ELP cross-linking mechanism illustration depicting how the formation of cross-links can either occur between (1) one genipin molecule and two primary amine groups from the same ELP backbone, or (2) one genipin molecule and two primary amine groups from two separate ELP backbones.

In *chapter 1.4.1.1*, the structural arrangement of in  $\beta$ -turns was described as follows: ' *$\beta$ -turns are composed of four polypeptide chains and often connect antiparallely, causing the polypeptide chains to turn back onto themselves [129].*'

Since FTIR data convolution suggested  $\beta$ -turn formation over  $\beta$ -sheet formation in the sequential protein secondary structure formation in genipin-ELP gels, it was assumed that two primary amine groups from the same ELP backbone formed cross-links with one genipin molecule (**Figure 3.14** (1)), thereby causing antiparallel alignment within the cross-linked polypeptide chains to turn back onto themselves and forming  $\beta$ -turns.

It was assumed that towards the end of the supramolecular self-assembly process, as lysine primary amines were gradually saturated, residual genipin molecules were more likely to bond to two separate ELP (**Figure 3.14** (2)) and form parallel polypeptide chain alignment and thereby stabilizing  $\beta$ -sheets [130].

### 3.3. Characterization of ELP-based membranes

To enhance comparability between the previously reported HDI-ELP membrane formulation and its protein secondary structure conformation [140], PMDI- and genipin-ELP membranes were herein synthesised and analysed. HDI-ELP membranes served as a control group.

Membranes were analysed towards their underlying secondary structure *via* FTIR spectra deconvolution. Different cross-linker volumes were integrated into the formulations to understand how this affected the protein secondary structure configuration of synthesized membranes. The distribution of ordered and disordered regions as well as the corresponding FTIR spectra of the formulations of interest are stated in Appendix B. To obtain representative values, three ELP membrane samples (S) of the same formulation were scanned in two different positions (P) (**Figure 3.15**).

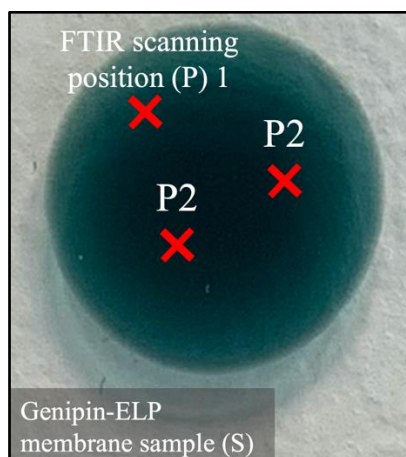


**Figure 3.15:** Example of scanning position (P) selection in ELP membrane samples (S), displayed on a genipin-ELP membrane.

This was done to account for potential variability of the cross-linking density across membranes. This variability was considered a risk due to the physical state of assessed CLA in the pure state. PMDI displays a higher viscosity in its pure form than the previously proposed CLA HDI. Furthermore, it was demonstrated that the use of PMDI shows comparatively higher reactivity in the processing of ELP based materials, compared to HDI, which was assumed to potentially lead to a non-homogenously cross-linked network. On the other hand, powdered genipin CLA required dissolution in organic solvents prior to ELP membrane synthesis, which may also impact cross-linking homogeneity due to the risk of residual undissolved powder particles.

shows and example of position selection in membrane samples.

Additionally, membranes of the same formulation ( $n = 3$ ) were tested towards their swelling capacity in accordance with the method described in *chapter 2.2.2*. Membranes of interest were submerged in DI water and stored at  $38^{\circ}\text{C}$  for 24 h to mimic physiological conditions [188]. Numerical values that correspond to the presented swelling capacity results can be found in Appendix C.

### 3.3.1. PMDI-ELP membrane characterization

PMDI-ELP membranes with varying PMDI concentrations (0.1 wt%, 0.2 wt%, 0.3 wt%) were prepared by dissolving 4% ELP and the desired PMDI volume in two separate Eppendorf tubes. The constituents were dissolved in 50% of the total solvent mixture. The synthesized solutions were thereafter mixed in an Eppendorf tube *via* vortex. This was conducted in a fume hood, at room temperature. The PMDI-ELP solution was drop casted onto PDMS substrate and cross-linked in a fume hood. To achieve drop casting of 0.3 wt% PMDI formulations, which, as mentioned, showed fast gelation kinetics at room temperature, the constituents were cooled down in a fridge ( $4^{\circ}\text{C}$ ) for 30 minutes before mixing. The rationale of this method was to decelerate the molecular entropy and thereby extend the gelation time window. Within 24 h, the formation of PMDI-ELP membranes was achieved. The described fabrication method is illustrated in **Figure 3.16**.

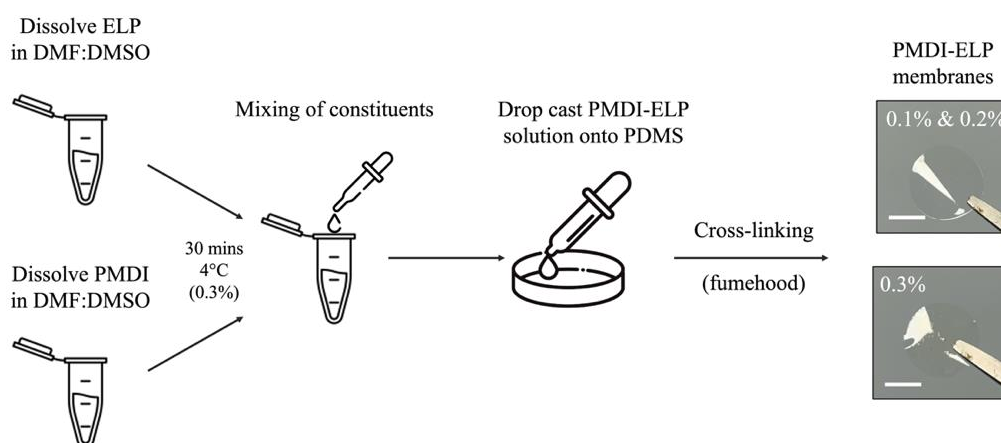


**Figure 3.16:** Fabrication method PMDI-ELP membranes, where ELP and PMDI were dissolved separately in 50% solvent mixture before being mixed and drop casted onto PDMS. Scale bars: 500  $\mu\text{m}$ .

It was observed that in ELP membranes that were left to dry on a PDMS substrate, drying commenced at the outer edge of the membrane and from there on continued towards membrane centre (**Figure 3.17A, B**), until a membrane is formed (**Figure 3.17C**).

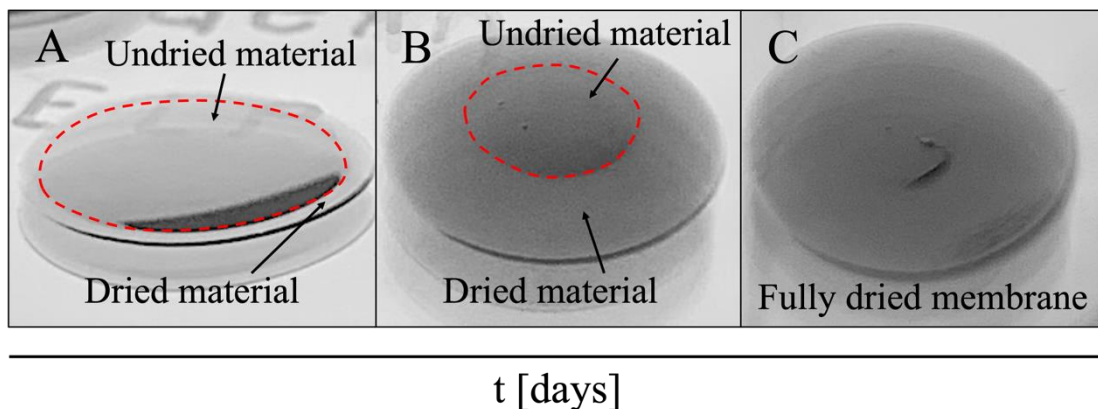


**Figure 3.17:** Images showing how drop casted ELP-CLA-membranes dry over time, from the edge of the membrane towards (A, B) the centre of it (C).

It was assumed that this spatial drying behaviour was encountered due to the applied drop casting method, where a droplet was deposited onto the substrate *via* pipetting. This resulted in a dome shaped droplet with uneven distribution of liquid ELP-CLA-solution across the cross-section of the sample. Due to the comparatively lower solvent volume, ELP-CLA-solution that was deposited at the membrane edges showed faster drying than solution in the membrane centre.

In PMDI-ELP membranes, a yellowish tone was observed, which is characteristic for aliphatic poly-isocyanates [189]. It has also been reported that oxidation reactions on the backbone of the aliphatic poly-isocyanate triggers change of colour in curing samples, a process which is accelerated under the influence of UV light [190].

PMDI-ELP membranes were also found to be more brittle, compared to the other investigated cross-linked ELP membranes. Membranes became more brittle as the PMDI concentration was increased. It was proposed that the brittleness was subject to the polymeric nature of the CLA, resulting in the membrane forming a tighter molecular network and thereby affecting the mechanical properties.

### 3.3.1.1. Protein secondary structure analysis of PMDI-ELP membranes

The bar chart in **Figure 3.18** depicts results gathered from FTIR spectra deconvolution of membranes, showing changes in the secondary structure conformation with an increasing amount of PMDI.

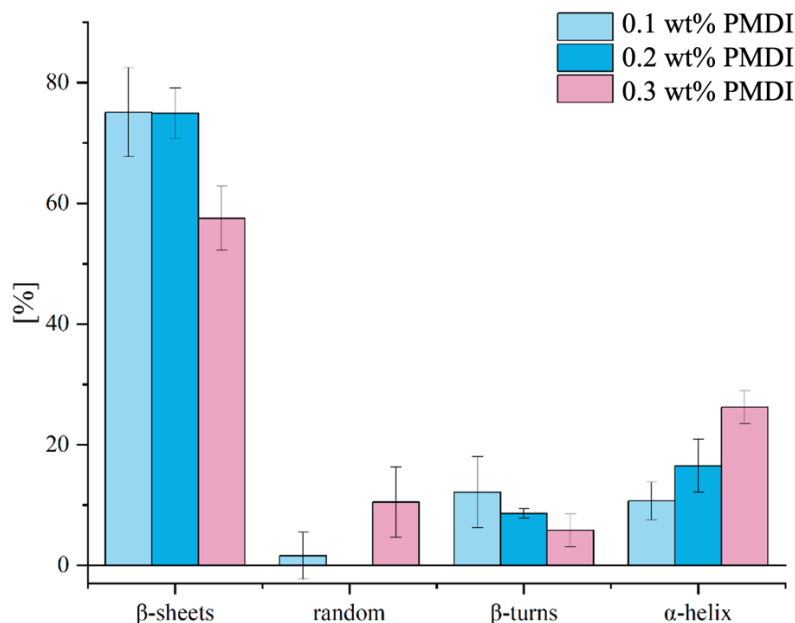


**Figure 3.18:** Numerical values obtained through the deconvolution of FTIR spectra, translated into a bar chart, showing how the secondary structure in PMDI-ELP membranes changed with increasing PMDI volumes. Overall, a decrease of  $\beta$ -sheet and  $\beta$ -turn formation was observed, whilst  $\alpha$ -helices increased. At a 0.2 wt% PMDI concentration, no random coils were detected upon FTIR deconvolution Appendix B. Hence, no error bar was added to this region. At a higher concentration (0.3 wt%) random coil presence increased.

FTIR spectra deconvolution showed 100% protein secondary structure translation into an ordered protein structure conformation at a PMDI concentration of 0.2 wt%. No standard deviation is displayed in the random coil bar of 0.2 wt% PMDI concentrations, as all scanned membrane locations showed 100% protein secondary structure translation into ordered coils.

Meanwhile, at a concentration of 0.1 wt% PMDI, 100% protein secondary structure translation was only observed in 4 out of 6 scanned membrane positions which in turn also impacted the resulting standard deviations for ordered coils.

In *chapter 3.1.2* and *3.2.1*, daily FTIR analysis of synthesized ELP results showed sequential formation of the underlying protein secondary structure in PMDI-ELP and genipin-ELP formulations (random coils  $\rightarrow$   $\alpha$ -helix  $\rightarrow$   $\beta$ -sheets  $\rightarrow$   $\beta$ -turns,

and random coils  $\rightarrow$   $\alpha$ -helix  $\rightarrow$   $\beta$ -turns  $\rightarrow$   $\beta$ -sheets, respectively), leading to the hypothesis that protein secondary structure formation was a time dependent process. In *chapter 3.1.2*, it was additionally hypothesized that once samples have solidified, molecular entropy is lost and the self-assembly process is terminated, leaving the samples' underlying protein secondary structure in a static state.

It was therefore assumed that deviations in secondary structure analysis may stem from the fact that, as shown in **Figure 3.17**, membrane solidification occurred at different time points, which was assumed to result in varying protein secondary structure configurations across analysed membranes of the same formulation.

Additionally, it was visually observed that an increase in PMDI concentration resulted in accelerated cross-linking kinetics of synthesized membranes. Results presented in *chapter 3.1.2.2* showed that  $\alpha$ -helices are the first ordered coils formed in the sequential protein secondary structure translation in PMDI-ELP formulation. In agreement with the results, FTIR spectra deconvolution in the herein presented results showed that  $\alpha$ -helices increased as the CLA concentration was increased, and sample solidification was accelerated.

In calculations that were presented in *chapter 3.1.1*, a PMDI volume of 0.28 wt% was suggested to saturate primary amines in 4% SN<sub>A</sub>15 ELP. These results were considered to be in good agreement with practical trials.

FTIR spectra deconvolution in this chapter showed that ordered coils diminished at a CLA concentration of 0.3 wt%. Considering the results gathered in *chapter 3.1.1* and the herein observed 100% protein secondary structure translation achieved at a PMDI concentration of 0.2 wt%, a parabolic behaviour for secondary structure formation in PMDI samples was hypothesized. In **Figure 3.19** depicts this proposed mechanism which illustrates the assumption that the formation of ordered secondary structure regions diminished once the lysine saturation threshold as exceeded.

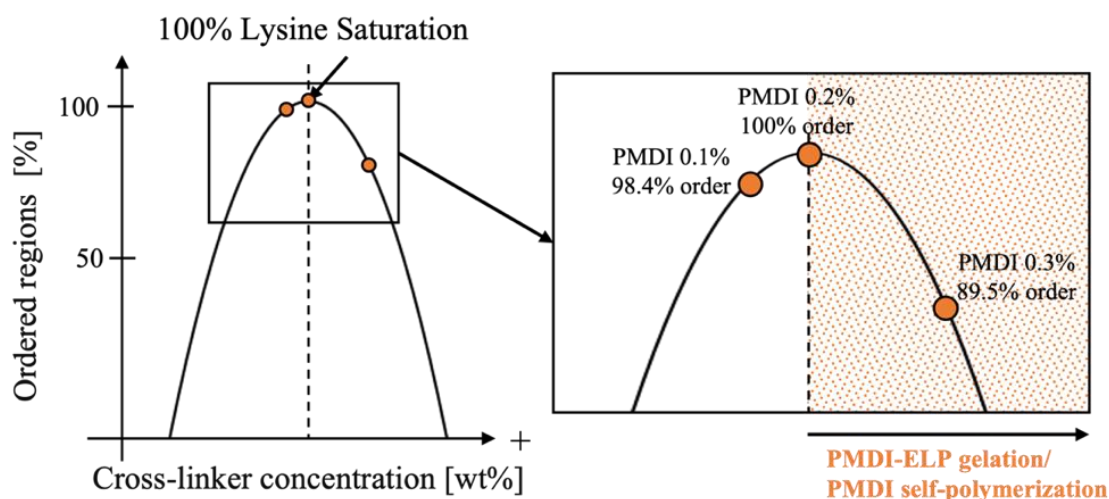


**Figure 3.19:** PMDI-ELP formulation schematic, describing how exceeding the lysine saturation threshold in terms of cross-linker concentration caused increased disorder protein secondary structure formation.

As previously stated, it was suggested that once the lysine saturation threshold was exceeded, polymerization amongst functional isocyanate groups within the CLA occurred. Furthermore, the protein secondary structure of PMDI-ELP gels in a sealed container was shown to maintain molecular entropy over time, until sample solidification was induced *via* drying or immersion in solution. Results showed that the protein secondary structure of contained gel was mainly composed of random coils ( $\approx$  95%). As samples solidified over time, an ordered protein secondary structure was formed.

Based on these results, it was suggested that once the lysine saturation threshold was exceeded, functional isocyanate groups in a gel conformation which initially saturated the lysine cross-linking sites, had the freedom to rearrange before the sample was fully solidified, thereby allowing polymerization within the CLA, resulting in higher disorder in the final protein secondary structure configuration.

### 3.3.1.2. Investigation of PMDI-ELP membrane swell capacity

Membrane swelling results show a statistically significant ( $P = 0.04$ ) difference between 0.1 wt% and 0.2 wt% membranes when compared to the 0.3 wt% PMDI formulations (Figure 3.20). The numerical swelling data is attached in Appendix C.

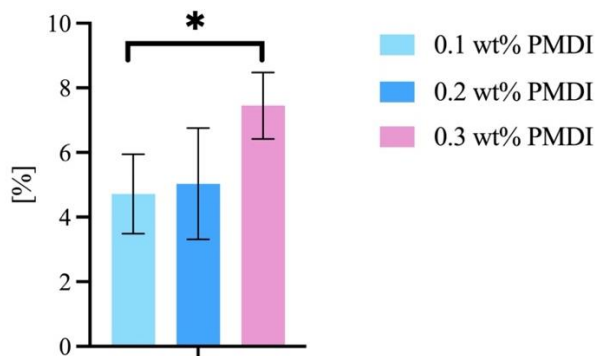


**Figure 3.20:** Membrane swell capacity in PMDI-ELP membrane formulations.

As FTIR analysis on PMDI-ELP membrane with different CLA concentrations have shown that at lower PMDI concentrations (0.1 wt% and 0.2 wt%), less random coils were observed in comparison with 0.3 wt% PMDI formulations, concluding higher cross-linking density in membranes with a lower CLA concentration.

It was proposed that the increased swelling behaviour was caused by the higher molecular disorder in 0.3% PMDI-ELP membranes, enhancing more water diffusion into the less tightly bound network.

### 3.3.2. Genipin-ELP membrane characterization

Genipin-ELP membranes with varying genipin concentrations (0.5 wt%, 1.0 wt%, 1.5 wt%) were prepared by dissolving 4% ELP and the desired genipin volume in separate Eppendorf tubes. 50% of the solvent mixture volume were used to dissolve each constituent before uniting and mixing the solutions in one Eppendorf tube, using a vortex (**Figure 3.21**). Synthesis was conducted at room temperature, in a fume hood.

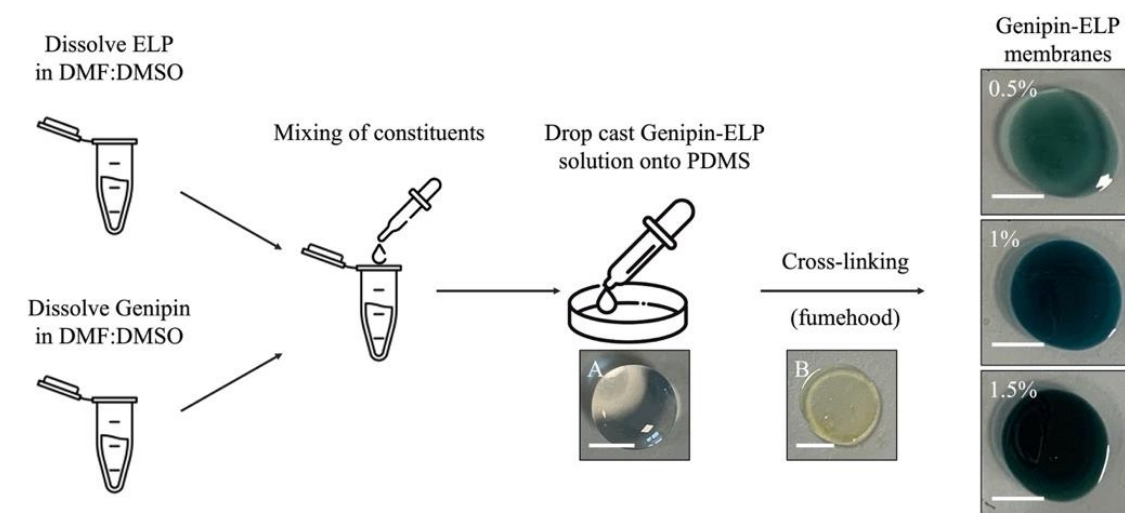


**Figure 3.21:** Fabrication method of genipin-ELP membranes, where ELP and genipin were dissolved in separate Eppendorf tubes to enhance CLA integration, before being mixed and drop casted onto PDMS. Scale bar: 500  $\mu\text{m}$ .

The drop casted genipin-ELP solution appeared as a colourless liquid. Flexible membranes were formed over different time periods, ranging from 3 – 4 days (0.5 wt%) to 2 – 3 days (1.0 wt% and 1.5 wt%). As cross-linking occurred, the membranes first developed an orange colour which turned into different shades of blue when cross-linking was completed. With an increasing genipin volume, a deeper shade of blue was developed. Literature research showed that this change of colour is characteristic in genipin cross-linking with primary amines and oxidation [158][191][183].

#### 3.3.2.1. Protein secondary structure analysis of genipin-ELP membranes

FTIR analysis of genipin-ELP membranes demonstrated that an increase in genipin concentration promoted the formation of  $\beta$ -turns and  $\alpha$ -helices, whilst  $\beta$ -sheets and random coils diminished (**Figure 3.22**).

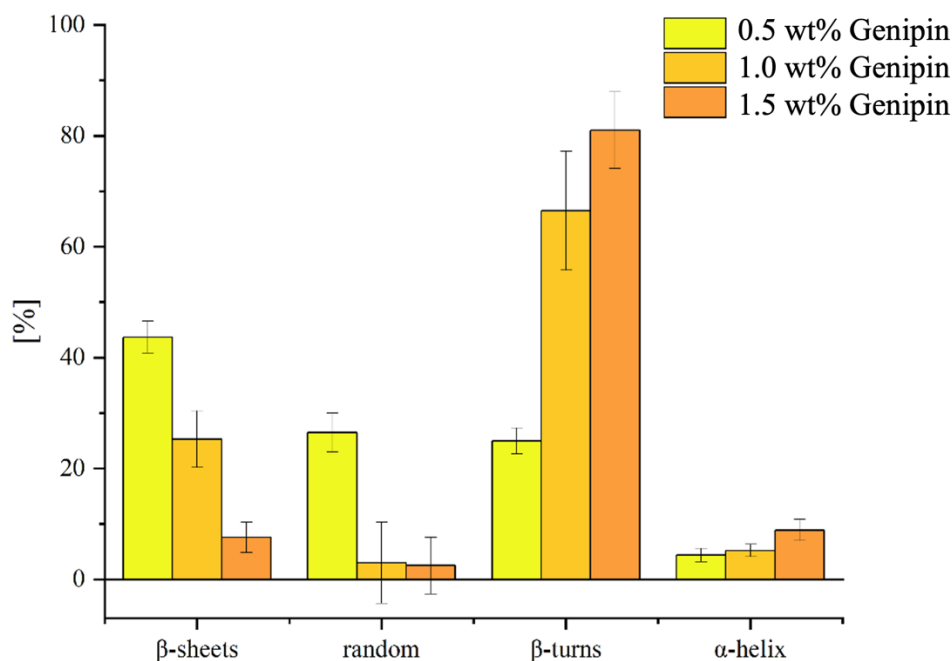


**Figure 3.22:** Bar chart of changes in secondary structure with increasing genipin volumes in ELP membranes. The results showed an overall decrease of  $\beta$ -sheet and random coils formation whilst  $\alpha$ -helices slightly increases with an increase in CLA concentration.

Comparatively high standard deviations were observed in the data from 1.0 wt% and 1.5 wt% genipin-ELP membranes. These deviations stem from the occurrence of 100% protein secondary structure translation in 4 out of 6 scanned positions in 1.0 wt% genipin-ELP membranes, and 5 out of 6 scanned positions in 1.5 wt% genipin-ELP membranes. This consequently affected the standard deviations in other detected protein secondary structures. Similar observations were made during the analysis of PMDI-ELP membranes, which were traced back to varying drying times across the membrane sample, where membrane edges dried faster than centres, leading to comparatively early membrane solidification and thereby termination of the protein secondary structure translation. The same reason for variations in secondary structure across samples was assumed in genipin-ELP membranes.

With regards to lysine saturation in 4% ELP solution, the calculations below demonstrate that in theory, a genipin concentration of 9.5 wt% is required to saturate lysine in 100 mg SNA15 ELP (100%). Consequently, 0.38 wt% genipin theoretically saturate 4% SNA15ELP.

- (1)  $\frac{4,707e^{-0.5}mol}{1} = 4,707 \cdot 2.353 e^{-05}mol$  genipin saturates  $4,707e^{-05} mol$  lysine (present in 100 mg SN<sub>A</sub>15 ELP)
- (2)  $4,707e^{-05}mol \times 226,2 g mol^{-1} = 0.00950g = 9.5mg$  required to cross-link 100 mg SN<sub>A</sub>15 ELP

The calculations follow the same method as those presented in *chapter 3.1.1*, wherein the theoretical PMDI concentration for lysine saturation was calculated. However, the herein presented calculations take the molecular weight of genipin ( $226.23 g mol^{-1}$ ) into account (equation (2)). Furthermore, sequential secondary structure formation results were considered, which suggested that two primary amine groups that stem from one ELP backbone form cross-links with the same genipin molecule (equation (1)). This was elaborated on in *chapter 3.1.2.1*.

Meanwhile, previous research proposed that functional groups in genipin can undergo oxidation [183], which is suggested potentially diminishes reactivity of genipin with primary amines, such as during SN<sub>A</sub>15 ELP cross-linking. It was herein proposed that a multiple fold in genipin concentration was necessary to achieve lysine saturation, to compensate for functional groups that have undergone oxidation instead reacting with primary amines.

As previously stated, 5 out of 6 FTIR scanned positions in 1.5 wt% genipin-ELP membranes showed 100% protein secondary structure translation into ordered coils. To understand how further increase in CLA affected the protein secondary structure conformation, FTIR spectra deconvolution was conducted on 2.5 wt% genipin-ELP membranes. The results, presented in **Table 3.6**, showed that an increase in cross-linker concentration did not significantly impact the outcome. As observed at a concentration of 1.5 wt% genipin-ELP membranes, 100% protein secondary structure translation was achieved in 5 out of 6 scanned membrane positions. Corresponding FTIR graphs can be found in Appendix B.

**Table 3.6:** Numerical values secondary structure in 2.5 wt% genipin-ELP membranes, showing 100% protein secondary structure translation into ordered coils in five out of six scanned sample (S) positions (P).

	S1P1	S1P2	S2P1	S2P2	S3P1	S3P2	Mean	St.Dev.
β-sheets	-	1.17	1.17	1.25	1.1	1.38	1.01	0.5
random coils	-	-	14.77	-	-	-	2.46	6.03
β-turns	70.13	60.39	76.09	64.62	63.74	91.41	71.06	11.39
α-helix	29.87	38.43	7.97	34.13	35.16	7.21	25.46	14.11

As previously presented, at 0.2wt% PMDI concentration, 100% protein secondary structure translation into an ordered protein secondary structure configuration was observed. It was hypothesised that once this threshold was exceeded, polymerization within the polymeric CLA caused functional isocyanate groups to rearrange during cross-linking, leaving previously saturated lysine primary amine sites uncross-linked and polymerizing within the polymeric isocyanate CLA instead, resulting in an increasing protein secondary structure disorder.

Unlike in PMDI-ELP formulations, where a parabolic correlation between the cross-linker concentration and the formation of ordered regions was assumed, a plateauing correlation between cross-linker concentration and the formation of ordered regions in the protein secondary structure was proposed for genipin-ELP formulations (**Figure 3.23**).

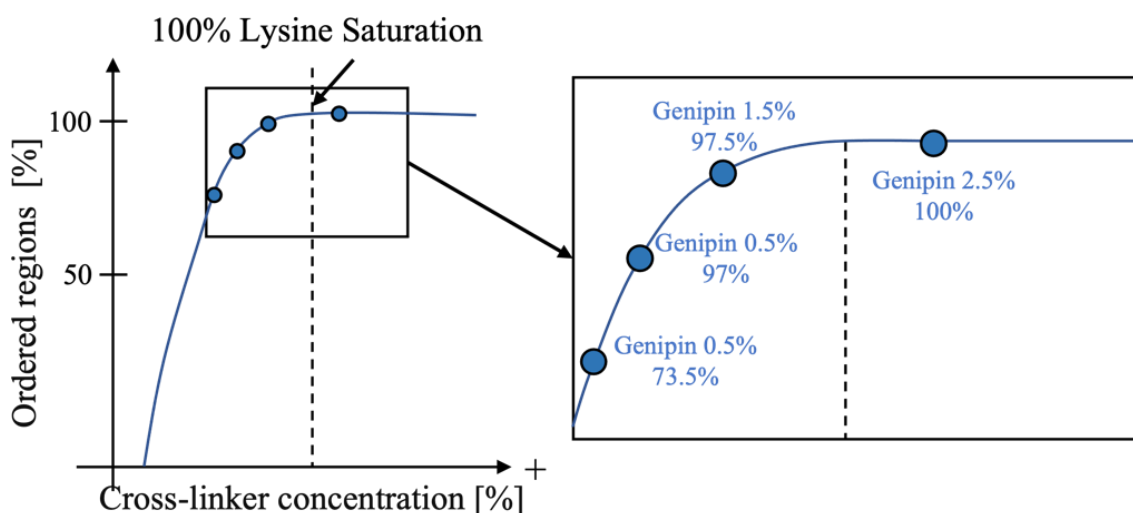


**Figure 3.23:** Genipin-ELP formulation schematic, according to which exceeding the threshold of 100% lysine saturation resulted in a plateau with respect to order:disorder in the final supramolecular protein secondary structure configuration.

As genipin is a monomeric CLA, a plateauing correlation between cross-linker concentration and the formation of ordered regions in the protein secondary structure was proposed, meaning that secondary structure translation peaked, and plateaued after the lysine saturation threshold was exceeded, as this CLA does not facilitate polymerization within itself.

Hence, excess functional groups in genipin were assumed to not further affect protein secondary structure formation.

### 3.3.2.2. Investigation of genipin-ELP membrane swell capacity

Swelling capacity tests showed a statistically significant ( $P = 0.007$ ) level of swelling in the 0.5 wt% genipin membranes compared to 1.0 wt% and 1.5 wt% genipin membranes (**Figure 3.24**). Respective numerical values are stated in Appendix C.

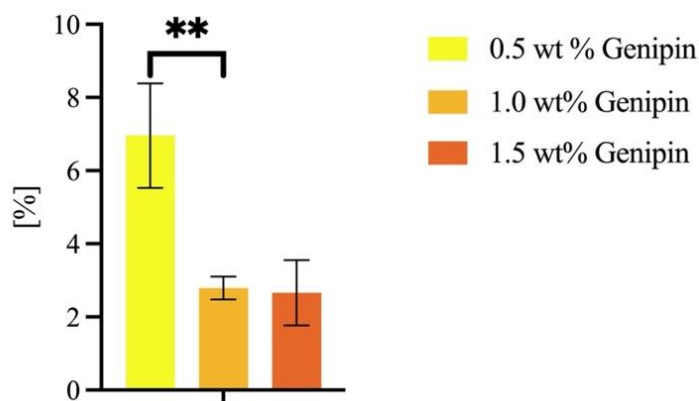


**Figure 3.24:** Swell capacity in genipin-ELP membrane formulations, showing statistically significant stronger swelling in 0.5 wt% genipin-ELP membranes, compared to other formulations.

As genipin-ELP membranes with the lowest CLA concentration (0.5 wt%) showed the highest disorder in protein secondary structure configuration, it was proposed that an increased presence of random coils, and hence less densely cross-linked network, enhanced water absorption.

### 3.3.3. HDI-ELP membrane characterization

Different formulations using HDI were produced following the reported method [140], wherein 5% SN<sub>A</sub>15 ELP molecules were dissolved in solvent mixture inside a glovebox, at room temperature and low humidity (< 20%). 0.1  $\mu$ l, 0.57  $\mu$ l and 1.14  $\mu$ l HDI were integrated into the ELP solutions. These formulations were henceforth referred to as ratio 1, ratio 4 and ratio 12, respectively. The ELP-HDI solution was drop-casted onto PDMS substrate and left to cross-link in a glovebox at > 20% humidity, overnight. The membrane fabrication method is depicted in *chapter 1.4.2*.

Using this method, the synthesis of transparent, flexible membranes was achieved. Specimens with an HDI ratio 12 were found to be most stable in solution. It was proposed that this was due to the formation of a more tightly bound cross-linking network.

#### 3.3.3.1. Protein secondary structure analysis of HDI-ELP membranes

The data obtained *via* deconvolution of FTIR spectra of HDI-ELP membranes with increasing CLA amounts is presented in **Figure 3.25**. With an increase in HDI, it was observed that random coils increased, whilst  $\beta$ -sheets and  $\alpha$ -helices diminished.

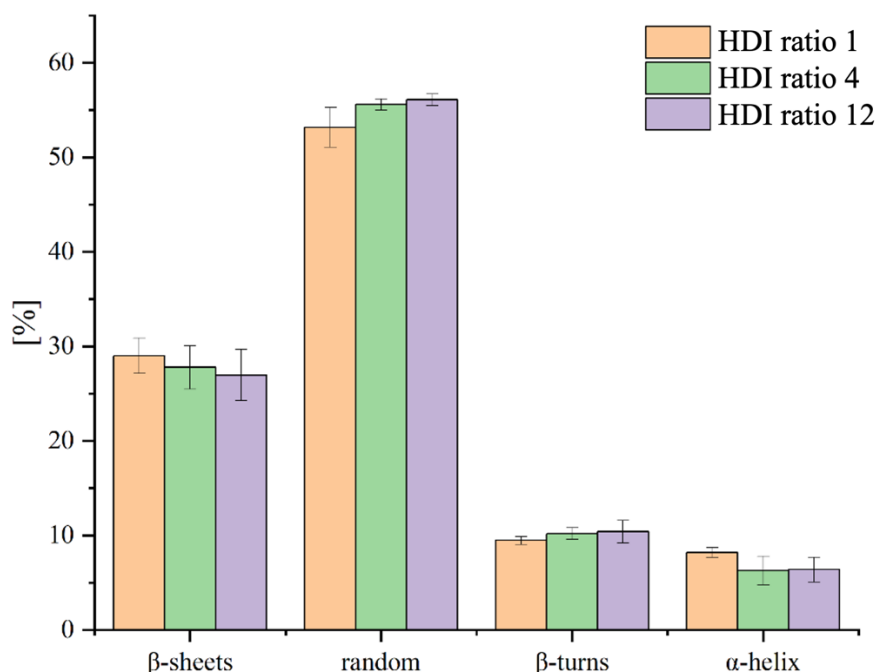


**Figure 3.25:** Bar chart of change in secondary structure with increasing HDI volumes in ELP membranes. Results showed a decrease of  $\beta$ -sheet and  $\alpha$ -helices, whilst random coils and  $\beta$ -turns slightly increased with HDI increase.

Under consideration of conclusions drawn in this study, where protein secondary structure transition was suggested to be a time dependent process, it was assumed that this increase in random coils was related accelerated cross-linking speed induced through an increase in HDI volume. Additionally, ELP-HDI membrane synthesis was conducted in a glovebox, which has also been noted to further accelerate solvent evaporation which could potentially cause increased molecular disorder, compared to other fume hood cross-linked formulations.

Generally,  $\beta$ -sheets were formed over  $\beta$ -turns. This was also observed in PMDI-ELP formulations, where it was suggested that the parallel alignment of ELP backbones upon cross-linking with functional isocyanate groups facilitated the formation of parallelly aligned polypeptide chains and thereby the formation of  $\beta$ -sheets. As PMDI and HDI share the same isocyanate functional group, the same circumstance was assumed for HDI-ELP formulations.

The cross-linking mechanism between functional isocyanate groups and primary amine cross-linking sites of lysine was displayed in **Figure 3.4**.

### 3.3.3.2. Investigation of HDI-ELP membrane swell capacity

The swelling capability results of HDI-ELP membranes showed no statistically significant difference between the examined formulations (**Figure 3.26**).

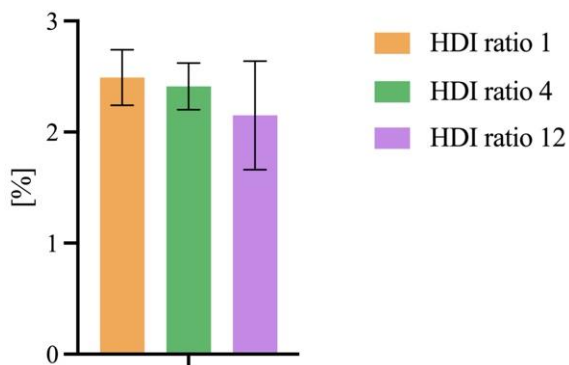


**Figure 3.26:** Membrane swell capacity tests in HDI-ELP membranes showed no significant differences.

Considering the similarity in order-disorder ratios in the assessed samples, these results stand to reason the previously drawn conclusion. Herein, the differences in molecular disorder were considered to be too insignificant to affect the membrane swell capacity.

### 3.4. Summary

The synthesis of novel SN<sub>A</sub>15 ELP based formulations was achieved by investigating the implementation of the two CLAs (1) PMDI and (2) genipin. Using these materials, fabrication methods were established that enabled the synthesis of both, ELP based membranes and gels. Whilst the use of PMDI could achieve instant formation of a ELP gel, genipin-ELP solutions displayed gelation over time.

The ability to synthesize ELP based gels opened the opportunity to investigate how the materials underlying protein secondary structure forms over time. Results showed that secondary structure formation was time dependent and occurred in a sequential manner. Furthermore, it was found material solidification and the time frame in which it occurred impacted the order-disorder interplay in the resulting protein secondary structure configuration. Acceleration of sample solidification, by means of alteration of the cross-linking environment, led to acceleration of the protein secondary structure formation, and compromised the order of the final protein secondary structure configuration.

Membrane formulations were established, that enabled 100% protein secondary structure translation from random- to ordered coils. Practical and theoretical results suggested that once all lysine cross-linking sites in the ELP sequence were saturated, 100% protein secondary structure translation into ordered coils achieved. Parabolic behaviour was proposed in PMDI-formulations, meaning that disorder was increased past the threshold of lysine saturation. In genipin-formulations, a plateauing behaviour was assumed, meaning that translation peaked and remained stable past the lysine saturation threshold. Additionally, it was proposed that a higher protein secondary structure disorder facilitated water absorption through the generation of a less tightly bound molecular network.

## **4. Biomineralization and underlying formation mechanism in ELP based membranes**

In the previous chapter, the deconvolution of FTIR spectra has shown that PMDI- and genipin cross-linked ELP membranes have an underlying protein secondary structure that can be tuned through the integration of varying cross-linker volumes, as previously investigated in HDI cross-linked ELP membranes [140].

In *chapter 1.4.2* the previously proposed biomineralization mechanism in HDI-ELP membranes was elaborated on, in which Maltese cross-patterned organic spherulites observed under the PLM were suggested to act as nucleic sites in the biomineralization process.

In this chapter, it was investigated whether the newly developed formulations had the ability to undergo stimuli triggered biomineralization and the potential underlying mechanism was investigated. Therefore, SEM images were obtained over time as samples were immersed in biomineralization solution. Additionally, the biomineralizations' crystallographic elemental composition was assessed.

### **4.1. Optical geometry assessment of unmineralized ELP membranes**

In this section, PLM was used to image unmineralized PMDI and genipin cross-linked ELP membranes. The principle of PLM was elaborated on in *chapter 1.4.2.1*, whilst the applied method in this project was stated in *chapter 2.2.4*. The surface and bulk region of unmineralized membranes were imaged *via* SEM imaging. The principle of PLM was elaborated on in *chapter 1.4.2.2*, whilst the applied method in this project was stated in *chapter 2.2.5*.

HDI-ELP membranes (ratio 12) served as a control group, as according to the referenced study, organic spherulites were observed to have the highest resolution in this formulation [140].

All ELP based membranes were synthesized in accordance with the methods described in *chapter 3.3*. By default, HDI-ELP membranes were cross-linked in a glovebox, whereas PMDI- and genipin-ELP were fume hood cross-linked.

4.1.1. Polarized light microscopy on PMDI and genipin cross-linked ELP membranes  
PLM imaging of HDI-ELP membranes confirmed the presence of Maltese cross-patterned organic spherulites. Observed organic spherulites varied in resolution but were evenly spread across the sample (**Figure 4.1A, B**). The spherulites diameter (approximately 3  $\mu\text{m}$ ) agreed with previously reported images [140].

No Maltese cross-patterns were observed in PMDI-ELP membranes (**Figure 4.1C**).

In genipin-ELP membranes, highly defined cross-patterned structures with a comparatively large diameter (approximately 10 – 15  $\mu\text{m}$ ) were observed in distinct locations (**Figure 4.1D**).

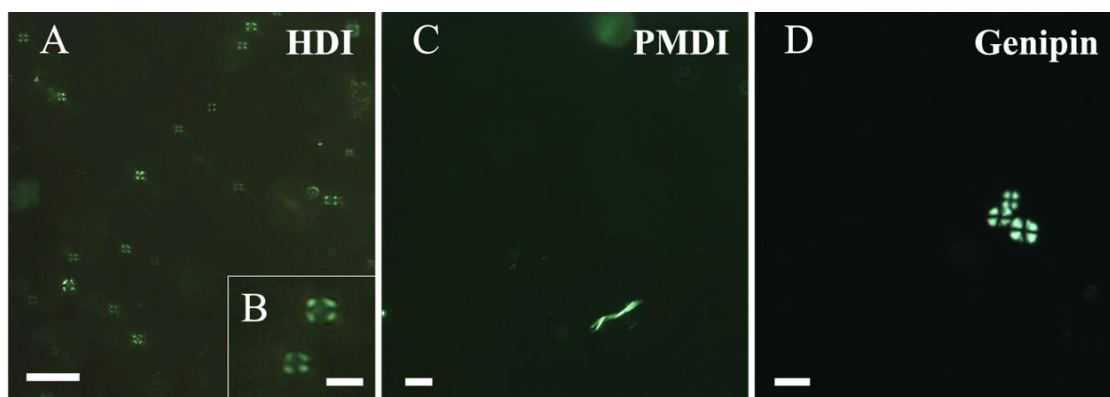


**Figure 4.1:** PLM images of unmineralized ELP membranes. (A) HDI-ELP membranes, confirming the presence of evenly distributed Maltese cross-patterned organic spherulites. (B) The spherulite diameter (approximately 3  $\mu\text{m}$ ) coincided with data reported by S. Elsharkawy et. al. (C) No cross-patterned structures were visible in PMDI-ELP membranes (D). In genipin-ELP membranes strongly defined cross-pattern structures with a comparatively large diameter (10 – 15  $\mu\text{m}$ ) were observed in distinct locations. Scale bars (A), (C), (D): 20  $\mu\text{m}$ , (D): 5  $\mu\text{m}$ .

#### 4.1.2. Scanning electron microscopy on unmineralized ELP membranes

##### 4.1.2.1. SEM imaging of unmineralized HDI-ELP membranes

The surface (**Figure 4.2A**) as well as the cross-section (**Figure 4.2B, C**) of HDI-ELP membranes was observed to be smooth, not showing any geometrical distinctive features.

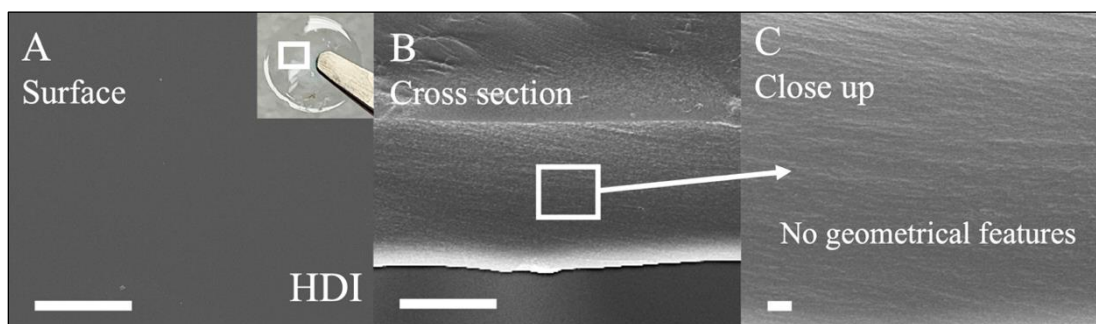


**Figure 4.2:** SEM images of HDI-ELP membranes showing (A) a smooth surface. (B) At lower and (C) higher magnifications, no geometrical features were observed in the bulk. Scale bars (A), (B): 10  $\mu\text{m}$ , (C): 1  $\mu\text{m}$ .

This suggested, that the spherulites observed under the PLM were of organic nature and did not stem from light diffraction caused by geometrical features in the bulk region.

#### 4.1.2.2. SEM imaging of unmineralized PMDI-ELP membranes

At first glance, both the surface (**Figure 4.3A**) and the cross-section (**Figure 4.3B**) of PMDI-ELP membranes had a smooth appearance. At higher magnifications (**Figure 4.3C**), nanoscopic pores (approximately 200 – 500 nm in diameter) were evenly observed across the sample bulk. It was proposed that these geometric features were too small to create optical artefacts under the used PLM system.

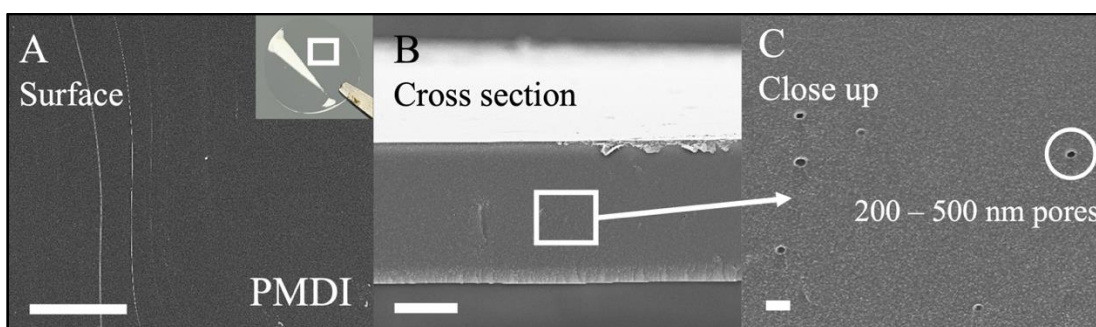


**Figure 4.3:** SEM images of PMDI-ELP membranes showing (A) a smooth membrane surface. (B) The cross-section appeared smooth at first sight. However, at higher magnification (C), nanoscopic pores were detected in the sample bulk. Scale bars (A): 100  $\mu\text{m}$ , (B): 10  $\mu\text{m}$ , (C): 1  $\mu\text{m}$ .

As mentioned in *chapter 3.1.1*, PMDI forms an intermediate, carbamic acid, upon hydrolysis. Upon extended hydrolysis,  $\text{CO}_2$  gas is released as this unstable intermediate decomposes [172]. It is herein hypothesized that observed pores may stem from commenced decomposition of the carbamic acid intermediate, as the investigated

membranes were cross-linked in an uncontrolled environment and thereby exposed to humidity.

#### 4.1.2.3. SEM imaging of unmineralized genipin-ELP membranes

Whilst the surface of genipin-ELP membranes appeared to be mostly smooth, apart from indistinct impurities (**Figure 4.4A**), microscopic pores (approximately 1 – 3  $\mu\text{m}$  in diameter) were observed in the cross-section (**Figure 4.4B, C**).

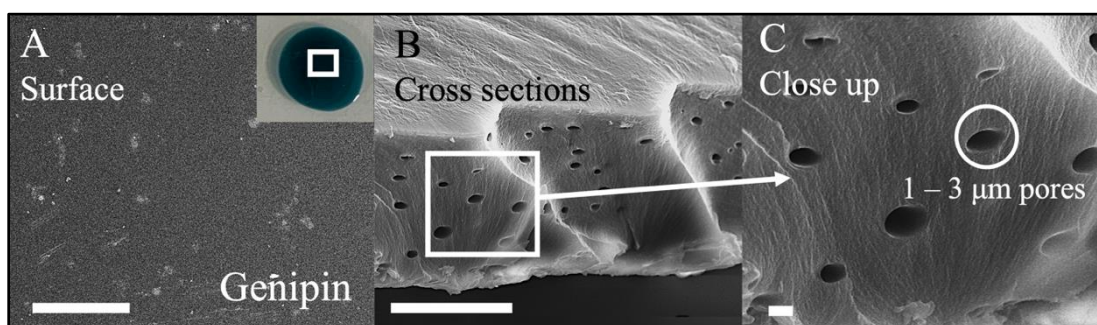


**Figure 4.4:** SEM images of genipin-ELP membranes showing (A) a smooth membrane surface with indistinct surficial impurities. (B, C) The formation of spherical, microscopic pores in the membrane bulk was observed. Scale bars (A): 100  $\mu\text{m}$ , (B): 10  $\mu\text{m}$ , (C): 1  $\mu\text{m}$ .

It was assumed that cross-patterns observed under the PLM stemmed from the detection of hollow pores within which the transmitted light was diffracted. Previous research has previously shown that such hollow spheres can cause cross-patterned artefacts in PLM [192]. To test this hypothesis, PLM images were overlapped with optical microscopy images in regions where Maltese cross-patterns were observed. In optical microscopy images, distinct circular structures were observed in the same locations as cross-patterns were seen during PLM imaging (**Figure 4.5**).

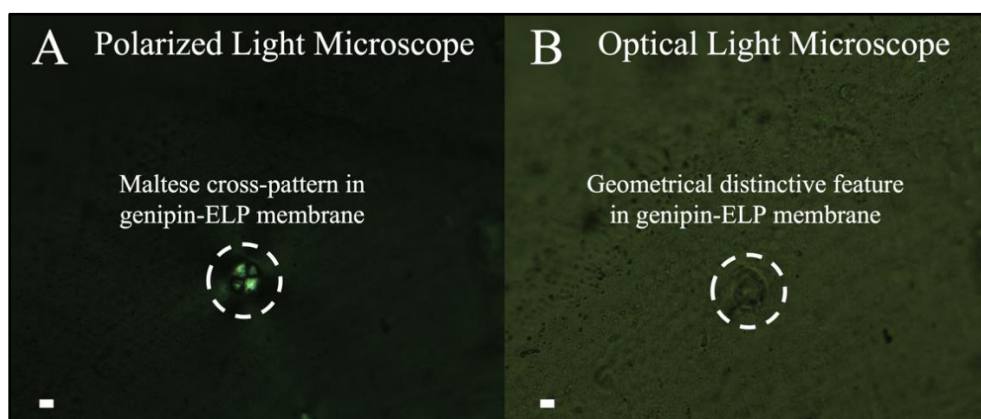


**Figure 4.5:** (A) PLM and (B) optical light microscopy images of the same area in a genipin cross-linked ELP membrane, showing a distinct geometrical feature in the same location, as indicated with a dotted circle. Scale bars: 10  $\mu\text{m}$ .

This further supported the hypothesis that the cross-patterns observed in genipin-ELP membranes were optical artefacts, caused by light diffraction in hollow spheres in the membrane bulk.

As cross-linking interactions between genipin and primary amines do not result in the release of CO<sub>2</sub> gas, a different root cause is assumed. It was suggested that the pores formed during the membrane solidification process. During this process, it was observed that a gel-like skin formed on the membrane surface before the bulk region had fully solidified. It was assumed that air bubbles, which formed as the pressure beneath this gel-like skin layer decreased, were trapped in bulk region.

This phenomenon has previously been studied. It was established that the gas in bubbles that form during the drying of polymer solution is composed of a mixture of air dissolved into the solution and solvent vapor. It was further concluded that bubble nucleation was promoted by the time dependent decrease of pressure experienced in the solution as a surficial skin layer forms [193].

It was herein suspected that genipin-ELP membranes were more prone to the formation of bubbles, as membrane solidification occurred over the course of two to four days, as opposed to HDI- and PMDI-ELP membranes, which cross-linked within 24-48 h. This extended time window was suggested to promote significant pressure decrease in the sample bulk, enabling the formation of air bubbles.

Due to their high boiling point, the solvents used in this project, DMF (153°C) and DMSO (189°C) evaporate slowly under atmospheric pressure. Genipin-ELP membranes were cross-linked in a vacuum oven (at room temperature) to test the above stated hypothesis. Vacuum evaporation is often employed to lower the boiling point of such solvents, resulting in accelerated evaporation [184] [185]. Genipin-ELP membranes were selected, as the observed pores were larger in size than those observed in PMDI-ELP membranes.

Vacuum oven cross-linking of genipin-ELP membranes was conducted with the aim to accelerate evaporation and thereby impede air bubble formation. Thus, by accelerating the cross-linking process, solvent vapor and air mixed into the solution shall escape the sample bulk before a gel-skin layer could develop on the membrane surface.

SEM images of the cross-section of vacuum cross-linked genipin-ELP membranes showed a significant decrease pore density (**Figure 4.6A**) and size (**Figure 4.6B**). Nanoscopic pores (approximately 200 nm in diameter) were predominantly observed close to the membrane surface.

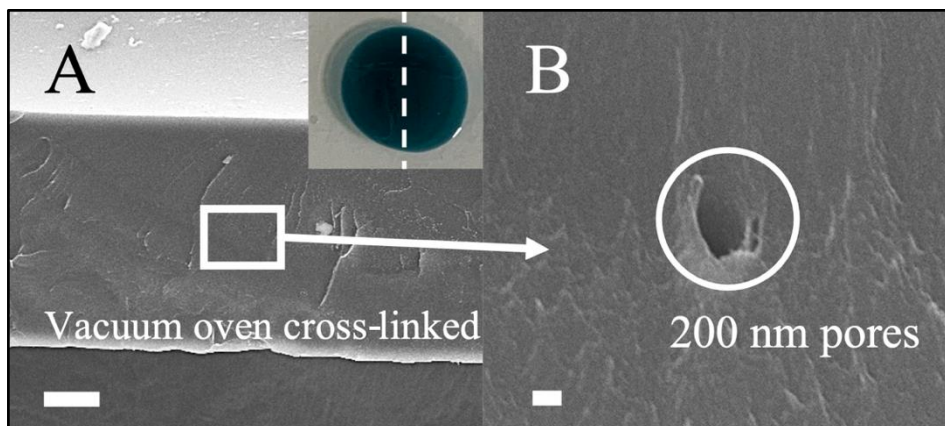


**Figure 4.6:** SEM imaging of vacuum oven cross-linked genipin-ELP membrane. (A) Macroscopic image of the cross-section showing a significant decrease in pore density, compared to fume hood cross-linked specimens. (B) Nanoscopic pores were mainly observed close to the membrane surface. Scale bars (A): 10  $\mu\text{m}$ , (B): 200 nm.

## 4.2. Biomineralization assessment in PMDI- and genipin-ELP membranes

The biomineralization ability of PMDI- and genipin-ELP membranes was assessed by immersing samples in saturated  $\text{Ca}_3(\text{PO}_4)_2$  solution (pH = 6). The preparation method applied for the synthesis of biomineralization solution was stated in *chapter 2.2.3*. To mimic physiological conditions, immersed samples were stored at 38°C, in an INCU-Line® digital incubator. The biomineralization solution was refreshed every other day to maintain a stable pH. Due to time constraints, the biomineralization period was limited to maximum one month.

### 4.2.1. Optical imaging of mineralized ELP membranes

#### 4.2.1.1. *Optical microscopy on mineralized HDI-ELP membranes*

After eight days in biomineralization solution, HDI-ELP membranes were fully biomineralized. Mineralized structures, composed of rod-shaped strings, emerged from different nucleation points, and grew in a circular manner, until they intersected with

bordering volcanos (**Figure 4.7A**). At higher magnifications, rod-like structures were observed at the volcanos' outer regions (**Figure 4.7B**).

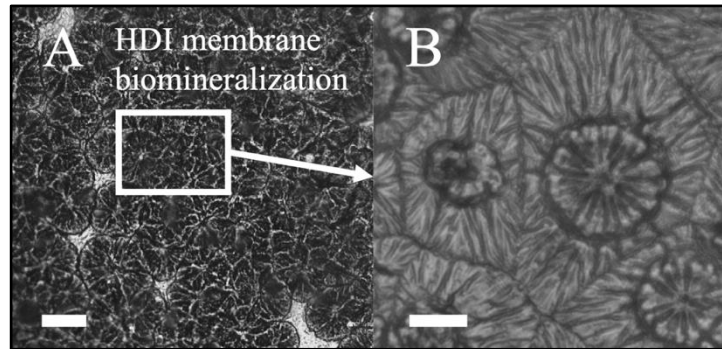


**Figure 4.7:** Optical microscopy images of mineralized HDI-ELP membrane after eight days in mineralization solution, (A) showing full mineralization at 10 x magnification and (B) rod like structures at 20 x magnification. Scale bars (A): 50  $\mu\text{m}$ , (B): 20  $\mu\text{m}$ .

#### 4.2.1.2. *Optical microscopy on mineralized PMDI-ELP membranes*

Biom mineralization was achieved in PMDI-ELP membranes. However, after three to four weeks in mineralization solution, specimens were not as densely mineralized as HDI-ELP membranes (**Figure 4.8A**). Emerging structures grew in a circular manner, as observed in the control group. However, the formation of rod like structures was not observed (**Figure 4.8B**). Instead, ring-like structures were visible.

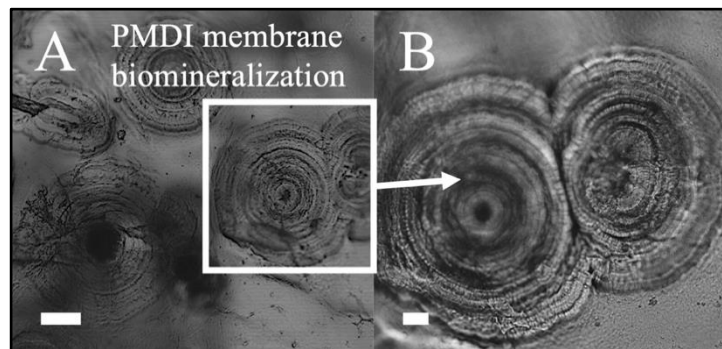


**Figure 4.8:** Optical microscopy images of mineralized PMDI-ELP membrane after 31 days in mineralization solution, (A) showing sparse biomineralization, compared to the control group. (B) Ring like structures were observed at higher magnifications. Scale bars (A): 50  $\mu\text{m}$ , (B): 20  $\mu\text{m}$ .

#### 4.2.1.3. *Optical microscopy on mineralized genipin-ELP membranes*

After three weeks in mineralization solution, more extensive biomineralization was observed in genipin-ELP membranes, compared to PMDI-ELP membranes. It was observed that at different focal points, different regions of emerging volcanos came in

and out of focus (**Figure 4.9A, B**). Therefore, it was assumed that mineralized structures grew at different levels on the z-axis of the membranes. This hypothesis was tested in the later *chapter 4.2.2.3*.

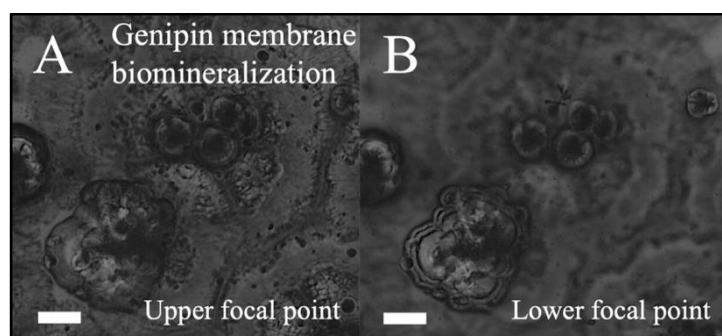


**Figure 4.9:** Optical microscopy images of mineralized genipin-ELP membrane after 21 days in mineralization solution, showing mineralized structures at different focal points, that achieved high definition imaging at (A) higher levels in respect to the membranes' z axis and (B) lower levels. Scale bars: 50  $\mu\text{m}$ .

#### 4.2.2. SEM imaging of mineralized ELP membranes

In the following, SEM images of the surface and the cross-section of mineralized PMDI (0.1 wt%, 0.2 wt%, 0.3 wt%) and genipin (0.5 wt%, 1.0 wt%, 1.5 wt%) cross-linked 4% ELP membranes were obtained to assess their nanoscopic structure on the surface and in the cross-section. HDI-ELP membranes (ratio 1, ratio 4, ratio 12), were used as a control group.

##### 4.2.2.1. SEM imaging of mineralized HDI-ELP membranes

As previously reported, the integration of varying HDI volumes in ELP solution affected the volcano morphology (**Figure 4.10A, B, C**) [140].

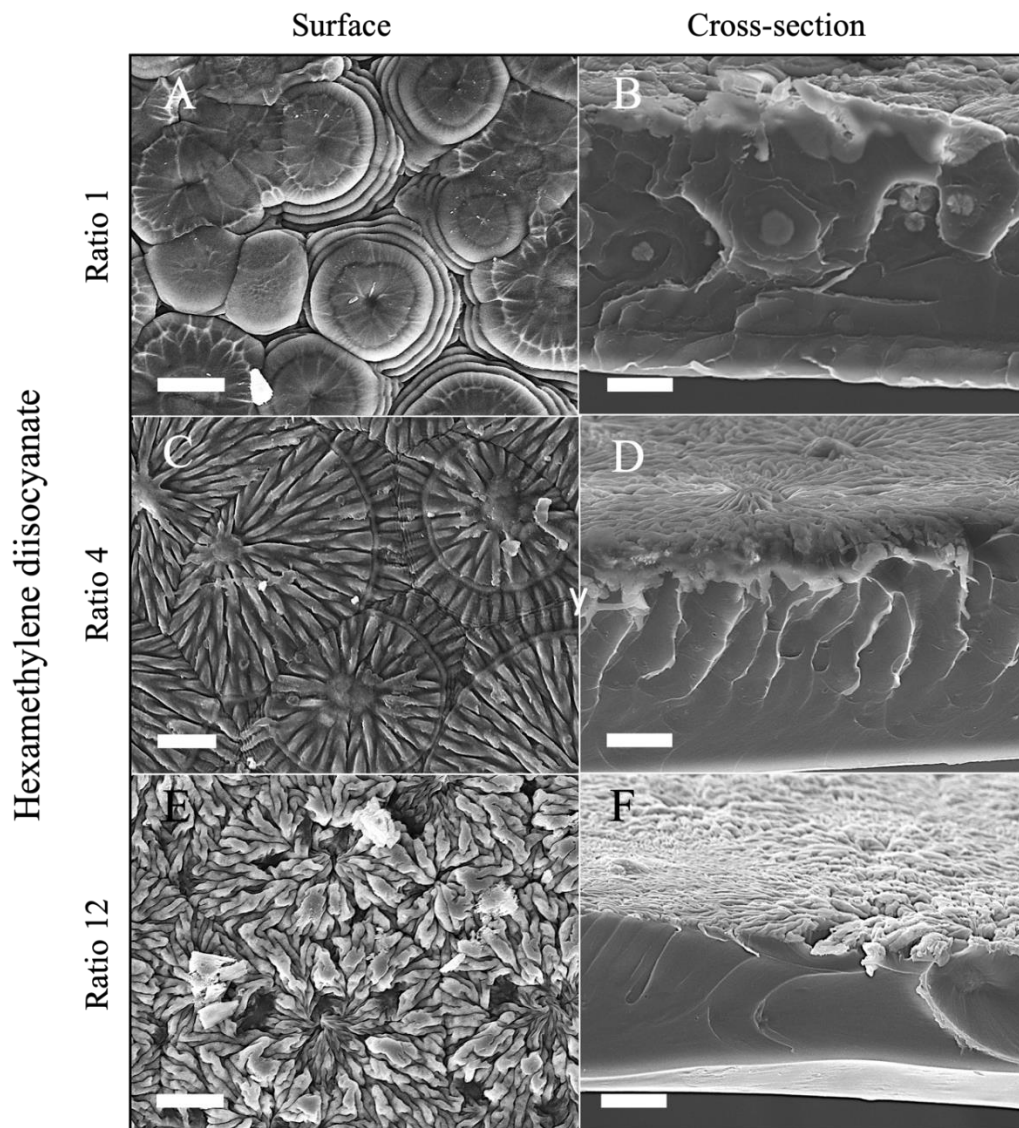


**Figure 4.10:** SEM images of the surfaces (A, C, E) and cross-sections (B, D, F) of HDI-ELP membranes. (A) Ring like structures were observed on the surface of ratio 1 membranes. Mineralization in the (B) bulk region was revealed. Ratio 4 (C, D) and ratio 12 (E, F) showed defined rod-like structures on the surface and no bulk mineralization. The morphology of surface mineralization became more condensed with an increase in cross-linker volume. Scale bars: 10  $\mu$ m.

In ratio 1 HDI-ELP membranes, structures that emerged to the surface grew circularly with no apparent formation of rod-like structures (**Figure 4.10A**). As singular volcanos intersected, the formation of ripples at the edges was observed. Cross-sectional images of this formulation revealed the presence of mineralized structures in the bulk region (**Figure 4.10B**).

**Figure 4.11A** shows nanocrystals in HDI ratio 1 membranes, covered by a layer (approximately 15 nm) of unmineralized organic matter.

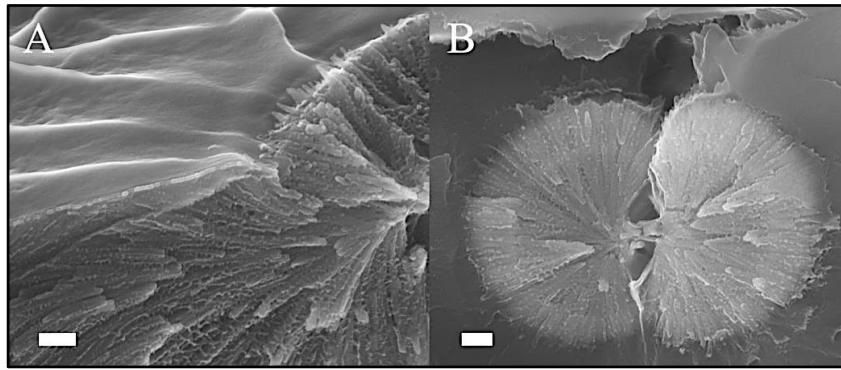


**Figure 4.11:** Close up SEM images of ratio 1 HDI-ELP membranes showing nanocrystals in the sample bulk, (A) covered with a thin layer of unmineralized organic matter. (B) Nanocrystals in the sample bulk were observed to have a dumbbell shape at an early stage of mineralization. Scale bars: 500 nm.

This layer is henceforth referred to as ‘blanket’. The blanket caused the smooth appearance of biomineralized structures on the membrane surface. It was proposed that, as adjacent volcanoes coincided, the blanket ‘folded’, forming rippled volcano edges. In the centre of the HDI ratio 1 membrane, dumbbell shaped, aligned nanocrystals were observed (**Figure 4.11B**).

At higher HDI concentrations (ratio 4 and 12), the mineralized structures formed rod like structures on the sample surfaces (**Figure 4.10C, E**). However, nanocrystals were not visible from a top view, nor in the cross-sections (**Figure 4.10D, F**). Rippled volcano edges were observed in ratio 4 HDI-ELP membranes as volcanoes intersected on the surface (**Figure 4.12A**).

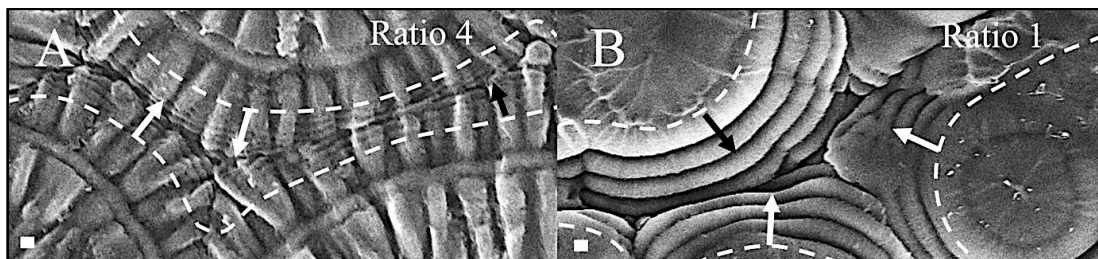


**Figure 4.12:** Close up SEM images of coinciding mineralized structures on the surface of (A) ratio 4 HDI-ELP membranes and (B) ratio 1 HDI-ELP membranes, highlighting ‘folding’ of the thin unmineralized blanket in volcano growth direction. Scale bar: 1  $\mu$ m.

The arrows in **Figure 4.12** highlight the growth direction of intersecting volcanoes. It was assumed that at higher cross-linker ratios, nanocrystals were covered by an unmineralized blanket, as previously observed in ratio 1 HDI-ELP membranes (**Figure 4.12B**).

#### 4.2.2.2. SEM imaging of mineralized PMDI-ELP membranes

In comparison with the HDI control group, less extensive biomineralization was observed on the surface of PMDI-ELP membranes (**Figure 4.13A, C, E**). Bulk mineralization occurred in all tested formulations (**Figure 4.13B, D, F**).

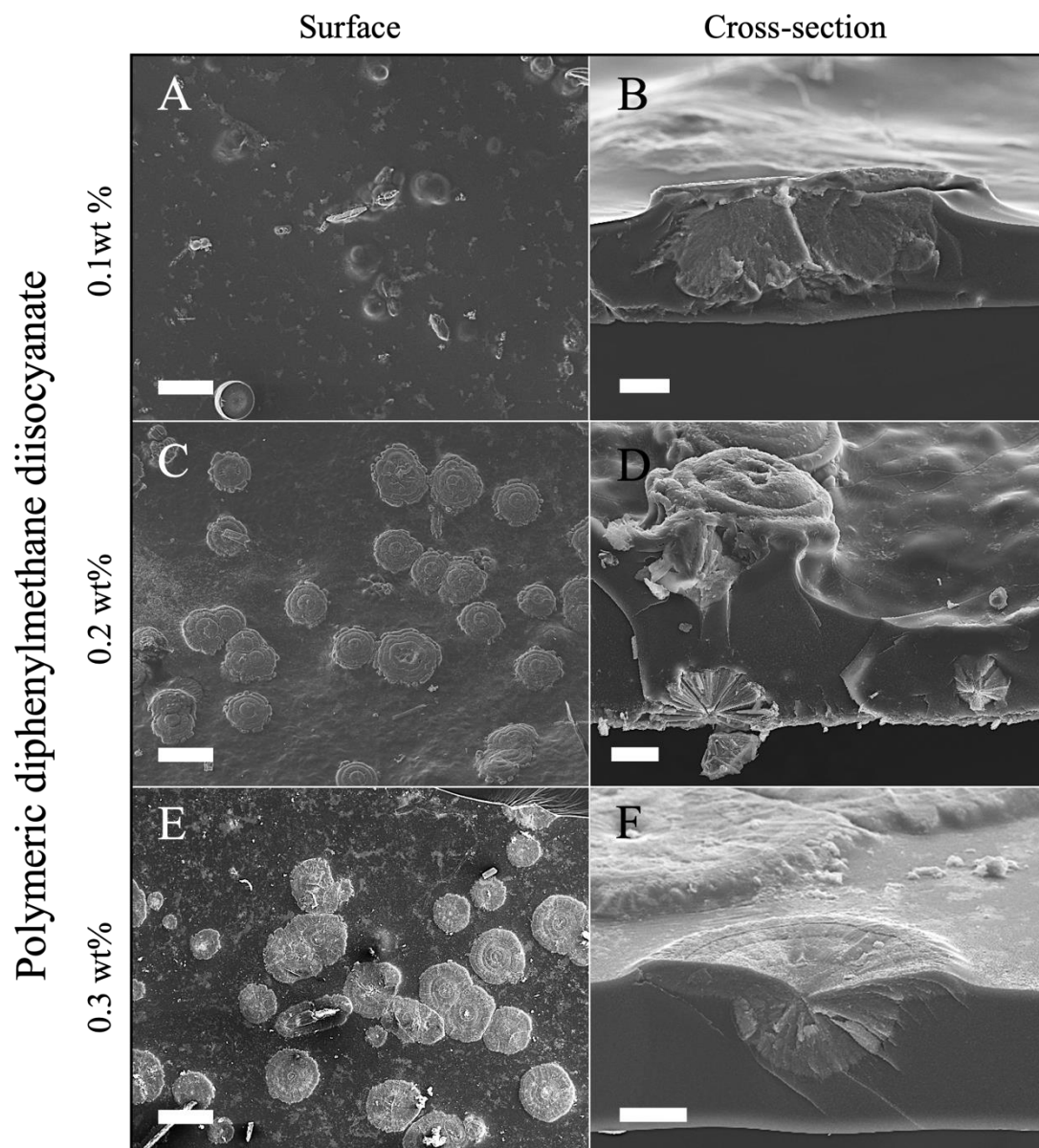


**Figure 4.13:** SEM images of the surfaces (A, C, E) and cross-sections (B, D, F) of PMDI-ELP membranes. All formulations showed bulk mineralization. No defined volcano morphology was observed on the surface of 0.1 wt% PMDI-ELP membranes (A), due to unmineralized blankets (approximately 3 – 5  $\mu\text{m}$ ) covering nanocrystals in the bulk (B). More extensive mineralization and defined volcano morphologies were observed on the surface of 0.2 wt% (C) and 0.3 wt% PMDI (E) ELP membranes. Scale bars (A, C, E): 100  $\mu\text{m}$ , (B, D, F): 10  $\mu\text{m}$ .

As mentioned in *chapter 3.3.1.*, ‘PMDI-ELP membranes were found to be more brittle, compared to the other investigated cross-linked ELP membranes’.

It was herein assumed that the biomineralization ability and kinetics was diminished, in comparison to HDI-ELP. It was suggested that the PMDI-ELP membranes’ brittleness negatively impacted ion diffusion into the organic matter. Furthermore, membrane swelling capacity experiments in *chapter 3.3* suggested that the presence of random coils may affect the water absorption capacity of synthesized membranes. It was established *via* FTIR spectra deconvolution that the protein secondary structure conformation of PMDI-ELP formulations had a significantly lower ratio of random coils, compared to HDI-ELP formulations. This is suggested to introduce an additional factor that may impede ion diffusion into the organic matter.

In 0.1 wt% PMDI-ELP membranes, scarce mineralization was observed. Mineralized structures, composed of nanocrystals, nucleated in the sample bulk, and remained covered by a blanket (approximately 3 - 5  $\mu\text{m}$  thick) of unmineralized matter (**Figure 4.13B**). This blanket was suggested to have caused a less distinct volcano morphology (**Figure 4.14A**) than that observed in HDI-ELP membranes, where the unmineralized blanket thickness was observed to be 15 nm thin.

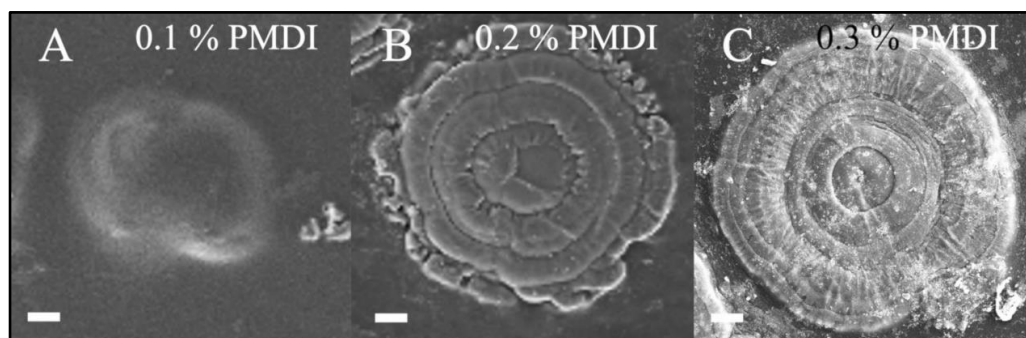


**Figure 4.14:** SEM images showing how increasing in cross-linker volume caused the volcano morphology to become more distinct on the surface of 0.1 wt% (A), 0.2 wt% (B) and 0.3 wt% (C) PMDI-ELP membranes. Scale bars: 10  $\mu\text{m}$ .

With an increasing CLA volume, the morphology of mineralized structures became more distinct (**Figure 4.14B, C**). Close up images showed that at higher concentrations, the unmineralized blanket was comparatively thin (approximately 0.5 - 1  $\mu\text{m}$ ) (**Figure 4.15**), which was suggested to cause a more distinct volcano morphology (**Figure 4.14C**).

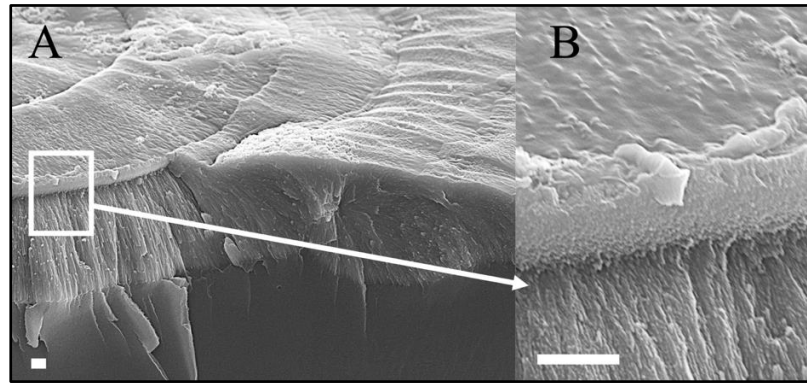


**Figure 4.15:** Close up images of (A) nanocrystals in a 0.3 wt% PMDI 4% ELP membrane, (B) covered by an unmineralized blanket. Scale bars: 1  $\mu\text{m}$ .

Furthermore, as previously observed in HDI-ELP membranes, the unmineralized blanket in PMDI-ELP membranes ‘folded’ as adjacent volcanoes grew into proximity (**Figure 4.16**)

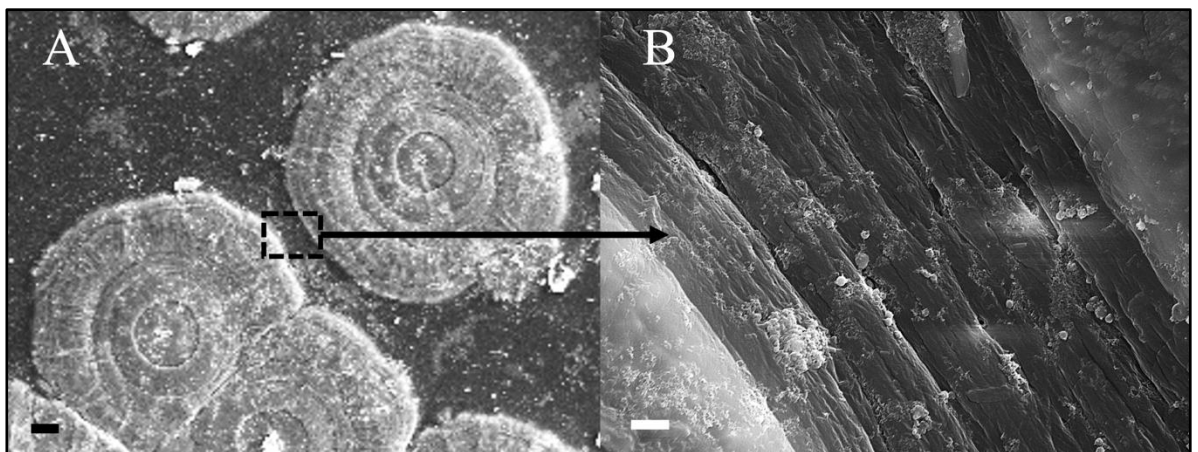


**Figure 4.16:** Images showing how the unmineralized blanket ‘folded’ between two adjacent volcanoes. (A) Macroscopic image of mineralized structures emerging in proximity. (B) Close up image of folding motion occurring between two volcanos. Scale bars (A): 10  $\mu\text{m}$ , (B): 1  $\mu\text{m}$ .

#### 4.2.2.3. SEM imaging of mineralized genipin-ELP membranes

SEM images obtained after 21 days of immersion in mineralization solution showed extensive bulk mineralization in all tested genipin-ELP formulations (**Figure 4.17B, D, F**). The emergence of volcano-like structures was observed from a top view (**Figure 4.17A, C, E**). 1.0 wt% genipin-ELP membranes were found to be most densely mineralized.

In the cross-section, mineralized structures appeared to grow in a spherical manner, nucleating from hollow pores. These pores were either circular (**Figure 4.17B**) or oval shaped (**Figure 4.17D, F**). Furthermore, these mineralizing spheres grew at different z-axis levels of the membrane, as suspected upon optical sample imaging (*chapter 4.1.2.3*).

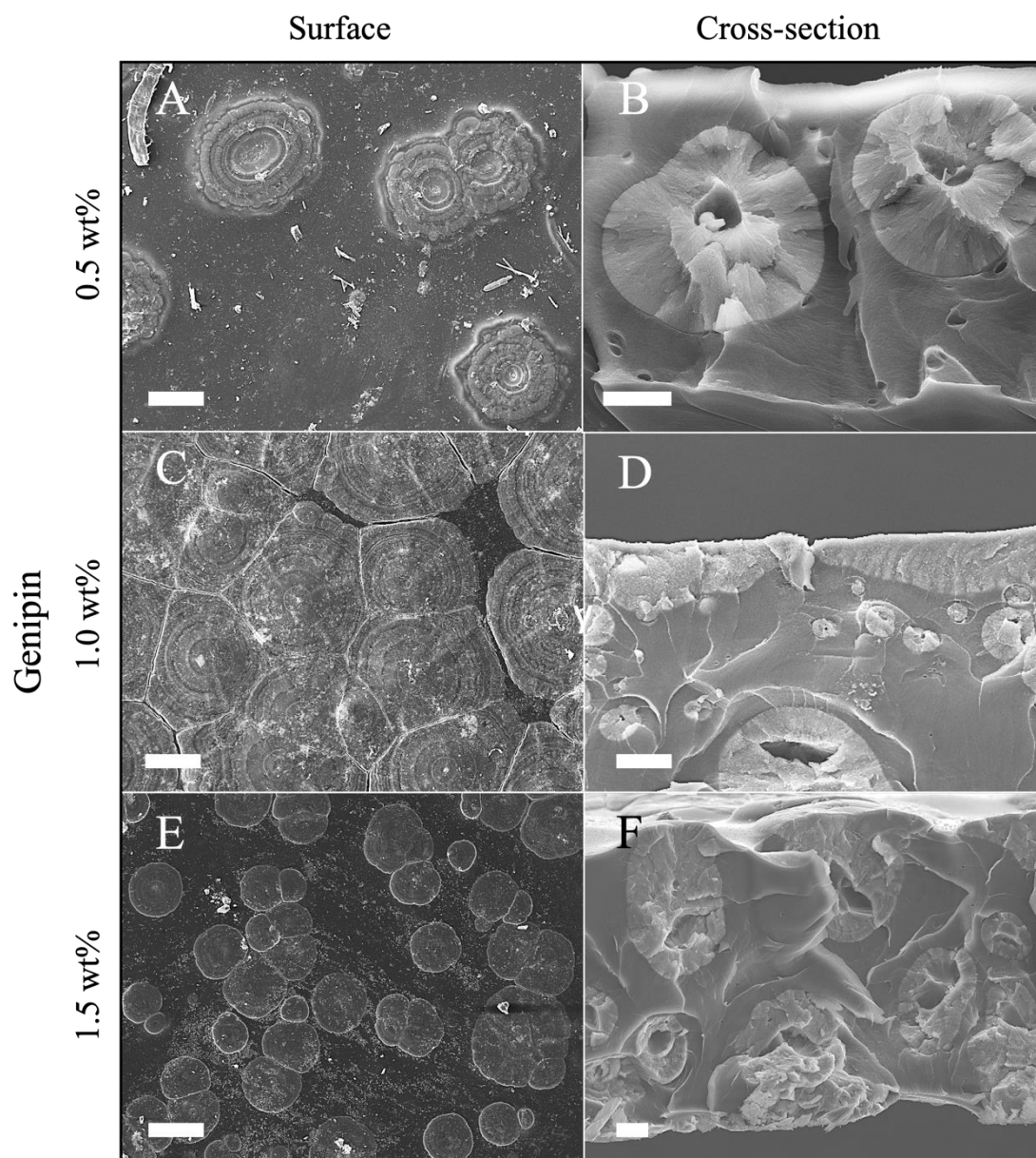


**Figure 4.17:** SEM images of the surfaces (A, C, E) and cross-sections (B, D, F) of genipin-ELP membranes. All formulations showed bulk mineralization. (A) Comparatively low mineralization density was observed in 0.5 wt% genipin-ELP membranes, whilst comprehensive mineralization was achieved in (C) 1.0 wt% and (D) 1.5 wt% genipin-ELP formulations. Scale bars (A, C, E): 100  $\mu\text{m}$ , (B, D, F): 10  $\mu\text{m}$ .

When volcanos grew close to the membrane surface, nanocrystals grew in a horizontal, circular fashion, originating from the volcano centre (**Figure 4.18A**).

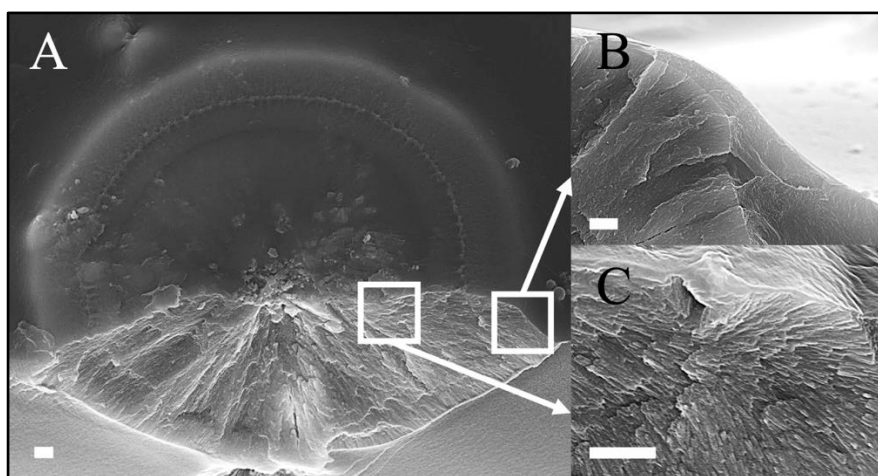


**Figure 4.18:** Cross-sectional SEM images of mineralized structure close to the surface of a genipin-ELP membrane, revealing (A, C) nanocrystals, covered by a (B) thin layer of organic matter. Scale bars: 1  $\mu\text{m}$ .

Nanocrystals (**Figure 4.18C**) were covered by an unmineralized blanket (**Figure 4.18B**), which was assumed to retain nanocrystals inside the organic matter whilst redirecting nanocrystals growth away from the membrane surface and thereby promoting volcano growth in a horizontal, circular manner.

No significant difference was observed between the volcano morphologies of 1.0 wt% (**Figure 4.19B**) and 1.5 wt% (**Figure 4.19C**) genipin-ELP membranes.

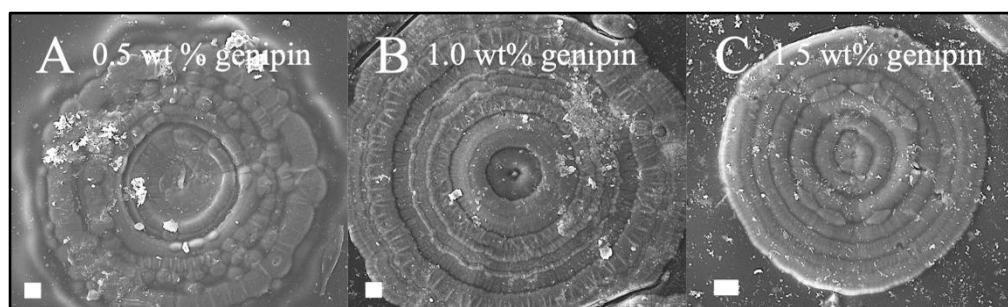


**Figure 4.19:** SEM images of singular volcanoes in mineralized genipin-ELP membranes. (A) At a 0.5 wt% genipin concentration, ‘bubble’ shaped subunits were observed within the ‘main’ volcano. No major difference in morphology was observed between (B) 1.0 wt% (B) and (C) 1.5 wt% genipin formulations. Scale bars: 10  $\mu\text{m}$ .

At 0.5 wt% genipin, circular ‘bubble’ shaped ‘subunits’ within the ‘main’ volcano were observed (**Figure 4.19A**).

It was proposed that these ‘subunits’ represented smaller, spherical mineralized structures, located within the sample bulk (**Figure 4.20**).

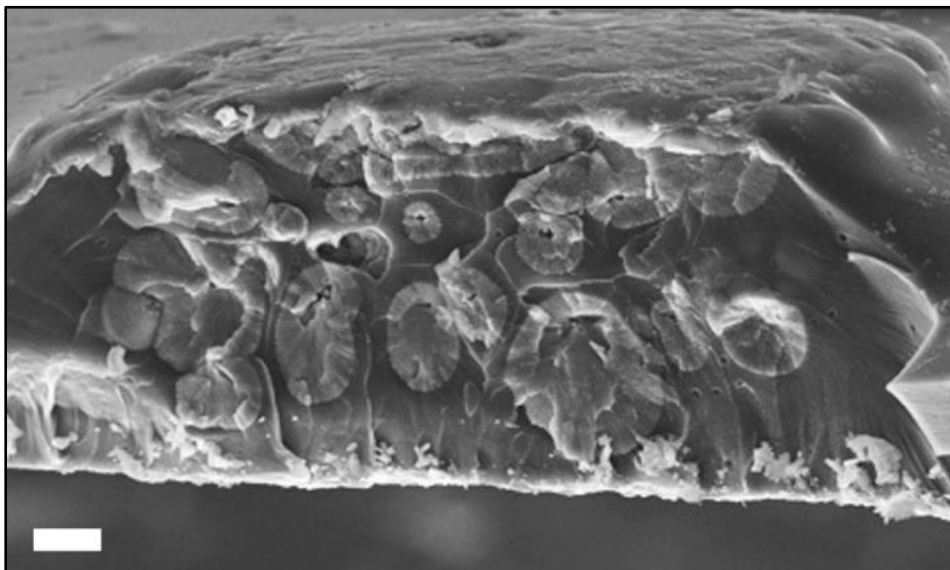


**Figure 4.20:** Cross-sectional SEM image of a mineralizing ‘main’ volcano with several underlying ‘subunits’ in the bulk region. Scale bar: 10  $\mu\text{m}$ .

Presumably, at lower genipin concentrations, due to the less tightly bound cross-linked network, the blanket was more prone to yielding, causing it to distort on the membrane surface. This less tightly bound cross-linked network was additionally suggested to increase the membrane swelling capacity (*chapter 3.3.2.2*). Based on previously stated assumptions, it was therefore suggested that the membrane swelling capacity in this formulation enhanced ion diffusion into the membrane bulk and thereby enabled more extensive bulk biomineralization.

#### 4.2.3. Crystallographic assessment of mineralized ELP membranes *via* X-Ray diffraction

XRD analysis was carried out to assess the elemental composition of biomineralized structures. Close-up SEM images of biomineralizing spheres in genipin-ELP membranes hinted towards the presence of apatite, as hexagonal shaped crystals were observed in the sample bulk (**Figure 4.21**). The hexagonal nanocrystal shape is characteristic for apatite crystallisation [194].

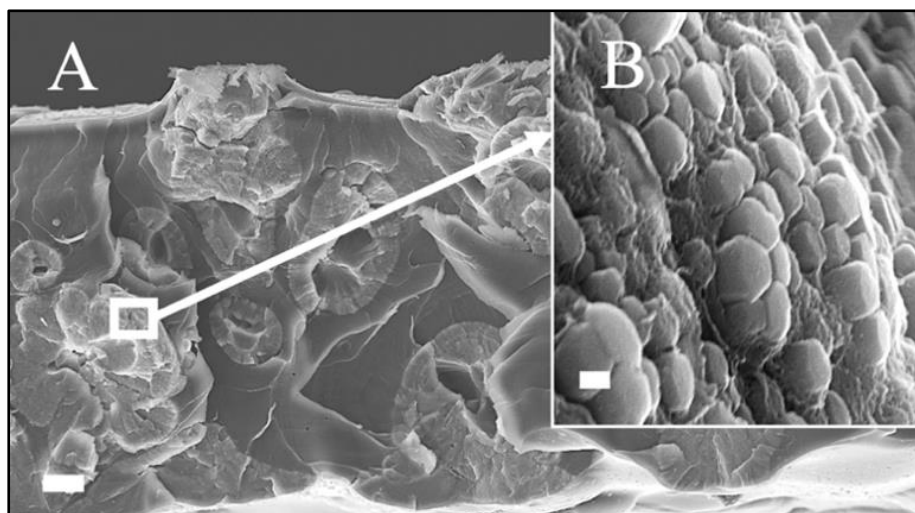


**Figure 4.21:** SEM close up images of (A) mineralizing sphere in the sample bulk of mineralized genipin-ELP membranes, revealing the (B) presence of hexagonal nanocrystals, suggesting apatite mineralization. Scale bars (A): 1  $\mu\text{m}$ , (B): 100 nm.

HDI-ELP membranes were used as a control group in XRD analysis. The experiments were carried out in accordance with the methods described in *chapter 2.2.6*.

In the herein referenced study, it was shown that the observed biomineralizing structures in HDI-ELP membranes were composed of FAp nanocrystals [140].

This was established by comparing the peaks obtained *via* X-Ray diffraction to literature, according to which the main peaks of interest in the FAp specific crystallographic profile are present at  $2\text{-}\theta$  values of 25.95 (002), 32.04 (121), 33.02 (300), 34.07 (202), 39.98 (310), 47.06 (22), 49.67 (123) and 53.26 (004) [195]. These values represent the X-ray intensity observed at each angle  $2\text{-}\theta$  values. The corresponding numerical values stated in parenthesis represent the Miller index at each  $2\text{-}\theta$  angle of the associated crystal planes. These indices describe the orientation and spacing of the crystal lattice that is analysed [196]. The peaks found in mineralized HDI membranes corresponded with the FAp  $2\text{-}\theta$  specific peaks.

In this study, XRD results showed that the crystalline peaks of the HDI control group (black) coincided with the peaks in mineralized PMDI (red) and genipin (blue) membranes (**Figure 4.22**).

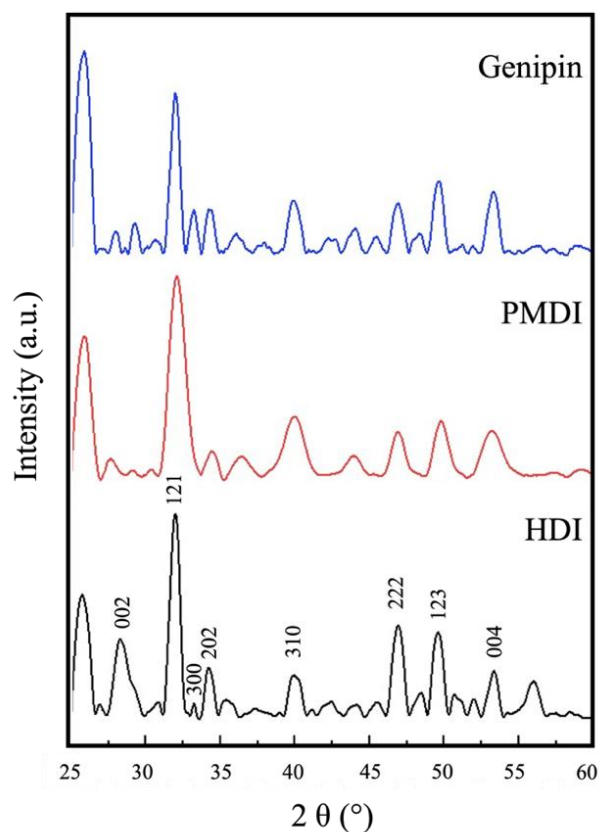


**Figure 4.22:** XRD spectra of mineralized genipin- (blue), PMDI- (red) and HDI- (black) ELP membranes, showing peaks in the same regions and thereby confirming the presence of FAp.

Peaks in the XRD spectrum of biom mineralized PMDI-ELP membranes were less prominent compared to those in genipin-ELP and HDI-ELP spectra. It was assumed that this occurred due to the presence of comparatively less biom mineralized structures, causing a weaker intensity of X-rays emitted from the samples of interest. The correspondence of peaks presented in the herein examined formulations with those in the control group confirms the presence of FAp nanocrystals in all formulations.

### 4.3. Understanding the biomineralization mechanism in PMDI- and genipin-ELP membranes

It was previously proposed that biomineralization in HDI-ELP membranes was nucleated in organic spherulites observed *via* PLM [140]. Whilst Maltese cross-patterns in HDI-ELP membranes were of organic nature, cross-patterns observed in newly established ELP membrane formulations were suggested to be caused by hollow pores in the membrane bulk, resulting in optical artefacts. Thus, it was assumed that PMDI- and genipin-ELP membranes underwent a different biomineralization path.

To study the biomineralization mechanisms in PMDI- and genipin-ELP formulations, membranes removed from biomineralization solution at different time points (after 7, 14 and 21 days) and imaged *via* SEM. The objective was to understand the path of FAp nanocrystal emergence and to distinguish factors affect their growth path.

#### 4.3.1. Mineralization mechanism in genipin-ELP membranes

At an early stage of biomineralization in genipin-ELP membranes, spherical mineralized structures were engulfed in individual pockets (Figure 4.23A).

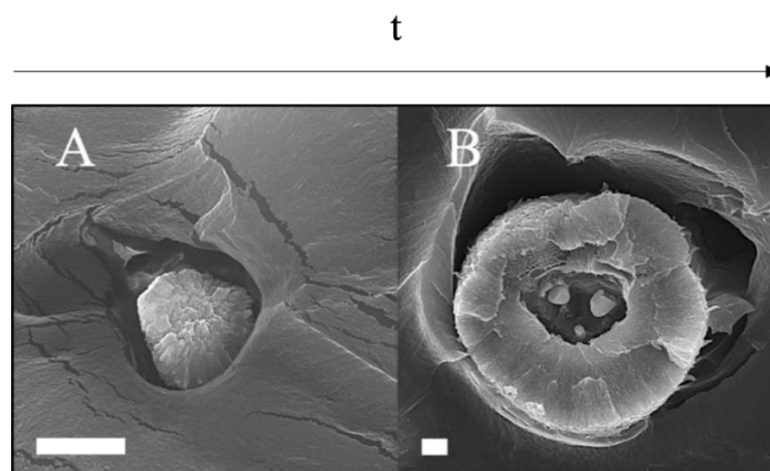


**Figure 4.23:** SEM images of (A) spherically aligned nanocrystals at an early mineralization stage, engulfed in individual pockets. (B) As the spheres expanded, a hollow centre formed. Scale bars: 1  $\mu\text{m}$ .

As presented in *chapter 4.1.2.3*, SEM imaging of unmineralized genipin-ELP membranes showed numerous pores in the bulk region. The diameter of the individual pockets engulfing nanocrystals, were found to be similar to the pore sizes explored in unmineralized membranes (approximately 1 – 3  $\mu\text{m}$ ). As these structures expanded, a hollow centre formed within the biomineralized sphere (Figure 4.23B).

At the beginning of the mineralization process, mineralized spheres in the sample bulk caused the unmineralized matter blanket that covered the spheres to yield. This led to the formation of bumps from a membrane surface (**Figure 4.24A**).

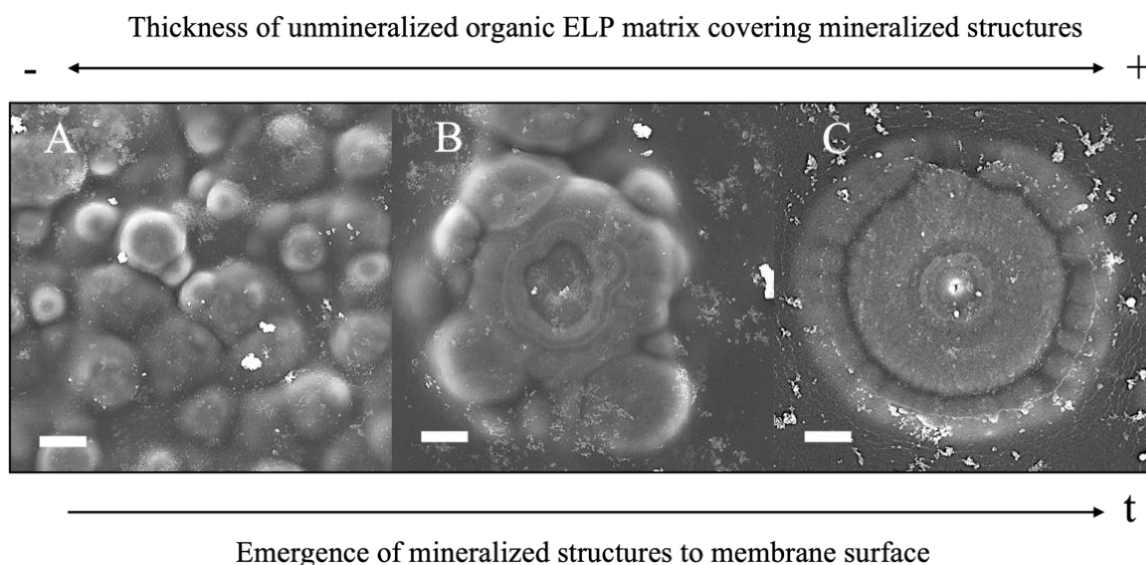


**Figure 4.24:** SEM images from the top view of biom mineralizing structures, which (A) appear as bubbles underneath the surface at an early stage (B) and grew closer to the surface as they increased in diameter. (C) The thickness of the unmineralized blanket covering the nanocrystals decreased as the structures expanded, causing a more distinct volcano morphology. Scale bars: 10  $\mu\text{m}$

As biom mineralizing sphered expanded, they grew closer to the membrane surface (**Figure 4.24B**). As presented in *chapter 4.2.2.3*, the thickness of the unmineralized blanket was found to affect the volcano morphology observed on the sample surface. Conclusively, as the layer thickness diminished as biom mineralized spheres grew closer to the membrane surface, the volcano morphology became more distinct (**Figure 4.24C**).

When spherically aligned nanocrystals expanded and emerged towards membrane surface, nanocrystals rearranged and grew away from the membrane surface, back into the organic matter. The nanocrystal growth direction is highlighted in **Figure 4.25B**.

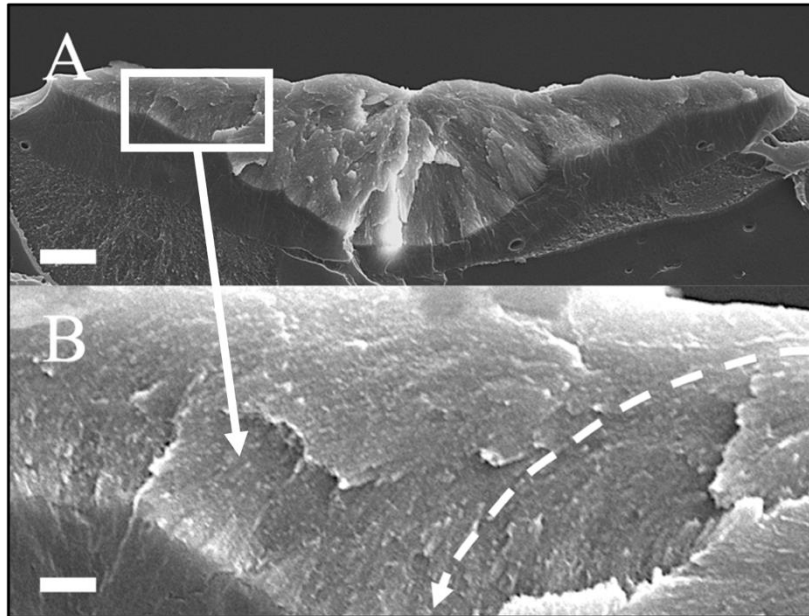


**Figure 4.25:** Cross-sectional SEM images of (A) mineralized structure that expanded towards the membrane surface, which caused nanocrystals to (B) divert away from the surface. Scale bars (A): 5  $\mu\text{m}$ , (B): 1  $\mu\text{m}$ .

At this stage, mineralization diverted from spherical to horizontal growth (**Figure 4.25A**), It was assumed that the redirection of the growth path occurred due to nanocrystals choosing the path of least resistance.

When two volcanos collided (**Figure 4.26A**), nanocrystal growth appeared to be redirected back towards the nucleation centre. This caused nanocrystals to grow into the unmineralized blanket that was previously formed, leaving a nanoscopic protective layer on the surface that retained biomineralized matter within the membrane (**Figure 4.26B**).

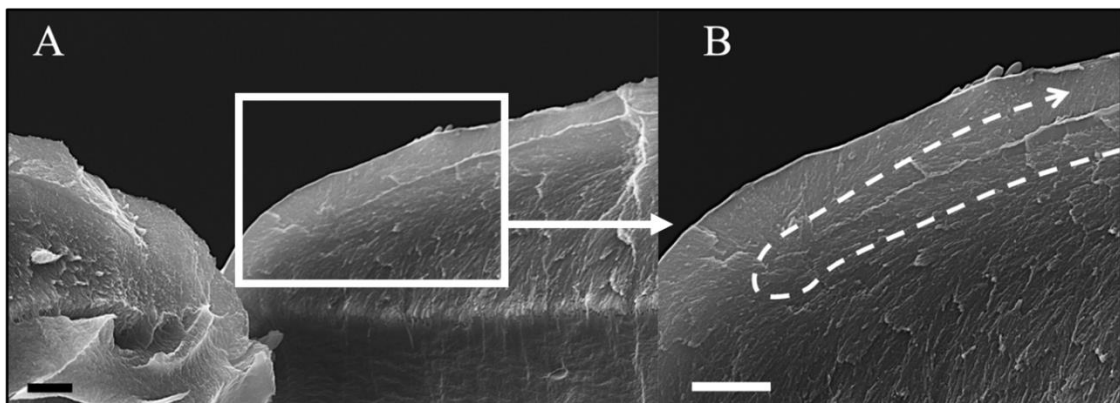


**Figure 4.26:** Cross-sectional SEM images of (A) two colliding volcanoes at the membrane surface, causing (B) nanocrystals to grow back into the previously formed organic blanket. Scale bars: 1  $\mu\text{m}$ .

When multiple mineralizing spheres collided in the sample bulk, the initially circular hollow structure changed to an oval configuration, due to the forces exerted onto mineralizing sphere edges (**Figure 4.27A**). When spheres however emerged to the surface uninterrupted, the initially hollow centre transformed to represent the centre of mineralizing volcanos, as highlighted in **Figure 4.27B**.

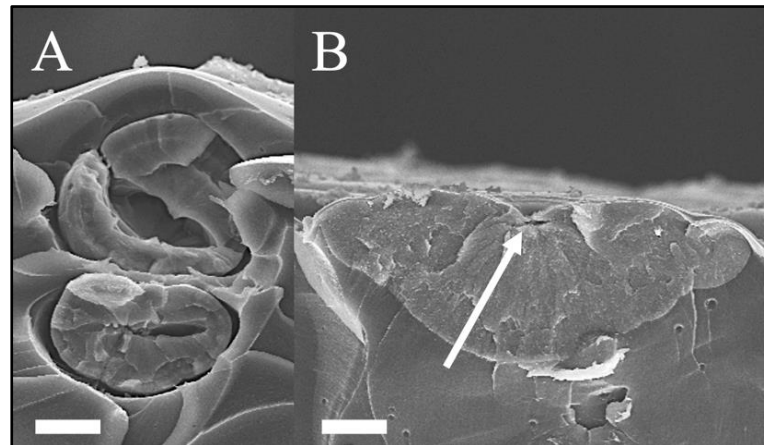


**Figure 4.27:** SEM images showing how different circumstances can affect the geometry of hollow structures in the centre of mineralizing spheres. Initially circular spheres turn oval upon (A) collision with adjacent mineralizing spheres. (B) When mineralizing spheres emerged to the surface uninterrupted, initially hollow centres transformed into the volcano centre. Scale bars: 10  $\mu\text{m}$ .

Considering the evidence presented, it was assumed, that pores in the membrane bulk functioned as nucleic sites for biomineralization in genipin-ELP membranes.

To test this hypothesis, vacuum oven cross-linked samples were immersed in mineralization solution for 21 days. As mentioned in *chapter 4.1.2.3*, vacuum oven cross-linking strongly reduced pore formation in the sample bulk. Therefore, it was assumed that the biomineralization capability should be reduced in comparison with fume hood cross-linked samples.

1.0 wt% genipin 4% ELP membranes were synthesized for this purpose, as it was previously observed that this formulation showed the most extensive biomineralization capability (*chapter 4.2.2.3*).

In **Figure 4.28**, SEM images of biomineralized vacuum oven cross-linked (left column) and fume hood cross-linked membranes (right column) were put into comparison.

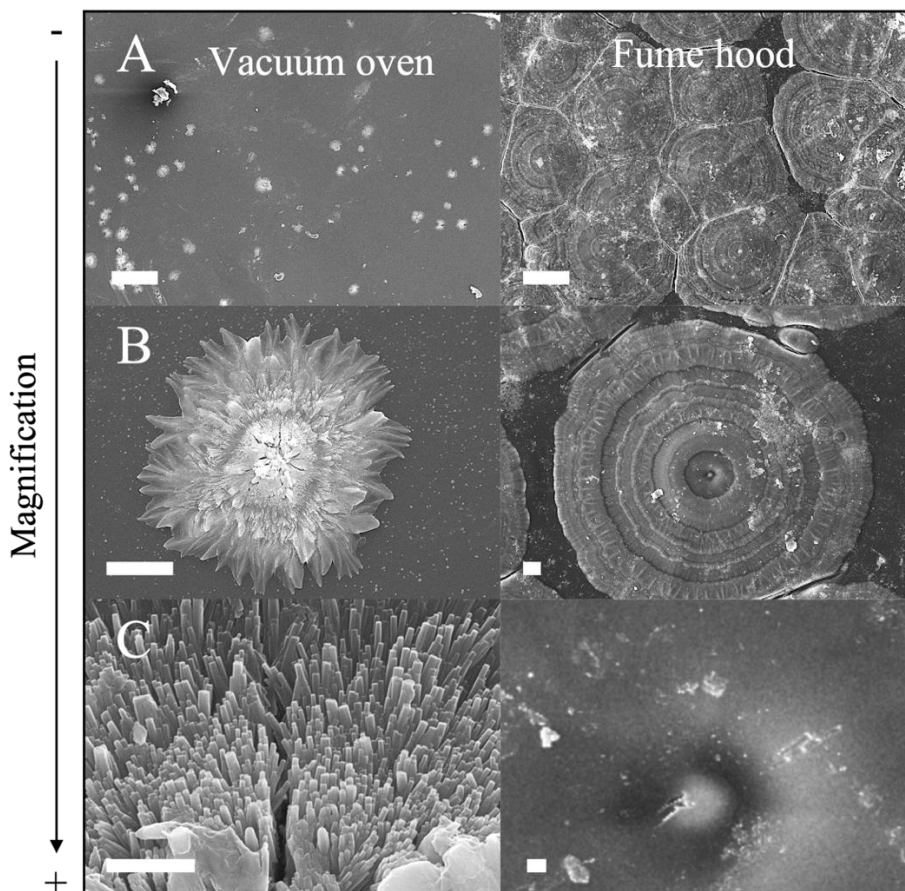


**Figure 4.28:** SEM images of mineralized vacuum-oven (left) and fume hood (right) 1.0 wt% genipin 4% ELP membranes that were immersed in mineralization solution for 3 weeks. (A) Compared to vacuum oven cross-linked samples, more extensive biomineralization was observed in fume hood cross-linked samples. (B) The cross-linking environment affected the volcano morphology. (C) Whilst in fume hood cross-linked samples, nanocrystals remained covered by a blanket of unmineralized matter, nanocrystals in vacuum oven cross-linked samples were exposed to the surface. Scale bars (A): 100  $\mu\text{m}$ , (B): 10  $\mu\text{m}$ , (C): 1  $\mu\text{m}$ .

Top view images showed strongly reduced biomineralization in vacuum cross-linked membranes (**Figure 4.28A**). Furthermore, the volcano morphology was affected. Whilst fume hood cross-linking showed circular biomineralization growth with defined edges, biomineralized structures in vacuum oven cross-linked samples grew in a more random manner (**Figure 4.28B**). Furthermore, it was observed that nanocrystals in vacuum cross-linked samples were exposed to the surface (**Figure 4.28C**), whilst in fume hood cross-linked membranes, they were covered by a blanket of unmineralized matter.

As previously mentioned, nanoscopic pores in vacuum oven cross-linked samples were predominantly located close to the membrane surface. It was therefore assumed that this proximity impeded the formation of a protective unmineralized blanket that could contain nanocrystals in the membrane bulk.

This assumption was supported *via* SEM imaging of sample cross-sections, wherein mineralization in vacuum oven cross-linked membranes was mainly observed close to the membrane surface of (**Figure 4.29A**).

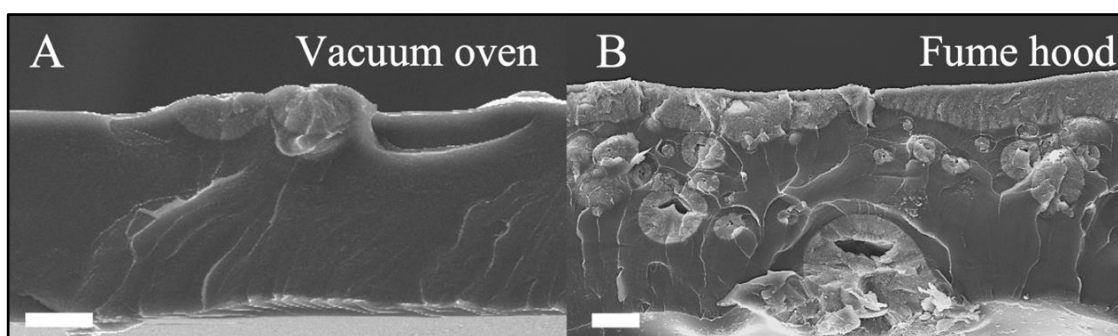


**Figure 4.29:** Cross-sectional SEM images of mineralized 1.0 wt% genipin 4% ELP membranes after experiencing (A) vacuum oven cross-linking and (B) cross-linking under a fume hood, showing that fume hood cross-linked samples stronger mineralization capability. Scale bars: 10  $\mu\text{m}$ .

Compared to fume hood cross-linked samples (**Figure 4.29B**), vacuum oven cross-linking significantly diminished bulk region biomineralization (**Figure 4.29A**).

Based on these results it was assumed that pores acted as nucleic sites in the biomineralization process of genipin-ELP membranes.

Under consideration of the aim to fabricate bone tissue scaffolds, the formation of an intact protective organic blanket was considered favourable in the biomineralization process of ELP-based scaffolds. It was herein proposed that *in vivo*, under exposure to external forces exhibited onto the scaffold by surrounding tissue, the protective blanket could act as a barrier to avoid FAp nanocrystals to divert from the scaffold surface. This was suggested to enhance the controllability of the process and avoid inflammatory responses *in vivo* post implantation of the mineralized scaffold.

#### 4.3.2. Mineralization mechanism in PMDI-ELP membranes

A similar mineralization mechanism was observed in PMDI-ELP membranes.

Whilst in genipin-ELP membranes, mineralizing spheres at early stages of mineralization were loosely engulfed in individual pores, the organic matter surrounding emerging nanocrystal spheres was prone to form cracks (**Figure 4.30A, B**).

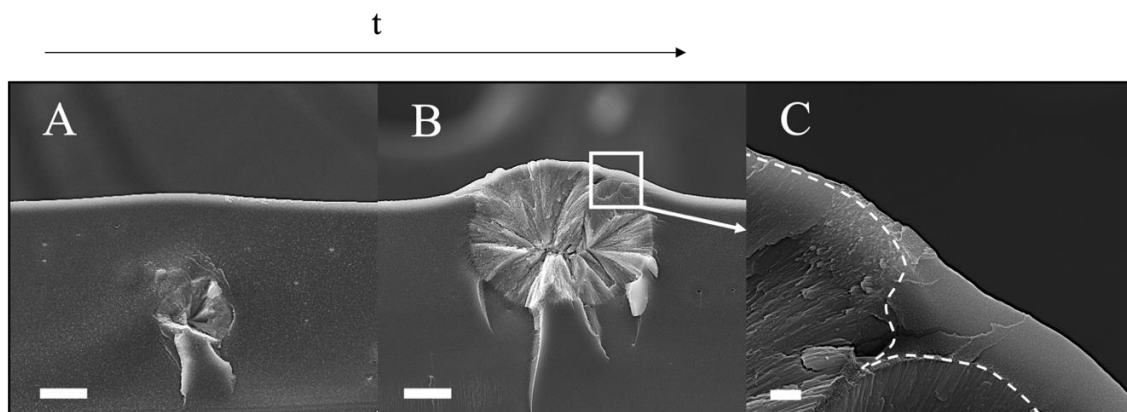


**Figure 4.30:** SEM images of early-stage bulk mineralization in PMDI-ELP membranes showing (A) spherically aligned nanocrystals, tightly engulfed in unmineralized matter. (B) Nanocrystals emerged to the surface as they grew in diameter, (C) remaining covered by an unmineralized blanket. Scale bars (A, B): 10  $\mu\text{m}$ , (C): 1  $\mu\text{m}$ .

It was assumed that this occurred due to the comparatively small pore size and brittleness of PMDI-ELP membranes. As the biomineralization process was continued, emerging biomineralizing structures expanded and emerged towards the surface (**Figure 4.30B**). Nanocrystals in the sample bulk were covered by an unmineralized organic blanket (**Figure 4.30C**).

At a later stage in the biomineralization process, FAp nanocrystal growth was diverted to expand in a horizontal manner, if the integrity of the unmineralized blanket remained intact (**Figure 4.31**).

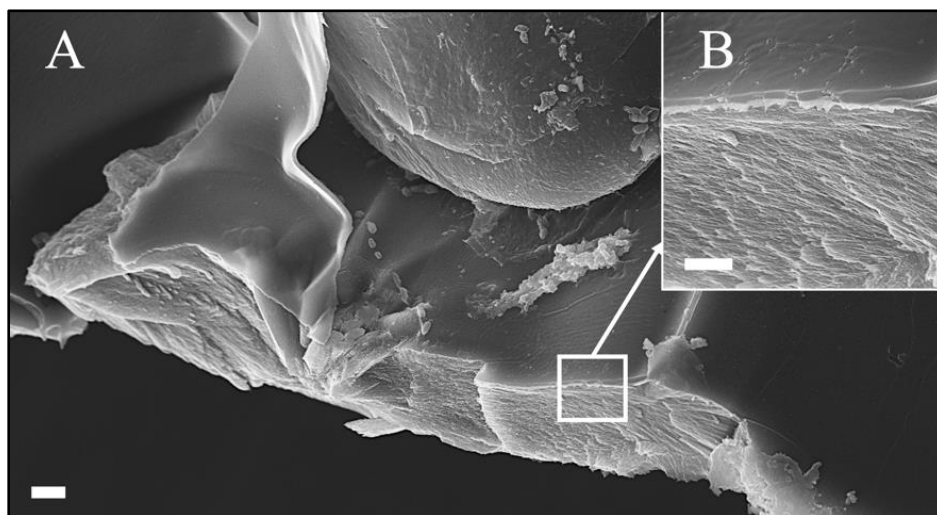


**Figure 4.31:** SEM image of (A) mineralizing PMDI-ELP membrane at an advanced biomineralization stage, showing redirected horizontal nanocrystal growth. (B) Nanocrystals remained covered by an unmineralized blanket. Scale bars: 1  $\mu\text{m}$

As previously mentioned, biomineralization in PMDI-ELP membranes was less dense than in genipin-ELP membranes. Under consideration of the results presented in this section, it was assumed that the biomineralization ability was restricted due to the sparse distribution of smaller nucleic pores.

Furthermore, as previously mentioned, it was suspected that the tightly bound cross-linked network of PMDI-ELP membranes and their brittle nature impeded ion diffusion from the biomineralization solution into the membrane bulk.

#### 4.3.3. Summary of the mineralization mechanism in PMDI- and genipin-ELP membranes

It was herein suggested that nano- and macroscopic pores in the newly established ELP membrane formulations acted as nucleic biomineralization sites. **Figure 4.32** visualizes the proposed mineralization mechanism.

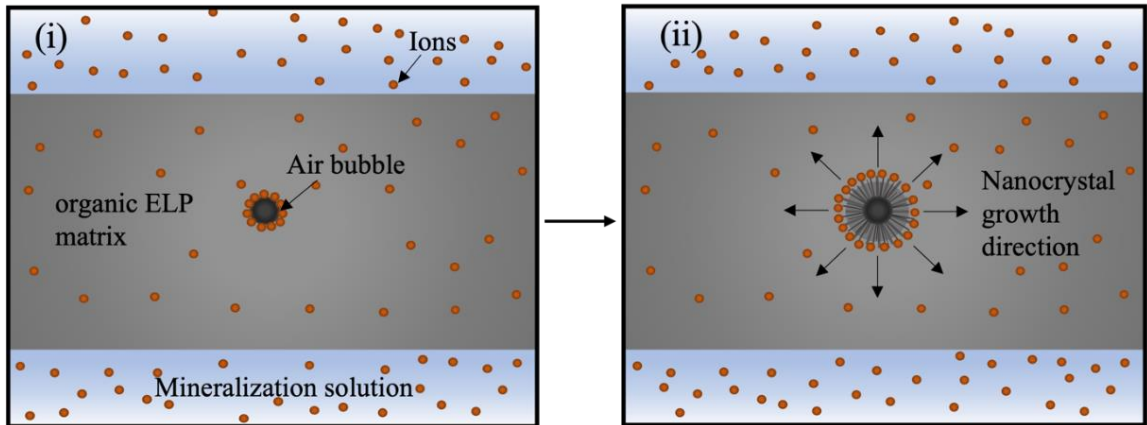


**Figure 4.32:** Visualization of proposed mineralization mechanism in PMDI- and genipin-ELP membranes, wherein (i) ions from the mineralization solution came to an arrest at the interface between the pore and the organic matter. (ii) The interface between nucleic pore and the organic matter was assumed to promote spherical nanocrystal growth, away from circumference surface of the pore.

The interface between the nucleic pore and the organic ELP matter was suggested to have brought ions that diffused from the mineralization solution into the membrane bulk to an arrest (**Figure 4.32 (i)**). Results showed that the directional growth of FAp nanocrystals was redirected upon interference with interfaces. At this stage, the unmineralized matter blanket retained nanocrystals within the sample bulk, causing them to grow away from the surface.

Thus, the interface between nucleic pore and the organic matter was assumed to promote spherical nanocrystal growth, away from the hollow centre of the pore (**Figure 4.32 (ii)**).

Once mineralization was commenced, a new interface formed between the organic matter and circumference of spherically aligned nanocrystals. Arrest of diffusing ions at this newly established interface enabled expansion of the mineralizing sphere.

Henceforth, the growth faith of mineralizing spheres was determined by

- The mechanical properties of the membrane (flexible vs. brittle) and its swelling capacity, which determined ion diffusion capability and biomineralization kinetics and
- The interference of mineralizing spheres with (1) adjacent spheres or (2) the membrane surface

#### 4.4. Summary

FAp biomineralization was achieved on the surfaces and in the bulk regions of all newly formulated ELP membranes.

Whilst Maltese cross-patterned organic spherulites in the HDI-ELP membrane control group appeared to be of organic nature, cross-patterns observed *via* PLM in PMDI- or genipin-ELP membranes were proposed to be optical artefacts, caused by light diffraction in pores [192] that were formed in the sample bulk during the cross-linking process [193]. Therefore, a different mineralization mechanism was assumed for the new formulations.

Results gathered *via* SEM imaging suggested that pores in the membrane bulk acted as nucleic sites in biomineralization. It was proposed that ions from the mineralization solution accumulated at the interface between the nucleic pore and the organic ELP matter. From this interface, aligned nanocrystal growth was promoted in a spherical outward fashion, leaving mineralizing spheres engulfed by organic matter. As the spheres expanded, they emerged to the membrane surface, remaining covered by a blanket of unmineralized matter. The thickness of the blanket determined the morphology of mineralizing volcanoes. Growth faith of mineralizing spheres was proposed to be determined by the samples' mechanical properties and interference of mineralizing spheres with the membrane surface, or adjacent spheres.

## 5. 3D-Printing of ELP-based constructs

The aim of this chapter is to integrate the newly developed PMDI- and genipin-ELP formulations into material extrusion (ME) and investigate the materials' suitability for the layer-by-layer deposition of shapely structures. This printing method was deemed suitable as it employs low printing temperatures [197], which is important in the processing of temperature sensitive proteins.

After assessing whether extruded material can guide FAp biomineralization, the formulations shall be used to fabricate two-dimensional and three-dimensional constructs that can undergo stimuli triggered biomineralization.

Presented experiments in this section were designed to:

- Assess whether biomineralization can be achieved in extruded PMDI-ELP gels.
- Define material transfer methods into 3D-printing cartridges, that were tailored towards the materials' gelation kinetics.
- Optimize the printing parameters for synthesized EL-based materials.
- Assess print accuracy of grid structures post printing and post cross-linking.

### 5.1. Preliminary experiments – PMDI-ELP gel extrusion

The ability to instantly (< 3 seconds) form ELP gel upon mixing 4% ELP-solution with 0.3 wt% PMDI-solution qualified this formulation for the conduction of preliminary material extrusion experiments. In this section, PMDI-ELP filaments were extruded manually and *via* ME. Manually extruded filaments and 3D-printed structures were assessed towards their biomineralization ability. Furthermore, it was investigated how sample cross-linking in different environments affected filament shape, its integrity and biomineralization capability.

### 5.1.1. Manual 0.3% PMDI 4% ELP gel extrusion

The PMDI-ELP gel was prepared in accordance with the method described in *chapter 3.1.1*. Using tweezers, the fabricated ELP based gel was manually transferred into a conventional syringe. Gel filaments were manually extruded onto PDMS substrate through a 25G needle (inner diameter = 0.25 mm). This substrate was selected due to its low surface roughness and hydrophobicity, which allowed sample removal from the substrate post extrusion. Presence of air in the extrusion set-up interrupted continuous filament extrusion, as shown in **Figure 5.1**.

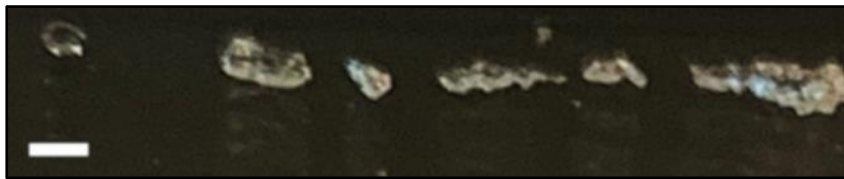


**Figure 5.1:** Air in manual extrusion system causing discontinuous PMDI-ELP filament extrusion. Scale bar: 1 mm.

To enhance the extrusion setup, a conventional syringe was cut to size using a scalpel, to match the gel volume (**Figure 5.2A**). A 25G needle was attached to the syringe. PMDI-ELP gel was transferred into the syringe by putting a 600 $\mu$ l Eppendorf upside down onto the syringe and flicking the gel into the syringe (**Figure 5.2B**). Upon extrusion, a continuous filament was, which could be handled with tweezers (**Figure 5.2C**). The filament remained stable in biomineralization solution (**Figure 5.2D**).

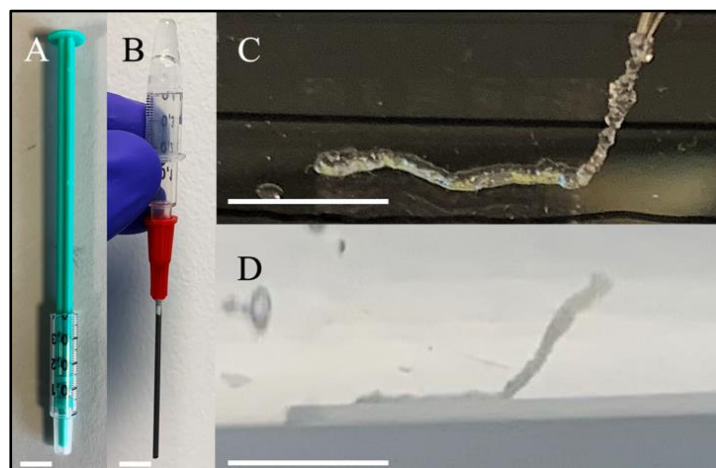


**Figure 5.2:** Experimental set-up for manual PMDI-ELP gel extrusion that minimizes air turbulence in the gel. (A) A conventional syringe, that was cut to match the prepared material volume. (B) A 25G needle was attached to syringe before ELP gel was transferred into the it *via* manual flicking, (C) Extruded PMDI-ELP filament on PDMS, handled with tweezers after extrusion and (D) in mineralization solution. Scale bars: 5 mm.

It was assumed that by shortening the travel distance from the Eppendorf tube to the tip of the syringe, less turbulence was created in the gel, thereby reducing the presence of air in the extrusion setup.

The extruded filament was imaged *via* optical microscopy. The sample showed different thicknesses across its length (**Figure 5.3**).

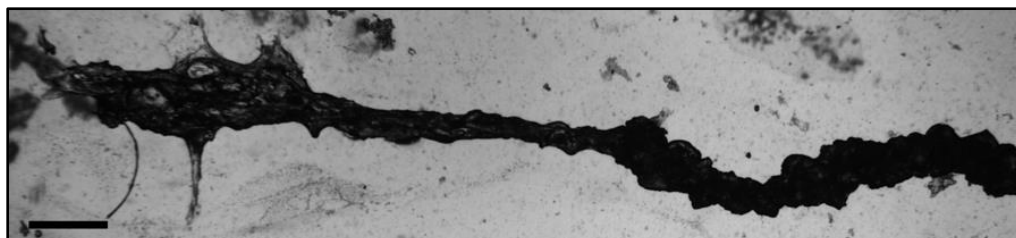


**Figure 5.3:** PMDI-ELP filament extruded through 25G needle showed irregular filament thickness across the sample length. Scale bar: 500  $\mu\text{m}$ .

Using the analysis tool in the ImageJ software, the diameters were measured to vary between 142  $\mu\text{m}$  and 365  $\mu\text{m}$ .

In previous research, the effect of print speed on filament width and length has been investigated [198]. In this work, different print speeds and pressures were tested and the effect of these parameters on filament dimensions (width and height) were studied. It was herein suggested that both these print parameters strongly correlated and affected the dimensions of deposited filaments. Furthermore, it was established that pressure had a stronger impact on filament height than print speed.

Similar work was conducted in a different study wherein it was shown that filament height and width could be decreased by employing increasing print speed and decreasing the applied pressure during gel extrusion [97].

Under consideration of the syringe needle diameter (250  $\mu\text{m}$ ), it was herein suggested that the observed irregularities in extruded PMDI-ELP filaments stemmed from the application of inconsistent extrusion speeds and pressure during manual extrusion.

The extruded PMDI-ELP filament was immersed in biomineralization solution and incubated at 38°C. The biomineralization solution was prepared as described in *chapter 2.2.3*

After two days in mineralization solution, close up optical microscopy images of the extruded PMDI-ELP filament revealed the presence of biomineralized structures, that were distributed uniformly across the sample (**Figure 5.4**).

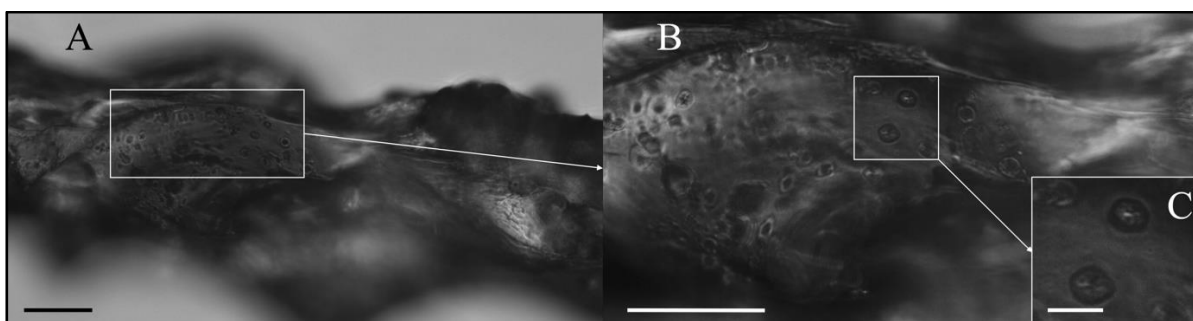


**Figure 5.4:** Close up of extruded PMDI-ELP filament revealing the presence of biomineralized structures on the surface of the sample. Scale bars (A, B): 50  $\mu\text{m}$ ; (C): 10  $\mu\text{m}$ .

After ten days in biomineralization solution, the ELP filament was SEM imaged. **Figure 5.5A** shows a macroscopic image of the sample, in which irregularities along the filament edge are highlighted with arrows.

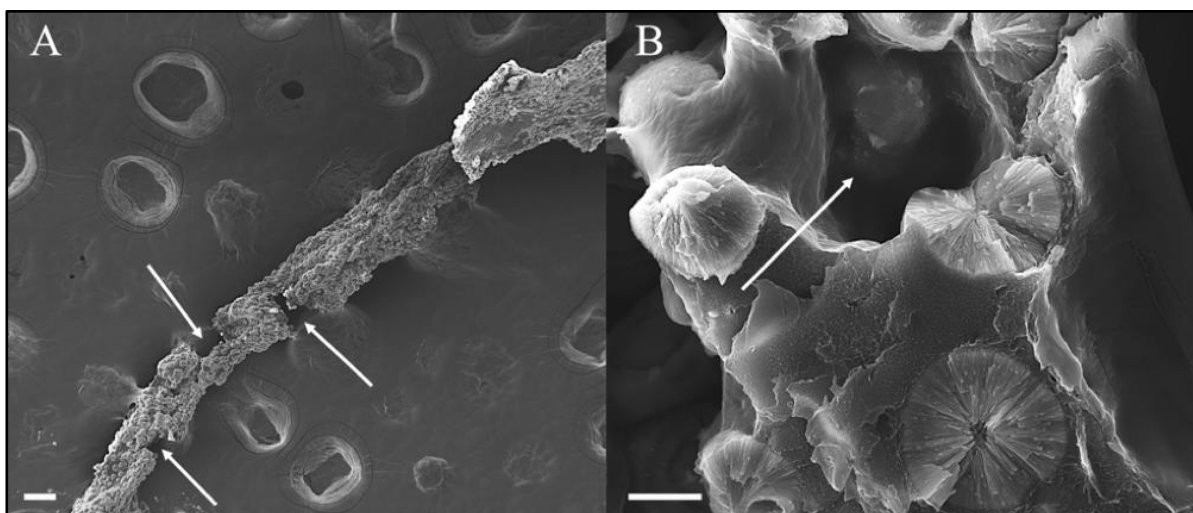


**Figure 5.5:** SEM images of PMDI-ELP filament after ten days in mineralization solution highlighting (A) gaps at the edge of the filament and (B) holes in the bulk, which stemmed from air in the extrusion system that resulted from manual transfer from the mixing container into the extrusion syringe. Scale bars: (A) 100  $\mu\text{m}$ ; (B) 5  $\mu\text{m}$ .

Despite the improved extrusion setup, it was suspected that the highlighted gaps at the filament edge (**Figure 5.5A**) and holes in its cross-section (**Figure 5.5B**) were a result of the turbulence experienced in the gel during gel transfer from the mixing container, into the syringe.

**Figure 5.6A** shows microscale images of mineralized volcanos on the surface, which were composed of spherically aligned nanocrystals in the cross-section (**Figure 5.6B**). These nanocrystals were covered by a thin blanket of unmineralized matter (**Figure 5.6C**), as observed in biomineralized membrane configurations (*chapter 4.2.2.2*).

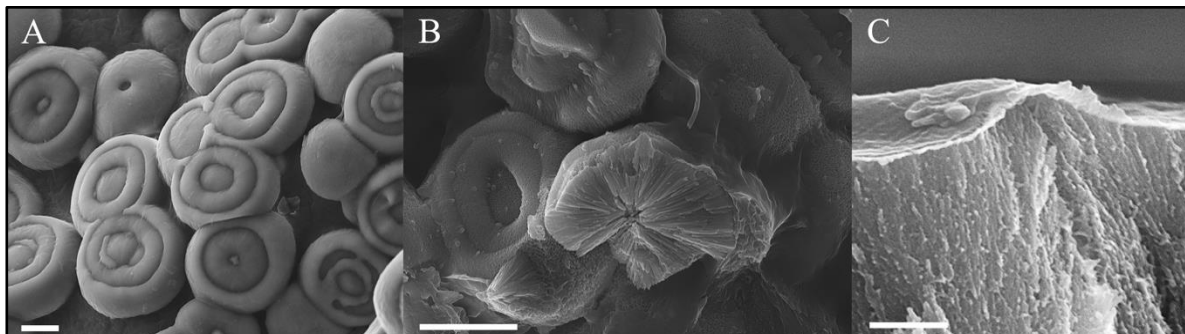


**Figure 5.6:** SEM images of mineralized PMDI-ELP filament, showing (A) mineralized structures on the sample surface, that are composed of (B) spherically arranged aligned nanocrystals in the filament bulk. (C) Nanocrystals were covered by a thin layer of unmineralized matter. Scale bars (A) (B): 5 µm; (C): 500 nm.

#### 5.1.2. Automated material extrusion of PMDI-ELP gel

In the above, it was suggested that the PMDI-ELP gel transfer method-imposed challenges with regards to the manual extrusion of continuous filaments. Therefore, a material transfer method was developed, wherein gelation occurred within the print cartridge.

0.3 wt% PMDI and 4% ELP were separately dissolved in in 500 µl solvent mixture. Thereafter, the solutions were transferred into two conventional 1 ml syringes, that were fed into a cell mixer device (Bico, Gothenburg, Sweden) (**Figure 5.7A**). The cell mixer device was equipped with two separate inlets, which fed into a single outlet with an integrated static mixer nozzle. This outlet could be interconnected with a printing cartridge *via* a female lure lock. The two separate PMDI and ELP solutions were mixed *via* simultaneous injection through the static mixer nozzle. Within 5 seconds, a homogenous gel was formed within the print cartridge (**Figure 5.7B**).

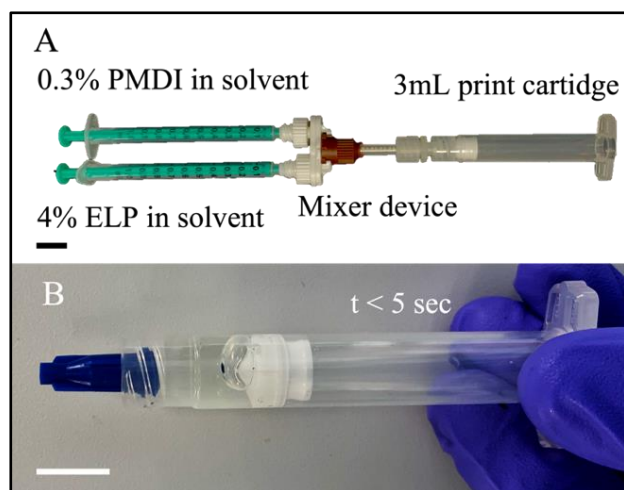


**Figure 5.7:** Setup for PMDI-ELP solution transfer to achieve homogenous gelation. (A) Two 1 ml syringes feeding into a mixer device that is connected to a printing cartridge *via* a female lure lock. (B) PMDI-ELP gel in 3mL printing cartridge. Scale bars: 1 cm.

22G nozzles with an inner diameter of 0.41 mm were tested in this study. Two different print nozzles typed were available for the Cellink Inkredible extrusion 3DP system:

- (1) Conical precision nozzles (**Figure 5.8A**), wherein the material encounters an extrusion needle with the desired nozzle diameter immediately after it is forced out of the print cartridge, and
- (2) Conical standard nozzles (**Figure 5.8B**), which display gradual diameter reduction, until the final extrusion diameter is reached prior to extrusion.

A conical standard nozzle was chosen for PMDI-ELP extrusion, as nozzle blockage occurred upon extrusion through a conical precision nozzle.

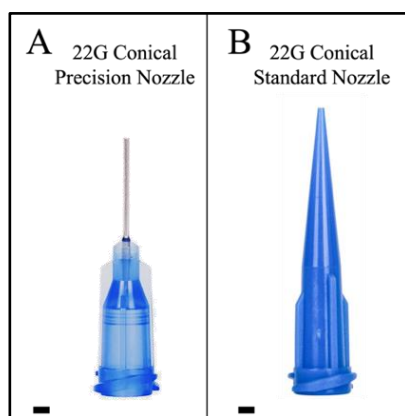


**Figure 5.8:** Print nozzles variants considered for PMDI-ELP extrusion printing. (A) 22G conical precision nozzle. (B) 22G conical standard nozzle. Scale bar: 1 mm.

### 5.1.2.1. PMDI-ELP gel printability assessment

By gradually increasing the pneumatic pressure on the Incredible Extrusion system, it was established that continuous filament extrusion could be achieved at approximately 40-50 kPa. Print speed tests, wherein material was deposited onto PDMS substrate at different speeds, showed that continuous filaments could be extruded at a speed of 4.4 mm s<sup>-1</sup> (**Figure 5.9**). At higher speeds, the nozzle movement was too fast to allow the extruded material to deposit as the print head moved, whilst slower movement caused material build up, reducing filament resolution.

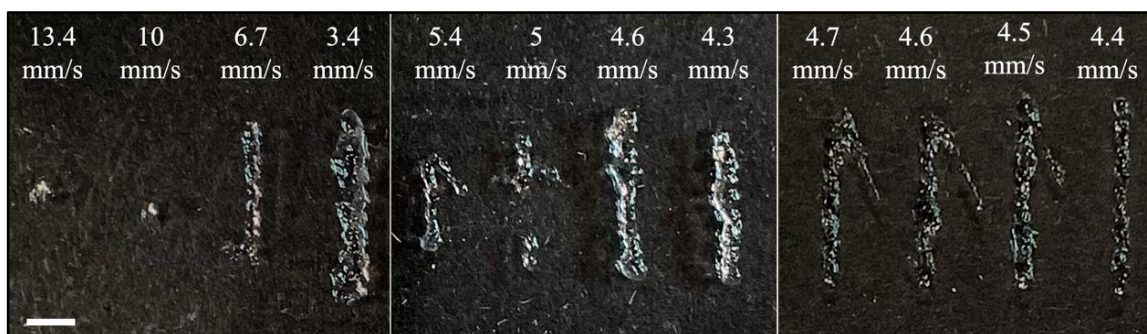


**Figure 5.9:** Printing speed tests, concluding an idea print speed of 4.4 mm s<sup>-1</sup> for continuous filament deposition onto PDMS substrate whilst applying a pneumatic pressure of 40-50 kPa. Scale bar: 10 mm.

To assess the materials' 3D-printability, a 3 layered STL file was created (**Figure 5.10A**) as a template for the deposition of a 10 x 10 x 1 mm, hollow circle. The layer height was set to 0.4 mm to coincide with the print nozzle diameter. The optimized print speed (4.4 mm s<sup>-1</sup>) was considered in the g.code file generation.

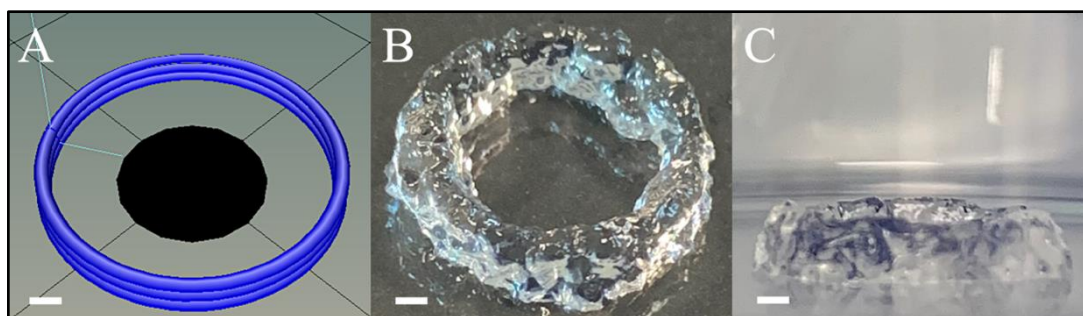


**Figure 5.10:** Translation of an STL file into a 3D-printed PMDI-ELP gel sample. (A) STL file of a hollow circular structure (10 x 10 x 1 mm). (B) Additively manufactured, three layered PMDI-ELP gel, showing (C) offset layer heights and undefined filament edges. Scale bars: 1 mm.

Layer-by-layer fabrication of PMDI-ELP filaments was achieved (**Figure 5.10B**). However, poor filament resolution in both X- and Z-direction was observed, resulting

in undefined filament edges and offset layer heights, leading to a sample height of approximately 1.5 mm, instead of the desired sample height of 1.2 mm (**Figure 5.10C**).

#### 5.1.2.2. *Post-processing and assessment of shape maintenance in PMDI-ELP prints*

Printed samples were post-processed in different ways to assess how this affected their shape integrity. In the following, the print structure behaviour encountered in the different circumstances is reported.

##### (1) *Immersion in biomineralization solution post 3D-printing*

**Figure 5.11A** shows the three layered PMDI-ELP print after extrusion. This construct remained stable upon handling with tweezers. However, as the construct got into contact with biomineralization solution, the filaments immediately collapsed (**Figure 5.11B**). After 1 h in solution, the sample had mostly disintegrated (**Figure 5.11C**).

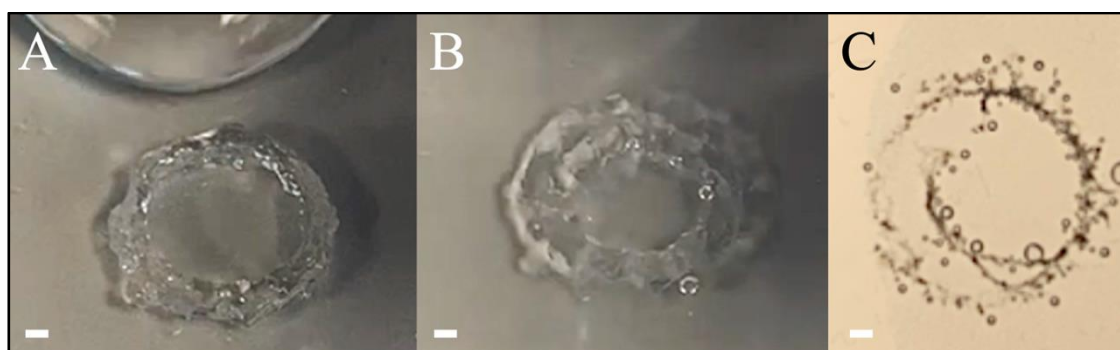


**Figure 5.11:** Collapse of (A) a printed PMDI-ELP gel sample after fabrication (B) upon immersion in mineralization solution, leading to (C) strong disintegration after 1h in solution. Scale bar: 1 mm

This PMDI-ELP gel behaviour upon immersion in DI water was previously observed in *chapter 3.1.2.2*, wherein synthesized PMDI-ELP gels were FTIR scanned over time. It was herein suggested that ‘*protein secondary formation was a time dependent process*’. FTIR spectra deconvolution also showed that the underlying protein secondary structure in contained PMDI-ELP gel was composed of approximately 95% random coils. Since the PMDI-ELP gel was extruded from a sealed print cartridge, right after synthesis, the same molecular disorder was assumed for extruded PMDI-ELP filaments. It was therefore assumed that the solvent incorporated in this formulation is entrapped in this network of random coils.

Therefore, it was proposed that sample immersion into solution before a certain threshold of molecular self-assembly was reached, caused the highly disordered protein secondary structure to disintegrate as it was penetrated by solution.

Additionally, literature research was conducted in *chapter 3.1.2.2* to understand interactions between water and the solvents of interest, DMF and DMSO:

*‘Both DMF and DMSO are polar aprotic solvents that can form hydrogen bonds. Water molecules can equally form hydrogen bonds due to their inherent polar covalent bonds [177]. As a result, these organic solvents interact with water, hydrogen bonds form between the respective polar groups, leading to the dispersion of solvent molecules in water, and vice versa [178][179].*

*In addition to that, DMF, which is the main component of the solvent mixture, is not stable in water over a long period of time as degrades to the secondary amine dimethylamine (DMA) and the carboxylic acid, formic acid (FA).’*

### (2) Cross-linking in a sealed petri dish (glovebox and fume hood)

PMDI-ELP prints were contained in a parafilm sealed petri dish and left to cross-link in a glovebox or in a fume hood for three days. This post-processing method has shown to restrict sample vertical collapse (**Figure 5.12A**). Furthermore, their gel-like conformation was maintained as shown **Figure 5.12B**, where the gel stuck to a metal spatula as highlighted.

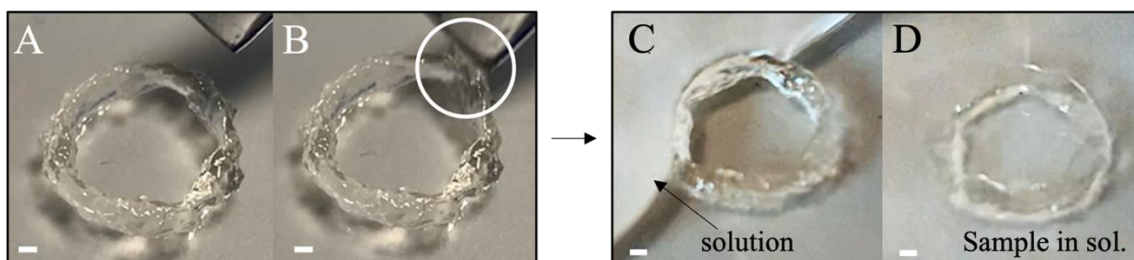


**Figure 5.12:** Printed PMDI-ELP gel samples after 3 days of cross-linking in a parafilm sealed petri dish, showing (A) maintained three-dimensional shape and (B) gel conformation, as highlighted upon touching the gel with a spatula. (C, D) The sample remained stable upon immersion in mineralization solution (sol.) Scale bar: 1mm.

It was suspected that the materials’ gel-like characteristics were maintained through sample containment in a sealed petri dish, causing limited solvent evaporation, compared to open containment.

When the sample was immersed in biomineralization solution, the circular filament arrangement was maintained (**Figure 5.12C**). Overtime, solvent leaching occurred, which led to sample collapse (**Figure 5.12D**). The reason for organic solvent leaching

into the aqueous solution was further elaborated on in *chapter 3.1.2.2* and in the section above.

Furthermore, the sample developed a slight yellow tone. This discolouration was also observed PMDI-ELP membranes, where a yellowish tone was observed. Literature states that this is characteristic for aliphatic poly-isocyanates [189]. It has also been reported that oxidation reactions on the backbone of the aliphatic poly-isocyanate triggers change of colour in curing samples, a process which is accelerated under the influence of UV light [190]. This suggested that even though the contained sample was sealed with parafilm, the system was not fully airtight.

Based on previously drawn conclusions, which stated that protein secondary structure was both time and collapse dependent, it was assumed that cross-linking in a sealed petri dish enabled the formation of protein secondary structure, that was sufficiently developed to form a network that was stable in solution.

### (3) Cross-linking in an unsealed petri dish (glovebox and fume hood)

Samples that were left to cross-link in an unsealed petri dish vertically collapsed whilst maintaining their two-dimensional circular filament alignment.

**Figure 5.13A** shows a print that was cross-linked in a glovebox environment. This sample displayed better shape maintenance in z-direction than the sample cross-linked in a fume hood (**Figure 5.13B**). Both cross-linked samples transformed from a gel-like configuration into brittle structures, whilst obtaining an aliphatic poly-isocyanate characteristic yellowish tone.

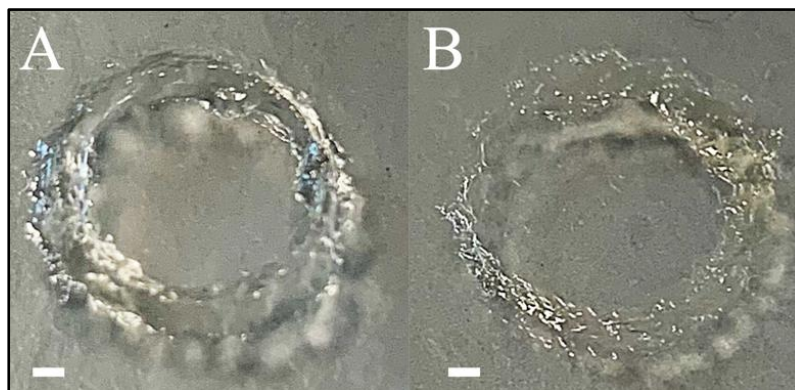


**Figure 5.13:** PMDI-ELP prints after 3 days in an open petri dish in a (A) glovebox and (B) fume hood, showing maintenance of the circular filament arrangement. However, sample collapse was experienced. The fume hood cross-linked sample showed stronger collapse than the glovebox cross-linked print. Scale bar: 1 mm.

In the following, sample dimensions were measured and quantified post cross-linking in different environments (i.e., in a fume hood and in a glovebox) *via* SEM imaging.

**Figure 5.14A** shows the top view of a glovebox cross-linked print, displaying a filament diameter of approximately 365  $\mu\text{m}$ . Cross-section images (**Figure 5.14B**) revealed a peak sample height of approximately 580  $\mu\text{m}$ , which concludes a 42% vertical collapse in comparison with the programmed sample height of 1.2 mm. Closer observation of the cross-section showed the presence of pores (**Figure 5.14C**), which have been proposed to act as nucleic sites in biomineralization (*chapter 0*).

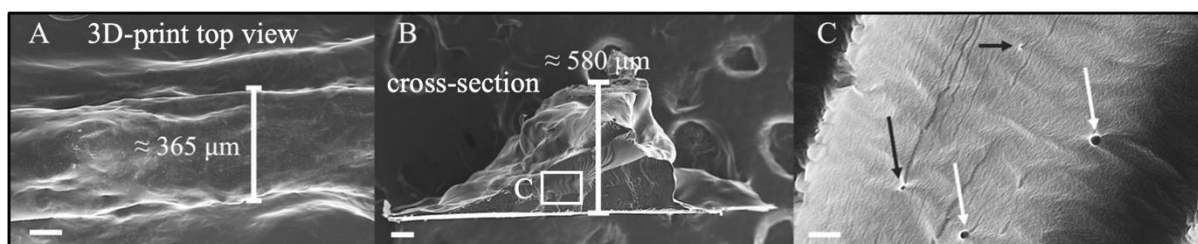


**Figure 5.14:** SEM images of glovebox cross-linked PMDI-ELP prints. (A) Top view showing a measured filament thickness of approximately 365  $\mu\text{m}$ , (B) Cross-sectional view showing a sample peak height of approximately 580  $\mu\text{m}$ . (C) Close up image, revealing the presence of circular in the sample bulk. Scale bars (A, B): 100  $\mu\text{m}$ , (C): 1  $\mu\text{m}$ .

In **Figure 5.15**, SEM images of a fume hood cross-linked samples are shown. From the top view, at the samples' thinnest area, a filament thickness of approximately 450  $\mu\text{m}$  was measured (**Figure 5.15A**), whilst the cross-sectional image showed a peak sample height of approximately 280  $\mu\text{m}$  (**Figure 5.15B**), concluding 77% vertical sample collapse. Close examination of the cross-section exposed oval shaped pores in the sample bulk (**Figure 5.15C**)

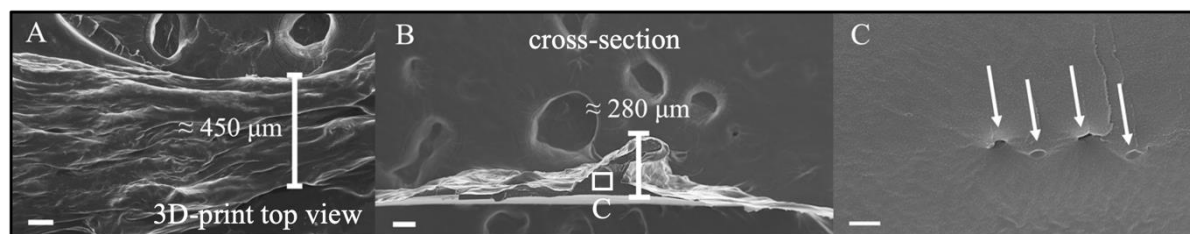


**Figure 5.15:** SEM images of fume hood cross-linked PMDI-ELP prints. (A) Top view showing a measured filament thickness of approximately 450 $\mu\text{m}$ , (B) Cross-sectional view showing a sample peak height of approximately 280 $\mu\text{m}$ . (C) Close up image, revealing the presence of oval shaped pores in the sample bulk. Scale bars (A, B): 100  $\mu\text{m}$ , (C): 1  $\mu\text{m}$ .

It was proposed that due to accelerated cross-linking, the pores in the bulk region of glovebox cross-linked samples were more prone to shape maintenance, compared to fume hood cross-linked samples. In fume hood cross-linking, stronger sample collapse was experienced, which was suggested to affect the pore structure integrity.

More pores were observed in glovebox cross-linked samples. The reason for the formation of pores was hypothesized on in *chapter 4.1.2.3*, where it was proposed that *‘PMDI forms an intermediate, carbamic acid, upon hydrolysis. Upon extended hydrolysis, CO<sub>2</sub> gas is released as this unstable intermediate decomposes [172]. It is herein hypothesized that observed pores may stem from commenced decomposition of the carbamic acid intermediate, as the investigated membranes were cross-linked in an uncontrolled environment and thereby exposed to humidity.’*

In the processing of genipin-ELP membranes it was furthermore suggested that *‘pores formed during the membrane solidification process. During this process, it was observed that a gel-like skin formed on the membrane surface before the bulk region had fully solidified. It was assumed that air bubbles, which formed as the pressure beneath this gel-like skin layer decreased, were trapped in bulk region.’*

It is herein assumed that this mechanism also applies to PMDI-ELP print structures, due to their increased volume and the increased cross-linking time, compared to their membrane configuration.

It was suggested that compared to fume hood cross-linking, more pores formed in glovebox cross-linked samples, because solvent evaporation was accelerated in a low humidity environment, which sped up the formation of a gel-like skin. This conclusively led to the entrapment of more air bubbles during cross-linking. It was furthermore assumed that due to accelerated cross-linking kinetics in a glovebox environment, shape maintenance in z-direction was enhanced, compared to fume hood where an extended cross-linking time was experienced. This was evidenced *via* experiments conducted in *chapter 3.1.2.2*, where cross-linking kinetics in different environments were studied. Additionally, due to the PMDIs’ hygroscopicity and thereby its ability to form bonds with water present in the environment, as presented in *chapter 3.1.1*, it was assumed that the CLAs’ reactivity diminished over time in an environment that was not humidity controlled, which was suggested to have led to a loss of shape fidelity during cross-linking.

5.1.2.3. *Assessment of biomineralization ability in 3D-printed PMDI-ELP samples*  
Post cross-linking in different environments (i.e., in a fumehood and glovebox), samples were immersed in biomineralization solution for 10 days at 38°C. During the biomineralization process, the printed samples remained on the PDMS substrate. After the samples were removed from the biomineralization solution, they were dried overnight at 60°C in preparation for subsequent SEM imaging.

The drying step induced evaporation of biomineralization trapped in the sample, which enabled shape maintenance after removal from the substrate PDMS. **Figure 5.16** shows a dried PMDI-ELP print post mineralization, maintaining its shape as it was held by a spatula.

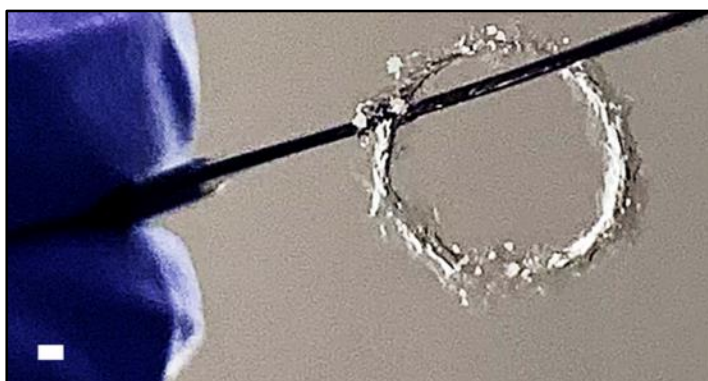


**Figure 5.16:** Circular PMDI-ELP print after 10 days in biomineralization solution and overnight drying at 60°C, maintaining its shape as it was held by a spatula. Scale bar: 1mm.

Thereafter, samples were prepared for SEM analysis in accordance with the methods stated in *chapter 2.2.5*. Via SEM imaging, the ideal cross-linking environment (glovebox/fume hood/sealed or unsealed container) with respect to most extensive biomineralization ability, was assessed.

Overall, samples that were openly contained (**Figure 5.17A, C**), showed the emergence of more biomineralized structures than samples kept in a sealed container (**Figure 5.17B, D**).

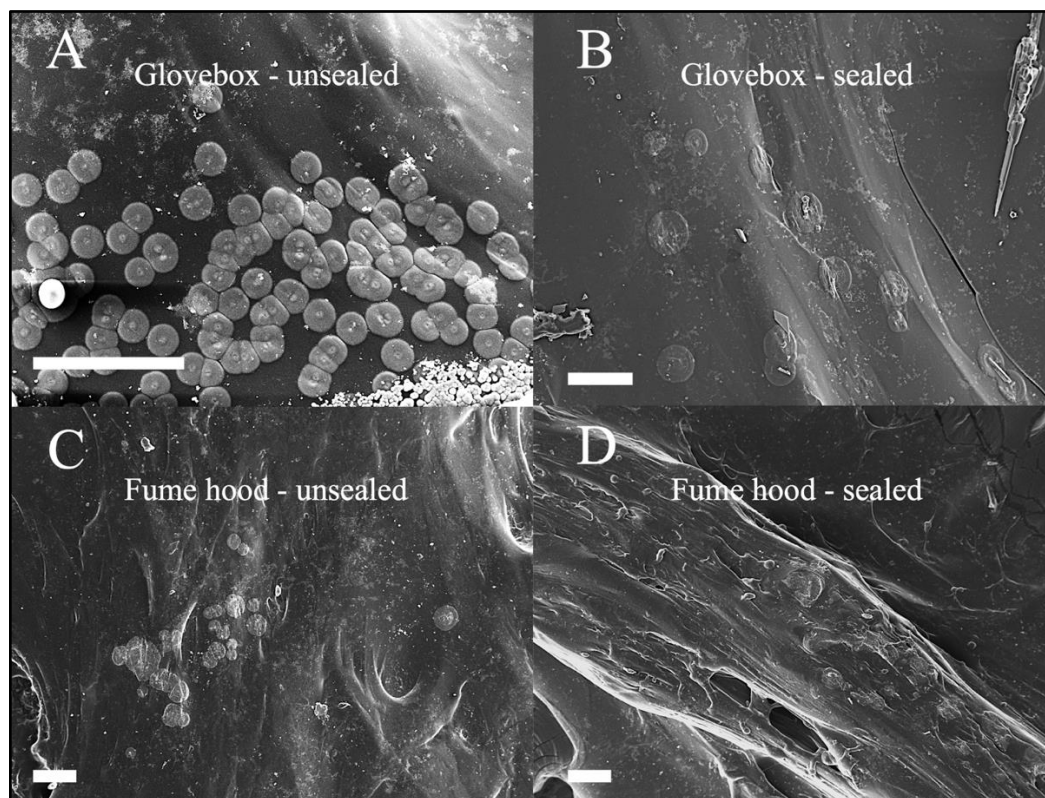


**Figure 5.17:** Printed PMDI-ELP constructs, cross-linked in different environments. (A) Glovebox cross-linked samples in an open container showed more mineralization than (B) samples cross-linked in a sealed container. (C) The fume hood cross-linked sample (open container) showed less mineralization than the glovebox cross-linked sample, whilst the fume hood cross-linked sample that was contained in a sealed container (D) showed the weakest mineralization ability. Scale bars: 100  $\mu\text{m}$ .

Under consideration of the previously made hypothesis, which stated that pores in the sample bulk act as nuclei in the biomineralization process, it was assumed that the increased presence of nucleic pores in glovebox dried samples enhanced biomineralization ability, in comparison to fume hood cross-linked samples.

As samples that were contained in a sealed petri dish, retained a gel conformation, it was proposed that air bubbles forming in the bulk were more likely to escape the sample bulk than in unsealed samples, in which solvent evaporation caused samples to turn brittle as cross-linking took place.

## 5.2. Concluding experiments – genipin-ELP gel extrusion

In *chapter 3.2*, the method for the synthesis of a homogenous genipin-ELP gel was established. Therein, it was observed that genipin-ELP solution in a contained environment underwent gelation over time. The ability to tune gelation in genipin-ELP gels made it a promising formulation for the fabrication integration in ME.

In this section, genipin-ELP gels with different cross-linker concentrations were synthesised and their incubation times were optimized with the aim to enhance printability. Printing parameters were tailored to the gel behaviour.

For the gel synthesis, genipin and SN<sub>A</sub>15 ELP molecules were dissolved in solvent mixture (500  $\mu$ l for initial experiments, 1 ml for concluding experiments) and transferred into a 3 ml printing cartridge, using a conventional syringe that was interconnected to the print cartridge *via* a female lure lock. Thereafter, the solution was incubated in a sealed printing cartridge, that was additionally contained in a sealed beaker.

As previously mentioned, genipin is prone to oxidation, which can lead to impeded reactivity with the ELPs' lysine cross-linking sites. By double-containing the gel during incubation, oxidation was aimed to be reduced. The following image depicts the changing gel colour over time.

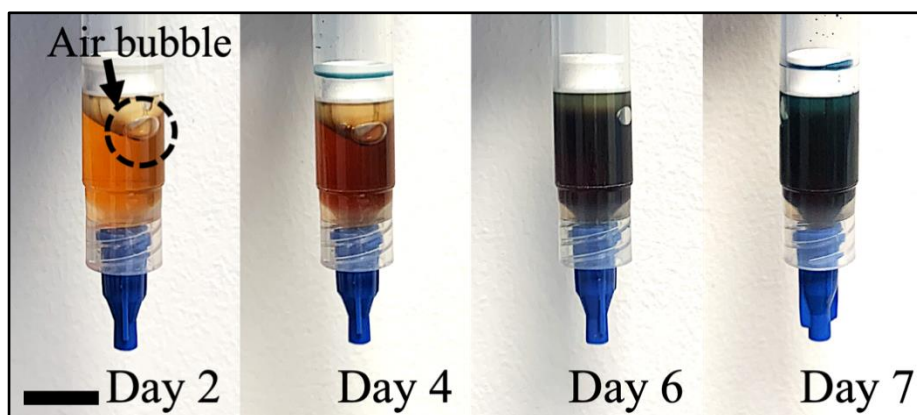


**Figure 5.18:** Change of colour over time in an incubating genipin-ELP gel, progressing from a light orange that progressively turns into a dark blue. In the Day 2 image, an air bubble is highlighted, that is used to monitor gelation over-time. Scale bar: 1 cm.

The initially colourless solution attained an intermediate orange colouring that progressively, as the material gelled, turned into a dark blue. This change of colour is

characteristic for genipin cross-linking [158][191]. Observation of the mobility of the highlighted air bubble was used to monitor the materials' gelation.

To gain an understanding of the material properties whilst making economical use of the CLA, a comparatively low concentration of genipin (0.5 wt%) was used for initial printing experiments. In previously presented experiments (*chapter 4.2.2.3 and 0*), a 1.0 wt% genipin concentration has been established to achieve most extensive biomineralization ability, as well as a highly ordered secondary structure. Therefore, 1.0 wt% genipin-ELP gel was synthesised to gather conclusive data.

### 5.2.1. Printability assessment – 0.5 wt% genipin 4% ELP gel

In the following, a 0.5 wt% genipin 4% ELP solution was tested towards its printability after **six and nine days of incubation** in a sealed print cartridge. The printing parameters, i.e., applied pneumatic pressure and print speed, were optimized towards the material behaviour at different incubation time points.

Using a precision conical 22G printing nozzles, two dimensional grids (10 x 10 mm) (**Figure 5.19A**) were extruded onto a PDMS substrate with the previously introduced Cellink Inkredible extrusion system.

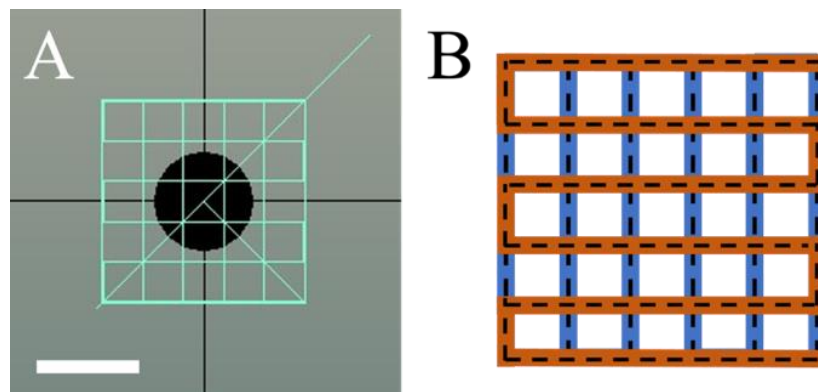


**Figure 5.19:** (A) STL print file for the fabrication of a 10x10 mm grid (Scale bar: 5 mm) (B) Illustration of printhead movement, travelling along two perpendicular sets of lines.

The illustration in **Figure 5.19B** depicts the printhead movement that was followed to create a grid by depositing two perpendicular sets of lines on top of another.

### *Gel printability assessment after 6 days of material incubation in closed cartridge*

At an applied pneumatic pressure of 145 kPa, continuous material extrusion achieved the deposition of uniform filaments at print speeds between 4.4–4.7 mm s<sup>-1</sup> (**Figure 5.20A**).

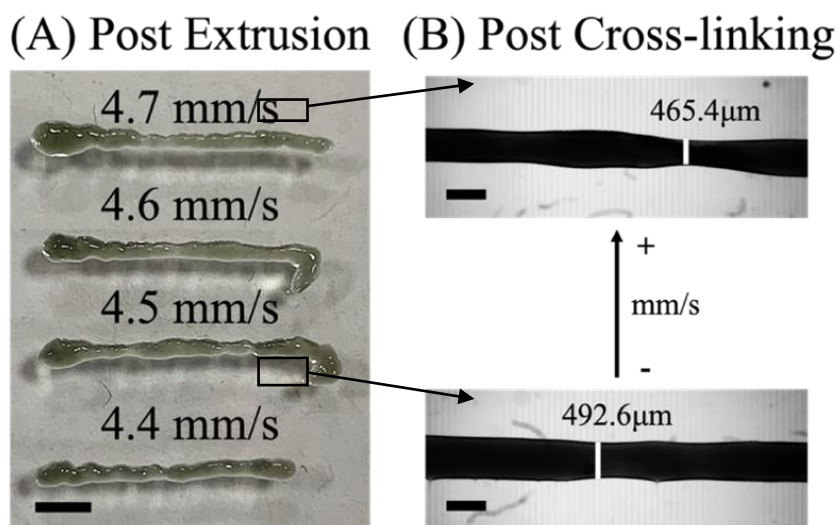


**Figure 5.20:** (A) After incubating 0.5 wt% genipin-ELP gel for six days in a closed cartridge, uniform filament deposition was achieved under the application of a pneumatic pressure of 145 kPa, at print speeds between 4.4–4.7 mm s<sup>-1</sup>. (B) Optical microscopy images of extruded filaments, showing how printing speed did not significantly affect the filament diameter post cross-linking. Scale bars (A): 10 mm, (B): 500 μm.

Due to the deposition of low material volumes, filaments were fully cross-linked in a matter of hours. Optical images obtained post cross-linking in a fume hood, showed insignificant differences in filament thickness at tested print speeds (**Figure 5.20B**).

### *Gel printability assessment after 9 days of material incubation in closed cartridge*

After nine days of gel incubation, pneumatic pressure was increased to 165 kPa to achieve material extrusion through a 22G precision nozzle. This pressure increase reflected the visually observed material gelation progression between day 6 and day 9. Nozzle blockage was experienced using a precision conical 22G printing nozzle (**Figure 5.21A**). Therefore, the nozzle was substituted for a 28G standard conical nozzle, through which extrusion was achieved at a significantly lower pneumatic pressure of 30 kPa. The accuracy of two-dimensional (2D) grid structure prints was however deemed unsatisfactory as it lacked resolution to the extent that desired pores were filled up with material (**Figure 5.21B**).

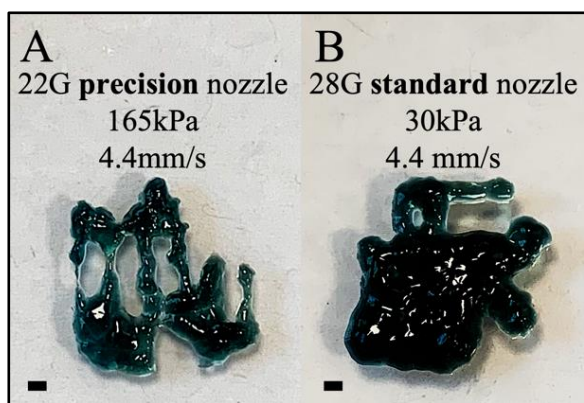


**Figure 5.21:** Grid structure prints after nine days of gel incubation in a closed cartridge, showing excessive material gelation that does not allow for high print accuracy through neither (A) precision nozzle nor (B) standard nozzle. Scale bar: 1mm.

Conclusively, genipin-ELP gel incubated for nine days were disregarded for further print assays. In the following section, the print accuracy for gel incubated for 6 days was investigated *via* the fabrication of two-dimensional grids.

0.5 wt% genipin 4% ELP gel that was incubated for six days, was extruded at the previously established print speeds of 4.4 and 4.7 mm s<sup>-1</sup>. The prints were compared against each other to assess how print speed affected print resolution accuracy (**Figure 5.22**).

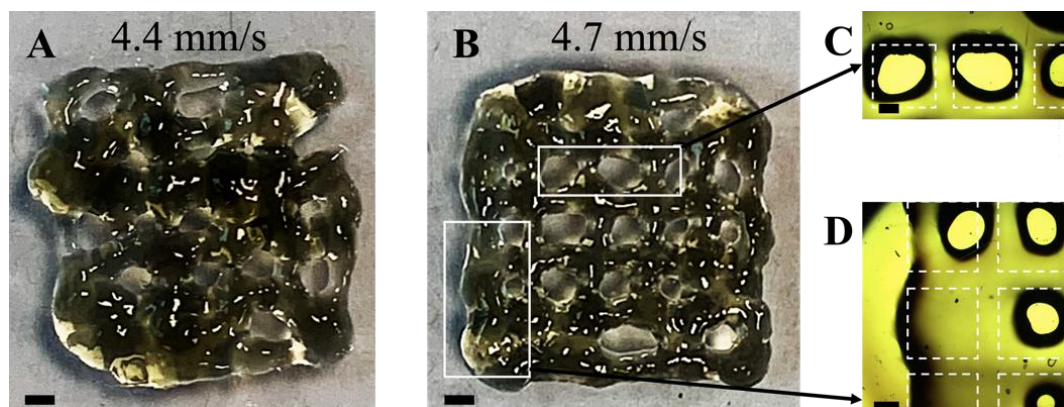


**Figure 5.22:** Print accuracy in 0.5 wt% genipin 4% ELP prints (six days gel incubation in a closed cartridge). (A) Slower printing speed causing material build up and pore closure. (B) Print accuracy was improved at an increased print speed. Pores in the inner scaffold region were printed more accurately (C) than those at the sample edge (D), which were prone to close. Scale bars (A), (B): 1 mm; (C), (D): 500  $\mu\text{m}$ .

Both tested speeds achieved continuous material extrusion. At a lower print speed of  $4.4 \frac{mm}{s}$ , material build up caused the majority of pores in the scaffold to close (**Figure 5.22A**). Increasing the print speed to  $4.7 \text{ mm s}^{-1}$  visibly improved print resolution (**Figure 5.22B**). However, pores located at the scaffold edge were still prone to close up (**Figure 5.22D**), whilst pores in the scaffolds' inner region were printed more reliably (**Figure 5.22C**). Optical microscopy images obtained post printing (**Figure 5.22C, D**) showed that perpendicularly aligned filaments collapsed into another, causing loss of their initially circular cross-sectional geometry. It was therefore suggested that after six days of incubation, the material was not sufficiently gelled to support its own weight, which was deemed non-beneficial for layer-by-layer manufacturing.

Close observation of the printing process revealed that due to the low roughness of PDMS substrate, the deposition of the second printing layer caused the first layer to get dragged across the substrate, causing print inaccuracies, especially at the sample edge (**Figure 5.23A, B**).

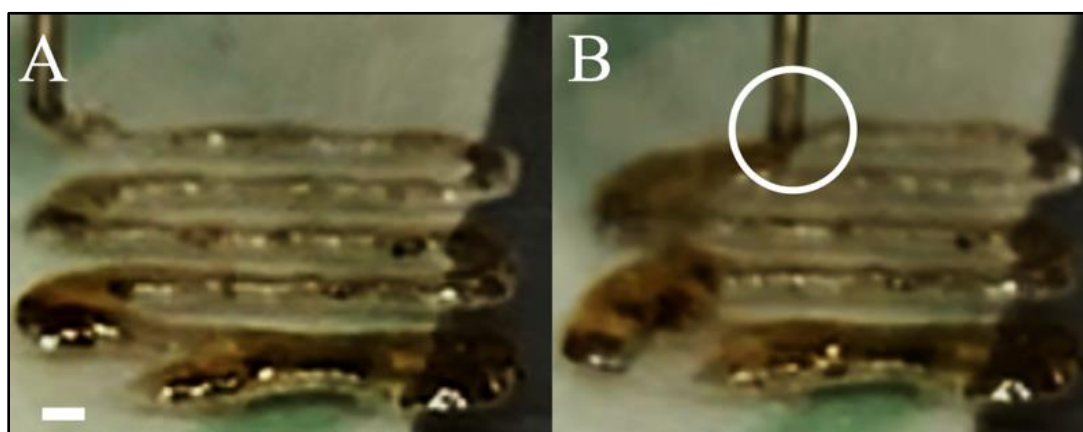


**Figure 5.23:** Negative effect of low surface roughness substrate on print accuracy in genipin-ELP gel. (A) High print accuracy of first deposited layer was achieved. However, (B) deposition of a second layer exerted traction on the below layer, affecting print accuracy. Scale bar: 1 mm.

It was therefore suggested that the print geometry was unsuitable for the selected substrate. It was assumed that the chosen pore sizes in combination with the low substrate roughness facilitated filament traction across the substrate during the printing process.

To test these hypotheses, a scaffold (30 x 30 mm) with larger pores was printed, to understand whether this could enhance the print accuracy (**Figure 5.24A**). Additionally, a 10 x 10 mm scaffold was printed onto masking tape to introduce a substrate with higher surface roughness into the experimental setup (**Figure 5.24B**).

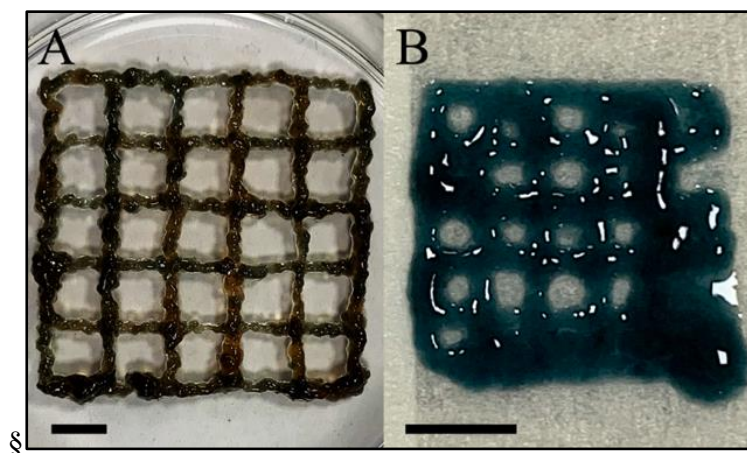


**Figure 5.24:** Improved print accuracy was achieved by (A) printing larger scaffolds and (B) using masking tape to increase substrate surface roughness. Scale bars: 5mm.

Results for both trials showed that the alteration of those two parameters impeded traction to improve print accuracy.

However, the filament shape fidelity in 2D scaffold printed onto masking tape (**Figure 5.24B**) was compromised by the substrate's hydrophilicity, causing the gel to be absorbed into the masking tape. Solvent absorption into the substrate was avoided through gel deposition onto hydrophobic PDMS substrate (**Figure 5.24A**), allowing the filament to maintain its shape integrity.

#### *5.2.1.1. Post-processing of 0.5 wt% genipin 4% ELP prints*

2D grid structures that were printed after six days of incubation were used for post-processing experiments. Based on results obtained from preliminary ME experiments, wherein PMDI-ELP gels were extruded, it was established that supramolecular self-assembly and structural print integrity can be enhanced by allowing samples to cross-link in a fume hood and in a glovebox, in an open petri dish (*chapter 5.1.2.2*). Genipin-ELP prints post-processing methods were based on these established results.

Fume hood cross-linked genipin-ELP prints displayed a deeper dark colour (**Figure 5.25A**) than glovebox cross-linked samples (**Figure 5.25D**).

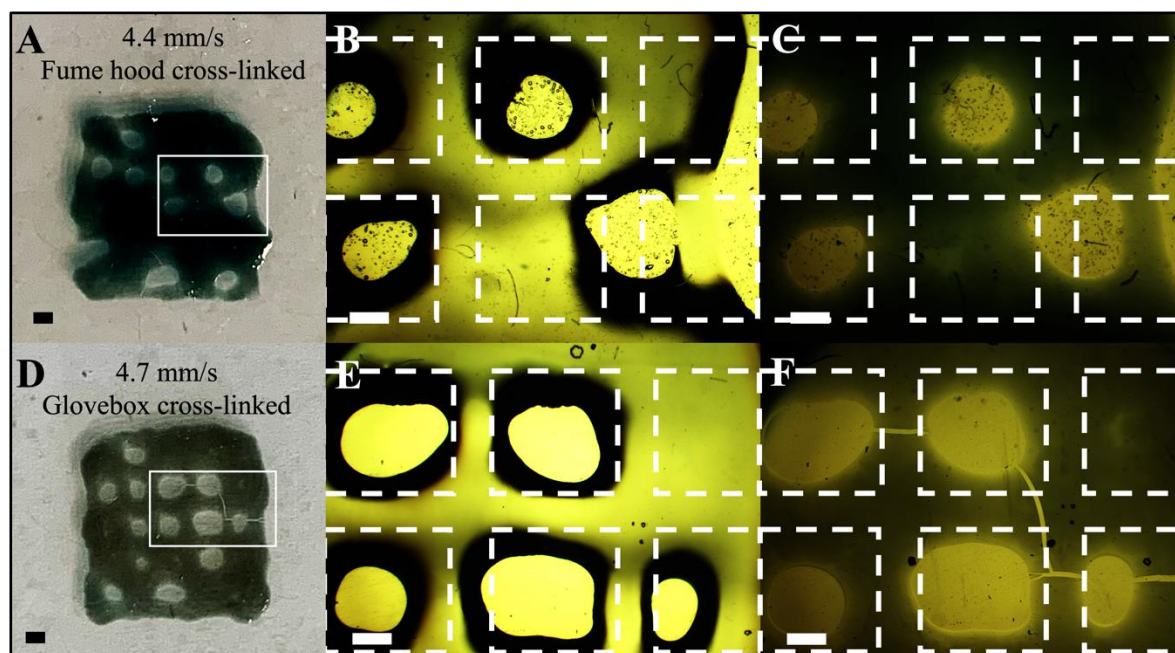


**Figure 5.25:** Comparison of print accuracy in (A, B, C) fume hood cross-linked and (D, E, F) glovebox cross-linked genipin-ELP prints after six days of gel incubation in a closed cartridge, showing sample collapse into 2D grid structures. Sample collapse did not cause a significant change in pore sizes post cross-linking (C, F), compared to post-extrusion (B, E). Scale bars (A, D): 1 mm, (B, C, E, F): 500  $\mu\text{m}$ .

It was assumed that this difference in colour stemmed from the comparatively higher oxidation that genipin underwent in an environment that was not humidity controlled. Optical microscopy images showed that samples collapsed into 2D grid structures (**Figure 5.25C, F**). The pore sizes, however, were seemingly maintained, upon comparison with images taken post extrusion (**Figure 5.25B, E**).

### 5.2.1.2. Assessment of biomineralization ability in 0.5 wt% genipin 4% ELP prints

After 10 days of immersion in biomineralization solution, biomineralized structures emerged in all tested samples (**Figure 5.26**).

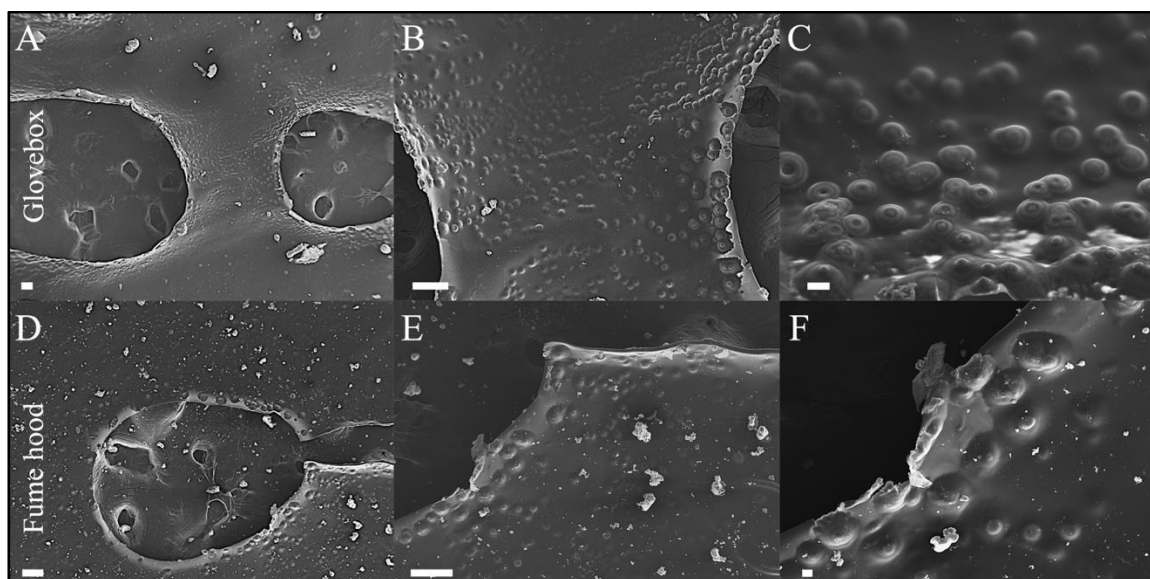


**Figure 5.26:** SEM images of glovebox (A, B, C) and fume hood (D, E, F) cross-linked samples after 10 days in mineralization solution, showing the emergence of biomineralized structures. (B) More biomineralization is observed in glovebox cross-linked genipin-ELP prints, where also directional growth in accordance with the printing direction is assumed. Scale bars (A, B, D, E): 100  $\mu\text{m}$ ; (C, F): 10  $\mu\text{m}$ .

Glovebox cross-linked samples showed more extensive biomineralization (**Figure 5.26A, B, C**) than fume hood cross-linked prints (**Figure 5.26D, E, F**).

It was assumed that biomineralization was enhanced through the formation of more nucleic pores, facilitating the emergence of biomineralized structures, as reported in *chapter 4*. Furthermore, the growth direction of mineralized structures appeared to follow a linear path (**Figure 5.26B**).

### 5.2.2. Printability assessment of 1.0 wt% genipin 4% ELP gel

In previously presented formulation optimization experiments (*chapter 4.2.2.3 and 0*), a 1.0 wt% genipin concentration was established to display favourable results in terms of biomineralization ability, as well as the formation of a highly ordered secondary structure. Therefore, 1.0 wt% genipin-ELP gel was synthesised to gather conclusive results.

### 5.2.2.1. Protein secondary structure analysis on 1.0 wt% genipin 4% ELP filaments

In *chapter 0*, the underlying protein secondary structure of genipin cross-linked ELP membranes was analyzed *via* FTIR by scanning 3 different membranes of the same formulation in two different membrane locations. 100% protein secondary structure transition from random coils into ordered protein structure conformations in 4 out of 6 scanned positions in 1.0 wt% genipin-ELP membranes was observed.

Herein, extruded 1.0 wt% genipin-ELP filament was cross-linked in a fume hood and subsequently FTIR scanned in two different locations along the filament length. Deconvolution of the gathered FTIR data showed strongly varying protein secondary structures along the filament length. Significantly more random coils were detected, compared to membranes investigated in *chapter 0* (**Table 5.1**).

**Table 5.1:** Protein secondary structure deconvolution in different locations of a fume hood cross-linked 1.0 wt% genipin-ELP filament showed strong variation across the sample length (Filament location 1 and 2) and significantly more random coils than observed in membrane configurations (Average membranes).

	beta sheets	<b>random coil</b>	beta turns	alpha helix
Filament location 1	7.8	<b>39.2</b>	43.7	9.3
Filament location 2	11.5	<b>29.7</b>	54.1	4.7
Genipin-ELP membranes	25.3	<b>2.97</b>	66.5	5.2

In *chapter 0*, genipin-ELP gels were FTIR scanned daily as they underwent cross-linking. The results suggested that protein secondary structure formation was time dependent. Under consideration of these results, it was herein proposed that the different protein secondary structures that were observed across the filament length stemmed from varying cross-linking periods. Conclusively, regions that required a longer cross-linking period (higher material volume) showed a higher degree of protein secondary structure order, than those that cross-linked faster (lower material volume).

Overall, genipin-ELP filaments showed a lower degree of order, as opposed to membranes of the same formulation. It was suggested that this difference stemmed from the fact that membrane conformations cross-linked over the course of days, whereas filaments achieved full cross-linking within matter of hours and therefore molecular entropy was prematurely lost.

### 5.2.2.2. *Printability assessment – 1.0 wt% genipin 4% ELP gel*

In preliminary experiments, nine days of 0.5 wt% genipin 4% ELP gel incubation led to the synthesis of a gel that was unsuitable for 2D- and 3D-printing purposes. After six days of incubation, uniform filament extrusion was achieved. However, filaments collapsed under their own weight post-printing. Therefore, it was assumed that the ideal incubation time for 500  $\mu\text{l}$  of 0.5 wt% genipin-ELP gel would lay between 7–8 days. As the CLA concentration was increased to 1.0 wt% for concluding studies, it was assumed that material gelation would be accelerated due to an increased number of genipin cross-linking sites available. Consequently, incubation periods of six and seven days were tested.

### *Gel printability assessment after 6 days of material incubation in closed cartridge*

Opposed to the 0.5 wt% genipin-ELP gel that attained a blue colouring after six days of incubation, the herein synthesized gel with a higher CLA concentration was still at an orange stage of colour progression at this incubation time point. As previously stated, genipin has previously been reported to form a blue colour both upon oxidation [183]. It was suggested that colour change progression depended on the synthesised gel volume, wherein larger volumes presumably affected the genipin oxidation kinetics to be decelerated.

After six days of incubation, at an applied pneumatic pressure of 115 kPa, the ideal print speed for the extrusion of uniform genipin-ELP filament was found to lay at 4.6 – 4.7  $\text{mm s}^{-1}$  (**Figure 5.27**).

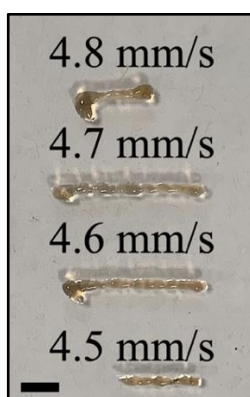


**Figure 5.27:** After six days of gel incubation in a closed cartridge 1.0 wt% genipin-ELP gel showed uniform and continuous filament deposition at an applied pneumatic pressure of 115 kPa and a print speed of 4.6 – 4.7  $\text{mm s}^{-1}$ . Scale bar: 1 cm.

### ***Gel printability assessment after 7 days of material incubation in closed cartridge***

As genipin-ELP gel was contained in a sealed print cartridge, due to higher exposure to the environment, change of colour and thereby gelation at the top of the cartridge occurred faster than at the bottom. The top and bottom of the print cartridge are highlighted in **Figure 5.28**.

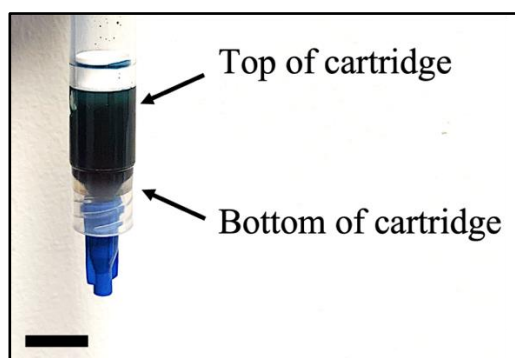


**Figure 5.28:** Depiction of considered top and bottom of print cartridge. Scale bar: 1 cm.

As a result, after seven days of gel incubation, the pneumatic pressure applied had to be altered manually as the plunger moved from the top of the cartridge towards the bottom. To achieve continuous filament extrusion, pneumatic pressure was adjusted at different levels in the cartridge. Thus, pressure varied between 230 kPa (gel from the bottom of the cartridge, less gelation) and 270 kPa (gel from the top of the cartridge, more gelation). At a print speed of  $3 \text{ mm s}^{-1}$ , uniform filament deposition PDMS substrate was achieved.

**5.2.2.3. Print accuracy in two-dimensional 1.0 wt% genipin 4% ELP grid structures**  
Print accuracy of 2D grid structures (10 x 10 mm) under consideration of the previously optimized print parameters was assessed.

### ***Print accuracy assessment after 6 days of material incubation in closed cartridge***

The following images depict genipin-ELP grid structures that were extruded at a print speed of  $4.7 \text{ mm s}^{-1}$  and an applied pneumatic pressure of 115 kPa. In optical microscopy images, dotted lines were used in to highlight where filaments and pores should be located according to the generated STL print file (**Figure 5.29**).

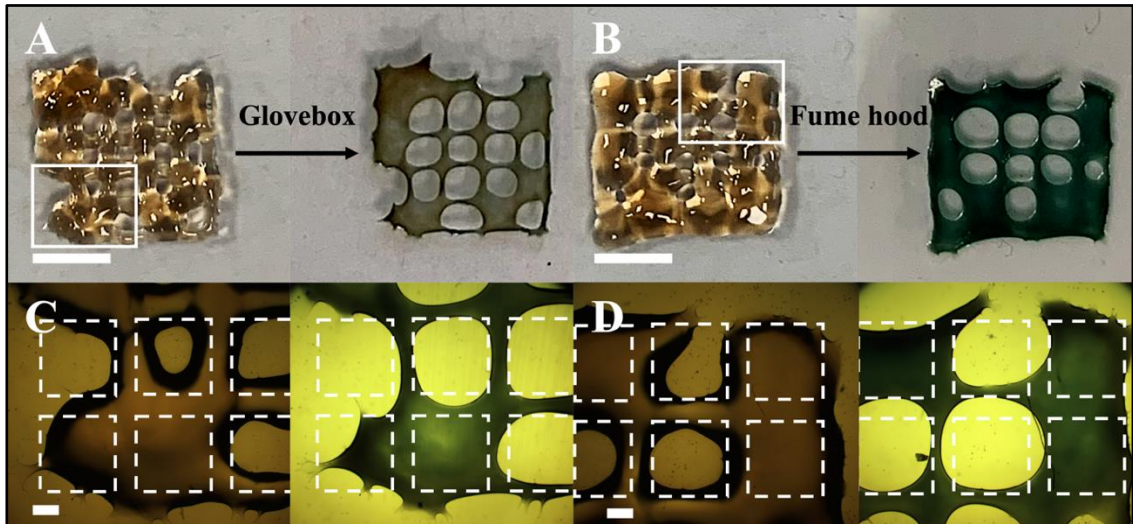


**Figure 5.29:** 2D grid structures extruded after six day of gel incubation in a closed cartridge (1.0 wt% genipin 4% ELP) at a print speed of  $4.7 \text{ mm s}^{-1}$  at 115 kPa. (A) Sample 1 (i) post printing and (ii) after cross-linking in a glovebox. (B) Sample 2 (i) post printing and (ii) after cross-linking in a fume hood. (C, D) Optical microscopy images of Sample 1 and 2 pre- and post-crosslinking with white squares depicting where pores should be located if they were in line with STL print file. The sample contracted towards the filament centres. Perpendicular filaments did not maintain their circular cross-section and collapsed into another instead. Scale bars (A, B): 5 mm; (C, D):  $500 \mu\text{m}$ .

Optical microscopy images taken after material extrusion showed that the filaments mostly collapsed under their own weight, losing their circular cross-sectional geometry (**Figure 5.29C, D**).

Overall, with regards to filament shape maintenance, improved print accuracy was observed post cross-linking in 1.0 wt% genipin-ELP prints (**Figure 5.29A, B**) in comparison to samples fabricated in preliminary studies, wherein 0.5 wt % genipin-ELP prints were fabricated.

This concluded that six days of gel incubation were not sufficient for the extrusion of shapely filaments. Additionally, it was observed that filaments underwent contraction towards their axial centre post cross-linking (**Figure 5.29C, D**). It was assumed that this contraction occurred due to the rearrangement of disordered random coils into ordered coils, occurring during cross-linking. It was proposed that this was more likely to occur in formulations with higher CLA concentrations, as the potential for protein secondary structure formation was assumed to be enhanced through the presence of more available cross-linking sites.

### ***Print accuracy assessment after 7 days of material incubation in closed cartridge***

As previously mentioned, different levels of material gelation across the print cartridge were experienced after seven days of incubation. This caused inconsistent results with regards to print accuracies.

Optical images obtained post printing of genipin-ELP gel that was extruded from the bottom of the cartridge showed an overlap of perpendicularly oriented filaments that were less prone to collapse into another (**Figure 5.30A, C**) than other herein tested formulations.

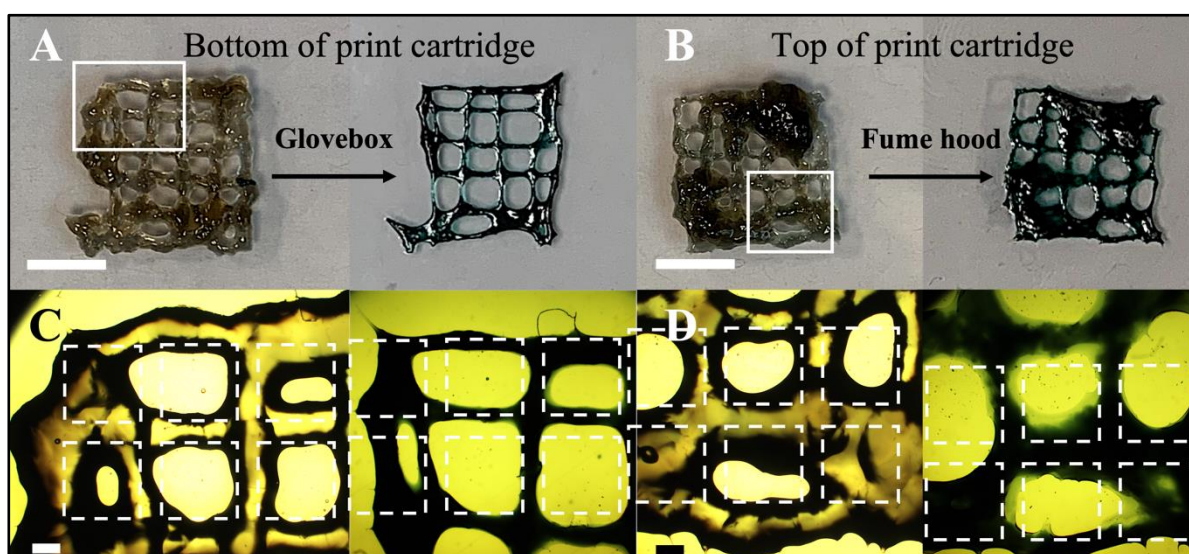


**Figure 5.30:** 2D grid structures extruded after seven day of gel incubation in a closed cartridge (1.0 wt% genipin 4% ELP) at a print speed  $3 \text{ mm s}^{-1}$  and an applied pneumatic pressure of 230 kPa for (A) Sample 1 and 270kPa for (B) Sample 2. (A) Sample 1 (i) post printing and (ii) after glovebox cross-linking. (B) Sample 2 (i) post printing and (ii) after fume hood cross-linking. (C, D) Optical microscopy images of Sample 1 and 2 pre- and post-crosslinking with white squares depicting where pores and filaments should be located according to the generated STL print file. The sample contracted towards the filament centres and changed colour from a light green to a dark blue, due to genipin oxidation. Filament shape maintenance was achieved in Sample 1 post printing. In Sample 2, due to the use of poor-quality, filaments were prone to collapse into another. Scale bars (A, B): 5 mm; (C, D): 500  $\mu\text{m}$ .

Material build-up in various areas was experienced upon material extrusion from the top of the cartridge, causing a visible decrease in print accuracy and closure of several pores (**Figure 5.30B**). This was assumed to occur due to the irregular material gelation behaviour. Filaments extruded from this part of the cartridge collapsed into another when perpendicularly overlapping (**Figure 5.30D**). Furthermore, these filaments showed less contraction towards their axial centre and stronger collapse was observed post cross-linking.

The non-uniform colour in the cross-linked sample suggested an uneven distribution of ELP in solution. It was assumed that gravitational forces dragged the ELP towards the bottom of the cartridge, causing an imbalance in solvent-ELP ratio at the top of the cartridge, negatively impacting print accuracy.

### *Print accuracy quantification*

In this section, printed pores were measured, using the software ImageJ, to evaluate the print accuracy after six and seven days of gel incubation. Under consideration of the printer nozzle diameter and the grid dimensions, 25 pores with a surface area of  $2.56\text{mm}^2$  per pore were considered to translate to 100% print accuracy.

### *Pore count quantification*

The bar chart shown in **Figure 5.31** depicts the count of successfully printed pores in the two-dimensional grid structure after six and seven days of gel incubation. The dotted line represents the desired pore count.

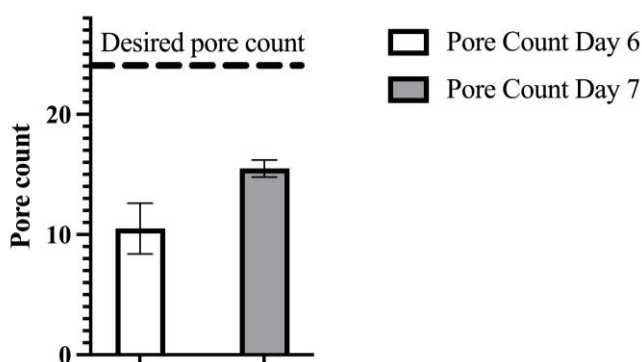


**Figure 5.31:** Bar graph, representing the count of successfully printed pores in 2D grid structures after six and seven days of 1.0 wt% genipin 4% ELP gel incubation in a closed cartridge. After 6 days an average of 10.5 printed pores ( $n = 2$ ) were successfully printed. Improved shape fidelity after seven days of incubation enabled the successful printing of 15.5 pores ( $n = 2$ ). The dotted line represents the desired pore count.

Due to the materials' comparatively low degree of gelation observed after six days of incubation, pores were prone to close, which resulted in 10.5 out of 25 pores printing successfully. The observed increased material gelation after 7 days of incubation enhanced the shape fidelity of extruded filaments, enabling the successful print of 15.5 pores on average.

### *Filament contraction quantification*

In the following, glovebox cross-linked samples were referred to as ‘Sample 1’ and fume hood cross-linked samples were referred to as ‘Sample 2’.

The captured optical images, corresponding pore size measurements and numerical values can be found in Appendix D. Print accuracies calculations considered printed pore sizes. Non-printed pores were disregarded.

### *Print accuracy under consideration of printed pores after 6 days of material incubation in closed cartridge*

In Sample 1 and 2, twelve and nine pores were printed respectively. The bar chart in **Figure 5.32** represents the calculated average pore sizes post printing and post cross-linking. The dotted line represents the ideal pore size ( $2.56 \text{ mm}^2$ ).

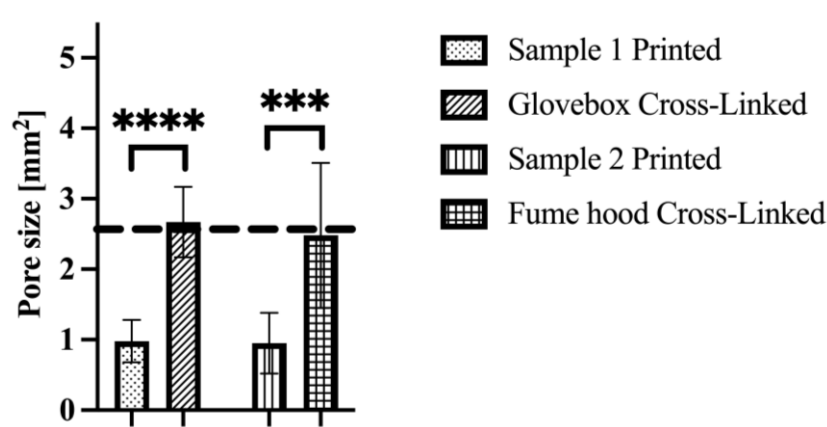


**Figure 5.32:** Bar chart representing pore sizes in 2D grid structures, printed with 1.0 wt% genipin 4% ELP gel after 6 days of gel incubation in a closed cartridge. Printed samples showed a similar average pore size ( $0.98 \text{ mm}^2$  and  $0.95 \text{ mm}^2$ ). Post cross-linking, extruded filaments in both samples underwent statistically significant contraction, leading to an increase in average pore sizes to  $2.67 \text{ mm}^2$  (glovebox cross-linked) and  $2.48 \text{ mm}^2$  (fume hood cross-linked) respectively. The dotted line represents the ideal pore size ( $2.56 \text{ mm}^2$ ) that considered the grid dimensions and nozzle diameter.

It was shown that extruded filaments in Sample 1 (glovebox cross-linked) underwent statistically significant contraction ( $P \leq 0.0001$ , \*\*\*\*), causing pore sizes to increase from  $0.98$  to  $2.67 \text{ mm}^2$  on average. Filaments in Sample 2 also experienced statistically significant contraction ( $P = 0.008$ , \*\*\*), causing an average pore size increase to  $0.98$  to  $2.48 \text{ mm}^2$ .

Overall, after 6 days of incubation, an average accuracy of 37.7% with respect to pore size post printing was observed. Due to filament contraction experienced post cross-

linking, the pore size accuracy increased to 104.17% and 96.96% for Sample 1 and 2 respectively.

The cross-linking environment did not seemingly affect filament contraction.

***Print accuracy under consideration of printed pores after 7 days of material incubation in closed cartridge***

After 7 days of gel incubation, printed pores were found to be less prone to close-up. As a result, 16 and 15 pores were printed in Sample 1 and Sample 2 respectively. In addition, filament contraction upon cross-linking, caused the pore count in Sample 2 to be increased by one pore, concluding 16 pores. The bar chart in **Figure 5.33** represents the calculated average pore sizes post printing and post cross-linking.

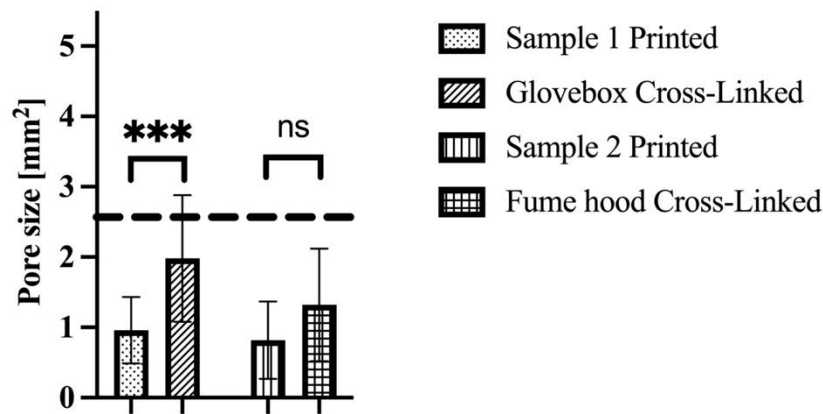


**Figure 5.33:** Bar chart representing pore sizes in 2D grid structures, printed with 1.0 wt% genipin 4% ELP gel after seven days of gel incubation in closed cartridge. Printed samples showed a similar average pore size (0.96 mm<sup>2</sup> and 0.82 mm<sup>2</sup>). Post glovebox cross-linking in a glovebox, filaments in Sample 1 showed statistically significant contraction, leading to an average pore size of 1.98 mm<sup>2</sup>. Due to poor bio gel quality, pore sizes in the fume hood cross-linked sample showed less contraction, with average pore sizes only reaching 1.32 mm<sup>2</sup>. The dotted line represents the ideal pore size (2.56 mm<sup>2</sup>) that considered the grid dimensions and nozzle diameter.

Post cross-linking in a glovebox, filaments in Sample 1 underwent statistically significant contraction ( $P = 0.004$ , \*\*\*), which on average caused pore sizes to increase from 0.96 mm<sup>2</sup> to 1.98 mm<sup>2</sup>. This concludes a print accuracy of 37.67% post printing and 77.29% post cross-linking.

Sample 2 showed a print accuracy of 32.2% post printing (average pore size = 0.82 mm<sup>2</sup>) and 51.42% (average pore size = 1.32 mm<sup>2</sup>) post fume hood cross-linking, concluding statistically insignificant ( $P = 0.0533$ ) filament contraction. Overall, this sample

displayed the lowest overall print accuracy. As previously mentioned, Sample 2 was fabricated with poor quality gel material that was situated at the top of the print cartridge throughout the incubation period, resulting in gel properties unfavourable for printing purposes. Furthermore, the sample colour post cross-linking indicated a predominant presence of solvent, which was assumed to negatively impact linear filament contraction upon cross-linking.

#### *Pore size increase – Summary*

The bar chart in **Figure 5.34** represents pore size increase post cross-linking in different environments (glovebox and fume hood) after six and seven days of gel incubation in the print cartridge.

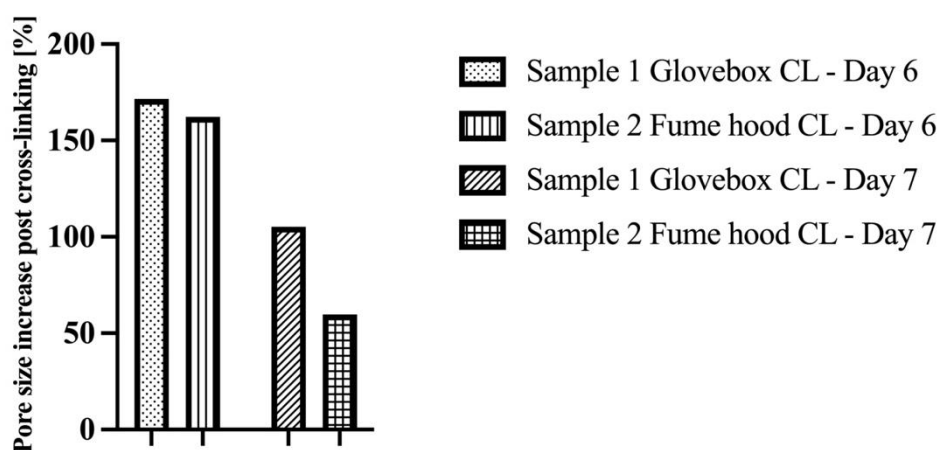


**Figure 5.34:** Bar chart, showing how incubation time affected sample contraction post cross-linking. Results showed that filament contraction decreased as gel incubation in a closed cartridge time was extended, which led to decreased percentual pores increase less post cross-linking. Furthermore, the cross-linking environments was not found to impact filament contraction.

Results showed that sample contraction decreased as genipin-ELP gel incubation was extended, which led to the average pore sizes increasing less post cross-linking. This was due to progressive material gelation over time, leading to increased shape fidelity in extruded filaments which conclusively reduced filament contraction capacity.

Furthermore, the contraction data gathered after six days of genipin-ELP gel incubation supported the previously stated hypothesis, stating that the choice of cross-linking environment did not significantly affect filament contraction. On incubation day 7, in Sample 2, the observed decrease in average filament contraction was caused by the utilization of poor-quality gel, which impacted print accuracy.

### Pore size accuracy - Summary

The bar chart in **Figure 5.35** summarizes the print accuracy of pore sizes post-printing and post cross-linking after six and seven days of genipin-ELP gel incubation.

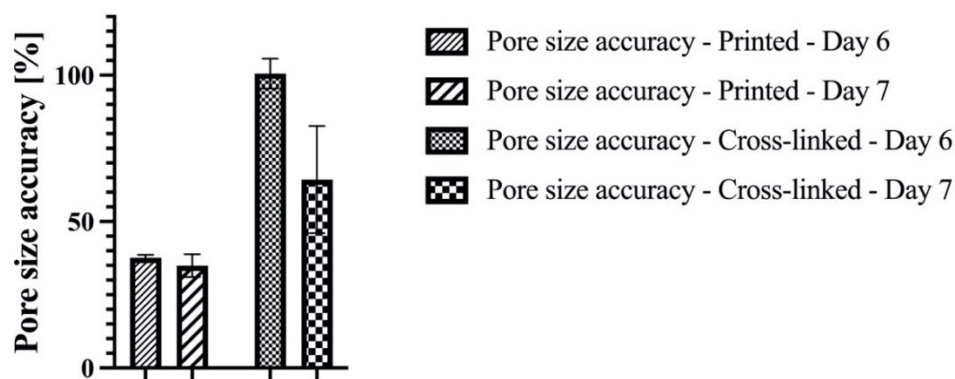


**Figure 5.35:** Bar chart summarizing pore size accuracy post printing and post cross-linking after different gel (1.0 wt% genipin 4% ELP) incubation periods (six days vs. seven days), showing that pore size accuracy post printing remained constant, whilst pore size accuracy post cross-linking decreases due to a decrease in filament contraction capacity.

Results showed that incubation time did not affect the average pore size accuracy post extrusion. However, these calculations do not consider the pore count, which was increased by 20% on day 7 of genipin-ELP gel incubation in a print cartridge.

Pore size accuracy post cross-linking averaged at 100.6% in prints extruded after 6 days of gel incubation. The decrease in filament contraction capacity led to a lower post cross-linking pore size accuracy (64.4%) in prints extruded after 7 days of gel containment. However, as previously mentioned, shape fidelity and pore count were significantly increased after seven days of genipin-ELP gel incubation.

#### 5.2.2.4. Assessment of biomineralization ability in 1.0 wt% genipin 4% ELP prints

1.0 wt% genipin 4% ELP prints were immersed in biomineralization solution for 10 days and thereafter imaged *via* SEM.

The utilization of 2mM biomineralization solution bears a risk of precipitation in immersed samples, resulting in mineral accretions on the sample surface. This can physically impede ion diffusion into the sample and thereby hinder the formation of biomineralized structures.

Precipitation occurred in samples printed after six days of genipin-ELP gel incubation, as well as in a fume hood cross-linked sample printed after seven days of genipin-ELP

gel incubation. **Figure 5.36** shows mineral accretions on Sample 2 (fume hood cross-linked), that was printed on incubation day 6.

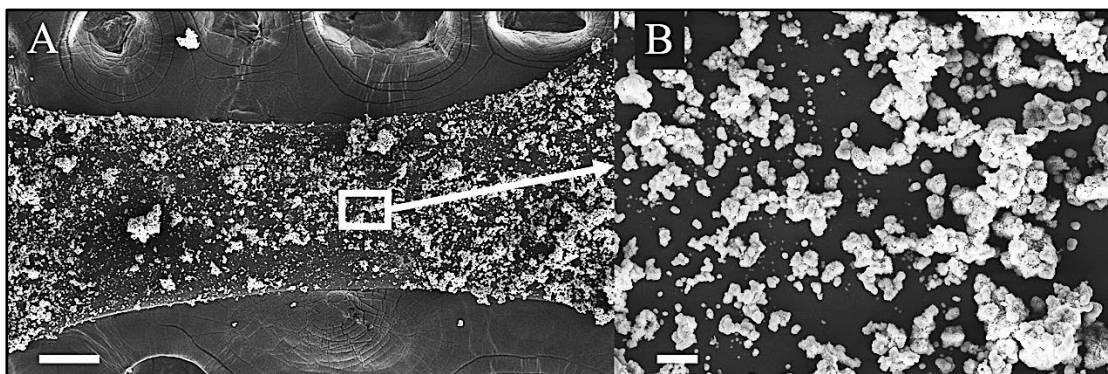


**Figure 5.36:** SEM image of fume hood cross-linked 1.0 wt% genipin 4% ELP print sample (six days of gel incubation in a closed cartridge), showing mineral accretions that formed in super saturated biomineralization solution and deposited onto the sample surface, impeding ion diffusion into the sample and thereby avoiding biomineralization. Scale bars: (A) 100  $\mu\text{m}$ , (B) 1  $\mu\text{m}$ .

It was assumed that precipitation was more likely to occur in 1.0 wt% genipin 4% ELP formulation than in 0.5 wt% genipin formulations that were tested in preliminary studies, as an increase in cross-linker was assumed to cause a more densely bound molecular network, which may hinder ion diffusion.

**Figure 5.37** shows that biomineralization was observed in a glovebox cross-linked sample that was fabricated after 7 days of gel incubation.

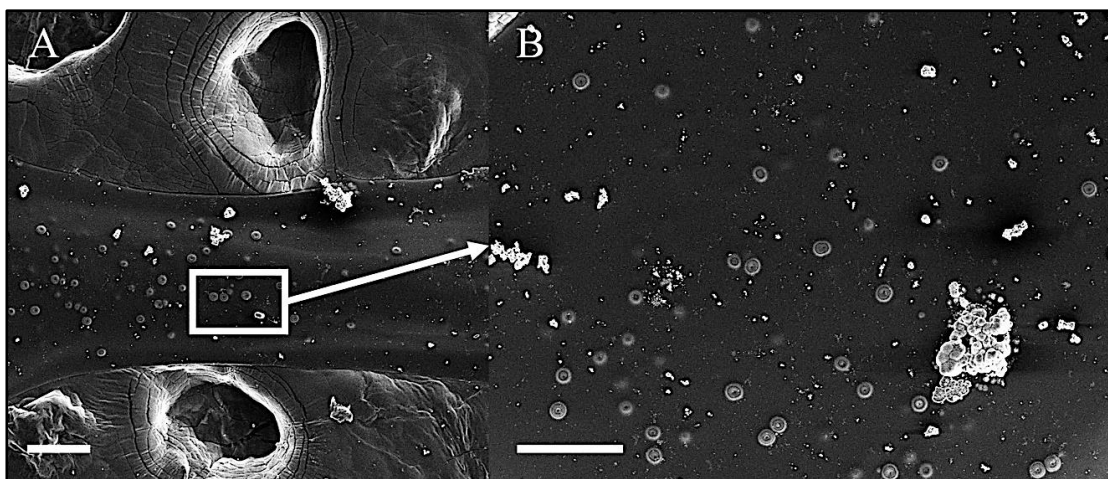


**Figure 5.37:** SEM image of glovebox cross-linked 1.0 wt% genipin 4% ELP print sample (seven days of gel incubation in a closed cartridge). (A) Filament three-dimensionality was maintained post cross-linking. (B) Emergence of biomineralized structures, which started growing in the sample bulk and rose to the surface was observed. Scale bars: 100  $\mu\text{m}$ .

'Bubbles' on the surface suggested that, like in genipin-ELP membranes, mineralized structures emerged in the sample bulk and rose to the surface as mineralization was continued (**Figure 5.37B**), remaining covered by unmineralized matter. **Figure 5.37A** suggests that the samples three-dimensionality was maintained post cross-linking.

#### 5.2.2.5. 3D-printing of 1.0 wt% genipin 4% ELP grid structures

As 1.0 wt% genipin 4% ELP gel showed comparatively high filament shape fidelity after 7 days of incubation, this formulation was used to attempt the fabrication of 3D samples. **Figure 5.38** show images of a 4-layered 10 x 10 mm grid scaffold.

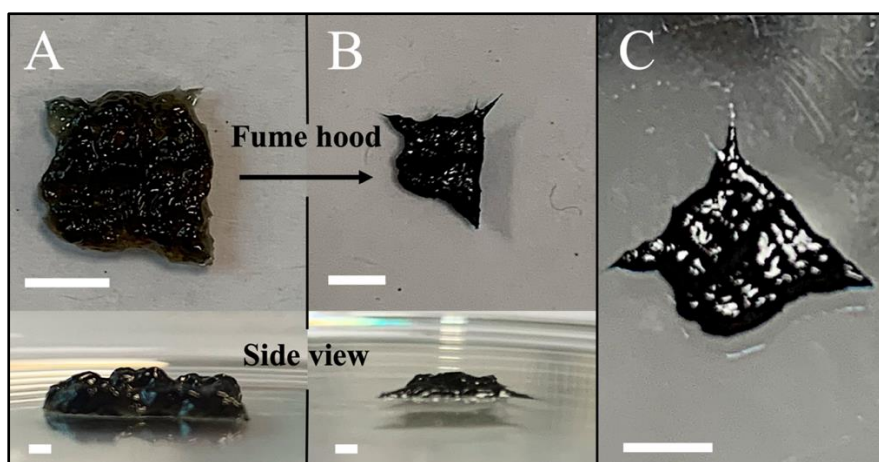


**Figure 5.38:** Fabrication of a four-layered 10 x10 mm grid scaffold showing (A) collapse of all pores as filaments were deposited on top of each other. (B) Fume hood cross-linking induced sample contraction towards the centre. Side views showed, that despite sample collapse, the sample did not fully collapse into a membrane configuration. (C) Upon close observation of the cross-linked sample, intended pores could be vaguely determined. Scale bars (A, B, C): 5 mm; (side view): 1 mm

The genipin-ELP gel was extruded at 230 kPa and a print speed of  $3\frac{mm}{s}$ .

Due to the sample geometry and the choice of a low surface roughness PDMS substrate, extruded filaments could not be reliably deposited in a layer-by-layer fashion, causing closure of all pores by the time the fourth layer was printed (**Figure 5.38A**). The lack of pores caused the sample to contract towards its centre upon fume hood cross-linking (**Figure 5.38B**). Side view images showed that the sample shrunk in z-direction, without however fully collapsing into a 2D membrane. Upon close observation of the cross-linked sample, locations where pores should be present could vaguely be determined (**Figure 5.38C**).

### 5.3. Summary

In this chapter, PMDI- and genipin-ELP gels were tested towards their suitability for ME printing.

Material transfer methods for both established formulations were developed which account for the gelation kinetics observed in the respective materials. In preliminary experiments, immediately gelling PMDI-ELP gels were used to establish whether biomineralization could be achieved in extruded gel filaments. It was shown that cross-linking in an open or partially sealed environment was required to maintain the shape of layered constructs in (biomineralization) solution. Proof of concept was achieved by providing evidence of the presence of biomineralized structures at the surface and the bulk of extruded PMDI-ELP filaments.

Due to the tuneability of gelation in genipin-ELP gels, this formulation was selected in concluding experiments. The cross-linker concentration as well as the gel incubation time were optimized to achieve the extrusion of shapely filaments. The fabrication of 2D grid structures was achieved. In the optimized gel formulation, the print accuracy of such structures was quantified by investigating grid pore sizes. It was observed that cross-linking induced filament contraction, causing the pore sizes in the grid to increase by up to 105%. The choice of cross-linking environment was found to not significantly affect filament contraction. Due to the generation of more nucleic pores, biomineralization was found to be improved through glovebox cross-linking, compared to fume hood cross-linking.

The fabrication of 3D scaffolds was unsuccessful. It was established that the use of a low surface roughness substrate, such as PDMS, was unsuitable for the generated scaffold dimensions.

## 6. Conclusion and Future Work

The aim of this thesis was to develop a novel polypeptide-based material that was suitable for material extrusion manufacturing, whilst displaying the integral ability to undergo hierarchically structured biomineralization. The herein developed formulations were inspired by a previously reported study, wherein polypeptide-based membranes were synthesized which could undergo stimuli triggered fluorapatite biomineralization. The membranes were shown to exhibit the same strength as bone and dentine. Thereby, a new approach for bone regeneration therapy was proposed.

In this thesis, two novel formulations were developed, in which the cross-linking agents (i) polymeric diphenylmethane diisocyanate (PMDI) and (ii) genipin, were shown to enable the synthesis of ELP-based membranes and gels.

Whilst immediate formation of a gel could be achieved by incorporating PMDI in the formulation, genipin-ELP solutions required incubation in a sealed container over the course of days to form a homogenous gel. The ability to synthesise ELP based gels was novel to this field and allowed the investigation of protein secondary structure assembly over time. FTIR analysis of ELP-based gels revealed that contained gels has an underlying protein secondary structure that was mainly disordered. It was observed that protein secondary structure could only be achieved if the sample was post processed in a way that allowed it to solidify, i.e., by allowing cross-linking in an open or partially closed container, or by immersing the sample in water. It was established that under these conditions, protein secondary structure formation was a time dependent process and the materials capacity to undergo supramolecular self-assembly was exhausted once the samples had solidified. Furthermore, it was shown that solidification acceleration, e.g., through cross-linking in a low humidity environment, lead to a compromised order of the underlying protein secondary structure of solidified samples.

Overall, it was shown that ordered protein secondary structures formed sequentially. Alpha-helices were found to form first. Thereafter, the formation sequence was be determined by the underlying cross-linking mechanism, wherein intermolecular cross-linking between the ELP's primary amine groups and the CLA formed beta-turns before beta-sheets were formed (genipin-ELP formulations) and intramolecular cross-linking formed beta-sheets before beta-turns (PMDI-ELP formulations).

Compared to the previously published membrane formulation, wherein HDI was used as a cross-linking agent, protein secondary structures with a higher molecular order were achieved in the newly developed ELP membrane formulations.

Furthermore, it was shown that stimuli triggered FAp biomineralization in both newly established formulations could be achieved. Especially in the sample bulk regions, biomineralization ability was improved, compared to the previously reported membrane configuration.

Whilst the previous study suggested that the protein secondary structure configuration guided the morphological appearance of biomineralized structures, it was herein suggested that the incorporation of varying cross-linker concentrations had an impact on the mechanical properties of the fabricated ELP-based samples. It has been suggested that in the presented novel formulations, a more tightly bound cross-linked network may impede water absorption and hence ion diffusion into the sample bulk. Conclusively, a less tightly interconnected molecular network was proposed to enhance water absorption and thereby ion diffusion. Furthermore, it was proposed that a less tightly bound cross-linking network is more likely to allow organic, unmineralized matter to yield as biomineralized structures emerge. This property was suggested to act in favour of the process by allowing more extensive biomineralization. It is recommended to conduct dynamic mechanical analysis (DMA) on membrane configurations to confirm the correlation between the samples biomineralization capability and its viscoelastic properties. This mechanical analysis method and its capabilities were elaborated on in *chapter 1.2.3*. Understanding whether increased viscoelasticity can enhance biomineralization can serve as an additional optimization tool.

Whilst spherulites of organic nature were suggested to give rise to biomineralized structures in drop cased HDI-ELP membranes, based on SEM images, it was suggested that nano- and microscopic pores, which formed during the sample cross-linking process, acted as nucleic sites in the growth of biomineralized structures in herein established formulations. Pore formation was found to be promoted upon sample cross-linking in a low humidity glovebox environment. For future work, it is recommended to develop methods that enhance pore formation during cross-linking to further enhance FAp biomineralization.

In the previously reported HDI-ELP formulation, the fabrication of solid samples relied on overnight drying in a low-humidity glovebox environment. This fabrication method and its inherent cross-linking kinetics were not suitable for the fabrication of three-dimensional structures. In contrast to that, ELP-based formulations developed in this project could be processed into drop casted membranes, but additionally, the platform was extended to allow automated gel extrusion *via* ME printing and the ability to mineralize extruded ELP filaments was confirmed.

Herein, initial experiments used readily synthesized PMDI-ELP gels to provide a proof of concept towards the biomineralization ability of extruded filaments. However, due to the CLAs' hygroscopicity, reproducibility of the method may be affected by environmental factors (e.g., rainy weather causing an increase in humidity and therefore altering the CLAs' reactivity). Furthermore, PMDI is highly toxic in an uncross-linked state, making it an undesirable for biomedical applications. Therefore, this formulation merely served as a proof of concept and shall not further be considered in future work. Nonetheless, since the formulation in this work was inspired by a formulation which was only suitable for the synthesis of membranes, the achievement of the extrusion of shapely filaments which can undergo biomineralization represents a major step towards the aim of the development of a novel route for bone regeneration therapy. The ability to integrate the manufacturing process into 3D printing is opening the opportunity to design biomineralizing three-dimensional structures which may be able to function as bone replacement implants. In comparison, the use of two-dimensional membranes as they were previously reported, is majorly restricted in the application field of interest.

The ability to tune the gelation of genipin-ELP gels by employing different incubation times enabled the fabrication of extruded filaments. Using this formulation, the fabrication of 2D grid structures was achieved *via* automated material extrusion. It was proposed that the self-assembly from random into ordered protein secondary structure coils caused extruded filaments to contract towards their centre, which caused pore sizes to significantly increase post cross-linking.

It was established that the pressure required to induce extrusion had to be increased as the material incubation time was extended. These findings suggest that the yield point of the formulation changed over time. In *chapter 2.2.7*, it has been

established which rheological properties are required in a formulation to achieve satisfactory print quality and material behaviour throughout the manufacturing process.

For future work the rheological properties of the material shall be investigated to gain a better understanding of its behaviour upon extrusion. Thereafter means shall be found to enhance the formulation to achieve the desired rheological properties which can enable successful printing of three-dimensional structures. Additionally, gaining an understanding of the viscosity and viscoelastic properties may open the opportunity to employ the use of a precision nozzle and thereby enable the fabrication of constructs with an enhanced print resolution. Furthermore, it is proposed to fabricate a sample size of at least 5 samples to thoroughly assess dimensional shrinkage. By understanding the material behaviour, print files can be generated under consideration of the percentual contraction and thereby improve shape accuracy.

3D-printing of genipin-ELP constructs was not only impeded through the materials' rheological properties, but it was additionally suggested that the choice of a substrate with a low surface roughness caused traction of the filaments during the printing process. It is therefore recommended to introduce a hydrophobic, high surface roughness substrate for future experiments to enable reliable layer-by-layer depositions of filaments, which can be peeled off post cross-linking in a non-destructive manner.

In this work, the biocompatibility of developed materials and synthesized unmineralized and mineralized constructs was not assessed. However, the cross-linking agent genipin was selected due to its reported biocompatibility. Therefore, the genipini-ELP formulation is considered promising with regards to its biocompatibility. It is however acknowledged that the organic solvents used for this study are not biocompatible. However, the biomineralization process which requires sample immersion in biomineralization solution, is assumed to wash out solvent remainders. For future work, it is therefore recommended to employ the extract biocompatibility testing method, in which the material of interest is added to the cell culture medium, and incubated at specific conditions, allowing the release of soluble components. Subsequently, the cell culture medium with the released components is added to cultured cells to evaluate the cytotoxicity. This method was further elaborated on in *chapter 1.2.2*. It is recommended to conduct this experiment, using both non biomineralized as well as biomineralized samples to understand if and how sample

immersion in biomineralization solution impacts the cytotoxicity outcome. Additionally, direct contact methods, such as live dead assay and presto blue assay shall be employed to provide complementary data on the formulation's biocompatibility performance. However, the blue colouring of genipin samples can interfere with presto blue assays as the fluorescence of the blue samples can interfere with the blue redox indicator. Hence, live dead assay is suggested as a preferred method. Furthermore, it shall be assessed *via* osteogenesis differentiation assays, whether osteogenesis can occur in biomineralized scaffold constructs.

Lastly, it is recommended to employ mechanical property tests on biomineralized membranes as well and printed structures to determine whether their mechanical properties are compatible with those of bone. Herein, nanoindentation is recommended as a method to assess the mechanical properties of biomineralized membranes. Not only is this method suitable for membrane samples, but also this method was used in the previously reported work wherein HDI-ELP membranes were tested towards their mechanical properties. Hence, a comparison between the newly developed formulations and the previously proposed method can be drawn. Once three-dimensional ELP based constructs can be manufactured, it is recommended to conduct compression tests on the samples to understand whether the mechanical properties of such constructs are in line of biomineralized structures tested in a membrane configuration and whether they match the mechanical properties of bone. As established in *chapter 1.1*, '*the mechanical properties in cancellous bone tissue are dependent on the arrangement of the individual trabeculae and the resulting porosity [1]*'. Hence, it shall furthermore be assessed which bone tissue type biomineralized ELP-based constructs are compatible with. The recommended mechanical analysis methods were further elaborated on in *chapter 1.2.3*.

## v. References

- [1] H. Qu, H. Fu, Z. Han, and Y. Sun, "Biomaterials for bone tissue engineering scaffolds: A review," *RSC Adv.*, vol. 9, no. 45, pp. 26252–26262, 2019.
- [2] A. G. Abdelaziz *et al.*, "A Review of 3D Polymeric Scaffolds for Bone Tissue Engineering: Principles, Fabrication Techniques, Immunomodulatory Roles, and Challenges," *Bioengineering*, vol. 10, no. 2, 2023.
- [3] M. J. Glimcher, "Chapter 2 - The Nature of the Mineral Phase in Bone: Biological and Clinical Implications," L. V. Avioli and S. M. B. T.-M. B. D. and C. R. D. (Third E. Krane, Eds. San Diego: Academic Press, 1998, pp. 23-52e.
- [4] A. J. Sophia Fox, A. Bedi, and S. A. Rodeo, "The basic science of articular cartilage: Structure, composition, and function," *Sports Health*, vol. 1, no. 6, pp. 461–468, 2009.
- [5] K. Alvarez and H. Nakajima, "Metallic scaffolds for bone regeneration," *Materials (Basel)*, vol. 2, no. 3, pp. 790–832, 2009.
- [6] X. Lin, S. Patil, Y.-G. Gao, and A. Qian, "The Bone Extracellular Matrix in Bone Formation and Regeneration.," *Front. Pharmacol.*, vol. 11, p. 757, 2020.
- [7] R. Naomi, P. M. Ridzuan, and H. Bahari, "Current insights into collagen type i," *Polymers (Basel)*, vol. 13, no. 16, pp. 1–19, 2021.
- [8] Q. Daniela, B. Federica, and F. D. Lofaro, *The biology of vascular calcification*, 1st ed., vol. 354. Elsevier Inc., 2020.
- [9] A. Singh, G. Gill, H. Kaur, M. Amhmed, and H. Jakhu, "Role of osteopontin in bone remodeling and orthodontic tooth movement: a review.," *Prog. Orthod.*, vol. 19, no. 1, p. 18, Jun. 2018.
- [10] L. Di Medio and M. L. Brandi, *Advances in bone turnover markers*, 1st ed., vol. 105. Elsevier Inc., 2021.
- [11] F. Lamoureux, M. Baud'huin, L. Duplomb, D. Heymann, and F. R dini, "Proteoglycans: Key partners in bone cell biology," *BioEssays*, vol. 29, no. 8, pp. 758–771, 2007.
- [12] R. Marcus, D. Feldman, D. W. Dempster, M. Luckey, and J. A. B. T.-O. (Fourth E. Cauley, Eds., "Osteoporosis," San Diego: Academic Press, 2013, p. iii.
- [13] L. F. Bonewald and G. R. Mundy, "Role of transforming growth factor-beta in bone remodeling.," *Clin. Orthop. Relat. Res.*, no. 250, pp. 261–276, Jan. 1990.
- [14] S. Kasagi and W. Chen, "TGF-beta1 on osteoimmunology and the bone component cells," *Cell Biosci.*, vol. 3, no. 1, pp. 1–7, 2013.
- [15] M. Kawai and C. J. Rosen, "The insulin-like growth factor system in bone: basic and clinical implications.," *Endocrinol. Metab. Clin. North Am.*, vol. 41, no. 2, pp. 323–33, vi, Jun. 2012.
- [16] C. J. Rosen and S. Yakar, "Chapter 42 - Growth hormone, insulin-like growth factors, and IGF binding proteins," J. P. Bilezikian, T. J. Martin, T. L. Clemens, and C. J. B. T.-P. of B. B. (Fourth E. Rosen, Eds. Academic Press, 2020, pp. 985–1015.
- [17] K. R. Garrison *et al.*, "Bone morphogenetic protein (BMP) for fracture healing in adults.," *Cochrane database Syst. Rev.*, vol. 2010, no. 6, p. CD006950, Jun. 2010.
- [18] A. Nahian and D. D. Davis, "Histology, Osteoprogenitor Cells.," Treasure Island (FL), 2023.
- [19] J. Y. Rho, L. Kuhn-Spearing, and P. Zioupos, "Mechanical properties and the hierarchical structure of bone.," *Med. Eng. Phys.*, vol. 20, no. 2, pp. 92–102, Mar. 1998.
- [20] A. M. Wu *et al.*, "Global, regional, and national burden of bone fractures in 204 countries and territories, 1990–2019: a systematic analysis from the Global Burden of Disease Study 2019," *Lancet Heal. Longev.*, vol. 2, no. 9, pp. e580–e592, 2021.
- [21] E. Guerado and E. Caso, "Challenges of bone tissue engineering in orthopaedic patients.," *World journal of orthopedics*, vol. 8, no. 2. United States, pp. 87–98, Feb-2017.
- [22] G. Fernandez de Grado *et al.*, "Bone substitutes: a review of their characteristics, clinical use, and perspectives for large bone defects management," *J. Tissue Eng.*, vol. 9, no. June, 2018.
- [23] L. S. Pryor *et al.*, "Review of Bone Substitutes," *Craniofac. Trauma Reconstr.*, vol. 2, no. 3–4, pp. 151–160, 2009.
- [24] Q. He, J. Johnston, J. Zeitlinger, K. City, and K. City, "骨组织工程构造中的血管形成," vol. 33, no. 4, pp. 395–401, 20155.
- [25] J. Huang, J. Pan, M. Xu, and S. Xu, "Successful open reduction and internal fixation for displaced femoral fracture in a patient with osteopetrosis," pp. 1–6.
- [26] Y. K. C. K. B. Nalini, J. Menon, D. K. Patro, and B. H. Banerji, "Calcium Sulfate as Bone Graft Substitute in the Treatment of Osseous Bone Defects , A Prospective Study," vol. 7, no. 12, pp. 2926–2928, 2013.
- [27] R. Masaeli, K. Zandsalimi, M. Rasoulianboroujeni, and L. Tayebi, "Challenges in Three-

- Dimensional Printing of Bone Substitutes,” *Tissue Eng. - Part B Rev.*, vol. 25, no. 5, pp. 387–397, 2019.
- [28] W. Wang and K. W. K. Yeung, “Bioactive Materials Bone grafts and biomaterials substitutes for bone defect repair : A review,” *Bioact. Mater.*, vol. 2, no. 4, pp. 224–247, 2017.
- [29] A. E. Eldeeb, S. Salah, and N. A. Elkasaby, “Biomaterials for Tissue Engineering Applications and Current Updates in the Field: A Comprehensive Review,” *AAPS PharmSciTech*, vol. 23, no. 7, 2022.
- [30] M. Vallet-Regí, “Evolution of Biomaterials,” *Front. Mater.*, vol. 9, no. March, pp. 1–5, 2022.
- [31] K. S. Ødegaard, J. Torgersen, and C. W. Elverum, “Structural and biomedical properties of common additively manufactured biomaterials: A concise review,” *Metals (Basel)*, vol. 10, no. 12, pp. 1–23, 2020.
- [32] C. Gao, S. Peng, P. Feng, and C. Shuai, “Bone biomaterials and interactions with stem cells,” *Bone Res.*, vol. 5, no. May, pp. 1–33, 2017.
- [33] I. Sheikh and Y. Dahman, “Chapter 2 - Applications of nanobiomaterials in hard tissue engineering,” A. M. B. T.-N. in H. T. E. Grumezescu, Ed. William Andrew Publishing, 2016, pp. 33–62.
- [34] C. A. Landes *et al.*, “Biology of implant osseointegration,” *Univ. Connect. Heal. Cent.*, vol. 103, no. 2, pp. e22-5, 2011.
- [35] L. Gritsch *et al.*, “Combining bioresorbable polyesters and bioactive glasses: Orthopedic applications of composite implants and bone tissue engineering scaffolds,” *Appl. Mater. Today*, vol. 22, 2021.
- [36] T. M. De Witte, L. E. Fratila-Apachitei, A. A. Zadpoor, and N. A. Peppas, “Bone tissue engineering via growth factor delivery: From scaffolds to complex matrices,” *Regen. Biomater.*, vol. 5, no. 4, pp. 197–211, 2018.
- [37] G. Sumithra, R. N. Reddy, G. Dheeraj Kumar, S. Ojha, G. Jayachandra, and G. Raghavendra, “Review on composite classification, manufacturing, and applications,” *Mater. Today Proc.*, 2023.
- [38] A. R. Boccaccini and J. J. Blaker, “Bioactive composite materials for tissue engineering scaffolds,” *Expert Rev. Med. Devices*, vol. 2, no. 3, pp. 303–317, May 2005.
- [39] J. A. Roether, J. E. Gough, A. R. Boccaccini, L. L. Hench, V. Maquet, and R. Jérôme, “Novel bioresorbable and bioactive composites based on bioactive glass and polylactide foams for bone tissue engineering,” *J. Mater. Sci. Mater. Med.*, vol. 13, no. 12, pp. 1207–1214, 2002.
- [40] W. B. Mattes, “In vitro to in vivo translation,” *Curr. Opin. Toxicol.*, vol. 23–24, pp. 114–118, 2020.
- [41] G. Thrivikraman, G. Madras, and B. Basu, “In vitro/In vivo assessment and mechanisms of toxicity of bioceramic materials and its wear particulates,” *RSC Adv.*, vol. 4, no. 25, pp. 12763–12781, 2014.
- [42] S. Maity and A. Sarkar, “4 - Monitoring fibrous capsule formation,” R. J. B. T.-M. and E. of B. and their P. I. V. Narayan, Ed. Woodhead Publishing, 2017, pp. 69–80.
- [43] M. N. Egorikhina *et al.*, “Biocompatibility Study of Hydrogel Biopolymer Scaffold with Encapsulated Mesenchymal Stem Cells,” *Polymers (Basel)*, vol. 15, no. 6, 2023.
- [44] W. Li, J. Zhou, and Y. Xu, “Study of the in vitro cytotoxicity testing of medical devices,” *Biomed. reports*, vol. 3, no. 5, pp. 617–620, Sep. 2015.
- [45] C. Eilenberger, S. R. A. Kratz, M. Rothbauer, E. K. Ehmoser, P. Ertl, and S. Küpcü, “Optimized alamarBlue assay protocol for drug dose-response determination of 3D tumor spheroids,” *MethodsX*, vol. 5, pp. 781–787, 2018.
- [46] J. Wang, B. Yuan, R. Yin, and H. Zhang, “Inflammation Responses to Bone Scaffolds under Mechanical Stimuli in Bone Regeneration,” *J. Funct. Biomater.*, vol. 14, no. 3, 2023.
- [47] S. Sakamoto *et al.*, “Enzyme-linked immunosorbent assay for the quantitative/qualitative analysis of plant secondary metabolites,” *J. Nat. Med.*, vol. 72, no. 1, pp. 32–42, 2018.
- [48] A. Kabiraj, J. Gupta, T. Khaitan, and P. T. Bhattacharya, “Principle and Techniques of Immunohistochemistry – a Review,” *Int J Biol Med Res*, vol. 6, no. 3, pp. 5204–5210, 2015.
- [49] S. Gretzinger, N. Beckert, A. Gleadall, C. Lee-Thedieck, and J. Hubbuch, “3D bioprinting – Flow cytometry as analytical strategy for 3D cell structures,” *Bioprinting*, vol. 11, no. March, pp. 1–11, 2018.
- [50] S. M. Manohar, P. Shah, and A. Nair, “Flow cytometry: principles, applications and recent advances,” *Bioanalysis*, vol. 13, no. 3, pp. 181–198, Feb. 2021.
- [51] B. Li, B. D. Hesar, Y. Zhao, and L. Ding, “Design and additive manufacturing of porous titanium scaffolds for optimum cell viability in bone tissue engineering,” *Proc. Inst. Mech. Eng. Part B J. Eng. Manuf.*, 2020.

- [52] A. M. Petrucci, K. Vahedi, M. Rahmani, and M. M. Petrucci, "Numerical and analytical simulation of ballistic projectile penetration due to high velocity impact on ceramic target," *Frat. ed Integrita Strutt.*, vol. 14, no. 54, pp. 226–248, 2020.
- [53] N. Saba, M. Jawaid, and M. T. H. Sultan, "1 - An overview of mechanical and physical testing of composite materials," in *Woodhead Publishing Series in Composites Science and Engineering*, M. Jawaid, M. Thariq, and N. B. T.-M. and P. T. of B. Saba Fibre-Reinforced Composites and Hybrid Composites, Eds. Woodhead Publishing, 2019, pp. 1–12.
- [54] C. J. G. Plummer, *Testing of Polymeric Materials*, vol. 1. Elsevier, 2014.
- [55] A. Dehghani and F. Aslani, "6 - Nano-modification of the rheological properties of cementitious composites," in *Woodhead Publishing Series in Civil and Structural Engineering*, M. Şahmaran, F. Shaikh, and G. B. T.-R. A. in N.-T. M.-F. C. C. Yıldırım, Eds. Woodhead Publishing, 2022, pp. 209–249.
- [56] L. Adrian Wei Hong, Teo, Gik Hong, Yeap, and Wei Jie, "Nanoindentation System for Material Properties Identification," *Int. J. Electr. Electron. Syst. Res. Spec. Issue Innov. Malaysia Des. Conf.*, pp. 16–22, 2015.
- [57] M. Bianchi *et al.*, "Nanomechanical mapping of bone tissue regenerated by magnetic scaffolds.," *J. Mater. Sci. Mater. Med.*, vol. 26, no. 1, p. 5363, Jan. 2015.
- [58] C. A. Schuh, "Nanoindentation studies of materials," vol. 9, no. 5, pp. 32–40, 2006.
- [59] X. Long, R. Dong, Y. Su, and C. Chang, "Critical Review of Nanoindentation-Based Numerical Methods for Evaluating Elastoplastic Material Properties," *Coatings*, vol. 13, no. 8, 2023.
- [60] B. Robert and E. B. Brown, *Thermal analysis of polymers*, no. 1. 2004.
- [61] X. Wu, K. Walsh, B. L. Ho, and G. Camci-unal, "Mineralization of Biomaterials for Bone Tissue Engineering," vol. 6, pp. 1–24, 2020.
- [62] W. M. GROENEWOUD, "CHAPTER 4 - DYNAMIC MECHANICAL ANALYSIS," W. M. B. T.-C. of P. by T. A. GROENEWOUD, Ed. Amsterdam: Elsevier Science B.V., 2001, pp. 94–122.
- [63] B. Gu and D. J. Burgess, *Polymeric Materials in Drug Delivery*. Elsevier Inc., 2014.
- [64] A. Gençer, "Design of rigid wheat gluten materials; Improved mechanical properties by blending with polyamides," 2014.
- [65] K. Dyamenahalli, A. Famili, and R. Shandas, "3 - Characterization of shape-memory polymers for biomedical applications," in *Woodhead Publishing Series in Biomaterials*, L. B. T.-S. M. P. for B. A. Yahia, Ed. Woodhead Publishing, 2015, pp. 35–63.
- [66] R. McClelland, R. Dennis, L. M. Reid, B. Palsson, and J. M. Macdonald, "7 - TISSUE ENGINEERING," in *Biomedical Engineering*, J. D. Enderle, S. M. Blanchard, and J. D. B. T.-I. to B. E. (Second E. Bronzino, Eds. Boston: Academic Press, 2005, pp. 313–402.
- [67] H. Jodati, B. Yilmaz, and Z. Evis, "A review of bioceramic porous scaffolds for hard tissue applications: Effects of structural features," *Ceram. Int.*, vol. 46, no. 10, pp. 15725–15739, 2020.
- [68] A. P. Moreno Madrid, S. M. Vrech, M. A. Sanchez, and A. P. Rodriguez, "Advances in additive manufacturing for bone tissue engineering scaffolds," *Mater. Sci. Eng. C*, vol. 100, no. March 2018, pp. 631–644, 2019.
- [69] A. Biotechnology, B. E. June, A. Shukla, N. Dasgupta, S. Ranjan, and S. Singh, "Nanotechnology towards prevention of anemia and osteoporosis : from concept to market," no. June, 2017.
- [70] Ž. Perić Kačarević *et al.*, "An introduction to bone tissue engineering," *Int. J. Artif. Organs*, vol. 43, no. 2, pp. 69–86, 2020.
- [71] I. M. Adel, M. F. Elmeligy, and N. A. Elkasabgy, "Conventional and Recent Trends of Scaffolds Fabrication: A Superior Mode for Tissue Engineering," *Pharmaceutics*, vol. 14, no. 2, 2022.
- [72] O. C. Chia, I. S. Suhaimin, S. A. Kassim, S. A. Zubir, and T. K. Abdullah, "Effect of modified solvent casting/particulate leaching (SCPL) technique on the properties of bioactive glass reinforced polyurethane scaffold for biomedical applications," *J. Phys. Sci.*, vol. 30, pp. 115–126, 2019.
- [73] B. Thavornnyutikarn, N. Chantarapanich, K. Sitthiseripratip, G. A. Thouas, and Q. Chen, *Bone tissue engineering scaffolding: computer-aided scaffolding techniques*, vol. 3, no. 2–4. 2014.
- [74] E. Capuana, F. Lopresti, F. Carfi Pavia, V. Bruccato, and V. La Carrubba, "Solution-based processing for scaffold fabrication in tissue engineering applications: A brief review," *Polymers (Basel)*, vol. 13, no. 13, 2021.
- [75] J. P. Fernández-Hernán, B. Torres, A. J. López, and J. Rams, *The Role of the Sol-Gel Synthesis Process in the Biomedical Field and Its Use to Enhance the Performance of Bioabsorbable Magnesium Implants*, vol. 8, no. 7. 2022.
- [76] B. Zhang, L. Gao, L. Ma, Y. Luo, H. Yang, and Z. Cui, "3D Bioprinting: A Novel Avenue for Manufacturing Tissues and Organs," *Engineering*, vol. 5, no. 4, pp. 777–794, 2019.
- [77] M. Jawaid and A. Haleem, "Additive manufacturing applications in medical cases: A literature

- based review,” *Alexandria J. Med.*, vol. 54, no. 4, pp. 411–422, 2018.
- [78] M. Revilla-León and M. Özcan, “Additive Manufacturing Technologies Used for Processing Polymers: Current Status and Potential Application in Prosthetic Dentistry,” *J. Prosthodont.*, vol. 28, no. 2, pp. 146–158, 2019.
- [79] M. Pagac *et al.*, “A Review of Vat Photopolymerization Technology: Materials, Applications, Challenges, and Future Trends of 3D Printing,” *Polymers (Basel)*, vol. 13, no. 4, Feb. 2021.
- [80] W. L. Ng *et al.*, “Vat polymerization-based bioprinting-process, materials, applications and regulatory challenges,” *Biofabrication*, vol. 12, no. 2, p. 22001, Feb. 2020.
- [81] B. Yuan, S.-Y. Zhou, and X.-S. Chen, “Rapid prototyping technology and its application in bone tissue engineering,” *J. Zhejiang Univ. Sci. B*, vol. 18, no. 4, pp. 303–315, 2017.
- [82] A. V. Do, B. Khorsand, S. M. Geary, and A. K. Salem, “3D Printing of Scaffolds for Tissue Regeneration Applications,” *Adv. Healthc. Mater.*, vol. 4, no. 12, pp. 1742–1762, 2015.
- [83] A. E. F. Eltom, G. Zhong, and A. Muhammad, “Scaffold Techniques and Designs in Tissue Engineering Functions and Purposes: A Review,” *Adv. Mater. Sci. Eng.*, 2019.
- [84] E. Jabari, F. Ahmed, F. Liravi, E. B. Secor, L. Lin, and E. Toyserkani, “2D printing of graphene: A review,” *2D Mater.*, vol. 6, no. 4, 2019.
- [85] M. P. Mani *et al.*, “A review on 3D printing in tissue engineering applications,” *J. Polym. Eng.*, vol. 42, no. 3, pp. 243–265, 2022.
- [86] M. Bahraminasab, “Challenges on optimization of 3D-printed bone scaffolds,” *Biomed. Eng. Online*, vol. 19, no. 1, p. 69, 2020.
- [87] D. B. Gilmer *et al.*, “Additive manufacturing of strong silica sand structures enabled by polyethyleneimine binder,” *Nat. Commun.*, vol. 12, no. 1, pp. 1–8, 2021.
- [88] A. Mostafaei *et al.*, “Binder jet 3D printing—Process parameters, materials, properties, modeling, and challenges,” *Prog. Mater. Sci.*, vol. 119, p. 100707, 2021.
- [89] T. Tancogne-Dejean, C. C. Roth, and D. Mohr, “Rate-dependent strength and ductility of binder jetting 3D-printed stainless steel 316L: Experiments and modeling,” *Int. J. Mech. Sci.*, vol. 207, p. 106647, 2021.
- [90] F. Dini, S. A. Ghaffari, J. Javadpour, and H. R. Rezaie, “Preparation of 3D Printable HAp-based Composite Powder for Binder Jetting Process,” 2020.
- [91] A. Kumar, S. Kargozar, F. Baino, and S. S. Han, “Additive Manufacturing Methods for Producing Hydroxyapatite and Hydroxyapatite-Based Composite Scaffolds: A Review,” *Front. Mater.*, vol. 6, no. December, pp. 1–20, 2019.
- [92] N. D. Dejene and H. G. Lemu, “Current Status and Challenges of Powder Bed Fusion-Based Metal Additive Manufacturing: Literature Review,” *Metals*, vol. 13, no. 2, 2023.
- [93] W. Zuo, L. Yu, J. Lin, Y. Yang, and Q. Fei, “Properties improvement of titanium alloys scaffolds in bone tissue engineering: a literature review,” *Ann. Transl. Med.*, vol. 9, no. 15, p. 1259, Aug. 2021.
- [94] J. Gonzalez-Gutierrez, S. Cano, S. Schuschnigg, C. Kukla, J. Sapkota, and C. Holzer, “Additive manufacturing of metallic and ceramic components by the material extrusion of highly-filled polymers: A review and future perspectives,” *Materials (Basel)*, vol. 11, no. 5, 2018.
- [95] S. C. Altıparmak, V. A. Yardley, Z. Shi, and J. Lin, “Extrusion-based additive manufacturing technologies: State of the art and future perspectives,” *J. Manuf. Process.*, vol. 83, no. July, pp. 607–636, 2022.
- [96] M. A. Azad, D. Olawuni, G. Kimbell, A. Z. Badruddoza, S. Hossain, and T. Sultana, *Polymers for Extrusion-Based 3D Printing of Pharmaceuticals: A Holistic Materials – Process Perspective*. .
- [97] J. E. Trachtenberg *et al.*, “Extrusion-Based 3D Printing of Poly(propylene fumarate) in a Full-Factorial Design,” *ACS Biomater. Sci. Eng.*, vol. 2, no. 10, pp. 1771–1780, Oct. 2016.
- [98] S. Bom, R. Ribeiro, H. M. Ribeiro, C. Santos, and J. Marto, “On the progress of hydrogel-based 3D printing: Correlating rheological properties with printing behaviour,” *Int. J. Pharm.*, vol. 615, p. 121506, 2022.
- [99] A. Das, E. L. Gilmer, S. Biria, and M. J. Bortner, “Importance of Polymer Rheology on Material Extrusion Additive Manufacturing: Correlating Process Physics to Print Properties,” *ACS Appl. Polym. Mater.*, vol. 3, no. 3, pp. 1218–1249, 2021.
- [100] H. Herrada-Manchón, M. A. Fernández, and E. Aguilar, “Essential Guide to Hydrogel Rheology in Extrusion 3D Printing: How to Measure It and Why It Matters?,” *Gels*, vol. 9, no. 7, 2023.
- [101] H. Ramli, N. F. A. Zainal, M. Hess, and C. H. Chan, “Basic principle and good practices of rheology for polymers for teachers and beginners,” *Chem. Teach. Int.*, vol. 4, no. 4, pp. 307–326, 2022.
- [102] I. D. Marinescu, W. B. Rowe, B. Dimitrov, and I. Inasaki, “14 - Process Fluids for Abrasive

- Machining,” I. D. Marinescu, W. B. Rowe, B. Dimitrov, and I. B. T.-T. of A. M. P. Inasaki, Eds. Norwich, NY: William Andrew Publishing, 2004, pp. 531–585.
- [103] N. Paxton, W. Smolan, T. Böck, F. Melchels, J. Groll, and T. Jungst, “Proposal to assess printability of bioinks for extrusion-based bioprinting and evaluation of rheological properties governing bioprintability,” *Biofabrication*, vol. 9, no. 4, 2017.
- [104] R. Trombetta, J. A. Inzana, E. M. Schwarz, S. L. Kates, and H. A. Awad, “3D Printing of Calcium Phosphate Ceramics for Bone Tissue Engineering and Drug Delivery,” *Ann. Biomed. Eng.*, vol. 45, no. 1, pp. 23–44, 2017.
- [105] S. Bose, S. Vahabzadeh, and A. Bandyopadhyay, “Bone tissue engineering using 3D printing,” *Mater. Today*, vol. 16, no. 12, pp. 496–504, 2013.
- [106] P. Chocholata, V. Kulda, and V. Babuska, “Fabrication of Scaffolds for Bone-Tissue Regeneration,” 2019.
- [107] K. Glenske *et al.*, “Applications of Metals for Bone Regeneration.,” *Int. J. Mol. Sci.*, vol. 19, no. 3, Mar. 2018.
- [108] L. Suamte, A. Tirkey, J. Barman, and P. Jayasekhar Babu, “Various manufacturing methods and ideal properties of scaffolds for tissue engineering applications,” *Smart Mater. Manuf.*, vol. 1, no. November, p. 100011, 2023.
- [109] Y. Guo *et al.*, “In Vitro and in Vivo Study of 3D-Printed Porous Tantalum Scaffolds for Repairing Bone Defects,” *ACS Biomater. Sci. Eng.*, vol. 5, no. 2, pp. 1123–1133, 2019.
- [110] R. Crichton, “Chapter 19 - Biomineralization,” R. B. T.-B. I. C. (Third E. Crichton, Ed. Academic Press, 2019, pp. 517–544.
- [111] H. Davis and J. Leach, “Hybrid and Composite Biomaterials in Tissue Engineering,” *Top. Multifunct. Biomater. devices*, no. 530, pp. 1–26, 2008.
- [112] M. U. Aslam Khan *et al.*, “Recent Advances in Biopolymeric Composite Materials for Tissue Engineering and Regenerative Medicines: A Review.,” *Molecules*, vol. 26, no. 3, Jan. 2021.
- [113] A. Ross, M. A. Sauce-Guevara, E. I. Alarcon, and M. A. Mendez-Rojas, “Peptide Biomaterials for Tissue Regeneration,” *Front. Bioeng. Biotechnol.*, vol. 10, no. August, pp. 1–16, 2022.
- [114] M. Shahruzzaman *et al.*, “Chapter 7 - Biological macromolecules as antimicrobial agents,” A. K. Nayak, A. K. Dhara, and D. B. T.-B. M. Pal, Eds. Academic Press, 2022, pp. 165–202.
- [115] A. Karadag, H. Iqbal, and H. Yazici, “Peptide-mediated Bone Tissue Engineering BT - Racing for the Surface: Antimicrobial and Interface Tissue Engineering,” B. Li, T. F. Moriarty, T. Webster, and M. Xing, Eds. Cham: Springer International Publishing, 2020, pp. 435–476.
- [116] J. Forbes and K. Krishnamurthy, “Biochemistry, Peptide.,” Treasure Island (FL), 2023.
- [117] “Molecular Biology of the Cell (4th Ed),” *J. Biol. Educ.*, vol. 37, no. 1, pp. 45–47, 2002.
- [118] B. Yue, “Biology of the extracellular matrix: an overview.,” *J. Glaucoma*, vol. 23, no. 8 Suppl 1, pp. S20-3, 2014.
- [119] J. Ozsvar, C. Yang, S. A. Cain, C. Baldock, A. Tarakanova, and A. S. Weiss, “Tropoelastin and Elastin Assembly,” *Front. Bioeng. Biotechnol.*, vol. 9, no. February, pp. 1–11, 2021.
- [120] H. Wang *et al.*, “Covalently Adaptable Elastin-Like Protein–Hyaluronic Acid (ELP–HA) Hybrid Hydrogels with Secondary Thermoresponsive Crosslinking for Injectable Stem Cell Delivery,” *Adv. Funct. Mater.*, vol. 27, no. 28, pp. 1–11, 2017.
- [121] M. R. H. Krebs, K. R. Domike, and A. M. Donald, “Protein aggregation: more than just fibrils,” *Biochem. Soc. Trans.*, vol. 37, no. Pt 4, p. 682–686, Aug. 2009.
- [122] S. Roberts, M. Dzuricky, and A. Chilkoti, “Elastin-like polypeptides as models of intrinsically disordered proteins,” *FEBS Lett.*, vol. 589, no. 19, pp. 2477–2486, 2015.
- [123] A. K. Varanko, J. C. Su, and A. Chilkoti, “Elastin-Like Polypeptides for Biomedical Applications,” *Annu. Rev. Biomed. Eng.*, vol. 22, pp. 343–369, 2020.
- [124] S. R. Macewan and A. Chilkoti, “Elastin-Like Polypeptides: Biomedical Applications of tunable Biopolymers,” vol. 94, no. 1, pp. 60–77, 2010.
- [125] R. Lu, X. Zhang, X. Cheng, Y. Zhang, X. Zan, and L. Zhang, “Medical Applications Based on Supramolecular Self-Assembled Materials From Tannic Acid,” *Front. Chem.*, vol. 8, no. October, 2020.
- [126] X. Zottig, M. Côté-Cyr, D. Arpin, D. Archambault, and S. Bourgault, “Protein supramolecular structures: From self-assembly to nanovaccine design,” *Nanomaterials*, vol. 10, no. 5, pp. 1–28, 2020.
- [127] E. Y. Chen *et al.*, “Chapter 3 - Understanding and utilizing the biomolecule/nanosystems interface,” in *Micro and Nano Technologies*, V. Uskoković and D. P. B. T.-N. in P. and R. M. Uskoković, Eds. Elsevier, 2018, pp. 207–297.
- [128] R. J. Ouellette and J. D. Rawn, “1 - Structure and Bonding in Organic Compounds,” R. J. Ouellette and J. D. B. T.-O. C. (Second E. Rawn, Eds. Academic Press, 2018, pp. 1–30.

- [129] M. M. Gromiha, "Chapter 1 - Proteins," M. M. B. T.-P. B. Gromiha, Ed. Singapore: Academic Press, 2010, pp. 1–27.
- [130] S. Choudhuri, "Chapter 8 - Additional Bioinformatic Analyses Involving Protein Sequences\*\*The opinions expressed in this chapter are the author's own and they do not necessarily reflect the opinions of the FDA, the DHHS, or the Federal Government.," S. B. T.-B. for B. Choudhuri, Ed. Oxford: Academic Press, 2014, pp. 183–207.
- [131] M. Parker and Z. Li, "Chapter 22 - Biotechnology and drugs," A. B. T.-R. (Twenty-third E. Adejare, Ed. Academic Press, 2021, pp. 397–415.
- [132] D. Titus, E. James Jebaseelan Samuel, and S. M. Roopan, "Chapter 12 - Nanoparticle characterization techniques," in *Micro and Nano Technologies*, A. K. Shukla and S. B. T.-G. S. Iravani Characterization and Applications of Nanoparticles, Eds. Elsevier, 2019, pp. 303–319.
- [133] K. Song, "4 - Interphase characterization in rubber nanocomposites," in *Woodhead Publishing Series in Composites Science and Engineering*, S. Thomas and H. J. B. T.-P. in R. N. Maria, Eds. Woodhead Publishing, 2017, pp. 115–152.
- [134] H. Yang, S. Yang, J. Kong, A. Dong, and S. Yu, "Obtaining information about protein secondary structures in aqueous solution using Fourier transform IR spectroscopy," *Nat. Protoc.*, vol. 10, no. 3, pp. 382–396, 2015.
- [135] L. Pasteur, "Organic Chemistry I," *A Hist. Chem.*, pp. 749–800, 1964.
- [136] A. A. Bunaciu, H. Y. Aboul-Enein, and V. D. Hoang, "Raman spectroscopy for protein analysis," *Appl. Spectrosc. Rev.*, vol. 50, no. 5, pp. 377–386, 2015.
- [137] J. Hniopek, T. Bocklitz, M. Schmitt, and J. Popp, "Probing Protein Secondary Structure Influence on Active Centers with Hetero Two-Dimensional Correlation (Resonance) Raman Spectroscopy: A Demonstration on Cytochrome C.," *Appl. Spectrosc.*, vol. 75, no. 8, pp. 1043–1052, Aug. 2021.
- [138] J. T. Pelton and L. R. McLean, "Spectroscopic methods for analysis of protein secondary structure.," *Anal. Biochem.*, vol. 277, no. 2, pp. 167–176, Jan. 2000.
- [139] A. Micsonai, É. Bulyáki, and J. Kardos, "BeStSel: From Secondary Structure Analysis to Protein Fold Prediction by Circular Dichroism Spectroscopy BT - Structural Genomics: General Applications," Y. W. Chen and C.-P. B. Yiu, Eds. New York, NY: Springer US, 2021, pp. 175–189.
- [140] S. Elsharkawy *et al.*, "Protein disorder–order interplay to guide the growth of hierarchical mineralized structures," *Nat. Commun.*, vol. 9, no. 1, 2018.
- [141] K. Shuturminska *et al.*, "Elastin-like protein, with statherin derived peptide, controls fluorapatite formation and morphology," *Front. Physiol.*, vol. 8, no. JUN, pp. 1–12, 2017.
- [142] G. B. Proctor, S. Hamdan, G. H. Carpenter, and P. Wilde, "A statherin and calcium enriched layer at the air interface of human parotid saliva," *Biochem. J.*, vol. 389, no. 1, pp. 111–116, 2005.
- [143] J. P. McCain and K. Kim, "Chapter 6 - Endoscopic Oral and Maxillofacial Surgery," in *Current Therapy In Oral and Maxillofacial Surgery*, S. C. Bagheri, R. B. Bell, and H. A. Khan, Eds. Saint Louis: W.B. Saunders, 2012, pp. 31–62.
- [144] E. C. Moreno, K. Varughese, and D. I. Hay, "Effect of human salivary proteins on the precipitation kinetics of calcium phosphate.," *Calcif. Tissue Int.*, vol. 28, no. 1, pp. 7–16, Aug. 1979.
- [145] T. W. T. Tsai and J. C. C. Chan, "Chapter 1 - Recent Progress in the Solid-State NMR Studies of Biomineralization," vol. 73, G. A. B. T.-A. R. on N. M. R. S. Webb, Ed. Academic Press, 2011, pp. 1–61.
- [146] M. Wei, J. Evans, T. Bostrom, and L. Grondahl, "Synthesis and characterization of hydroxyapatite, fluoride-substituted hydroxyapatite and fluorapatite," *J. Mater. Sci. Mater. Med.*, vol. 14, pp. 311–320, Apr. 2003.
- [147] K. Pajor, L. Pajchel, and J. Kolmas, "Hydroxyapatite and fluorapatite in conservative dentistry and oral implantology-a review," *Materials (Basel).*, vol. 12, no. 7, 2019.
- [148] K. A. DeRocher *et al.*, "Chemical gradients in human enamel crystallites," *Nature*, vol. 583, no. 7814, pp. 66–71, 2020.
- [149] L. Lei, L. Zheng, H. Xiao, J. Zheng, and Z. Zhou, "Wear mechanism of human tooth enamel: The role of interfacial protein bonding between HA crystals," *J. Mech. Behav. Biomed. Mater.*, vol. 110, p. 103845, 2020.
- [150] E. Beniash *et al.*, "The hidden structure of human enamel," *Nat. Commun.*, vol. 10, no. 1, pp. 1–13, 2019.
- [151] Y. Y. Zhang, Q. L. Li, and H. M. Wong, "Cell-free biomimetic mineralization strategies to regenerate the enamel microstructure," *Crystals*, vol. 11, no. 11, pp. 1–17, 2021.
- [152] J. H. Holgate and J. Webb, "MICROSCOPY | Light Microscopy and Histochemical Methods," B. B. T.-E. of F. S. and N. (Second E. Caballero, Ed. Oxford: Academic Press, 2003, pp. 3917–

3922.

- [153] A. F. Frandsen, "Polarized Light Microscopy," vol. 3, no. 321, 2016.
- [154] P. Raghavendra and T. Pullaiah, "Chapter 4 - Biomedical Imaging Role in Cellular and Molecular Diagnostics," P. Raghavendra and T. B. T.-A. in C. and M. D. Pullaiah, Eds. Academic Press, 2018, pp. 85–111.
- [155] R. Schmitt, "Scanning Electron Microscope BT - CIRP Encyclopedia of Production Engineering," L. Laperrière and G. Reinhart, Eds. Berlin, Heidelberg: Springer Berlin Heidelberg, 2014, pp. 1085–1089.
- [156] W.-S. Ryu, "Chapter 2 - Virus Structure," W.-S. B. T.-M. V. of H. P. V. Ryu, Ed. Boston: Academic Press, 2017, pp. 21–29.
- [157] K. Pal, A. T. Paulson, and D. Rousseau, "14 - Biopolymers in Controlled-Release Delivery Systems," in *Plastics Design Library*, S. B. T.-H. of B. and B. P. Ebnesajjad, Ed. Boston: William Andrew Publishing, 2013, pp. 329–363.
- [158] I. Neri Numa, M. Gabriel Pessôa, B. Paulino, and G. Pastore, "Genipin: A natural blue pigment for food and health purposes," *Trends Food Sci. Technol.*, vol. 67, Jun. 2017.
- [159] M. Hanson and A. Wypych, "3 - Curatives and Crosslinkers," in *Databook of Curatives and Crosslinkers*, M. Hanson and A. Wypych, Eds. ChemTec Publishing, 2019, pp. 15–537.
- [160] M. R. H. Krebs, K. R. Domike, D. Cannon, and A. M. Donald, "Common motifs in protein self-assembly," *Faraday Discuss.*, vol. 139, pp. 265–274, 2008.
- [161] B. R. Singh, D. B. DeOliveira, F.-N. Fu, and M. P. Fuller, "Fourier transform infrared analysis of amide III bands of proteins for the secondary structure estimation," in *Proc.SPIE*, 1993, vol. 1890.
- [162] T. M. Lim, M. Ulaganathan, and Q. Yan, "Chapter 14 - Advances in membrane and stack design of redox flow batteries (RFBs) for medium- and large-scale energy storage," in *Advances in Batteries for Medium and Large-Scale Energy Storage*, C. Menictas, M. Skyllas-Kazacos, and T. M. Lim, Eds. Woodhead Publishing, 2015, pp. 477–507.
- [163] H. Chen *et al.*, "Synthesis of fluorapatite nanorods and nanowires by direct precipitation from solution," *Cryst. Growth Des.*, vol. 6, no. 6, pp. 1504–1508, 2006.
- [164] S. S. Gosavi, S. Y. Gosavi, and R. K. Alla, "Local and systemic effects of unpolymerised monomers.," *Dent. Res. J. (Isfahan).*, vol. 7, no. 2, pp. 82–7, 2010.
- [165] S. Imazato, D. Horikawa, M. Nishida, and S. Ebisu, "Effects of monomers eluted from dental resin restoratives on osteoblast-like cells.," *J. Biomed. Mater. Res. B. Appl. Biomater.*, vol. 88, no. 2, pp. 378–386, Feb. 2009.
- [166] H. Azeredo, M. Rosa, M. Sá, M. Filho, and K. Waldron, "The use of biomass for packaging films and coatings," in *Advances in Biorefineries: Biomass and Waste Supply Chain Exploitation*, 2014, pp. 819–874.
- [167] Y. Yu, S. Xu, S. Li, and H. Pan, "Genipin-cross-linked hydrogels based on biomaterials for drug delivery: a review," *Biomater. Sci.*, vol. 9, no. 5, pp. 1583–1597, 2021.
- [168] C. Marques *et al.*, "Novel sintering-free scaffolds obtained by additive manufacturing for concurrent bone regeneration and drug delivery: Proof of concept," *Mater. Sci. Eng. C*, vol. 94, Sep. 2018.
- [169] K. Zafeiris *et al.*, "Additive manufacturing of hydroxyapatite–chitosan–genipin composite scaffolds for bone tissue engineering applications," *Mater. Sci. Eng. C*, vol. 119, p. 111639, 2021.
- [170] G. Montalbano *et al.*, "Collagen Hybrid Formulations for the 3D Printing of Nanostructured Bone Scaffolds: An Optimized Genipin-Crosslinking Strategy," *Nanomaterials*, vol. 10, no. 9. 2020.
- [171] J. G. Kennemur and B. M. Novak, "Advances in polycarbodiimide chemistry," *Polymer (Guildf).*, vol. 52, no. 8, pp. 1693–1710, 2011.
- [172] D. Kaikade and A. Sabnis, "Polyurethane foams from vegetable oil-based polyols: a review," *Polym. Bull.*, vol. 80, Mar. 2022.
- [173] G. T. Kilosanidze, "Analysis of forces that determine helix formation in  $\alpha$ -proteins," *Protein Sci.*, vol. 13, no. 2, pp. 351–357, 2004.
- [174] K. A. Jolliffe and P. A. Gale, "The supramolecular chemistry of anions," *Org. Biomol. Chem.*, vol. 20, no. 4, pp. 713–714, 2022.
- [175] A. M. C. Marcelino and L. M. Gierasch, "Roles of  $\beta$ -turns in protein folding: From peptide models to protein engineering," *Biopolymers*, vol. 89, no. 5, pp. 380–391, 2008.
- [176] A. J. Cunliffe, R. Wang, J. Redfern, J. Verran, and D. Ian Wilson, "Effect of environmental factors on the kinetics of evaporation of droplets containing bacteria or viruses on different surfaces," *J. Food Eng.*, vol. 336, p. 111195, 2023.
- [177] C. Di Mino *et al.*, "Weak Interactions in Dimethyl Sulfoxide (DMSO)-Tertiary Amide Solutions: The Versatility of DMSO as a Solvent.," *J. Phys. Chem. B*, vol. 127, no. 6, pp. 1357–1366, Feb.

- 2023.
- [178] B. Yang, H. Lang, Z. Liu, S. Wang, Z. Men, and C. Sun, "Three stages of hydrogen bonding network in DMF-water binary solution," *J. Mol. Liq.*, vol. 324, p. 114996, 2021.
- [179] D. Lv, L. Evangelisti, A. Maris, W. Song, G. Salvitti, and S. Melandri, "Characterizing the Interactions of Dimethyl Sulfoxide with Water: A Rotational Spectroscopy Study," *J. Phys. Chem. A*, vol. 126, no. 39, pp. 6882–6889, Oct. 2022.
- [180] J. K. Magtaan, M. Devocelle, and F. Kelleher, "Regeneration of aged DMF for use in solid-phase peptide synthesis," *J. Pept. Sci.*, vol. 25, no. 1, pp. 1–9, 2019.
- [181] M. E. O’Kane *et al.*, "Perovskites on Ice: An Additive-Free Approach to Increase the Shelf-Life of Triple-Cation Perovskite Precursor Solutions," *ChemSusChem*, vol. 14, no. 12, pp. 2537–2546, 2021.
- [182] F. Furlani *et al.*, "Biomimetic, Multiresponsive, and Self-Healing Lactose-Modified Chitosan (CTL)-Based Gels Formed via Competitor-Assisted Mechanism," *ACS Biomater. Sci. Eng.*, pp. 5539–5547, 2019.
- [183] C. Pizzolitto *et al.*, "On the mechanism of genipin binding to primary amines in lactose-modified chitosan at neutral pH," *Int. J. Mol. Sci.*, vol. 21, no. 18, pp. 1–17, 2020.
- [184] L. Cseri, M. Razali, P. Pogany, and G. Szekely, "Chapter 3.15 - Organic Solvents in Sustainable Synthesis and Engineering," B. Török and T. B. T.-G. C. Dransfield, Eds. Elsevier, 2018, pp. 513–553.
- [185] N. S. Radin, "Solvent Removal by Vacuum Evaporation," *Anal. Chem.*, vol. 28, no. 4, pp. 542–543, 1956.
- [186] L. Xu, Y. A. Huang, Q. J. Zhu, and C. Ye, "Chitosan in molecularly-imprinted polymers: Current and future prospects," *Int. J. Mol. Sci.*, vol. 16, no. 8, pp. 18328–18347, 2015.
- [187] V. G. Tacias-Pascacio *et al.*, "Genipin as an emergent tool in the design of biocatalysts: Mechanism of reaction and applications," *Catalysts*, vol. 9, no. 12, pp. 1–19, 2019.
- [188] T. D. Sargeant, A. P. Desai, S. Banerjee, A. Agawu, and J. B. Stopek, "An in situ forming collagen-PEG hydrogel for tissue regeneration," *Acta Biomater.*, vol. 8, no. 1, pp. 124–132, 2012.
- [189] F. M. De Souza, P. K. Kahol, and R. K. Gupta, "Introduction to Polyurethane Chemistry," *ACS Symp. Ser.*, vol. 1380, pp. 1–24, 2021.
- [190] D. Rosu, L. Rosu, and C. Cascaval, "IR-change and yellowing of polyurethane as a result of UV irradiation," *Polym. Degrad. Stab. - POLYM Degrad STABIL*, vol. 94, pp. 591–596, Apr. 2009.
- [191] R. Touyama *et al.*, "Studies on the blue pigments produced from genipin and methylamine. I. Structures of the brownish-red pigments, intermediates leading to the blue pigments," *Chem. Pharm. Bull.*, vol. 42, no. 3, pp. 668–673, 1994.
- [192] C. Etter, R. Russi, G. B. Fogazzi, R. P. Wüthrich, and A. L. Serra, "Maltese cross-like crystals in the urinary sediment of a diabetic patient," *NDT Plus*, vol. 2, no. 5, pp. 405–407, 2009.
- [193] S. Araia and M. Doi, "Skin formation and bubble growth during drying process of polymer solution," *Eur. Phys. J. E*, vol. 35, no. 7, pp. 1–9, 2012.
- [194] H. Wang, K. Sun, A. Li, W. Wang, and P. Chui, "Size-controlled synthesis and characterization of fluorapatite nanocrystals in the presence of gelatin," *Powder Technol.*, vol. 209, no. 1–3, pp. 9–14, 2011.
- [195] A. D. Anastasiou *et al.*, "Antibacterial properties and regenerative potential of Sr<sup>2+</sup> and Ce<sup>3+</sup> doped fluorapatites; a potential solution for peri-implantitis," *Sci. Rep.*, vol. 9, no. 1, pp. 1–12, 2019.
- [196] A. Linder, "X-ray diffraction studies on complex metal oxides," 2015.
- [197] I. Seoane-Viaño, P. Januskaite, C. Alvarez-Lorenzo, A. W. Basit, and A. Goyanes, "Semi-solid extrusion 3D printing in drug delivery and biomedicine: Personalised solutions for healthcare challenges," *J. Control. Release*, vol. 332, no. August 2021, pp. 367–389, 2021.
- [198] E. Sodupe-Ortega, A. Sanz-Garcia, A. Pernia-Espinoza, and C. Escobedo-Lucea, "Accurate calibration in multi-material 3D bioprinting for tissue engineering," *Materials (Basel)*, vol. 11, no. 8, pp. 1–19, 2018.

## vi. Appendices

### Appendix A

*Shrink capacity in PMDI gels (Chapter 3.1.2.3.)*

<b>Fume hood</b>	Before CL [mg]	After CL [mg]	Shrinkage [%]
S1	541,9	220,6	40,7
S2	303,6	110,9	36,5
		Mean	38,6
		St.Dev.	3,0

<b>Glovebox</b>	Before CL [mg]	After CL [mg]	Shrinkage [%]
S1	398	231,6	58,2
S2	308,7	114,6	37,1
		Mean	47,7
		St.Dev.	14,9

<b>Vacuum Oven</b>	Before CL [mg]	After CL [mg]	Shrinkage [%]
S1	479,8	160,6	33,5
S2	387,2	128,1	33,1
		Mean	33,3
		St.Dev.	0,3

<b>DI water</b>	Before CL [mg]	After CL [mg]	Shrinkage [%]
S1	316,9	55,3	17,5
S2	241,1	34,2	14,2
		Mean	15,8
		St.Dev.	2,3

CL = Cross-linking

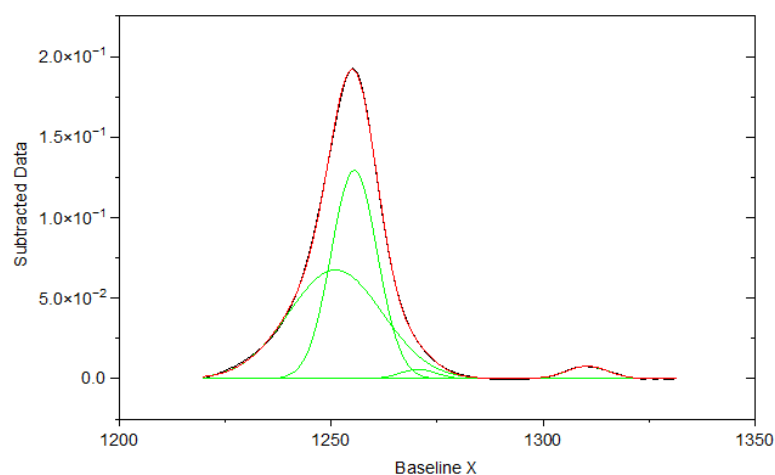
## Appendix B

### *Protein Secondary Structure Data*

In this section, graphs and numerical values related to the secondary structure formation are presented. They represent data obtained from the FTIR data deconvolution for the respective sample (S) position (P). The absorbance at the respective wavelength [ $\text{cm}^{-1}$ ] is expressed in [%].

#### *Contained 0.3 wt% PMDI-ELP gel (chapter 3.1.2.1)*

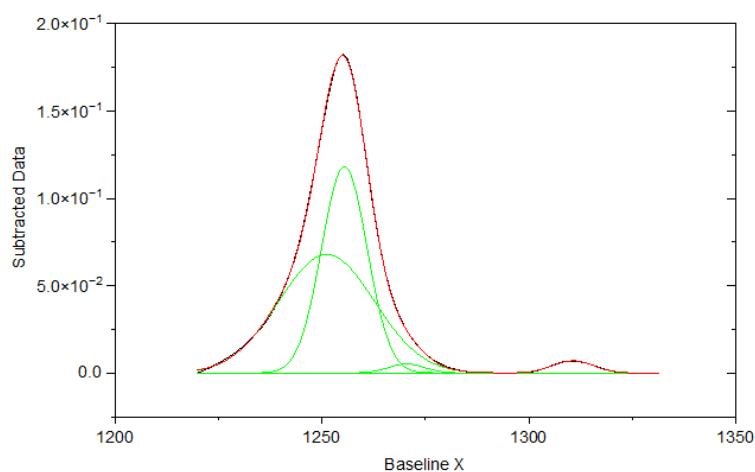
##### FTIR analysis – Day 0



Fitting Results

Peak Index	Peak Type	Area Intg	FWHM	Max Height	Center Grvty	Area IntgP
1	Gaussian	1.86572	26.02913	0.0675	1251.03357	49.32625
2	Gaussian	1.75923	12.79269	0.12919	1255.44511	46.51086
3	Gaussian	0.09603	11.62313	0.00776	1310.42778	2.53882
4	Gaussian	0.06143	9.99329	0.00577	1270.50919	1.62407

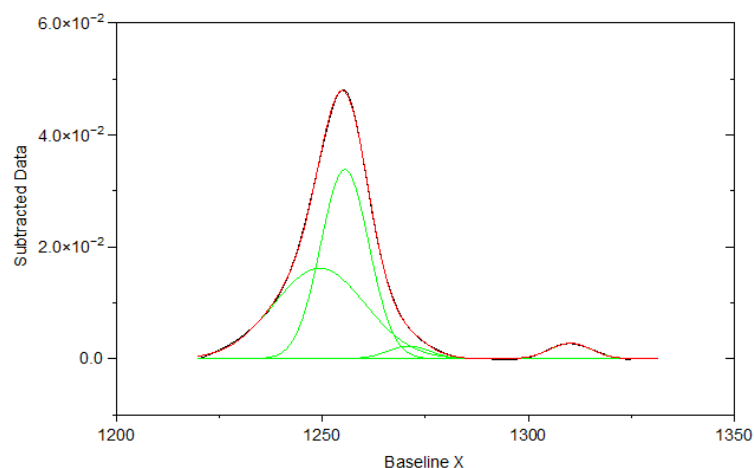
##### FTIR analysis – Day 1



Fitting Results

Peak Index	Peak Type	Area Intg	FWHM	Max Height	Center Grvty	Area IntgP
1	Gaussian	1.62925	12.95597	0.11814	1255.40347	43.71976
2	Gaussian	0.08708	11.6258	0.00704	1310.66551	2.33686
3	Gaussian	1.95306	27.13614	0.06784	1251.11717	52.40884
4	Gaussian	0.05719	10.38154	0.00517	1270.43247	1.53454

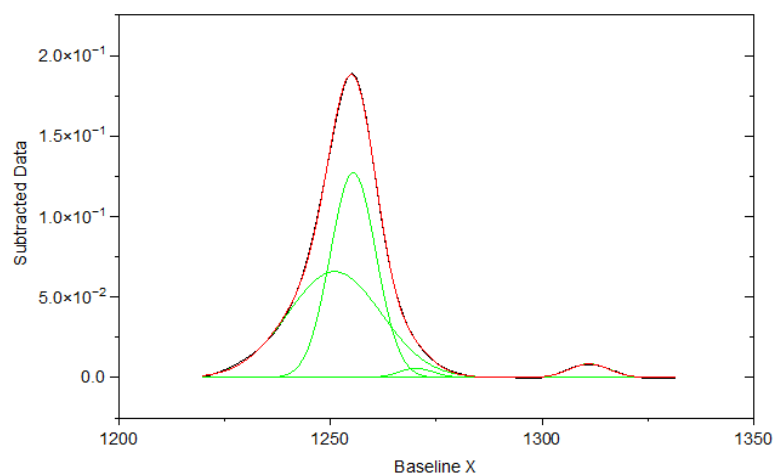
### FTIR analysis – Day 2



Fitting Results

Peak Index	Peak Type	Area Intg	FWHM	Max Height	Center Grvty	Area IntgP
1	Gaussian	0.4944	13.73961	0.0338	1255.45004	49.25755
2	Gaussian	0.44618	26.04098	0.01616	1249.32382	44.4534
3	Gaussian	0.03451	11.71281	0.00277	1310.27157	3.43804
4	Gaussian	0.02862	11.95098	0.00225	1270.94036	2.851

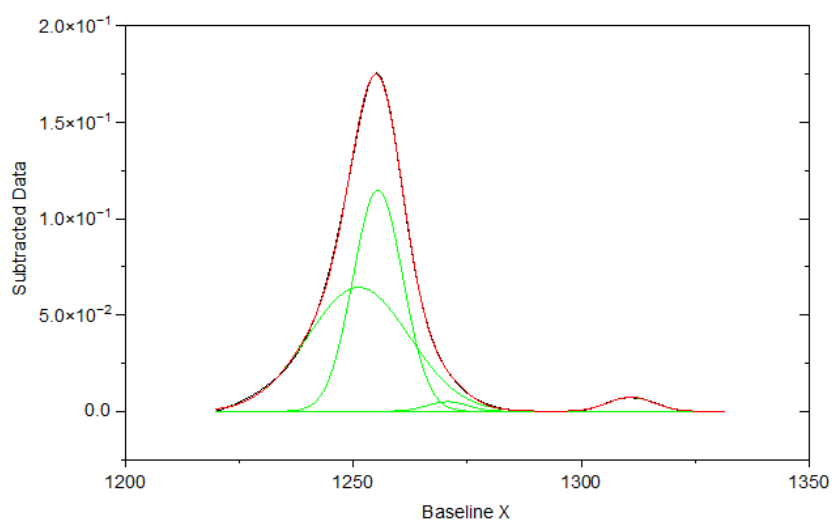
### FTIR analysis – Day 3



Fitting Results

Peak Index	Peak Type	Area Intg	FWHM	Max Height	Center Grvty	Area IntgP
1	Gaussian	1.72101	12.72319	0.12707	1255.38049	46.55129
2	Gaussian	0.10173	11.22226	0.00852	1311.14194	2.75162
3	Gaussian	1.81569	25.99334	0.06578	1250.95759	49.11242
4	Gaussian	0.05859	9.66117	0.0057	1270.25977	1.58468

## FTIR analysis – Day 4

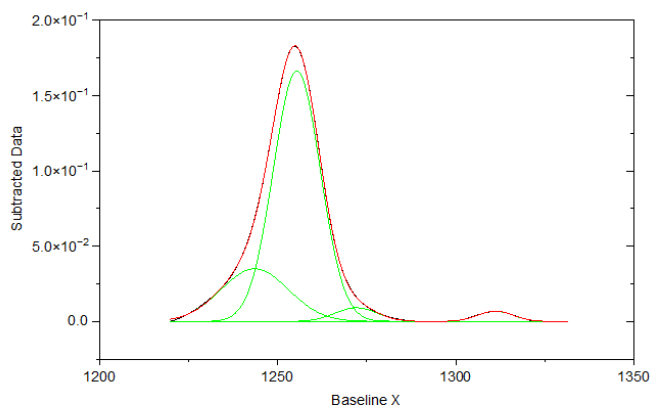


Fitting Results

Peak Index	Peak Type	Area Intg	FWHM	Max Height	Center Grvty	Area IntgP
1	Gaussian	1.5729	12.87325	0.11478	1255.408	44.85949
2	Gaussian	0.09175	11.75314	0.00733	1310.88325	2.61666
3	Gaussian	1.78664	26.17442	0.06428	1251.15456	50.95531
4	Gaussian	0.055	10.45261	0.00494	1270.65095	1.56853

*ELP in solvent (chapter 3.1.2.1)*

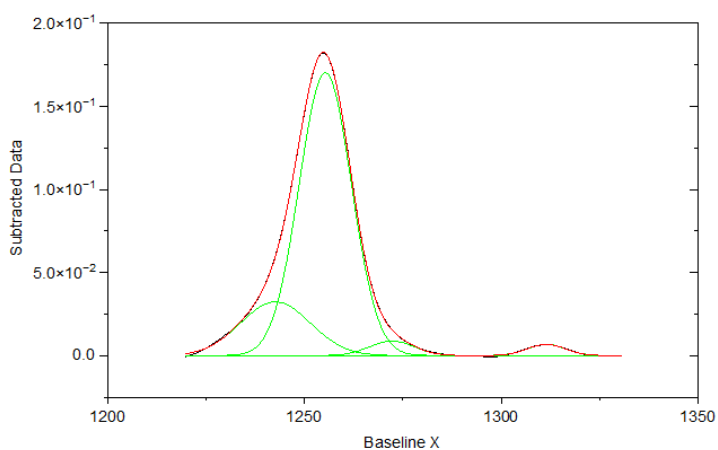
FTIR graph – Sample 1



Fitting Results

Peak Index	Peak Type	Area Intg	FWHM	Max Height	Center Grvty	Area IntgP
1	Gaussian	2.74796	15.51381	0.1664	1255.37022	72.49398
2	Gaussian	0.08521	11.69879	0.00684	1311.12403	2.24796
3	Gaussian	0.8234	22.25485	0.03497	1243.54879	21.72228
4	Gaussian	0.13403	13.92349	0.00904	1272.07704	3.53579

FTIR graph – Sample 2

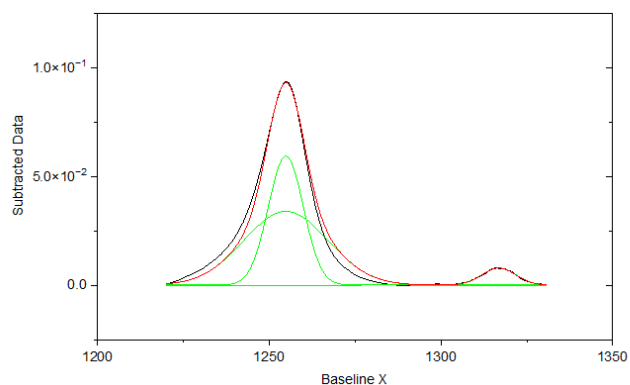


Fitting Results

Peak Index	Peak Type	Area Intg	FWHM	Max Height	Center Grvty	Area IntgP
1	Gaussian	2.83188	15.62758	0.17024	1255.29969	75.41658
2	Gaussian	0.71603	20.89327	0.03236	1242.62138	19.0688
3	Gaussian	0.08198	11.38955	0.00676	1311.48881	2.1832
4	Gaussian	0.12509	13.39597	0.00877	1272.20719	3.33142

PMDI-ELP gel cross-linked in fume hood (chapter 3.1.2.2)

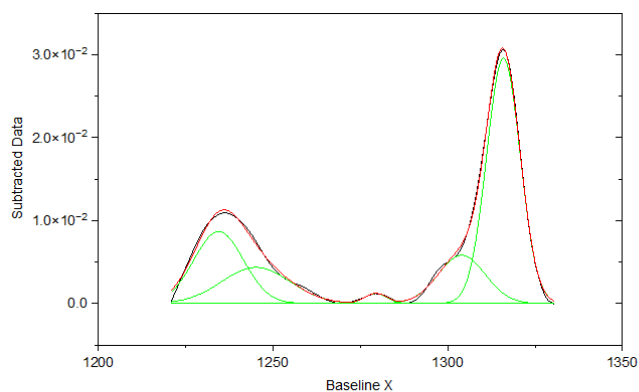
FTIR analysis – Day 1



Fitting Results

Peak Index	Peak Type	Area Intg	FWHM	Max Height	Center Grvty	Area IntgP
1	Gaussian	0.09688	11.62818	0.00784	1316.8583	5.11264
2	Gaussian	0.76078	12.07088	0.05921	1254.82312	40.14847
3	Gaussian	1.03726	28.80771	0.0339	1254.82313	54.73889

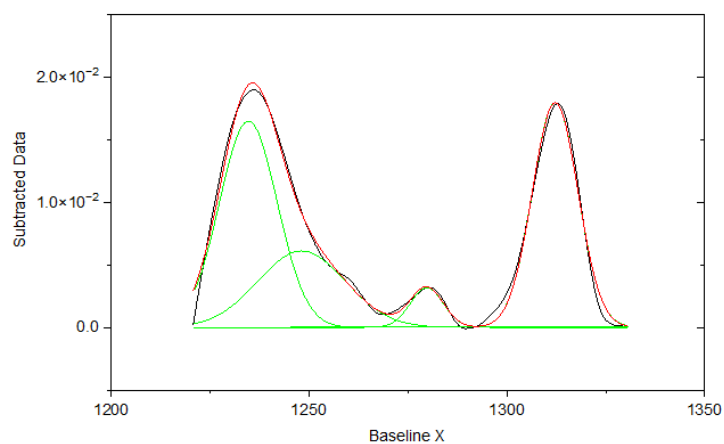
FTIR analysis – Day 2



Fitting Results

Peak Index	Peak Type	Area Intg	FWHM	Max Height	Center Grvty	Area IntgP
1	Gaussian	0.1501	16.7256	0.00866	1234.42424	20.88265
2	Gaussian	0.10601	23.04214	0.00435	1245.07424	14.74908
3	Gaussian	0.00944	7.32156	0.00121	1279.42062	1.31348
4	Gaussian	0.09807	15.85631	0.00581	1304.01072	13.64446
5	Gaussian	0.35515	11.29983	0.02956	1315.95078	49.41033

FTIR analysis – Day 3

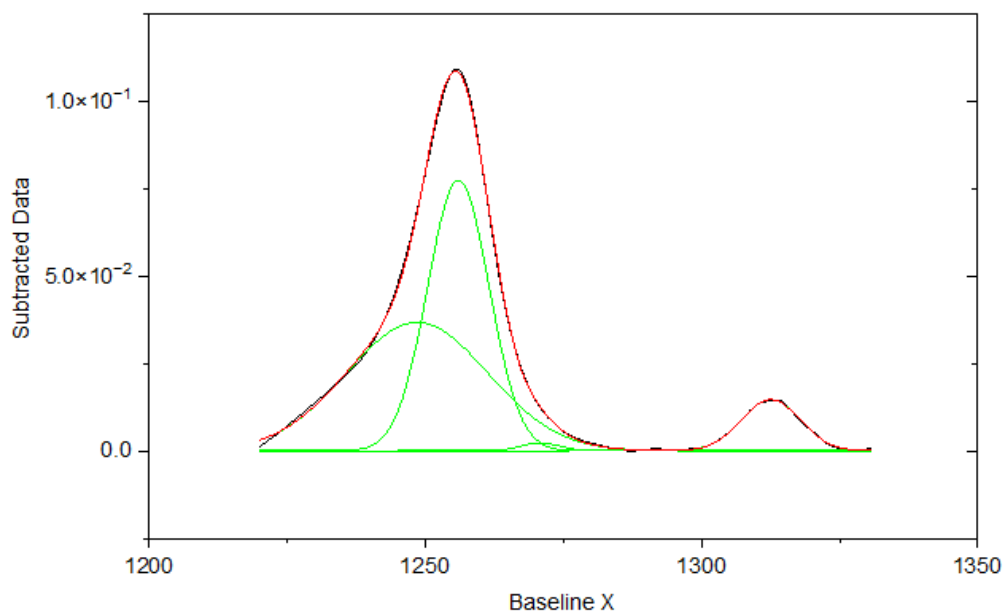


Fitting Results

Peak Index	Peak Type	Area Intg	FWHM	Max Height	Center Grvty	Area IntgP
1	Gaussian	0.29324	17.2274	0.01646	1234.64011	38.97514
2	Gaussian	0.16731	25.95491	0.0061	1248.09625	22.23677
3	Gaussian	0.03312	9.84441	0.00316	1279.7584	4.4016
4	Gaussian	0.25872	13.56074	0.01794	1312.21881	34.38649

*PMDI-ELP gel cross-linked in glovebox (chapter 3.1.2.2)*

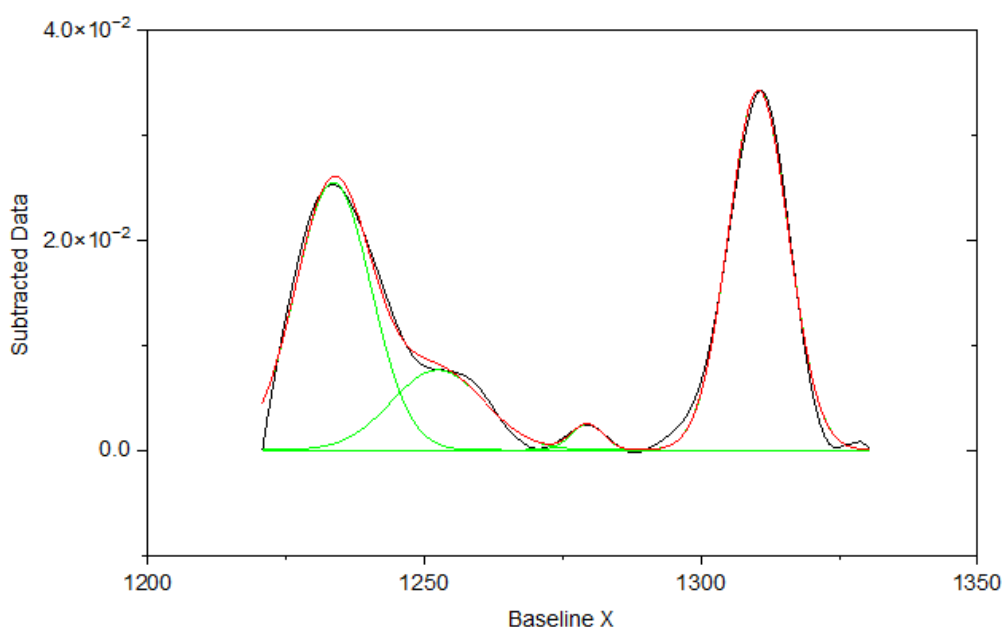
FTIR analysis – Day 1



Fitting Results

Peak Index	Peak Type	Area Intg	FWHM	Max Height	Center Grvty	Area IntgP
1	Gaussian	1.08017	13.126	0.07731	1255.97619	43.98512
2	Gaussian	0.19482	12.5101	0.01463	1312.56365	7.93314
3	Gaussian	1.16135	30.1231	0.03669	1248.49401	47.29086
4	Gaussian	0.01942	8.09915	0.00225	1270.85896	0.79088

FTIR analysis – Day 2

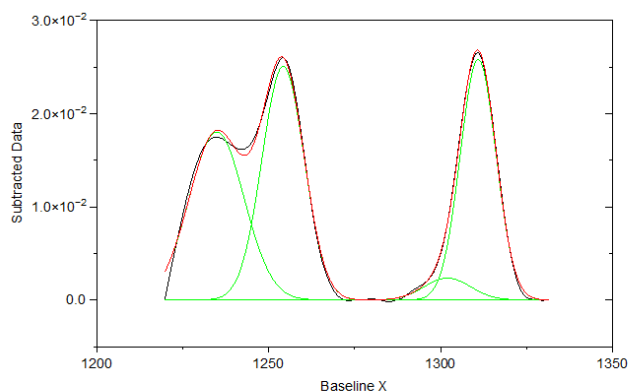


Fitting Results

Peak Index	Peak Type	Area Intg	FWHM	Max Height	Center Grvty	Area IntgP
1	Gaussian	0.4248	16.17522	0.02546	1233.52465	39.78998
2	Gaussian	0.15976	19.73283	0.00761	1252.43305	14.96462
3	Gaussian	0.46508	12.76037	0.03424	1310.4085	43.56302
4	Gaussian	0.01796	6.82636	0.00247	1279.4341	1.68238

PMDI-ELP gel cross-linked in vacuum oven (chapter 3.1.2.2)

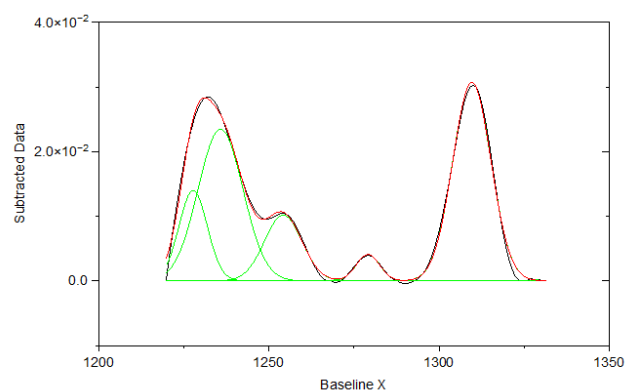
FTIR analysis – Day 1



Fitting Results

Peak Index	Peak Type	Area Intg	FWHM	Max Height	Center Gvnty	Area IntgP
1	Gaussian	0.38643	14.48353	0.02506	1254.20061	34.67527
2	Gaussian	0.3373	12.27144	0.02582	1310.94614	30.26693
3	Gaussian	0.03991	15.91313	0.00236	1301.98719	3.58106
4	Gaussian	0.35079	18.82775	0.01804	1234.85202	31.47674

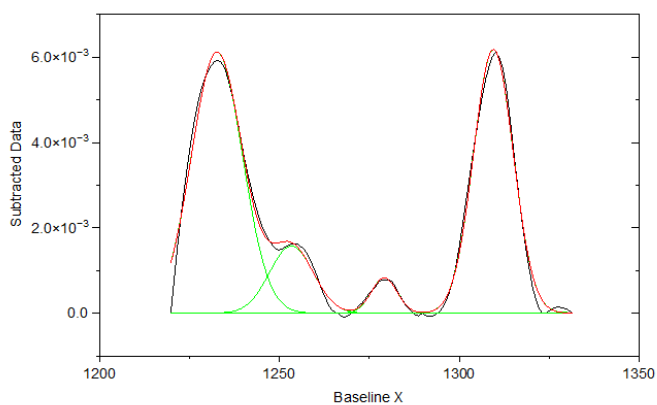
FTIR analysis – Day 2



Fitting Results

Peak Index	Peak Type	Area Intg	FWHM	Max Height	Center Gvnty	Area IntgP
1	Gaussian	0.43123	13.1951	0.0307	1309.65297	38.08659
2	Gaussian	0.14026	12.94984	0.01018	1254.18202	12.38807
3	Gaussian	0.14171	9.79346	0.01399	1227.71815	12.51576
4	Gaussian	0.03499	8.059	0.00408	1279.10454	3.09072
5	Gaussian	0.38404	15.47915	0.02348	1235.75645	33.91887

FTIR analysis – Day 3

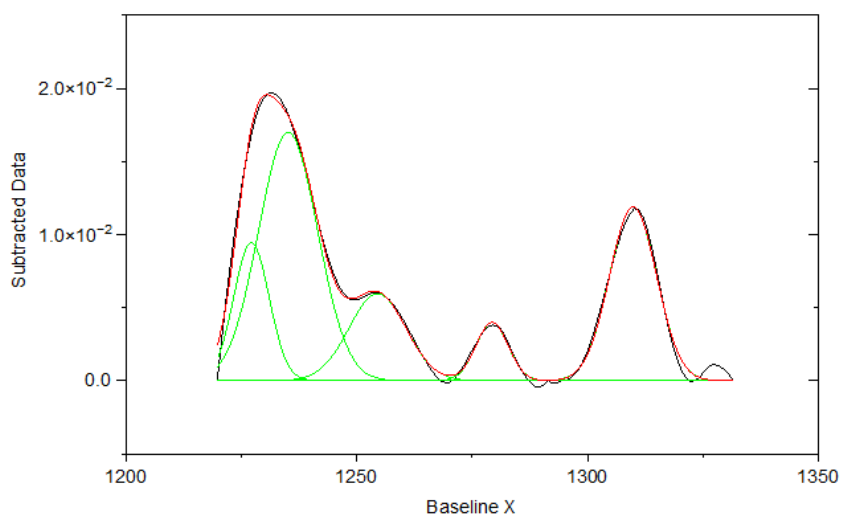


Fitting Results

Peak Index	Peak Type	Area Intg	FWHM	Max Height	Center Gvnty	Area IntgP
1	Gaussian	0.10484	16.68554	0.00612	1232.61125	47.23638
2	Gaussian	0.024	14.34013	0.00157	1253.30762	10.81511
3	Gaussian	0.00742	8.40009	8.293E-4	1279.13917	3.34104
4	Gaussian	0.08569	13.02903	0.00618	1309.50934	38.60747

## Drop casted solvent (chapter 3.1.2.2)

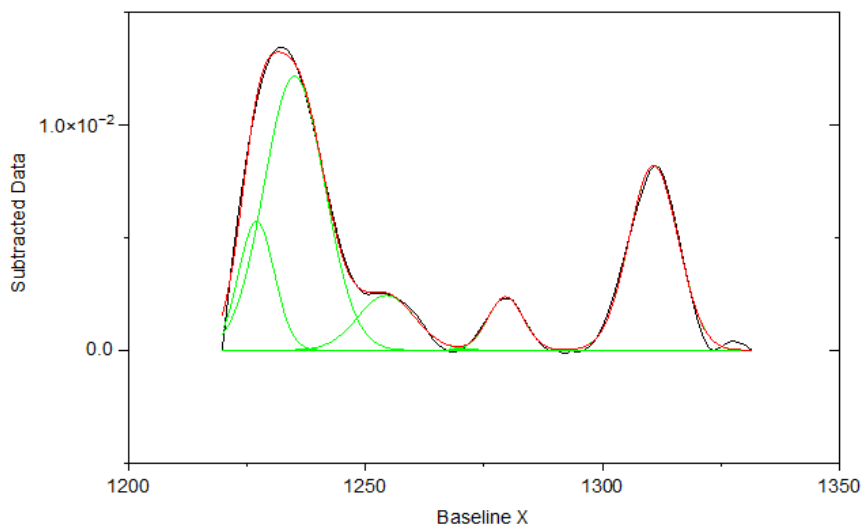
### FTIR graph – glovebox cross-linked



Fitting Results

Peak Index	Peak Type	Area Intg	FWHM	Max Height	Center Grvty	Area IntgP
1	Gaussian	0.27002	15.05451	0.01699	1235.11297	42.40156
2	Gaussian	0.09199	14.55384	0.00594	1254.46866	14.44528
3	Gaussian	0.03474	8.18406	0.00399	1279.32444	5.45461
4	Gaussian	0.15172	11.98607	0.01189	1309.88218	23.82529
5	Gaussian	0.08835	9.02831	0.00945	1227.15115	13.87325

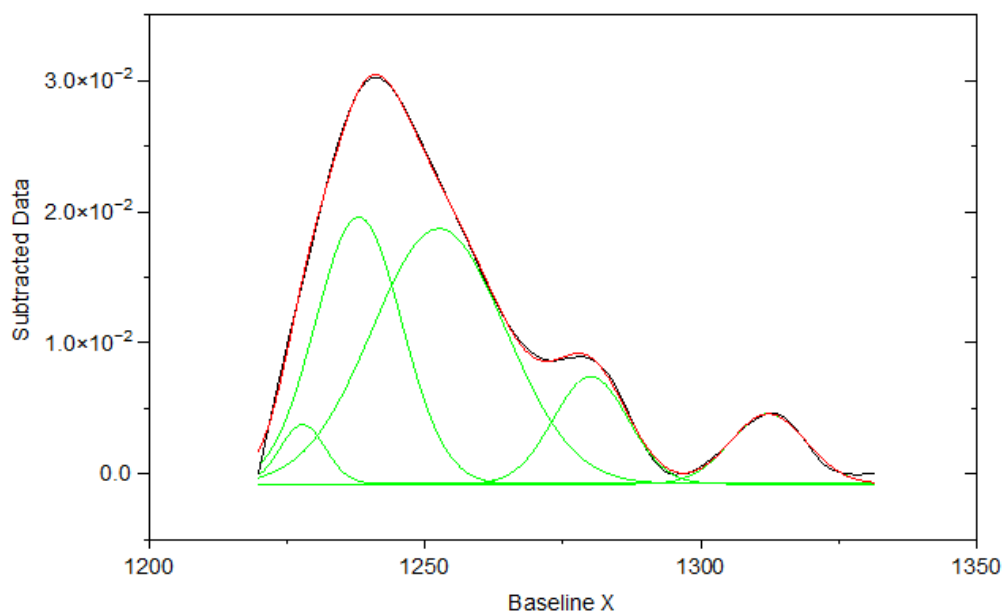
### FTIR graph – fume hood cross-linked



Fitting Results

Peak Index	Peak Type	Area Intg	FWHM	Max Height	Center Grvty	Area IntgP
1	Gaussian	0.19263	14.98781	0.01218	1235.00357	47.02857
2	Gaussian	0.03646	14.09112	0.00243	1254.37288	8.90122
3	Gaussian	0.02202	8.72427	0.00237	1279.55385	5.37708
4	Gaussian	0.10624	12.16053	0.00821	1310.78952	25.93835
5	Gaussian	0.05224	8.80504	0.00573	1227.00717	12.75477

*PMDI-ELP gel collapsed in DI water for 3 h(chapter 3.1.2.2)*

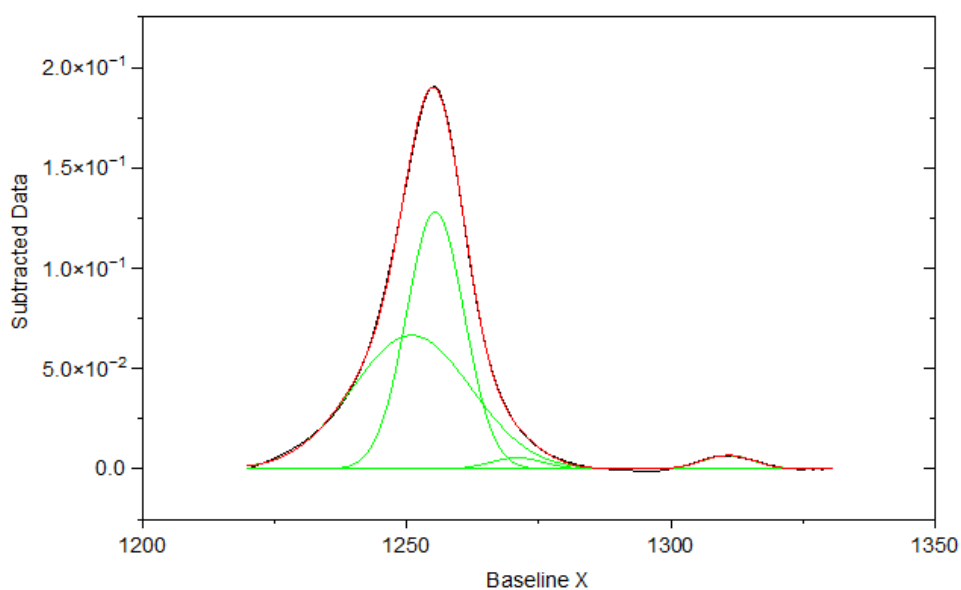


Fitting Results

Peak Index	Peak Type	Area Intg	FWHM	Max Height	Center Grvty	Area IntgP
1	Gaussian	0.04523	9.63675	0.00452	1227.84361	3.59335
2	Gaussian	0.39505	18.41253	0.02036	1237.96612	31.38359
3	Gaussian	0.58789	28.44752	0.01948	1252.53888	46.70311
4	Gaussian	0.13893	15.91888	0.0082	1280.03838	11.03669
5	Gaussian	0.09168	16.13645	0.00535	1312.25786	7.28325

Contained 0.5 wt% genipin-ELP gel (chapter 0)

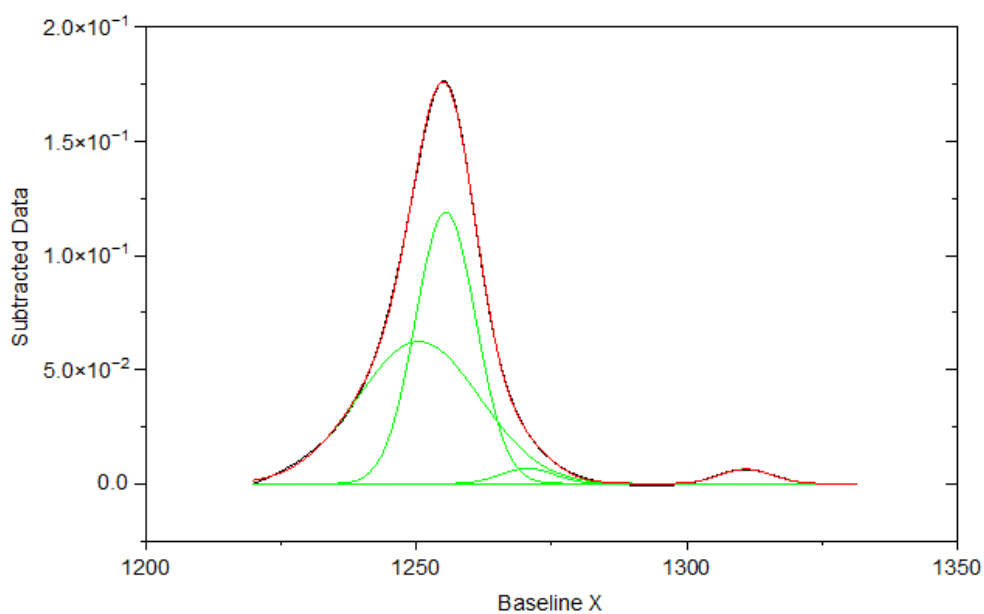
FTIR analysis – Day 0



Fitting Results

Peak Index	Peak Type	Area Intg	FWHM	Max Height	Center Grvty	Area IntgP
1	Gaussian	1.74882	12.82614	0.12809	1255.41387	46.4055
2	Gaussian	1.86709	26.43824	0.06653	1250.94456	49.54378
3	Gaussian	0.08292	11.37571	0.00685	1310.84295	2.2004
4	Gaussian	0.06973	11.56675	0.00566	1270.92255	1.85032

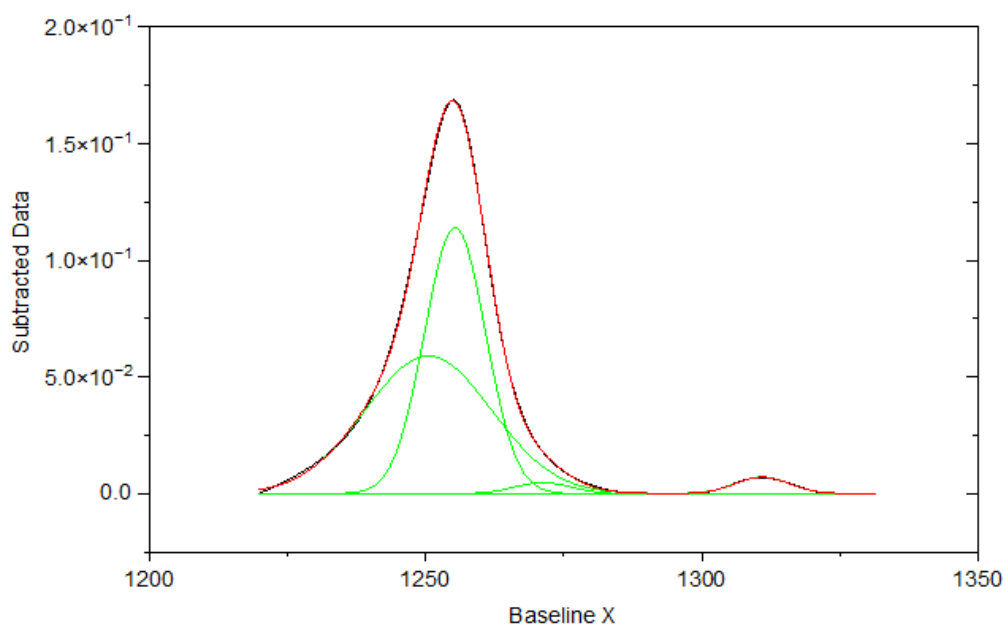
FTIR analysis – Day 1



Fitting Results

Peak Index	Peak Type	Area Intg	FWHM	Max Height	Center Grvty	Area IntgP
1	Gaussian	0.07682	11.29585	0.00639	1310.93157	2.14775
2	Gaussian	1.66091	13.11663	0.11896	1255.42318	46.4389
3	Gaussian	1.75592	26.57818	0.06227	1250.46223	49.0955
4	Gaussian	0.0829	11.48758	0.00678	1270.54831	2.31785

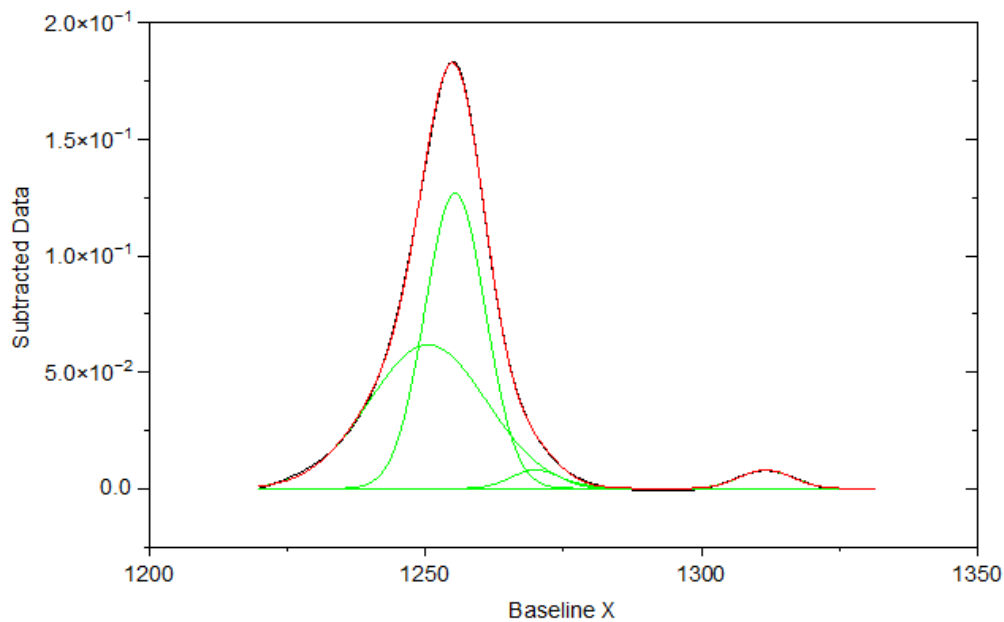
### FTIR analysis – Day 2



Fitting Results

Peak Index	Peak Type	Area Intg	FWHM	Max Height	Center Grvty	Area IntgP
1	Gaussian	1.57597	12.98882	0.11398	1255.32444	46.24907
2	Gaussian	1.68702	26.99513	0.05893	1250.49468	49.50795
3	Gaussian	0.08575	11.43624	0.00704	1310.94264	2.51658
4	Gaussian	0.05883	11.96584	0.00462	1271.2321	1.7264

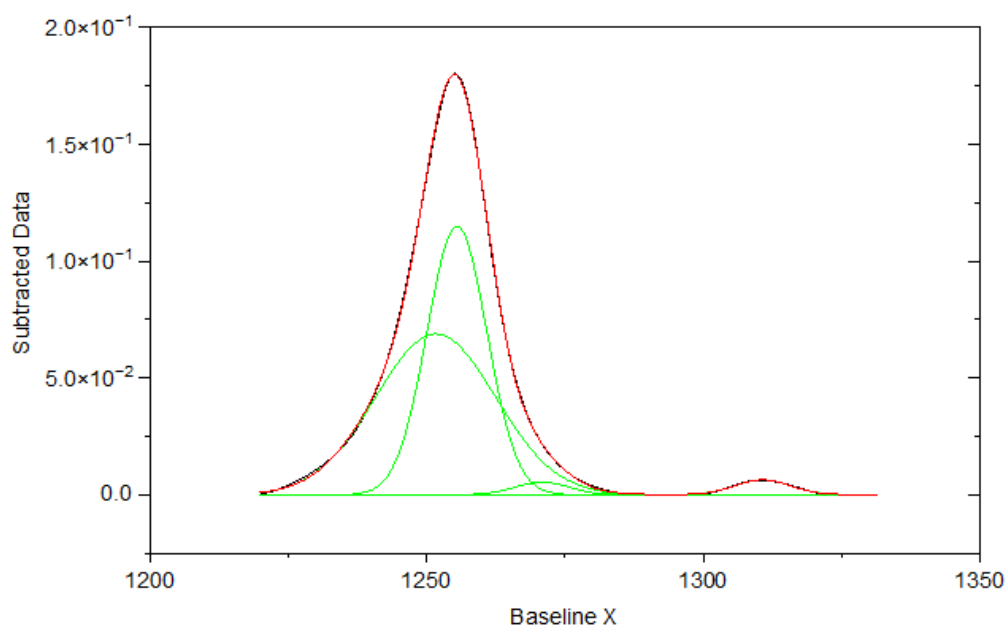
### FTIR analysis – Day 3



Fitting Results

Peak Index	Peak Type	Area Intg	FWHM	Max Height	Center Grvty	Area IntgP
1	Gaussian	1.7381	12.86002	0.12697	1255.39011	48.69183
2	Gaussian	0.09553	11.27427	0.00796	1311.66465	2.67627
3	Gaussian	1.64666	25.10459	0.06174	1250.45228	46.13023
4	Gaussian	0.0893	10.40243	0.00806	1269.97211	2.50167

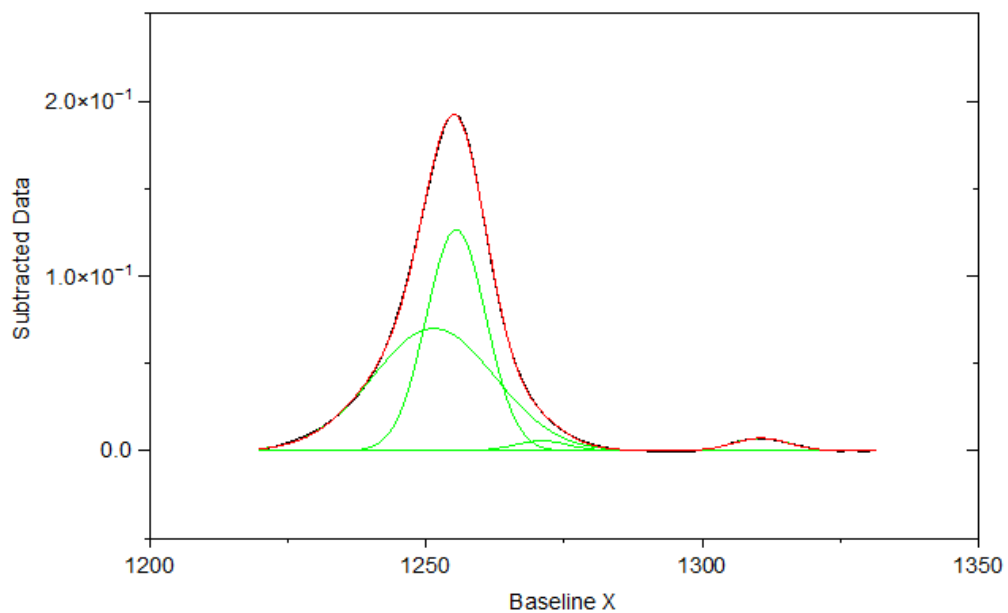
### FTIR analysis – Day 4



Fitting Results

Peak Index	Peak Type	Area Intg	FWHM	Max Height	Center Grvty	Area IntgP
1	Gaussian	0.07964	11.77009	0.00636	1310.76164	2.22604
2	Gaussian	1.5611	12.77197	0.11483	1255.46683	43.63581
3	Gaussian	1.87131	25.61262	0.06875	1251.61334	52.30674
4	Gaussian	0.06552	11.49671	0.00535	1270.83331	1.83141

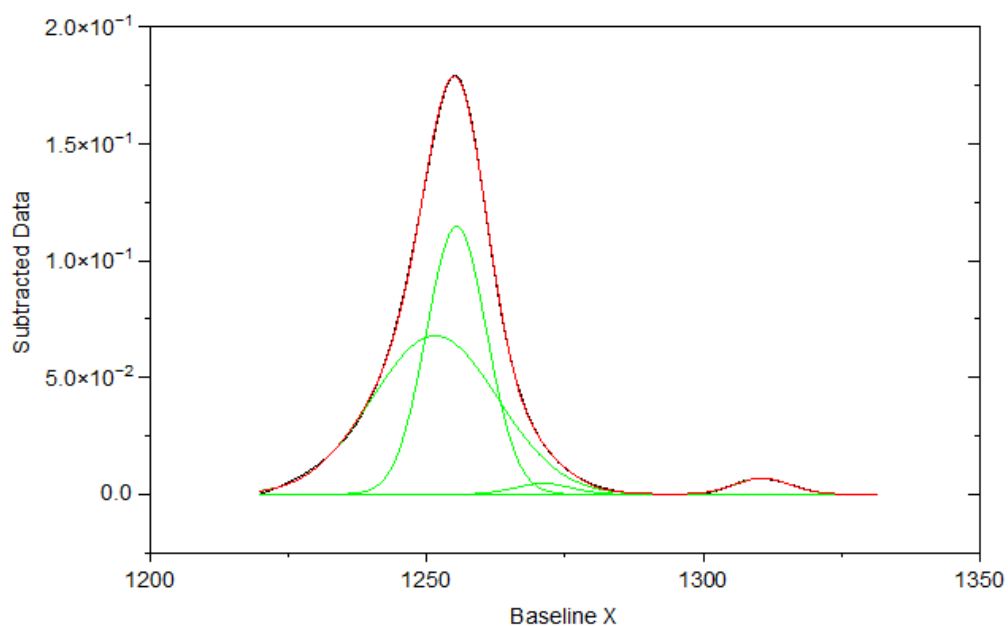
### FTIR analysis – Day 5



Fitting Results

Peak Index	Peak Type	Area Intg	FWHM	Max Height	Center Grvty	Area IntgP
1	Gaussian	1.71204	12.72114	0.12643	1255.44859	45.00381
2	Gaussian	1.93369	26.02837	0.06994	1251.39055	50.83005
3	Gaussian	0.09018	11.72989	0.00722	1310.62354	2.37064
4	Gaussian	0.0683	11.36174	0.00565	1270.86642	1.7955

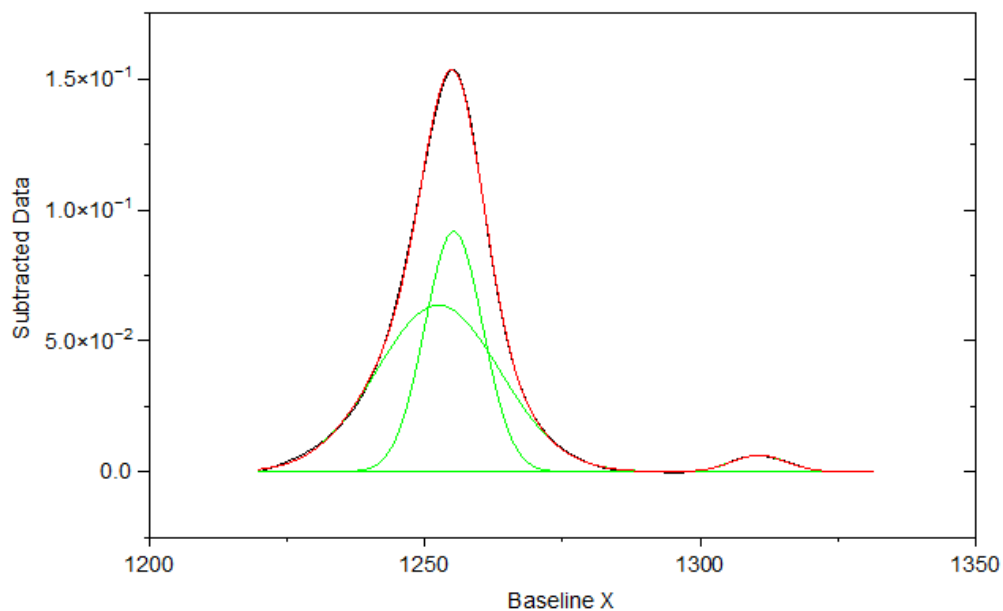
### FTIR analysis – Day 6



Fitting Results

Peak Index	Peak Type	Area Intg	FWHM	Max Height	Center Grvty	Area IntgP
1	Gaussian	1.5661	12.84122	0.11457	1255.40222	43.1312
2	Gaussian	0.08484	11.66834	0.00683	1310.66765	2.33646
3	Gaussian	1.92241	26.69496	0.06783	1251.505	52.94439
4	Gaussian	0.05766	11.79653	0.00459	1271.08158	1.58796

### FTIR analysis – Day 7

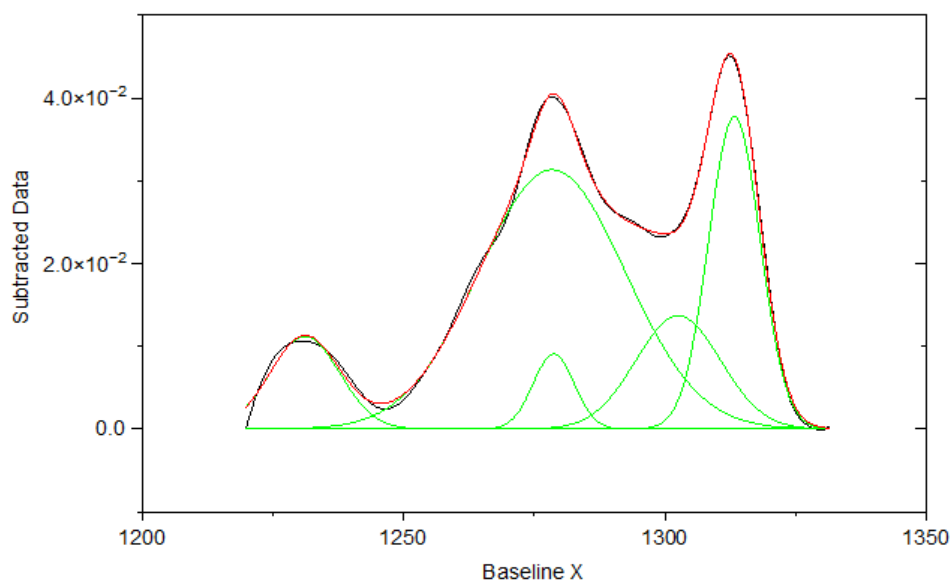


Fitting Results

Peak Index	Peak Type	Area Intg	FWHM	Max Height	Center Grvty	Area IntgP
1	Gaussian	1.20878	12.38942	0.09166	1255.26276	39.39774
2	Gaussian	1.78192	26.38139	0.06357	1252.4336	58.078
3	Gaussian	0.07745	11.60663	0.00627	1310.64896	2.52426

0.5 wt% genipin-ELP gel cross-linked in fume hood (chapter 0)

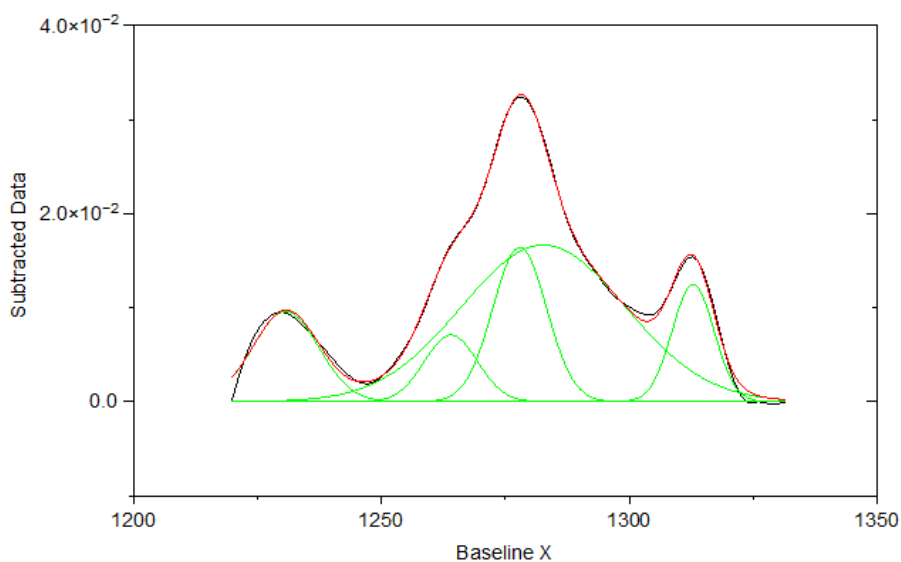
FTIR analysis – Day 1



Fitting Results

Peak Index	Peak Type	Area Intg	FWHM	Max Height	Center Grvty	Area IntgP
1	Gaussian	0.2783	19.11931	0.01368	1302.56395	13.17099
2	Gaussian	0.46605	11.60271	0.03774	1313.30457	22.05666
3	Gaussian	1.10141	33.02521	0.03133	1278.39493	52.12616
4	Gaussian	0.17851	15.64929	0.01121	1231.08745	8.44832
5	Gaussian	0.0887	9.22946	0.00903	1278.71367	4.19787

FTIR analysis – Day 2

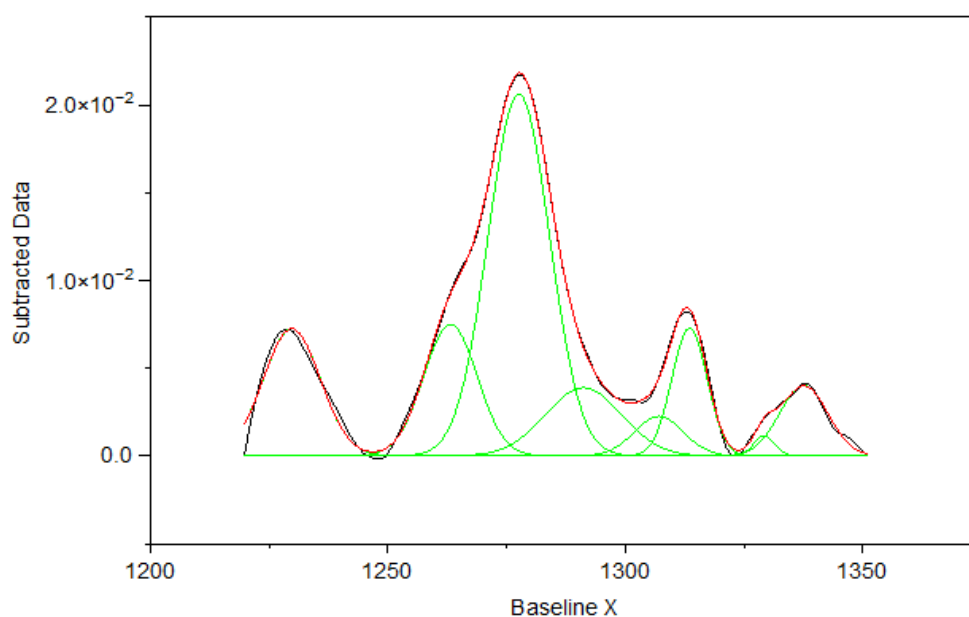


Fitting Results

Peak Index	Peak Type	Area Intg	FWHM	Max Height	Center Grvty	Area IntgP
1	Gaussian	0.13166	9.93174	0.01245	1312.89854	10.20118
2	Gaussian	0.68879	38.90923	0.01666	1282.68709	53.36969
3	Gaussian	0.1519	15.64444	0.00961	1230.66731	11.76999
4	Gaussian	0.2235	12.7816	0.01643	1277.90469	17.31789
5	Gaussian	0.09475	12.56162	0.00709	1264.02839	7.34126

0.5 wt% genipin-ELP gel cross-linked in glovebox (chapter 0)

FTIR analysis – Day 1

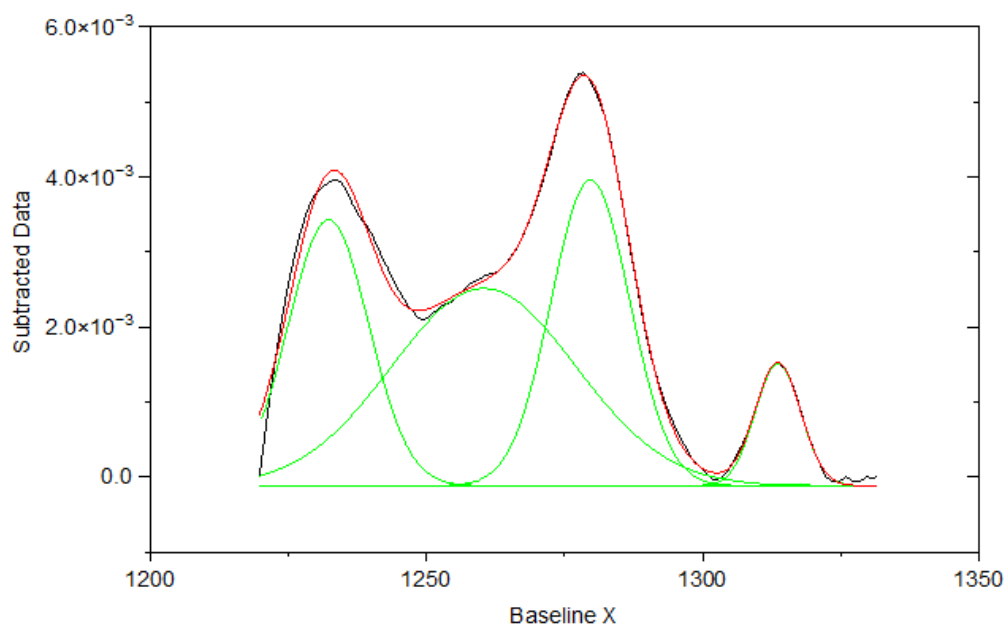


Fitting Results

Peak Index	Peak Type	Area Intg	FWHM	Max Height	Center Grvty	Area IntgP
1	Gaussian	0.10377	14.14515	0.00724	1229.78461	13.35644
2	Gaussian	0.10573	13.26575	0.00749	1263.2043	13.60871
3	Gaussian	0.33519	15.27952	0.02061	1277.6133	43.14112
4	Gaussian	0.06782	8.75678	0.00728	1313.55426	8.7284
5	Gaussian	0.05076	11.96748	0.004	1337.61372	6.53373
6	Gaussian	0.00636	5.20411	0.00115	1329.27436	0.81814
7	Gaussian	0.07817	18.92319	0.00388	1291.21292	10.0609
8	Gaussian	0.02916	12.17021	0.00225	1307.1044	3.75255

0.5 wt% genipin-ELP gel cross-linked in vacuum oven (chapter 0)

FTIR analysis – Day 1



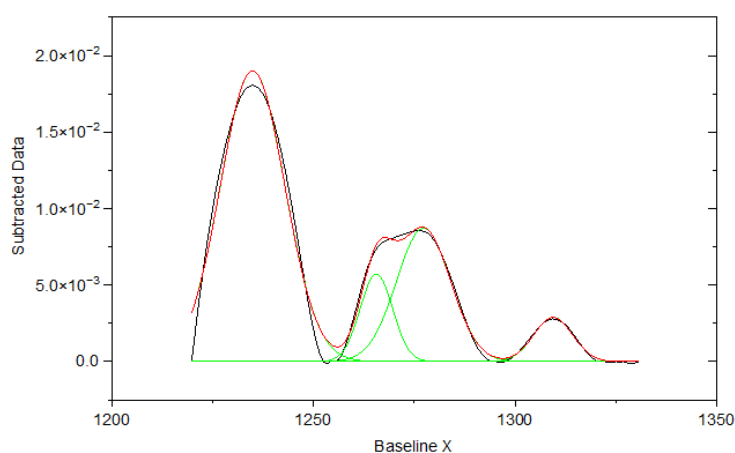
Fitting Results

Peak Index	Peak Type	Area Intg	FWHM	Max Height	Center Grvty	Area IntgP
1	Gaussian	0.0619	17.13669	0.00355	1232.26034	23.77466
2	Gaussian	0.10889	39.18362	0.00263	1260.37288	41.82072
3	Gaussian	0.07284	16.78312	0.00408	1279.6929	27.97549
4	Gaussian	0.01674	9.65251	0.00163	1313.64986	6.42913

0.1 wt% PMDI-ELP membranes (chapter 3.3.1.1)

	beta sheets	random coil	beta turns	alpha helix
S1P1	60.8	9.5	24	5.7
S1P2	76.8	-	7.7	12.8
S2P1	81.6	-	10	8.4
S2P2	77.5	-	10.4	12.1
S3P1	79.1	-	9.5	11.4
S3P2	75	-	11	13.9
<b>Average</b>	<b>75.12</b>	<b>1.58</b>	<b>12.10</b>	<b>10.72</b>
<b>St. Dev.</b>	<b>7.36</b>	<b>3.88</b>	<b>5.94</b>	<b>3.08</b>

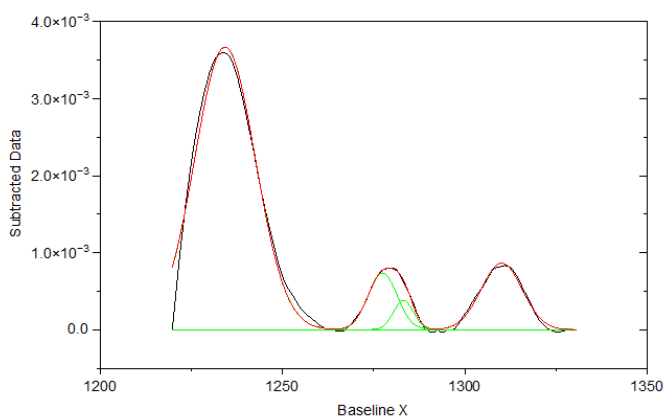
Corresponding FTIR graph S1P1



Fitting Results

Peak Index	Peak Type	Area Intg	FWHM	Max Height	Center Grvty	Area IntgP
1	Gaussian	0.36945	18.82649	0.01899	1234.8825	60.77571
2	Gaussian	0.05757	9.44763	0.00572	1265.60036	9.47046
3	Gaussian	0.1461	15.75635	0.00871	1277.30274	24.03428
4	Gaussian	0.03477	11.29342	0.00289	1309.46194	5.71954

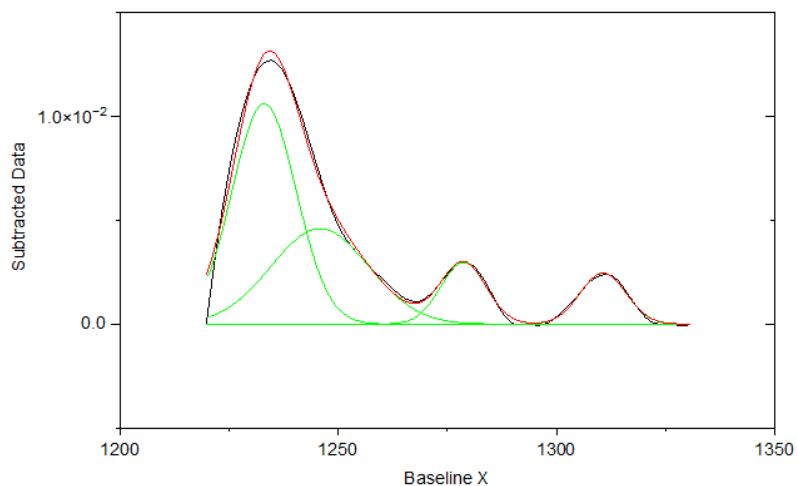
Corresponding FTIR graph S1P2



Fitting Results

Peak Index	Peak Type	Area Intg	FWHM	Max Height	Center Grvty	Area IntgP
1	Gaussian	0.07328	19.56506	0.00367	1234.21965	76.77844
2	Gaussian	0.00733	9.39537	7.33223E-4	1277.47139	7.68268
3	Gaussian	0.00261	6.44736	3.80331E-4	1283.17937	2.73468
4	Gaussian	0.01222	13.28272	8.64493E-4	1310.11992	12.8042

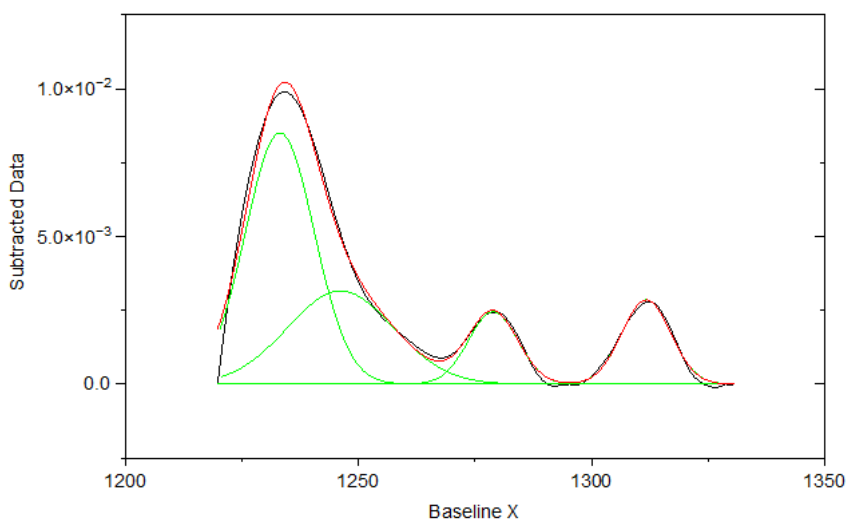
Corresponding FTIR graph S2P1



Fitting Results

Peak Index	Peak Type	Area Intg	FWHM	Max Height	Center Grvty	Area IntgP
1	Gaussian	0.18858	17.31179	0.01061	1233.0209	48.69467
2	Gaussian	0.03874	12.26862	0.00297	1278.67141	10.0028
3	Gaussian	0.12747	26.3161	0.0046	1245.77787	32.91532
4	Gaussian	0.03248	12.39574	0.00246	1310.69106	8.3872

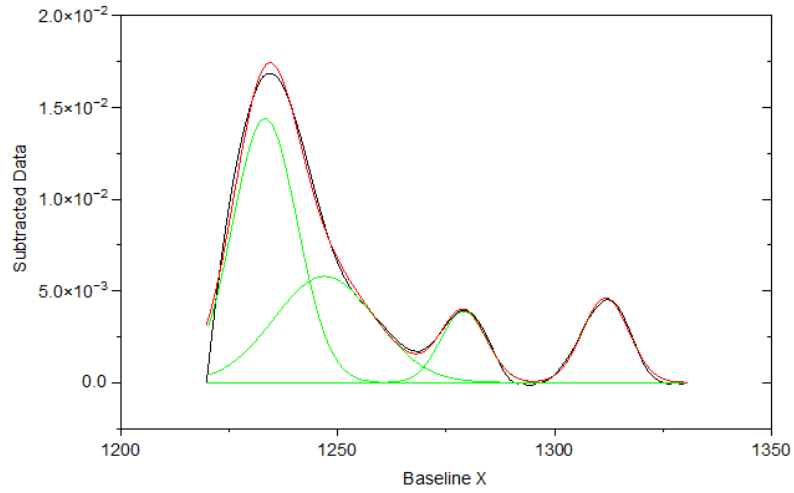
Corresponding FTIR graph S2P2



Fitting Results

Peak Index	Peak Type	Area Intg	FWHM	Max Height	Center Grvty	Area IntgP
1	Gaussian	0.15174	17.37958	0.0085	1233.12584	48.85338
2	Gaussian	0.03242	12.452	0.00245	1278.88896	10.43669
3	Gaussian	0.03755	12.38487	0.00285	1311.75061	12.08915
4	Gaussian	0.08889	26.77335	0.00315	1246.13396	28.62079

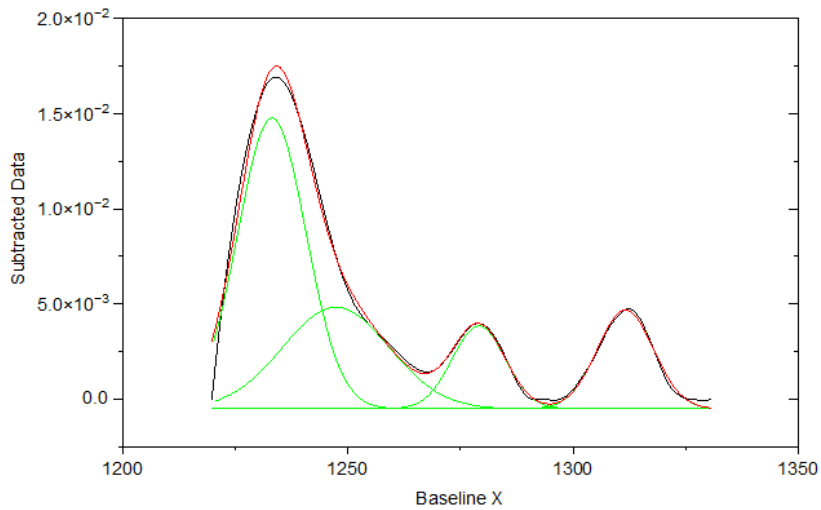
Corresponding FTIR graph S3P1



Fitting Results

Peak Index	Peak Type	Area Intg	FWHM	Max Height	Center Grvty	Area IntgP
1	Gaussian	0.25895	17.52911	0.01438	1233.26025	48.04667
2	Gaussian	0.05123	12.38502	0.00389	1279.01552	9.5058
3	Gaussian	0.06158	12.54517	0.00461	1311.78054	11.42611
4	Gaussian	0.16719	27.38613	0.00579	1246.9969	31.02143

Corresponding FTIR graph S3P2



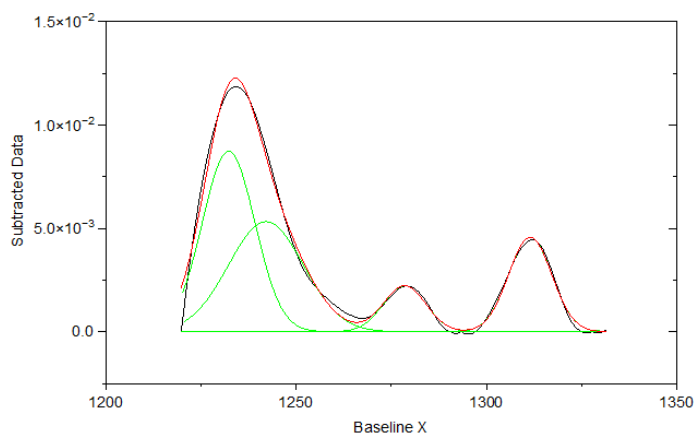
Fitting Results

Peak Index	Peak Type	Area Intg	FWHM	Max Height	Center Grvty	Area IntgP
1	Gaussian	0.27892	17.83677	0.01529	1233.1293	48.05717
2	Gaussian	0.0641	13.84318	0.00435	1279.06509	11.04505
3	Gaussian	0.08087	14.6495	0.00519	1311.6395	13.933
4	Gaussian	0.1565	27.76084	0.00535	1247.31944	26.96478

0.2 wt% PMDI-ELP membranes (chapter 3.3.1.1)

Summary	beta sheets	random coil	beta turns	alpha helix
S1P1	74.2	-	8.4	17.5
S1P2	67.8	-	8.3	23.8
S2P1	74	-	7.8	18.2
S2P2	75.1	-	10.2	14.7
S3P1	78.5	-	8.5	13
S3P2	79.7	-	8.6	11.7
<b>Average</b>	<b>74.88</b>	<b>-</b>	<b>8.63</b>	<b>16.48</b>
<b>St. Dev.</b>	<b>4.19</b>	<b>-</b>	<b>0.82</b>	<b>4.38</b>

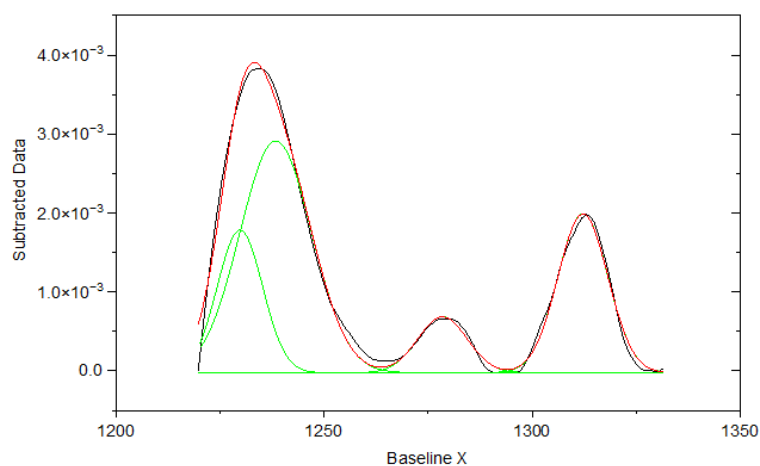
Corresponding FTIR graph S1P1



Fitting Results

Peak Index	Peak Type	Area Intg	FWHM	Max Height	Center Grvty	Area IntgP
1	Gaussian	0.14567	16.24965	0.00873	1232.23386	39.21355
2	Gaussian	0.03103	13.09203	0.00223	1278.51385	8.35427
3	Gaussian	0.06488	13.33426	0.00457	1311.50347	17.46509
4	Gaussian	0.12989	23.18161	0.00533	1242.05	34.96709

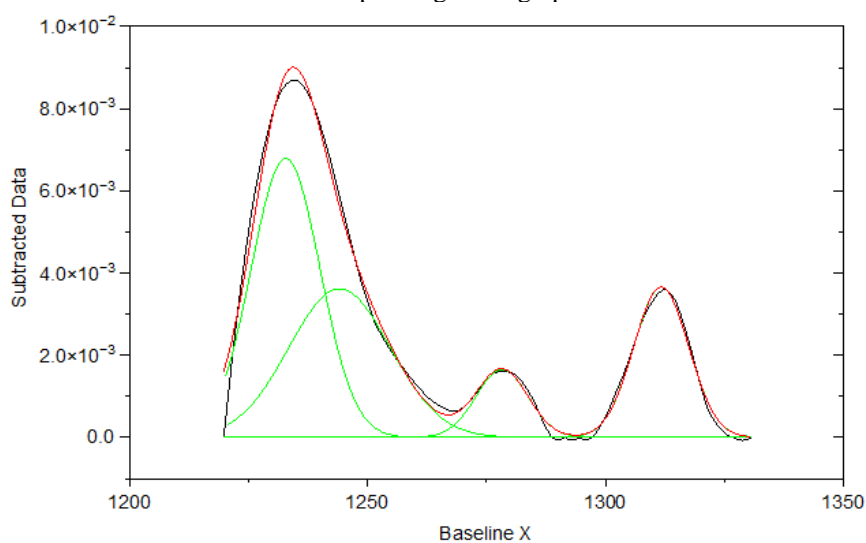
Corresponding FTIR graph S1P2



Fitting Results

Peak Index	Peak Type	Area Intg	FWHM	Max Height	Center Grvty	Area IntgP
1	Gaussian	0.02382	12.80269	0.00181	1229.77266	18.76498
2	Gaussian	0.01056	13.99177	7.09223E-4	1278.44933	8.3229
3	Gaussian	0.03024	14.12992	0.00201	1312.21647	23.82987
4	Gaussian	0.06229	20.24077	0.00294	1238.37467	49.08225

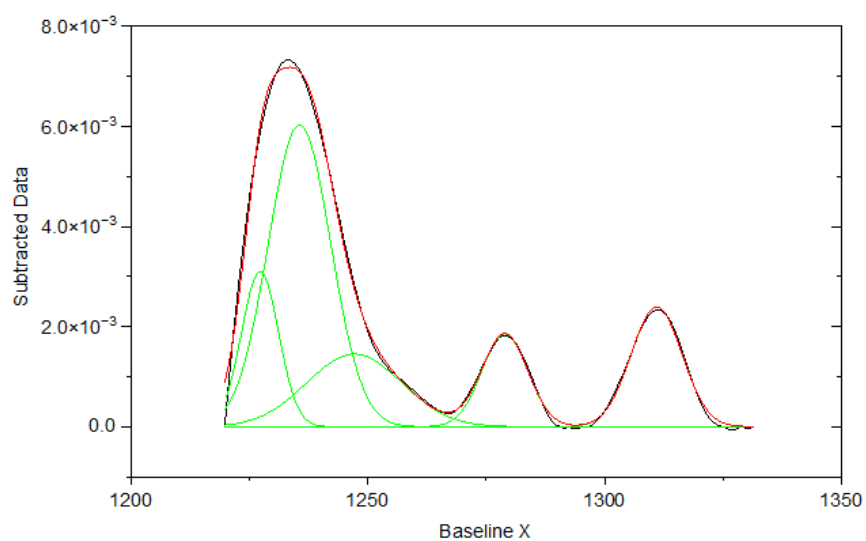
Corresponding FTIR graph S2P1



Fitting Results

Peak Index	Peak Type	Area Intg	FWHM	Max Height	Center Grvty	Area IntgP
1	Gaussian	0.11861	17.02747	0.00679	1232.77494	40.9939
2	Gaussian	0.09538	25.04202	0.00362	1244.09777	32.96655
3	Gaussian	0.0528	13.56164	0.00366	1311.73194	18.24943
4	Gaussian	0.02254	12.8098	0.00165	1278.25504	7.79012

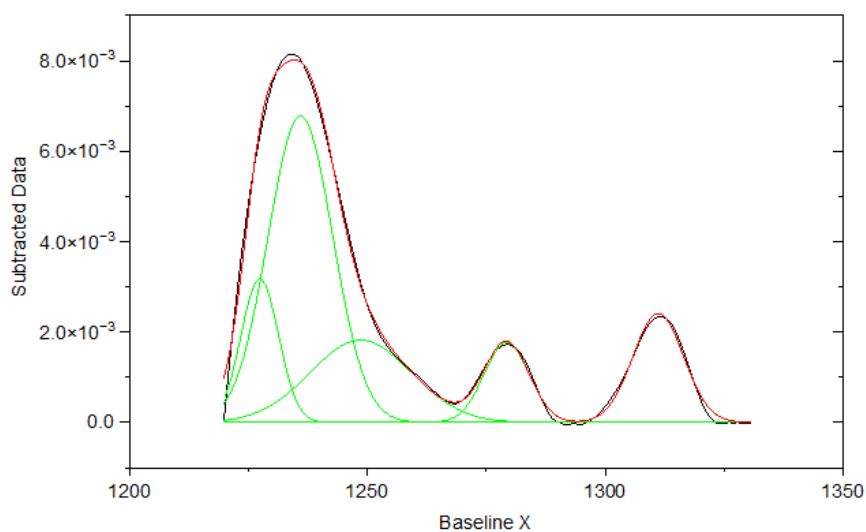
Corresponding FTIR graph S2P2



Fitting Results

Peak Index	Peak Type	Area Intg	FWHM	Max Height	Center Grvty	Area IntgP
1	Gaussian	0.02959	9.23201	0.0031	1227.23434	13.48034
2	Gaussian	0.02241	11.35892	0.00185	1278.9274	10.2096
3	Gaussian	0.03222	12.66065	0.00239	1310.98695	14.67823
4	Gaussian	0.09902	15.55465	0.00603	1235.56994	45.1153
5	Gaussian	0.03625	23.53294	0.00145	1247.14058	16.51652

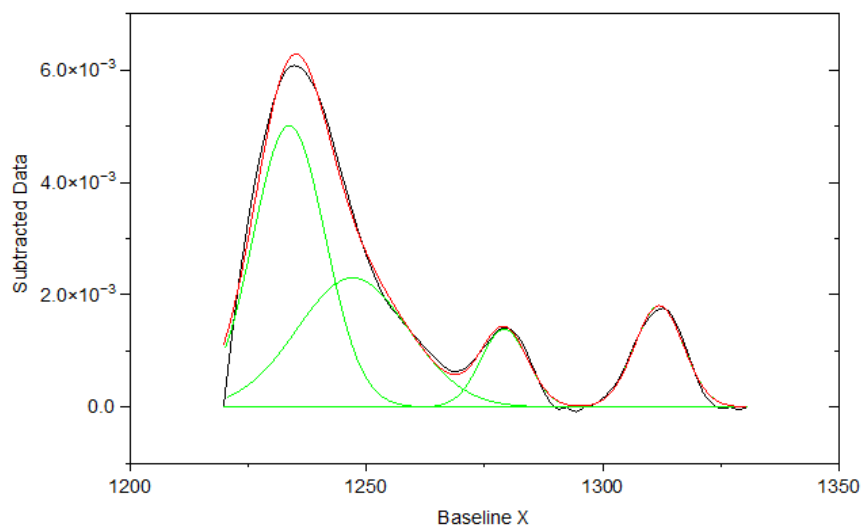
Corresponding FTIR graph S3P1



Fitting Results

Peak Index	Peak Type	Area Intg	FWHM	Max Height	Center Grvty	Area IntgP
1	Gaussian	0.0306	9.31843	0.00317	1227.36397	12.39681
2	Gaussian	0.02093	11.12358	0.00177	1279.26684	8.47988
3	Gaussian	0.03217	12.55388	0.00241	1311.16867	13.03428
4	Gaussian	0.1147	16.05417	0.00677	1235.91571	46.46945
5	Gaussian	0.04843	25.0868	0.00182	1248.56217	19.61958

Corresponding FTIR graph S3P2



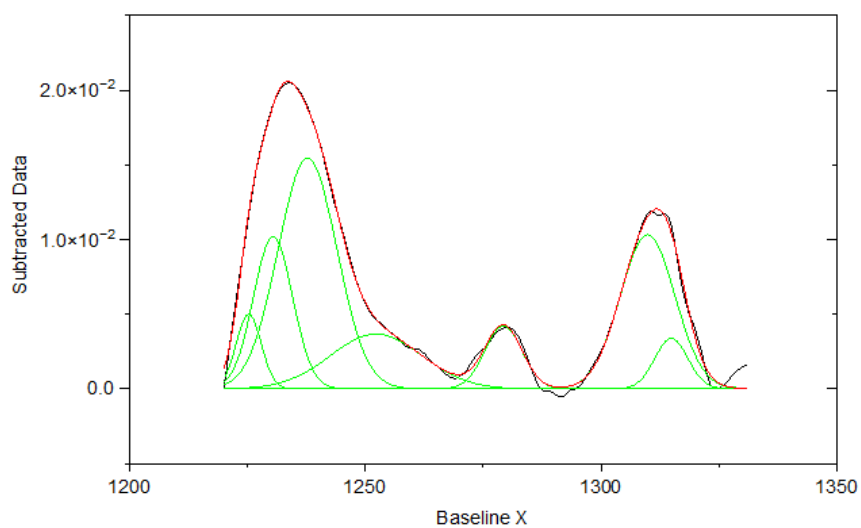
Fitting Results

Peak Index	Peak Type	Area Intg	FWHM	Max Height	Center Grvty	Area IntgP
1	Gaussian	0.09265	17.98478	0.00501	1233.67556	46.272
2	Gaussian	0.0669	27.61703	0.0023	1247.09908	33.41221
3	Gaussian	0.02339	12.18112	0.0018	1311.94887	11.68151
4	Gaussian	0.01729	11.73921	0.00138	1279.16571	8.63427

0.3 wt% PMDI-ELP membranes (chapter 3.3.1.1)

Summary	beta sheets	random coil	beta turns	alpha helix
S1P1	54.9	13	6.1	26.2
S1P2	57.7	9.4	6	26.9
S2P1	57.5	10.5	5.8	26.2
S2P2	63.1	0.4	5.8	30.7
S3P1	54.1	1.4	12.5	32
S3P2	67.9	-	6.4	25.7
<b>Average</b>	<b>59.20</b>	<b>5.78</b>	<b>7.10</b>	<b>27.95</b>
<b>St. Dev.</b>	<b>5.30</b>	<b>5.81</b>	<b>2.65</b>	<b>2.69</b>

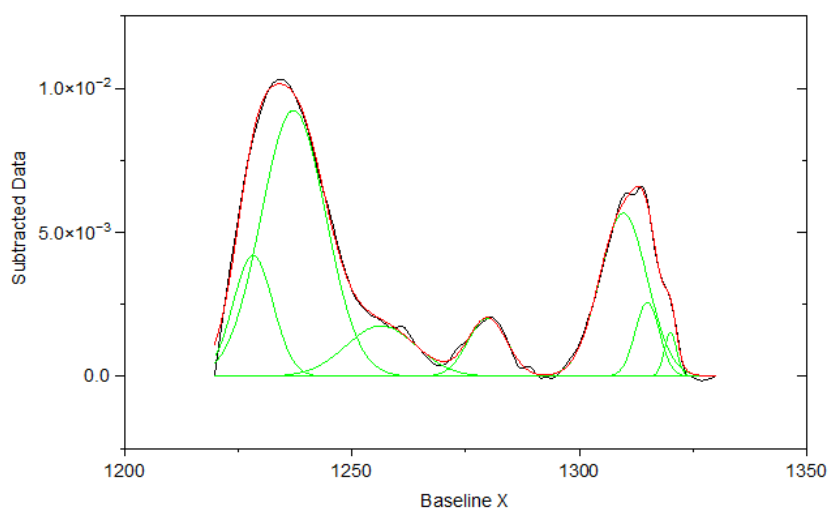
Corresponding FTIR graph S1P1



Fitting Results

Peak Index	Peak Type	Area Intg	FWHM	Max Height	Center Grvty	Area IntgP
1	Gaussian	0.24043	14.65327	0.01545	1237.75353	34.9418
2	Gaussian	0.0893	22.87154	0.00367	1252.30617	12.97814
3	Gaussian	0.0417	9.31474	0.00421	1279.3113	6.06031
4	Gaussian	0.14959	13.61443	0.01032	1309.89183	21.74053
5	Gaussian	0.02953	8.22066	0.00338	1314.91708	4.29231
6	Gaussian	0.10513	9.74649	0.01019	1230.43646	15.27865
7	Gaussian	0.0324	6.24303	0.00499	1225.27841	4.70826

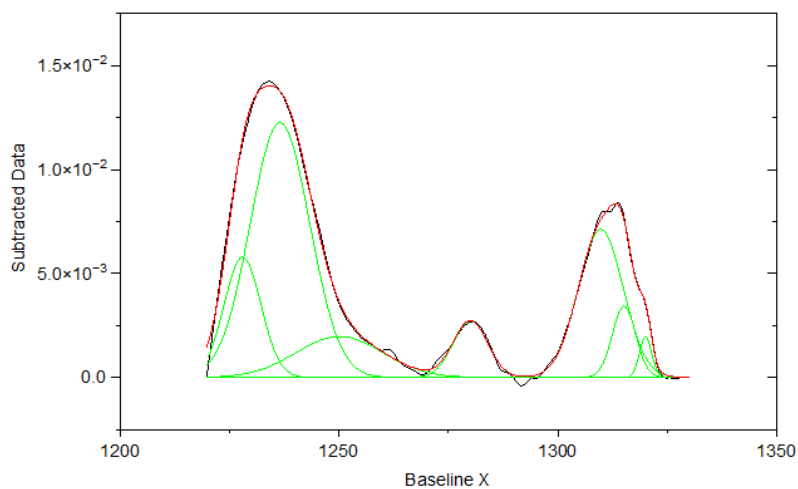
Corresponding FTIR graph S1P2



Fitting Results

Peak Index	Peak Type	Area Intg	FWHM	Max Height	Center Grvty	Area IntgP
1	Gaussian	0.04474	10.30145	0.00419	1228.22722	12.43471
2	Gaussian	0.16289	16.703	0.00923	1237.13399	45.27555
3	Gaussian	0.02157	9.98984	0.00203	1279.78891	5.99603
4	Gaussian	0.07443	12.34415	0.00566	1309.67916	20.68657
5	Gaussian	0.01712	6.26293	0.00257	1314.96735	4.75868
6	Gaussian	0.00512	3.18422	0.00151	1320.08713	1.4243
7	Gaussian	0.03391	18.17504	0.00175	1256.3979	9.42416

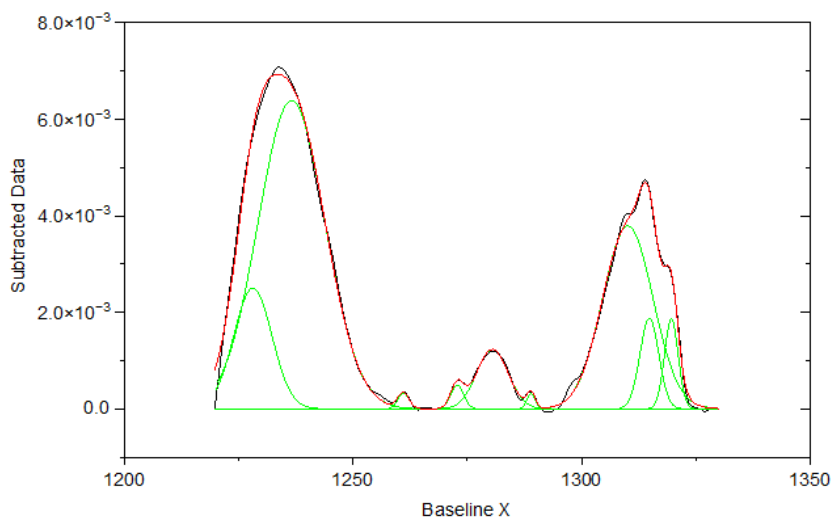
Corresponding FTIR graph S2P1



Fitting Results

Peak Index	Peak Type	Area Intg	FWHM	Max Height	Center Grvty	Area IntgP
1	Gaussian	0.20694	15.95893	0.01226	1236.51316	44.65873
2	Gaussian	0.02686	9.28067	0.00272	1280.03258	5.79661
3	Gaussian	0.09142	12.07352	0.00711	1309.82647	19.72889
4	Gaussian	0.023	6.30635	0.00343	1315.14395	4.96405
5	Gaussian	0.00681	3.25528	0.00197	1320.06956	1.47046
6	Gaussian	0.05949	9.90504	0.00579	1227.95316	12.83752
7	Gaussian	0.04886	23.34454	0.00197	1250.07783	10.54374

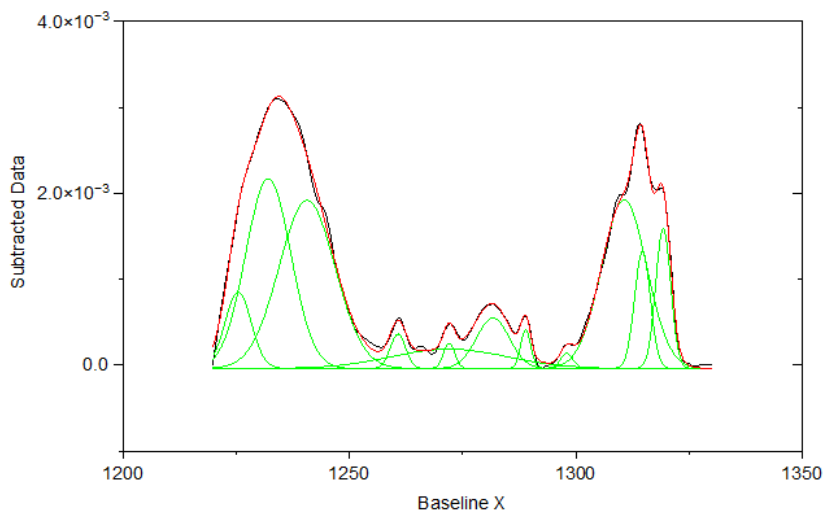
Corresponding FTIR graph S2P2



Fitting Results

Peak Index	Peak Type	Area Intg	FWHM	Max Height	Center Grvty	Area IntgP
1	Gaussian	0.02556	9.82585	0.0025	1228.08264	11.39349
2	Gaussian	9.88132E-4	2.85811	3.24791E-4	1261.05515	0.44054
3	Gaussian	0.00175	3.30742	4.96467E-4	1272.79955	0.77926
4	Gaussian	0.01061	8.10222	0.00123	1280.49318	4.732
5	Gaussian	6.87079E-4	2.05091	3.14723E-4	1288.9568	0.30632
6	Gaussian	0.05217	12.94002	0.00379	1310.14842	23.25687
7	Gaussian	0.00967	4.8523	0.00187	1314.85199	4.3108
8	Gaussian	0.00697	3.53024	0.00185	1319.64563	3.10571
9	Gaussian	0.11591	17.2382	0.00639	1236.5536	51.67501

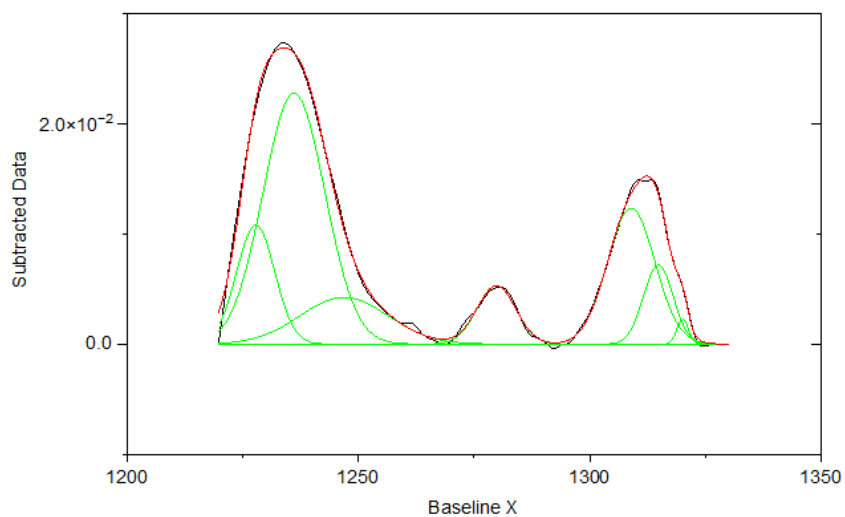
Corresponding FTIR graph S3P1



Fitting Results

Peak Index	Peak Type	Area Intg	FWHM	Max Height	Center Grvty	Area IntgP
1	Gaussian	0.02742	11.73905	0.00221	1232.0504	23.19894
2	Gaussian	0.03029	14.55148	0.00196	1240.61528	25.62792
3	Gaussian	0.0017	4.01112	3.98352E-4	1260.70102	1.43912
4	Gaussian	0.00726	30.31648	2.2512E-4	1272.02832	6.14674
5	Gaussian	0.00533	8.54411	5.86156E-4	1281.68088	4.51069
6	Gaussian	0.00593	4.08607	0.00136	1314.73358	5.01534
7	Gaussian	0.00677	3.90829	0.00163	1319.32168	5.72426
8	Gaussian	0.02447	11.71622	0.00196	1310.67877	20.70284
9	Gaussian	0.00627	6.82568	8.86043E-4	1225.38675	5.30346
10	Gaussian	9.11402E-4	2.95408	2.89838E-4	1272.02832	0.77115
11	Gaussian	0.00123	2.61241	4.43794E-4	1288.91778	1.04421
12	Gaussian	6.09062E-4	3.20483	1.78535E-4	1297.9916	0.51534

Corresponding FTIR graph S3P2



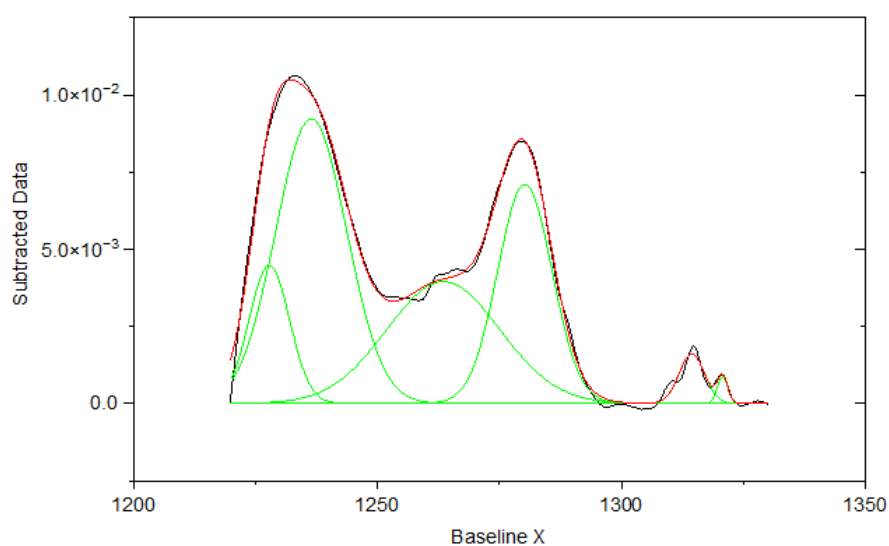
Fitting Results

Peak Index	Peak Type	Area Intg	FWHM	Max Height	Center Grvty	Area IntgP
1	Gaussian	0.37852	15.71306	0.0228	1236.07922	43.62875
2	Gaussian	0.10113	22.36061	0.00426	1246.86702	11.65641
3	Gaussian	0.05564	9.87664	0.00529	1279.82703	6.4131
4	Gaussian	0.15858	12.06734	0.01235	1308.98524	18.27798
5	Gaussian	0.05776	7.54408	0.00719	1314.83826	6.65735
6	Gaussian	0.0069	2.9103	0.00223	1320.09649	0.79536
7	Gaussian	0.10906	9.72964	0.01081	1227.79888	12.57105

0.5 wt% genipin-ELP membranes (chapter 0)

Summary	beta sheets	random coil	beta turns	alpha helix
S1P1	48.3	26.2	22.6	2.9
S1P2	46.2	22.9	25.5	5.3
S2P1	40.8	32.8	23	3.3
S2P2	42.2	27.7	23.5	3.7
S3P1	41.9	25.5	27.3	5.3
S3P2	42.6	23.8	27.9	5.7
<b>Average</b>	<b>43.67</b>	<b>26.48</b>	<b>24.97</b>	<b>4.37</b>
<b>St. Dev.</b>	<b>2.92</b>	<b>3.53</b>	<b>2.28</b>	<b>1.20</b>

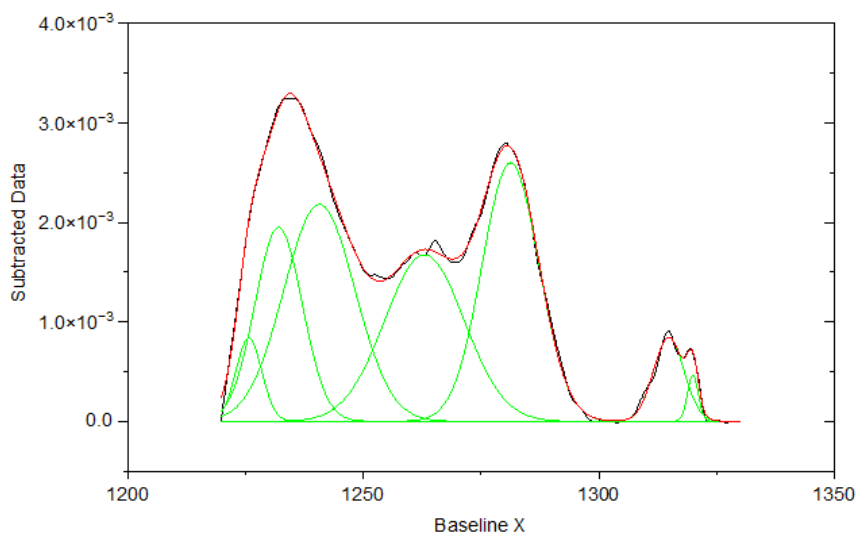
Corresponding FTIR graph S1P1



Fitting Results

Peak Index	Peak Type	Area Intg	FWHM	Max Height	Center Grvty	Area IntgP
1	Gaussian	0.1666	17.16077	0.00922	1236.39151	37.94239
2	Gaussian	0.11495	27.34897	0.00395	1263.48465	26.17871
3	Gaussian	0.09925	13.13032	0.0071	1280.21071	22.60322
4	Gaussian	0.01049	6.14731	0.0016	1314.45641	2.38799
5	Gaussian	0.00231	2.50571	8.65087E-4	1320.72765	0.52549
6	Gaussian	0.0455	9.8342	0.00447	1227.79442	10.3622

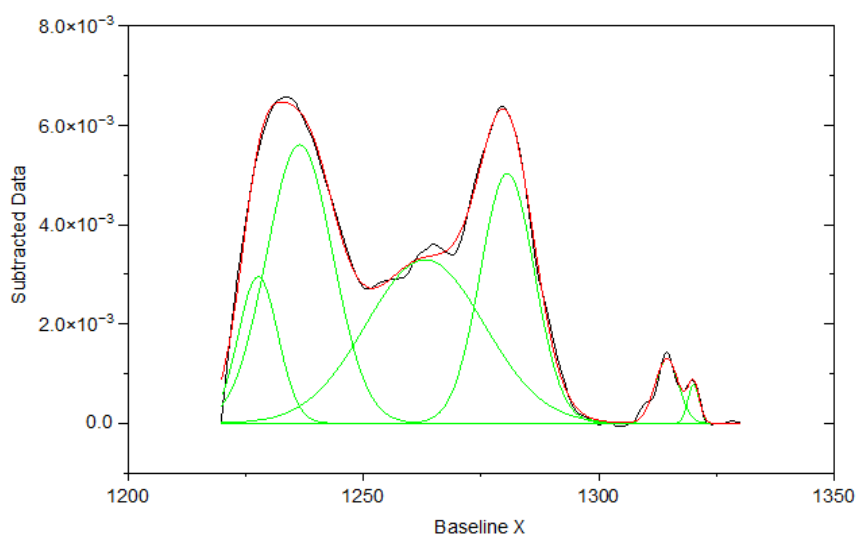
Corresponding FTIR graph S1P2



Fitting Results

Peak Index	Peak Type	Area Intg	FWHM	Max Height	Center Grvty	Area IntgP
1	Gaussian	0.02441	11.86751	0.00195	1231.99291	15.82136
2	Gaussian	0.03546	19.90256	0.00167	1262.96132	22.98464
3	Gaussian	0.03938	14.23937	0.0026	1281.2633	25.52272
4	Gaussian	0.00685	7.63166	8.43273E-4	1314.86351	4.44034
5	Gaussian	0.00134	2.71723	4.62973E-4	1319.97561	0.86798
6	Gaussian	0.00566	6.47655	8.34263E-4	1225.66581	3.66805
7	Gaussian	0.04118	17.79549	0.00218	1240.66294	26.69492

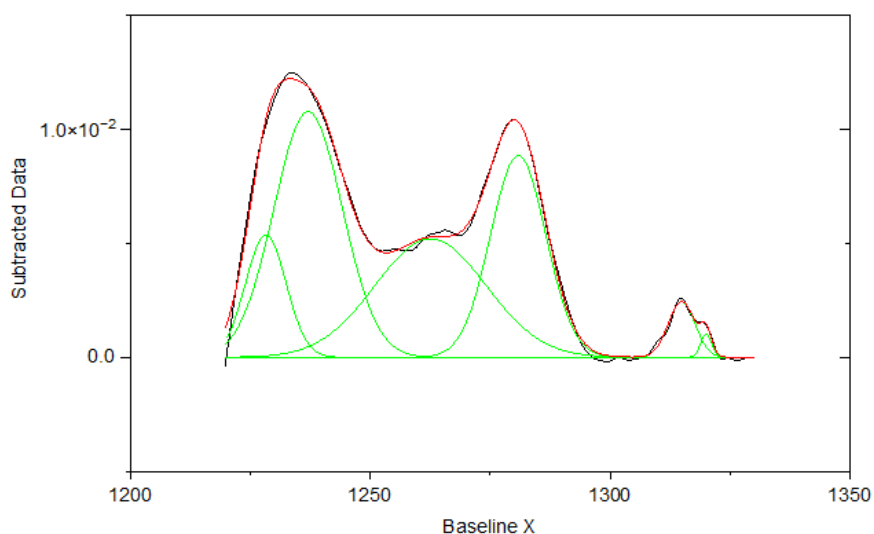
Corresponding FTIR graph S2P1



Fitting Results

Peak Index	Peak Type	Area Intg	FWHM	Max Height	Center Grvty	Area IntgP
1	Gaussian	0.0983	16.61866	0.00561	1236.45222	31.22343
2	Gaussian	0.07242	13.52713	0.00503	1280.59418	23.00078
3	Gaussian	0.00815	5.90609	0.0013	1314.4974	2.58929
4	Gaussian	0.00236	2.8497	7.78458E-4	1320.18191	0.75002
5	Gaussian	0.03022	9.93681	0.00295	1227.62432	9.59981
6	Gaussian	0.10338	29.5005	0.00329	1263.09667	32.83666

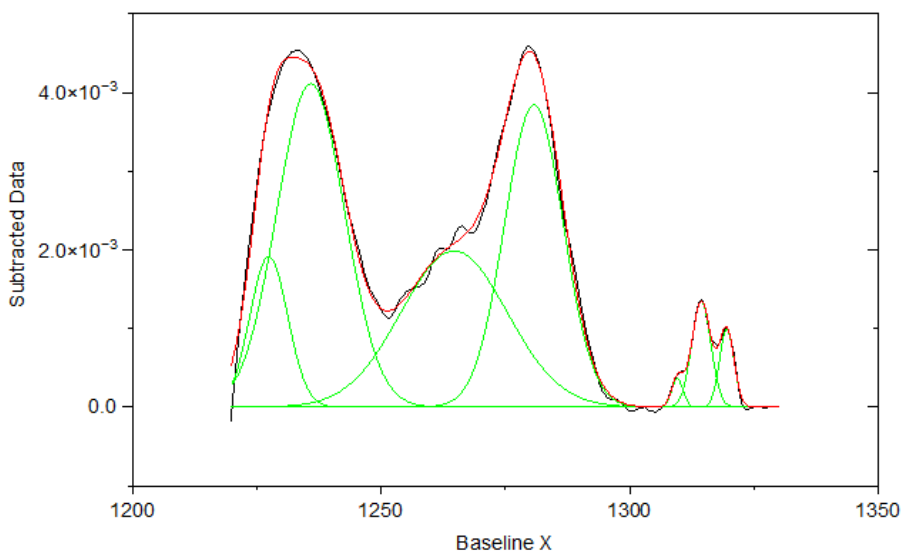
Corresponding FTIR graph S2P2



Fitting Results

Peak Index	Peak Type	Area Intg	FWHM	Max Height	Center Grvty	Area IntgP
1	Gaussian	0.05571	9.98437	0.00537	1228.20777	10.19073
2	Gaussian	0.12837	13.62559	0.00885	1280.84232	23.48187
3	Gaussian	0.01714	6.58231	0.00245	1314.93831	3.13584
4	Gaussian	0.00294	2.72026	0.00101	1320.05164	0.53728
5	Gaussian	0.19147	16.8127	0.01078	1237.03668	35.02471
6	Gaussian	0.15105	27.28451	0.0052	1262.5519	27.62956

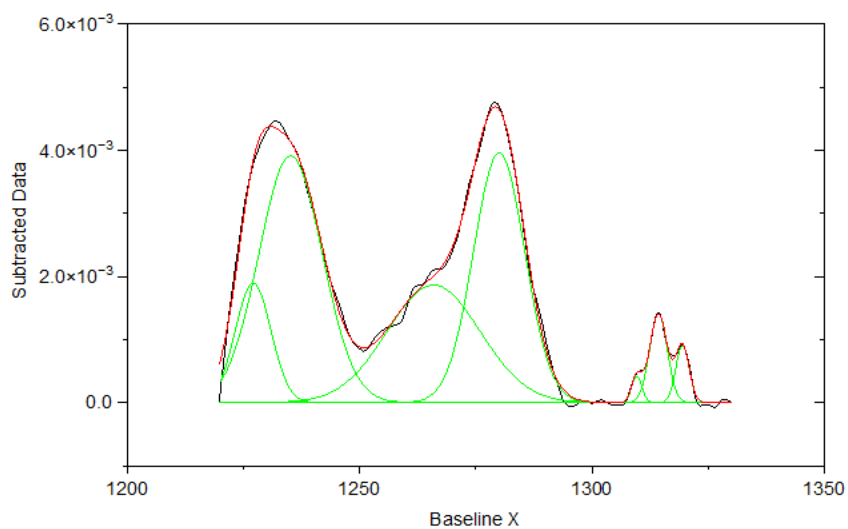
Corresponding FTIR graph S3P1



Fitting Results

Peak Index	Peak Type	Area Intg	FWHM	Max Height	Center Grvty	Area IntgP
1	Gaussian	0.01786	8.97771	0.00191	1227.37528	8.55337
2	Gaussian	0.05697	13.93562	0.00384	1280.74877	27.27678
3	Gaussian	0.0065	4.54485	0.00134	1314.43139	3.11305
4	Gaussian	0.00364	3.46725	9.86294E-4	1319.56168	1.74293
5	Gaussian	0.06961	16.05844	0.00411	1235.8202	33.32752
6	Gaussian	0.00103	2.67426	3.61171E-4	1309.61264	0.49227
7	Gaussian	0.05325	25.18747	0.00199	1264.67238	25.49409

Corresponding FTIR graph S3P2



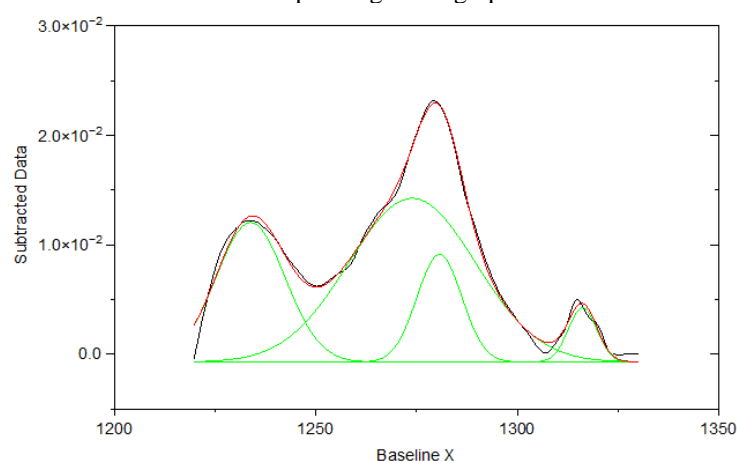
Fitting Results

Peak Index	Peak Type	Area Intg	FWHM	Max Height	Center Grvty	Area IntgP
1	Gaussian	0.01766	9.01289	0.00189	1227.0678	8.99933
2	Gaussian	0.05472	12.98232	0.00396	1280.032	27.89288
3	Gaussian	0.00669	4.4545	0.00141	1314.31659	3.4081
4	Gaussian	0.00328	3.40272	9.04685E-4	1319.49889	1.67024
5	Gaussian	0.00114	2.59019	4.14713E-4	1309.65759	0.58282
6	Gaussian	0.04676	23.58446	0.00186	1265.92424	23.83431
7	Gaussian	0.06594	16.03594	0.00391	1235.13225	33.61233

1.0 wt% genipin-ELP membranes (chapter 0)

Summary	beta sheets	random coil	beta turns	alpha helix
S1P1	25.2	-	70.5	4.3
S1P2	20.56	-	74	5.4
S2P1	19.7	-	73.6	6.7
S2P2	23.8	-	70	6.2
S3P1	30.9	-	65.3	3.7
S3P2	31.8	17.8	45.7	4.9
<b>Average</b>	<b>25.33</b>	<b>2.97</b>	<b>66.52</b>	<b>5.20</b>
<b>St. Dev.</b>	<b>5.09</b>	<b>7.27</b>	<b>10.76</b>	<b>1.13</b>

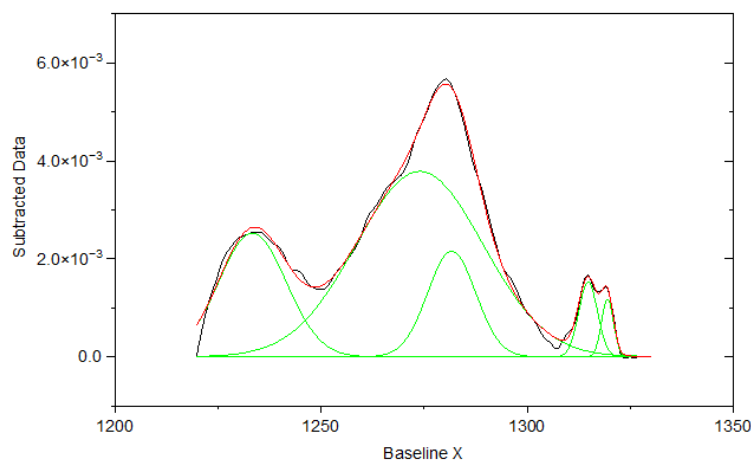
Corresponding FTIR graph S1P1



Fitting Results

Peak Index	Peak Type	Area Intg	FWHM	Max Height	Center Grvty	Area IntgP
1	Gaussian	0.26042	20.20614	0.01276	1233.77192	25.21449
2	Gaussian	0.13737	13.11284	0.00984	1280.6785	13.30038
3	Gaussian	0.04402	8.32752	0.00497	1316.20784	4.26246
4	Gaussian	0.591	37.08702	0.01498	1273.90945	57.22267

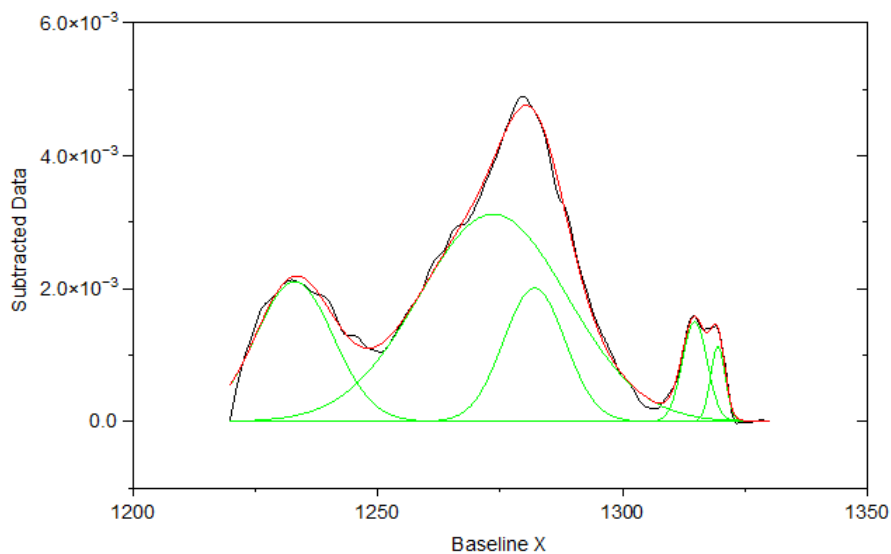
Corresponding FTIR graph S1P2



Fitting Results

Peak Index	Peak Type	Area Intg	FWHM	Max Height	Center Grvty	Area IntgP
1	Gaussian	0.04934	19.30246	0.00253	1233.31755	20.56238
2	Gaussian	0.00871	5.37312	0.00152	1314.81485	3.63188
3	Gaussian	0.00431	3.43224	0.00118	1319.50087	1.7964
4	Gaussian	0.14599	36.26336	0.00378	1273.91881	60.84654
5	Gaussian	0.03158	13.77782	0.00215	1281.68386	13.16281

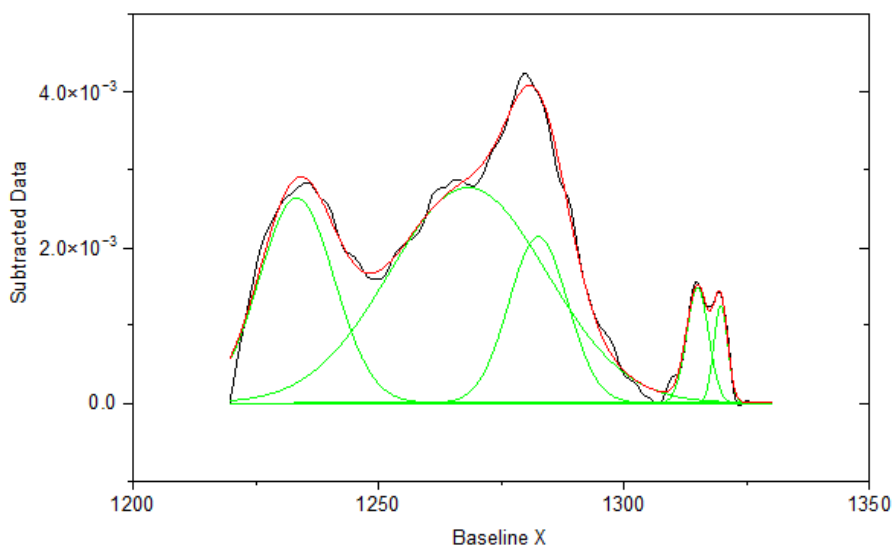
Corresponding FTIR graph S2P1



Fitting Results

Peak Index	Peak Type	Area Intg	FWHM	Max Height	Center Grvty	Area IntgP
1	Gaussian	0.04003	18.80992	0.0021	1232.96017	19.66952
2	Gaussian	0.11814	35.58174	0.00312	1273.56551	58.05056
3	Gaussian	0.00953	5.95463	0.0015	1314.76064	4.68234
4	Gaussian	0.00421	3.51471	0.00112	1319.49247	2.06741
5	Gaussian	0.03161	14.79531	0.00201	1281.99629	15.53017

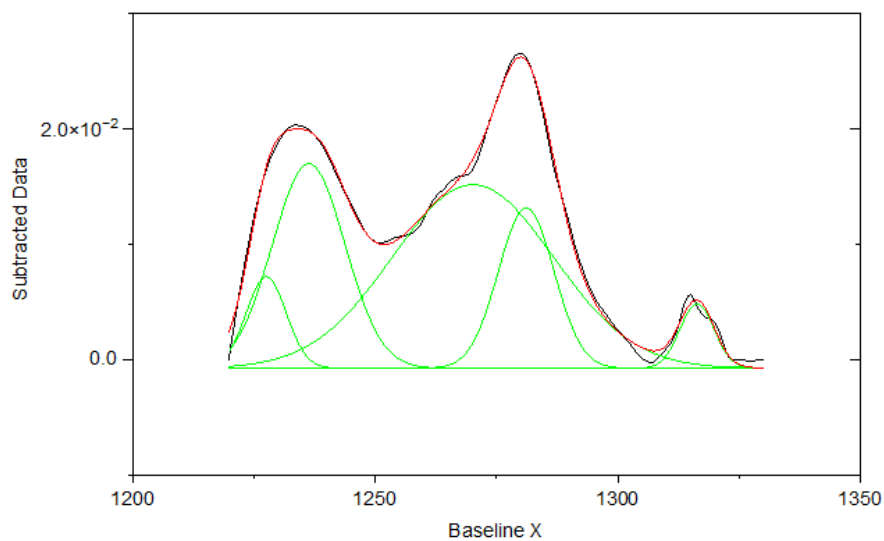
Corresponding FTIR graph S2P2



Fitting Results

Peak Index	Peak Type	Area Intg	FWHM	Max Height	Center Grvty	Area IntgP
1	Gaussian	0.04875	18.04199	0.00264	1233.36554	23.79968
2	Gaussian	0.11118	37.71264	0.00277	1268.27521	54.27875
3	Gaussian	0.00831	5.25769	0.00148	1315.01388	4.05674
4	Gaussian	0.00445	3.32548	0.00126	1319.72853	2.17242
5	Gaussian	0.03214	14.1097	0.00214	1282.58157	15.69241

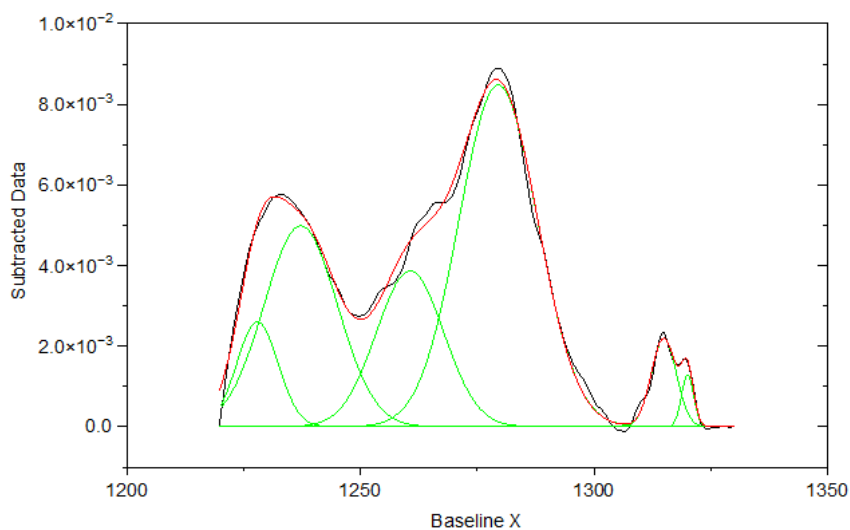
Corresponding FTIR graph S3P1



Fitting Results

Peak Index	Peak Type	Area Intg	FWHM	Max Height	Center Grvty	Area IntgP
1	Gaussian	0.32846	17.62463	0.01775	1236.26643	24.87559
2	Gaussian	0.66263	39.14022	0.01593	1270.13365	50.1836
3	Gaussian	0.20006	13.50113	0.01392	1281.11736	15.1512
4	Gaussian	0.07979	9.74587	0.00794	1227.487	6.04249
5	Gaussian	0.04948	8.31951	0.00559	1316.35337	3.74713

Corresponding FTIR graph S3P2



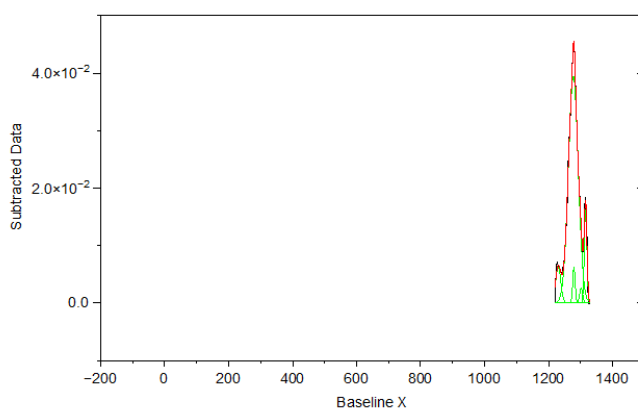
Fitting Results

Peak Index	Peak Type	Area Intg	FWHM	Max Height	Center Grvty	Area IntgP
1	Gaussian	0.02786	10.40537	0.0026	1227.91128	7.09438
2	Gaussian	0.17891	19.8315	0.00848	1279.51552	45.5621
3	Gaussian	0.01468	6.27748	0.0022	1314.97932	3.73761
4	Gaussian	0.0042	3.05242	0.00129	1320.06533	1.06997
5	Gaussian	0.09705	18.54547	0.00498	1237.18759	24.71466
6	Gaussian	0.06998	17.01543	0.00386	1260.60858	17.82128

### 1.5 wt% genipin-ELP membranes (chapter 0)

Summary	beta sheets	random coil	beta turns	alpha helix
S1P1	6.1	-	83.5	10.5
S1P2	6.9	-	81.8	11.3
S2P1	13	12.82	67.3	6.9
S2P2	6.7	-	86.1	7.2
S3P1	6.1	-	83.8	10.1
S3P2	6.6	2	83.7	7.7
<b>Average</b>	<b>7.60</b>	<b>2.47</b>	<b>81.03</b>	<b>8.95</b>
<b>St. Dev.</b>	<b>2.68</b>	<b>5.13</b>	<b>6.87</b>	<b>1.9</b>

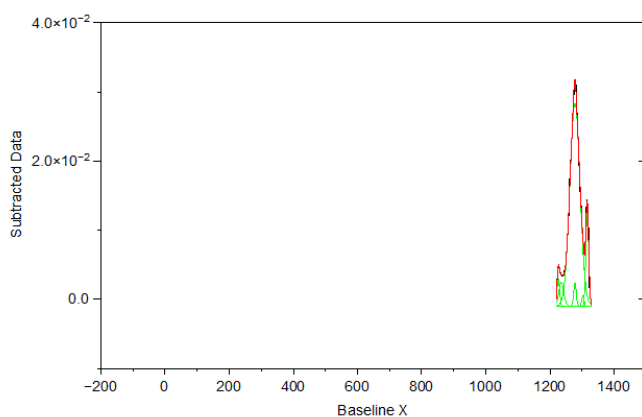
Corresponding FTIR graph S1P1



Fitting Results

Peak Index	Peak Type	Area Intg	FWHM	Max Height	Center Grvty	Area IntgP
1	Gaussian	0	0.14759	-2.26659E29	1148.20394	0
2	Gaussian	0.05818	8.68114	0.0063	1279.29423	3.08982
3	Gaussian	0.16723	9.71764	0.01617	1315.85154	8.88035
4	Gaussian	1.5134	36.06859	0.03943	1277.28114	80.36669
5	Gaussian	0.11412	18.98391	0.00627	1230.11689	6.05998
6	Gaussian	0.03019	10.73327	0.00264	1301.97448	1.60316

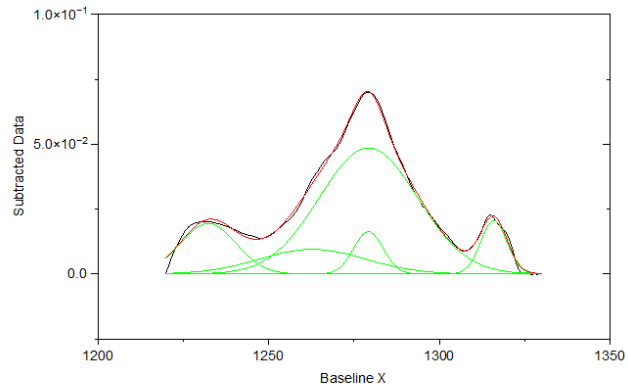
Corresponding FTIR graph S1P2



Fitting Results

Peak Index	Peak Type	Area Intg	FWHM	Max Height	Center Grvty	Area IntgP
1	Gaussian	-5.86735E-5	1.24574	-1.60861E14	1207.47053	-0.00403
2	Gaussian	1.15683	37.01396	0.02938	1277.91613	79.50433
3	Gaussian	0.15012	10.40693	0.01356	1316.30334	10.31743
4	Gaussian	0.03766	9.40271	0.00399	1226.0809	2.58797
5	Gaussian	0.0651	18.14988	0.00344	1235.35448	4.47395
6	Gaussian	0.03305	9.08422	0.00342	1277.91613	2.27171
7	Gaussian	0.01235	8.08896	0.00143	1302.60871	0.84864

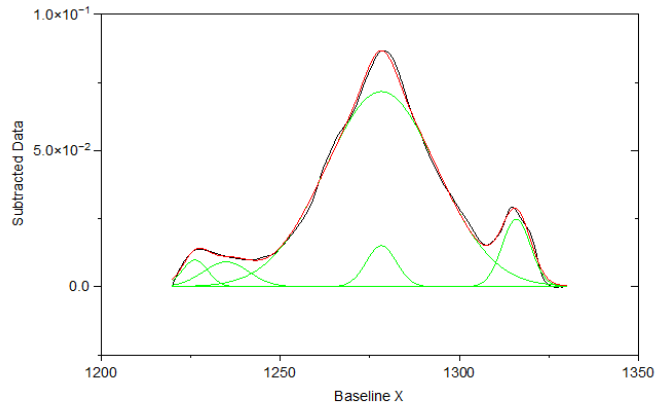
Corresponding FTIR graph S2P1



Fitting Results

Peak Index	Peak Type	Area Intg	FWHM	Max Height	Center Grvty	Area IntgP
1	Gaussian	1.75298	33.90708	0.04858	1279.22809	61.14305
2	Gaussian	0.19693	9.03875	0.02047	1315.99234	6.86896
3	Gaussian	0.17686	10.18627	0.01631	1279.22799	6.16873
4	Gaussian	0.36761	36.44578	0.0095	1262.79741	12.82215
5	Gaussian	0.37263	19.19925	0.01945	1232.27459	12.99711

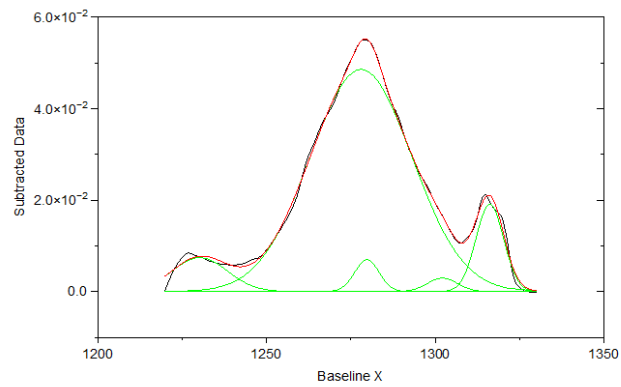
Corresponding FTIR graph S2P2



Fitting Results

Peak Index	Peak Type	Area Intg	FWHM	Max Height	Center Grvty	Area IntgP
1	Gaussian	0.14436	15.02165	0.00911	1234.86185	4.19467
2	Gaussian	2.80498	36.81255	0.07162	1278.22004	81.50173
3	Gaussian	0.24838	9.42175	0.02477	1315.91359	7.21682
4	Gaussian	0.15905	9.90359	0.01509	1278.22004	4.62131
5	Gaussian	0.08485	8.43402	0.00981	1226.21676	2.46547

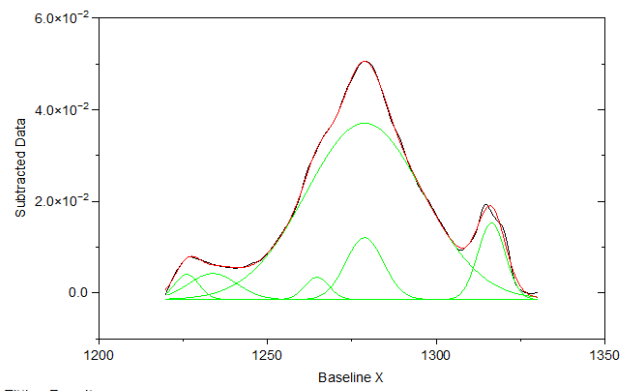
Corresponding FTIR graph S3P1



Fitting Results

Peak Index	Peak Type	Area Intg	FWHM	Max Height	Center Grvty	Area IntgP
1	Gaussian	0.06324	8.56202	0.00694	1279.7586	2.79153
2	Gaussian	0.19628	9.69486	0.01903	1316.19777	8.66417
3	Gaussian	0.0331	10.55721	0.00295	1302.1569	1.46096
4	Gaussian	1.83574	35.5309	0.04855	1278.02794	81.03228
5	Gaussian	0.13708	19.34027	0.00742	1230.16065	6.05106

### Corresponding FTIR graph S3P2



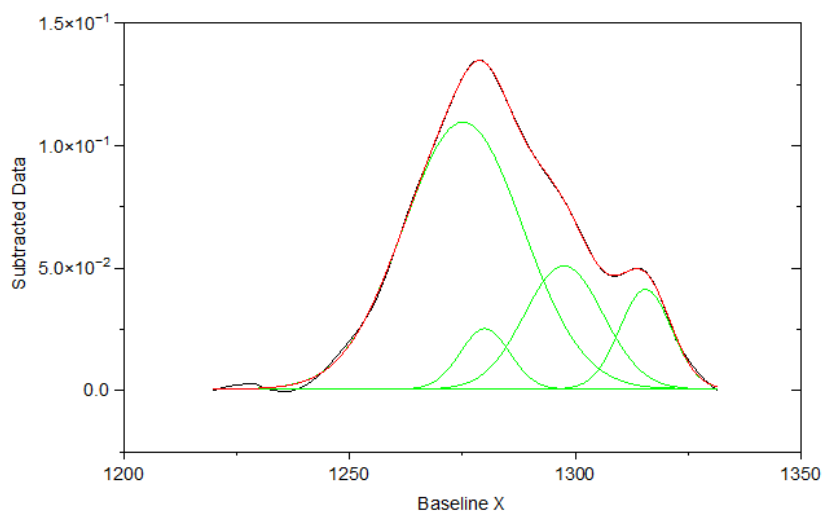
Fitting Results

Peak Index	Peak Type	Area Intg	FWHM	Max Height	Center Grvty	Area IntgP
1	Gaussian	0.04779	8.50904	0.0055	1226.04926	2.15121
2	Gaussian	0.18878	13.14354	0.01349	1278.78826	8.49841
3	Gaussian	0.17042	9.57173	0.01673	1316.42127	7.67177
4	Gaussian	0.09984	16.96408	0.00568	1233.75962	4.49456
5	Gaussian	0.04419	8.53464	0.00486	1264.65979	1.98932
6	Gaussian	1.67032	40.80686	0.03852	1278.78827	75.19474

## 2.5 wt% genipin-ELP membranes (chapter 0)

	S1P1	S1P2	S2P1	S2P2	S3P1	S3P2	Mean	St.Dev.
$\beta$ -sheets	-	1.17	1.17	1.25	1.1	1.38	1.01	0.5
random coils	-	-	14.77	-	-	-	2.46	6.03
$\beta$ -turns	70.13	60.39	76.09	64.62	63.74	91.41	71.06	11.39
$\alpha$ -helix	29.87	38.43	7.97	34.13	35.16	7.21	25.46	14.11

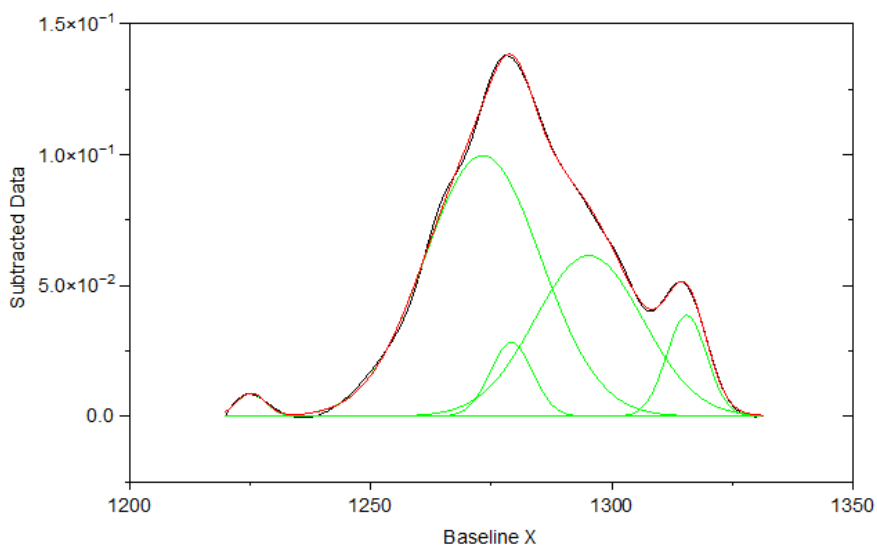
Corresponding FTIR graph – S1P1



Fitting Results

Peak Index	Peak Type	Area Intg	FWHM	Max Height	Center Grvty	Area IntgP
1	Gaussian	0.33839	12.90094	0.02464	1279.99418	5.98764
2	Gaussian	1.10203	20.56141	0.05035	1297.48033	19.4998
3	Gaussian	0.58598	13.57118	0.04068	1315.59472	10.36847
4	Gaussian	3.62511	31.23978	0.10902	1275.14611	64.14409

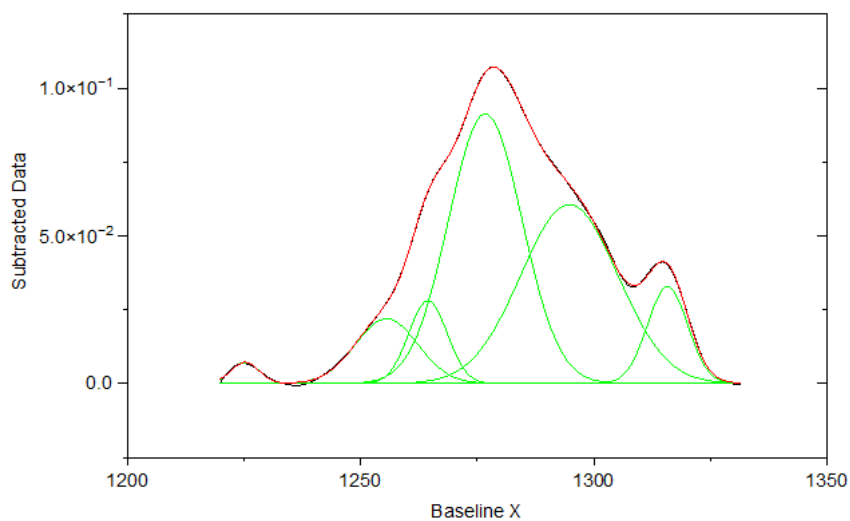
Corresponding FTIR graph – S1P2



Fitting Results

Peak Index	Peak Type	Area Intg	FWHM	Max Height	Center Grvty	Area IntgP
1	Gaussian	0.06441	7.15167	0.00879	1225.18532	1.16989
2	Gaussian	0.30988	10.33872	0.02816	1279.17215	5.62805
3	Gaussian	1.71396	26.25778	0.06136	1295.25739	31.1295
4	Gaussian	0.40202	9.79458	0.03856	1315.53891	7.30166
5	Gaussian	3.01564	28.42428	0.09967	1273.25543	54.7709

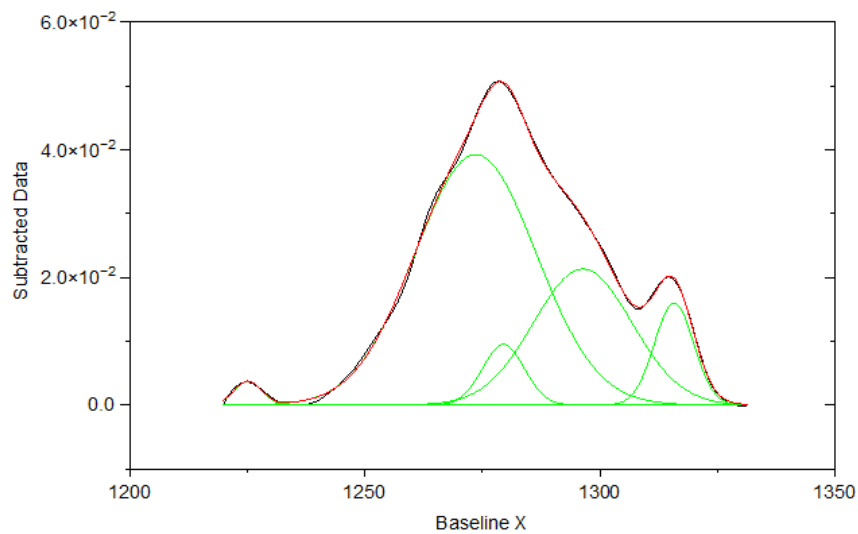
### Corresponding FTIR graph – S2P1



Fitting Results

Peak Index	Peak Type	Area Intg	FWHM	Max Height	Center Grvty	Area IntgP
1	Gaussian	0.2905	9.74785	0.028	1264.44036	6.52334
2	Gaussian	1.80748	18.60856	0.09125	1276.74174	40.5884
3	Gaussian	0.36723	15.73643	0.02192	1255.55499	8.24636
4	Gaussian	1.58071	24.5185	0.06058	1294.76517	35.49608
5	Gaussian	0.35489	10.1846	0.03274	1315.82751	7.9693
6	Gaussian	0.05239	7.11563	0.00718	1225.18077	1.17651

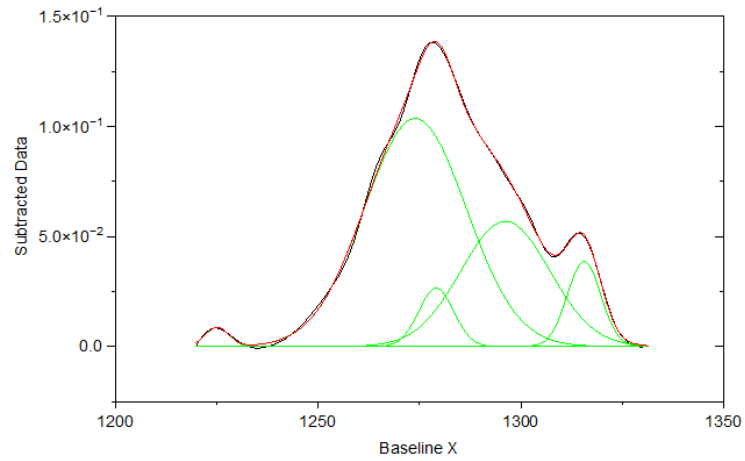
### Corresponding FTIR graph – S2P2



Fitting Results

Peak Index	Peak Type	Area Intg	FWHM	Max Height	Center Grvty	Area IntgP
1	Gaussian	0.0265	6.94776	0.00372	1225.08593	1.24695
2	Gaussian	1.26724	30.34074	0.03924	1273.56545	59.6327
3	Gaussian	0.10595	10.51704	0.00946	1279.48112	4.98554
4	Gaussian	0.16676	9.83281	0.01593	1315.79845	7.84725
5	Gaussian	0.55863	24.64352	0.0213	1296.36247	26.28755

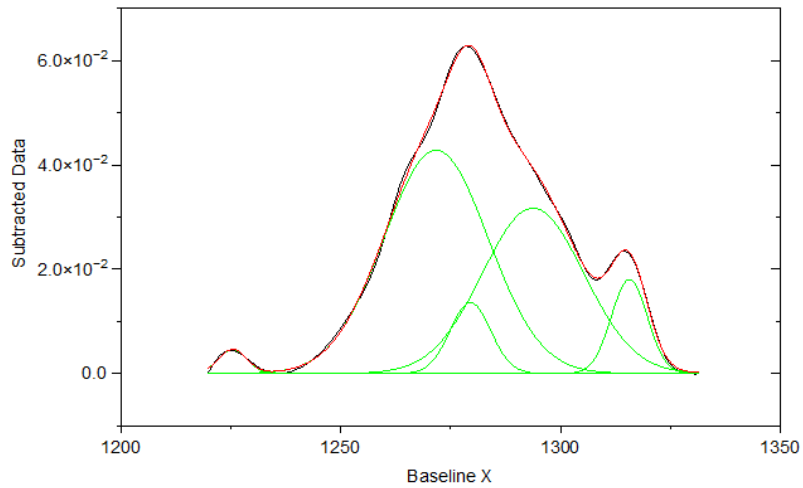
### Corresponding FTIR graph – S3P1



Fitting Results

Peak Index	Peak Type	Area Intg	FWHM	Max Height	Center Grvty	Area IntgP
1	Gaussian	0.06132	6.87604	0.00868	1225.07069	1.10059
2	Gaussian	0.2855	10.14298	0.02644	1279.11718	5.12419
3	Gaussian	1.55869	25.78762	0.05682	1296.17816	27.97589
4	Gaussian	0.40044	9.76788	0.03851	1315.60643	7.18722
5	Gaussian	3.2656	29.62073	0.10357	1273.95131	58.61211

### Corresponding FTIR graph – S3P2



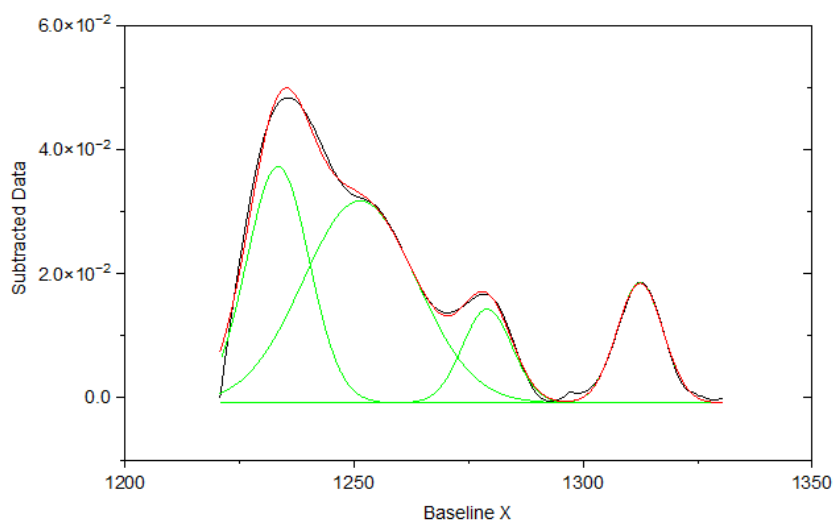
Fitting Results

Peak Index	Peak Type	Area Intg	FWHM	Max Height	Center Grvty	Area IntgP
1	Gaussian	0.03553	7.53633	0.00461	1225.39572	1.38374
2	Gaussian	1.2732	27.93936	0.04281	1271.69004	49.58879
3	Gaussian	0.91621	27.17131	0.03169	1293.75525	35.68482
4	Gaussian	0.18501	9.64977	0.01801	1315.67302	7.20598
5	Gaussian	0.15756	10.8811	0.0136	1279.49074	6.13667

HDI-ELP ratio 1 membranes (chapter 3.3.3.1)

	S1P1	S1P2	S2P1	S2P2	S3P1	S3P2	Mean	St.Dev.
$\beta$ -sheets	30.25	30.12	27.52	28.56	26.63	26.19	28.21	1.73
random coils	48.2	48.87	53.29	52.34	53.2	53.53	51.57	2.40
$\beta$ -turns	9.86	9.95	9.26	8.97	11.06	9.77	9.81	0.72
$\alpha$ -helix	11.69	11.07	9.94	10.13	9.11	10.49	10.41	0.90

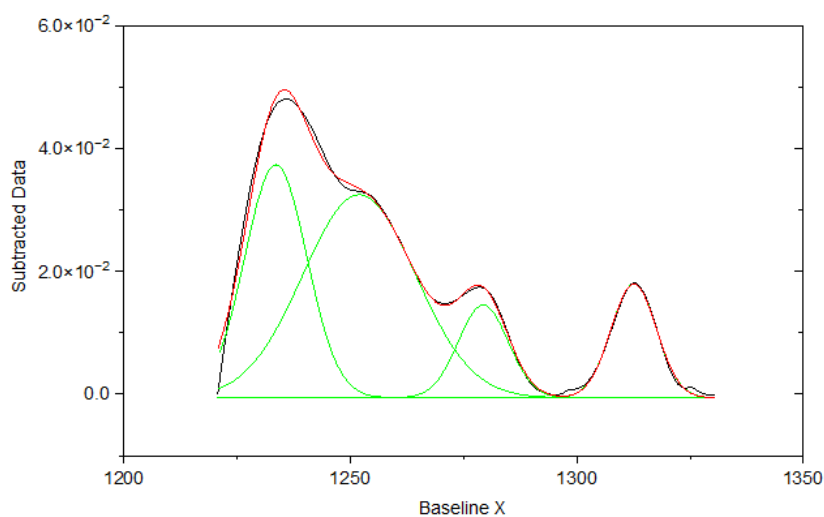
Corresponding FTIR graph – S1P1



Fitting Results

Peak Index	Peak Type	Area Intg	FWHM	Max Height	Center Grvty	Area IntgP
1	Gaussian	0.62886	16.01866	0.03807	1233.37193	30.24601
2	Gaussian	1.00226	29.12099	0.03255	1251.25186	48.20485
3	Gaussian	0.20502	12.73501	0.01512	1279.05796	9.86087
4	Gaussian	0.24302	11.8301	0.0193	1312.42265	11.68827

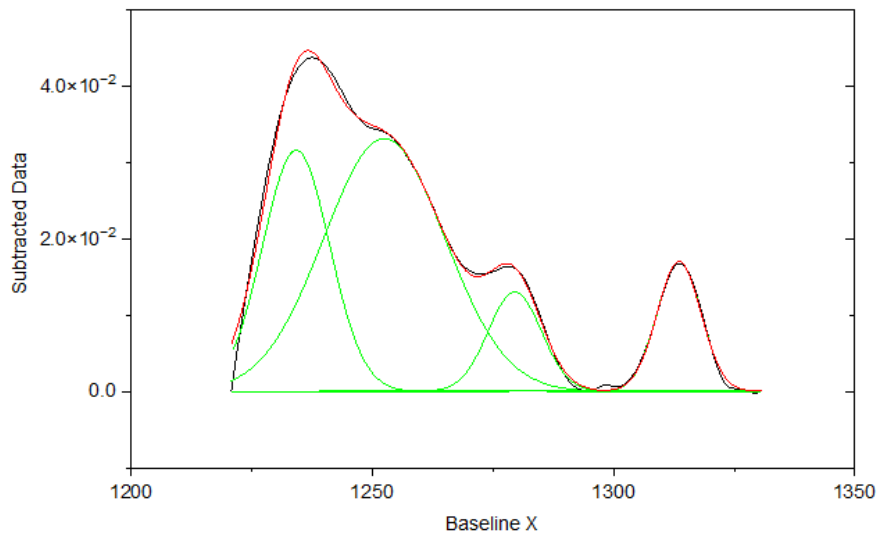
Corresponding FTIR graph – S1P2



Fitting Results

Peak Index	Peak Type	Area Intg	FWHM	Max Height	Center Grvty	Area IntgP
1	Gaussian	0.6306	16.12031	0.0379	1233.53623	30.11503
2	Gaussian	1.02329	29.25833	0.03305	1251.94517	48.86871
3	Gaussian	0.20825	12.96313	0.01509	1279.34123	9.94523
4	Gaussian	0.23182	11.74406	0.01855	1312.60348	11.07103

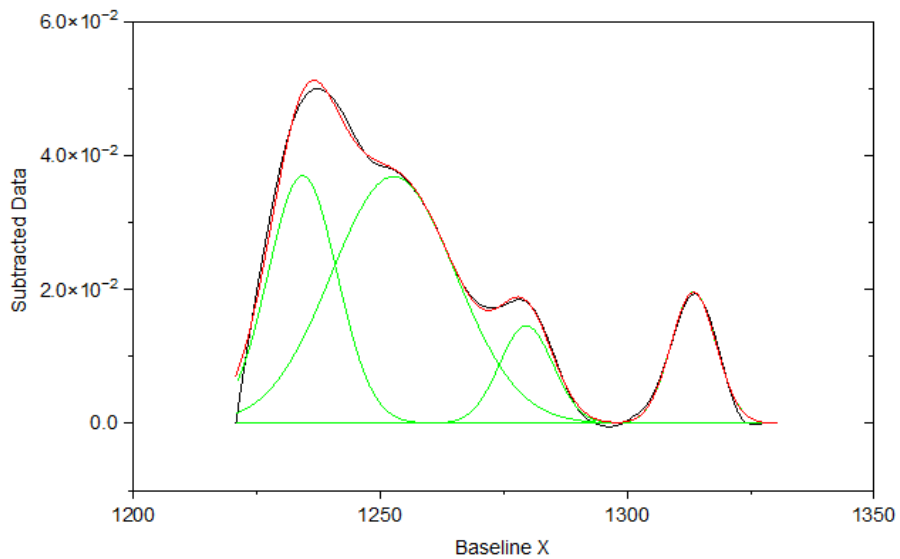
### Corresponding FTIR graph – S2P1



#### Fitting Results

Peak Index	Peak Type	Area Intg	FWHM	Max Height	Center Grvty	Area IntgP
1	Gaussian	0.5349	16.3542	0.03155	1234.17711	27.51577
2	Gaussian	1.036	29.60625	0.03306	1252.4569	53.29229
3	Gaussian	0.17995	12.99793	0.01301	1279.52164	9.25657
4	Gaussian	0.19314	10.69456	0.01697	1313.57766	9.93537

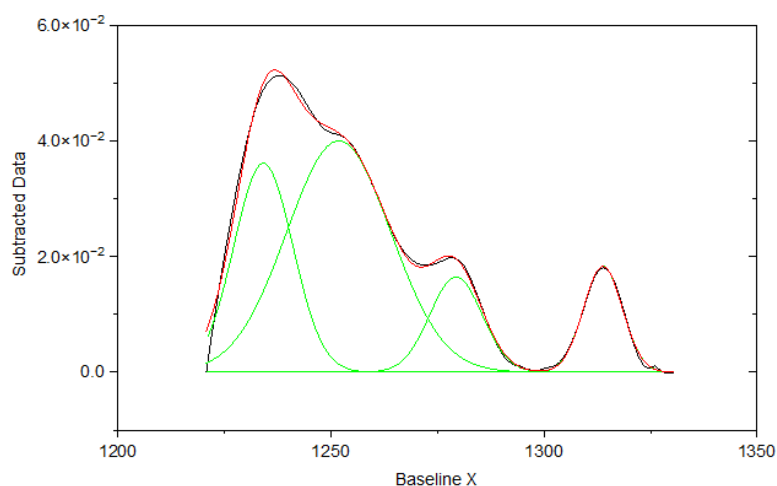
### Corresponding FTIR graph – S2P2



#### Fitting Results

Peak Index	Peak Type	Area Intg	FWHM	Max Height	Center Grvty	Area IntgP
1	Gaussian	0.63088	16.46334	0.03698	1234.2508	28.56443
2	Gaussian	1.15593	29.61832	0.03687	1252.69881	52.33703
3	Gaussian	0.19813	12.75758	0.01459	1279.55696	8.97072
4	Gaussian	0.22369	10.71793	0.01961	1313.45693	10.12781

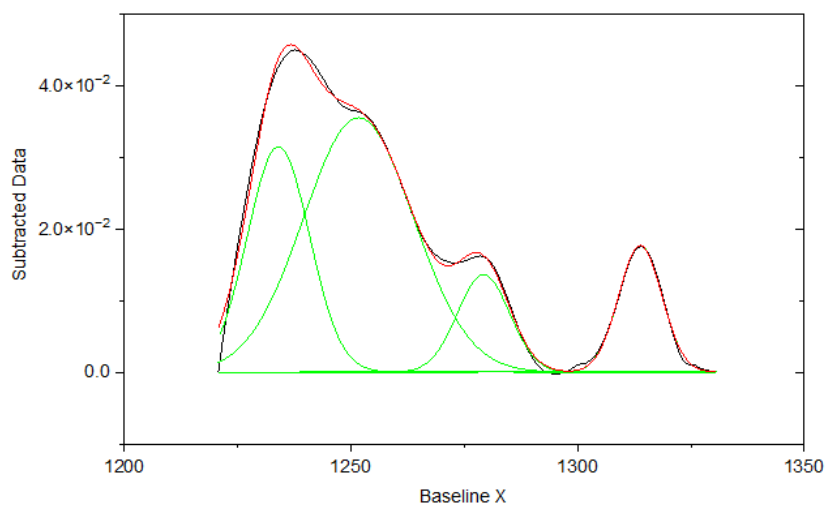
### Corresponding FTIR graph – S3P1



#### Fitting Results

Peak Index	Peak Type	Area Intg	FWHM	Max Height	Center Grvty	Area IntgP
1	Gaussian	0.60935	16.29524	0.03608	1234.12485	26.63168
2	Gaussian	1.21714	28.76186	0.03997	1251.82307	53.19507
3	Gaussian	0.25309	14.44527	0.01646	1279.34367	11.06132
4	Gaussian	0.20849	10.72054	0.01827	1313.84498	9.11193

### Corresponding FTIR graph – S3P2



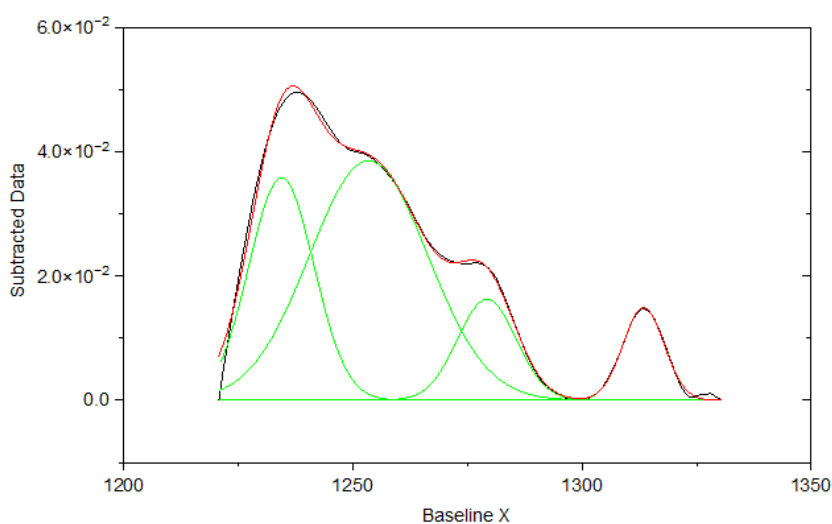
#### Fitting Results

Peak Index	Peak Type	Area Intg	FWHM	Max Height	Center Grvty	Area IntgP
1	Gaussian	1.07377	28.58461	0.03548	1251.67205	53.52866
2	Gaussian	0.19616	13.55746	0.01359	1279.25288	9.77874
3	Gaussian	0.21059	11.20052	0.01767	1313.84539	10.49837
4	Gaussian	0.52545	16.11673	0.03145	1234.00551	26.19423

*HDI-ELP membranes ratio 4 (chapter 3.3.3.1)*

	S1P1	S1P2	S2P1	S2P2	S3P1	S3P2	Mean	St.Dev.
$\beta$ -sheets	27.11	28.64	27.87	27.77	27.13	27.7	27.70	0.56
random coils	54.19	54.91	55.67	54.89	56.54	55.34	55.26	0.80
$\beta$ -turns	11.4	9.61	10.63	9.96	9.59	11.2	10.40	0.80
$\alpha$ -helix	7.3	6.84	5.83	7.39	6.74	5.76	6.64	0.70

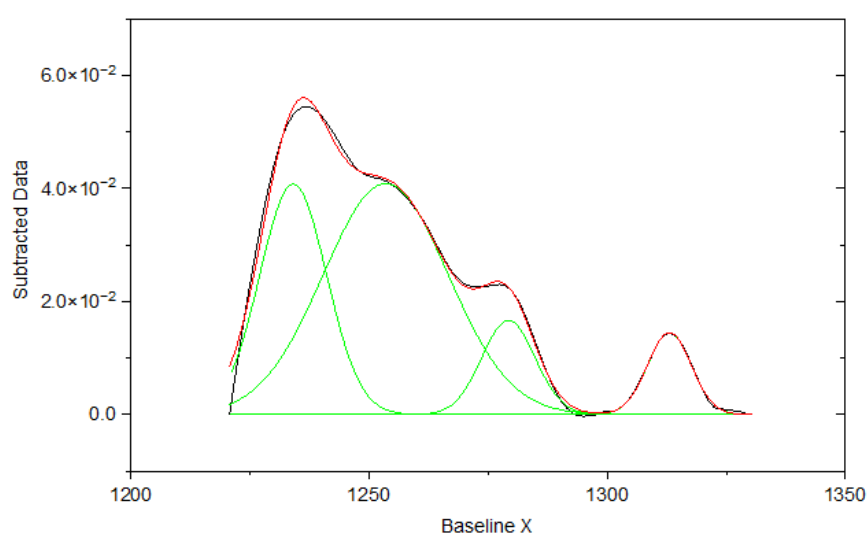
Corresponding FTIR graph – S1P1



Fitting Results

Peak Index	Peak Type	Area Intg	FWHM	Max Height	Center Grvty	Area IntgP
1	Gaussian	0.61914	16.7038	0.03578	1234.39428	27.1087
2	Gaussian	1.23759	30.33385	0.03854	1253.41622	54.1874
3	Gaussian	0.26041	15.07005	0.01623	1279.25464	11.40203
4	Gaussian	0.16677	10.51903	0.01489	1313.43756	7.30187

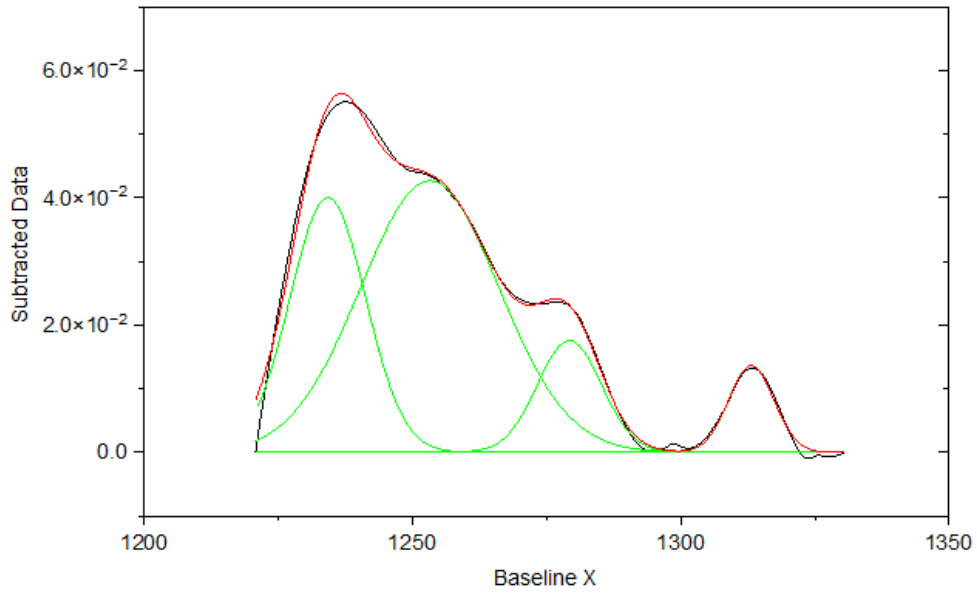
Corresponding FTIR graph – S1P2



Fitting Results

Peak Index	Peak Type	Area Intg	FWHM	Max Height	Center Grvty	Area IntgP
1	Gaussian	0.69624	16.52529	0.04075	1234.04949	28.64967
2	Gaussian	1.33441	30.89791	0.04083	1253.47874	54.90939
3	Gaussian	0.23342	13.17152	0.01665	1279.26809	9.605
4	Gaussian	0.16613	10.76015	0.0145	1313.06051	6.83594

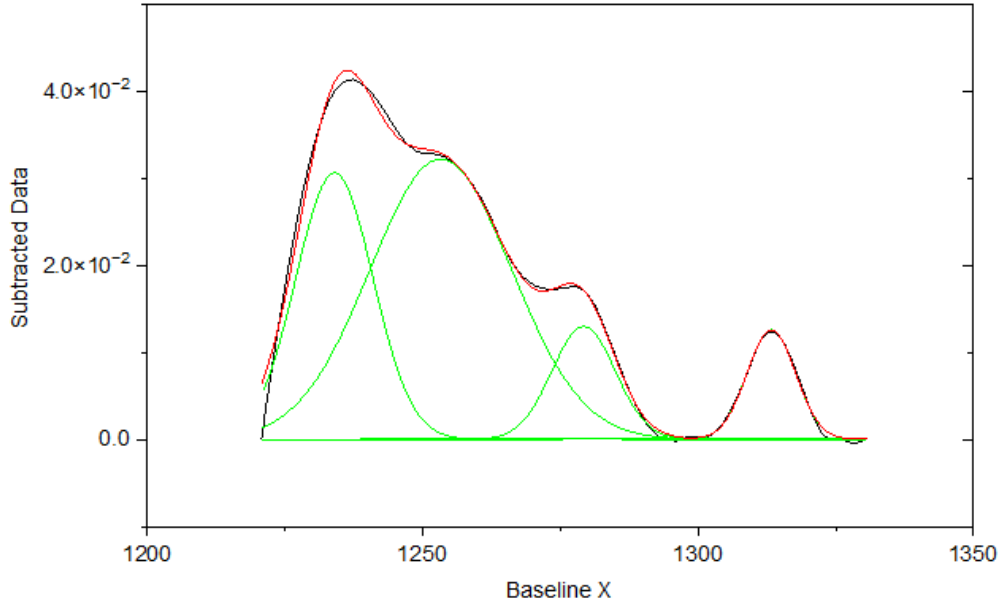
### Corresponding FTIR graph – S2P1



#### Fitting Results

Peak Index	Peak Type	Area Intg	FWHM	Max Height	Center Grvty	Area IntgP
1	Gaussian	0.68676	16.58348	0.04001	1234.20608	27.87076
2	Gaussian	1.37168	30.38884	0.04266	1253.20813	55.66643
3	Gaussian	0.26193	14.03213	0.01754	1279.2458	10.62989
4	Gaussian	0.14373	9.91476	0.01362	1313.14808	5.83292

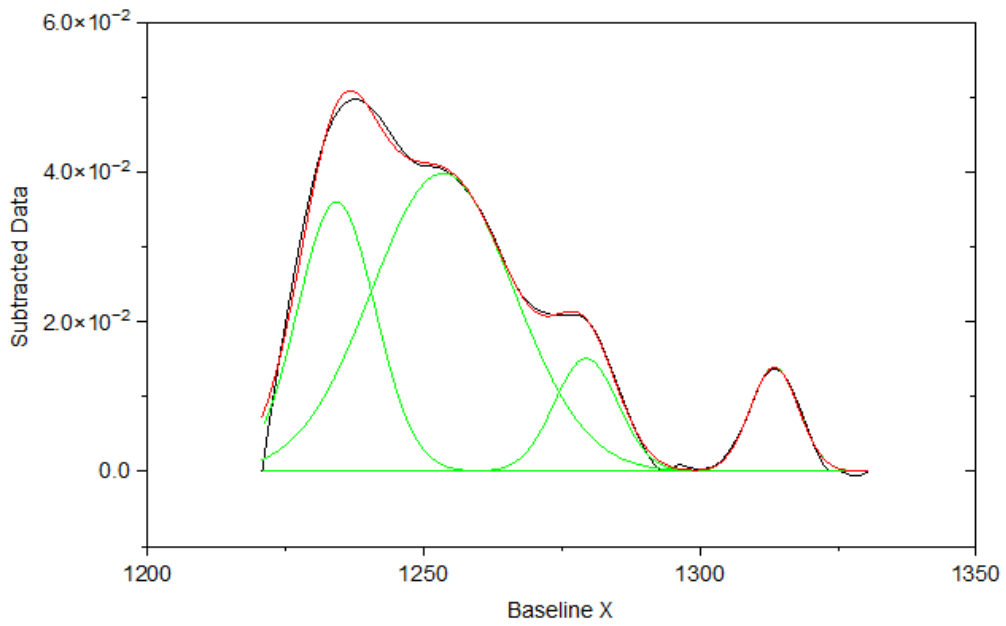
### Corresponding FTIR graph – S2P2



#### Fitting Results

Peak Index	Peak Type	Area Intg	FWHM	Max Height	Center Grvty	Area IntgP
1	Gaussian	0.52118	16.478	0.0306	1233.97695	27.76773
2	Gaussian	1.03017	30.2591	0.03216	1253.28929	54.88567
3	Gaussian	0.18688	13.55499	0.01295	1279.22781	9.95683
4	Gaussian	0.1387	10.36975	0.01257	1313.31364	7.38977

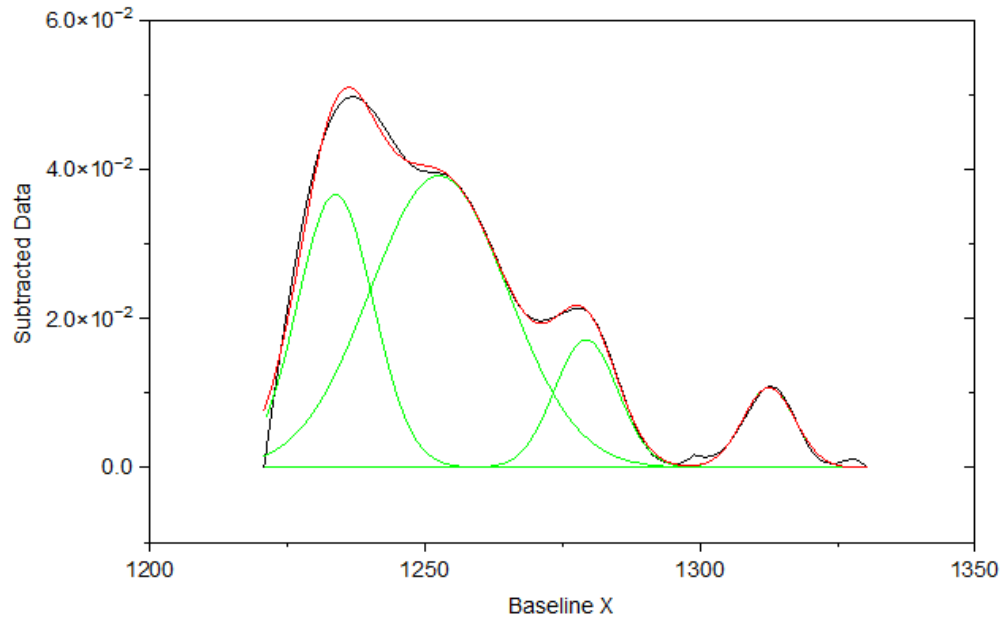
Corresponding FTIR graph – S3P1



Fitting Results

Peak Index	Peak Type	Area Intg	FWHM	Max Height	Center Grvty	Area IntgP
1	Gaussian	0.6149	16.51691	0.03596	1234.1896	27.13083
2	Gaussian	1.28133	30.40072	0.03982	1253.44833	56.53568
3	Gaussian	0.21733	13.52007	0.0151	1279.386	9.58907
4	Gaussian	0.15286	10.30503	0.01394	1313.4866	6.74443

Corresponding FTIR graph – S3P2



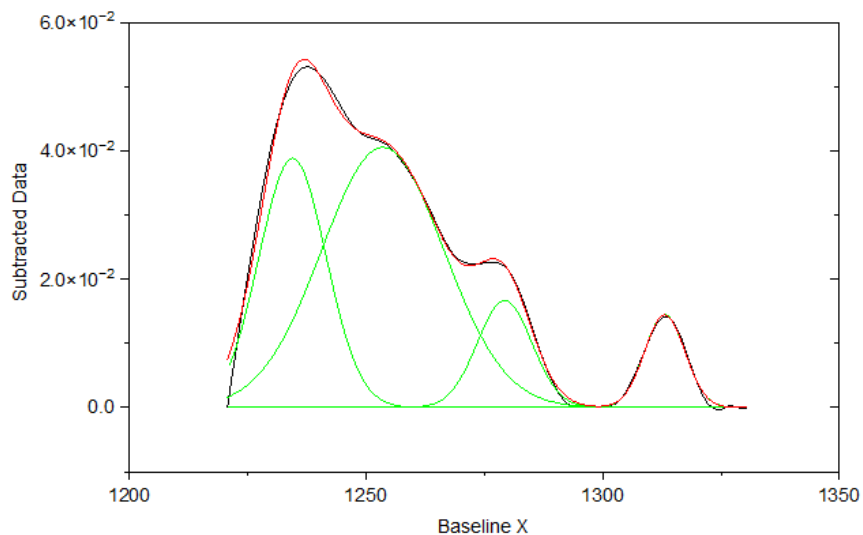
Fitting Results

Peak Index	Peak Type	Area Intg	FWHM	Max Height	Center Grvty	Area IntgP
1	Gaussian	0.61155	16.15749	0.03663	1233.69835	27.69592
2	Gaussian	1.22192	29.51859	0.0391	1252.55749	55.33817
3	Gaussian	0.24735	13.55924	0.01714	1279.28805	11.20217
4	Gaussian	0.12727	11.15959	0.01071	1312.54386	5.76373

HDI-ELP membranes ratio 12 (chapter 3.3.3.1)

	S1P1	S1P2	S2P1	S2P2	S3P1	S3P2	Mean	St.Dev.
$\beta$ -sheets	28.34	21.39	27.87	24.22	22.62	23.62	24.68	2.83
random coils	55.01	56.15	55.67	54.71	55.28	56.08	55.48	0.58
$\beta$ -turns	10.16	12.92	10.63	11.03	11.26	11.1	11.18	0.94
$\alpha$ -helix	6.49	9.54	5.83	10.04	8.85	9.19	8.32	1.73

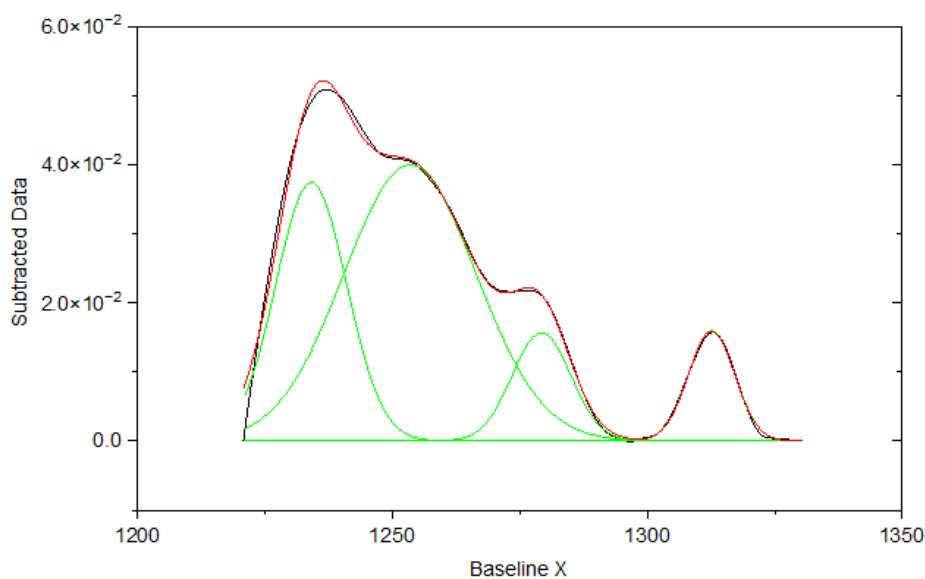
Corresponding FTIR graph – S1P1



Fitting Results

Peak Index	Peak Type	Area Intg	FWHM	Max Height	Center Grvty	Area IntgP
1	Gaussian	0.67185	16.71012	0.03879	1234.46726	28.33919
2	Gaussian	1.30404	30.39493	0.04053	1253.52642	55.0056
3	Gaussian	0.24076	13.57912	0.01666	1279.27968	10.15562
4	Gaussian	0.15409	10.01972	0.01445	1313.12773	6.49959

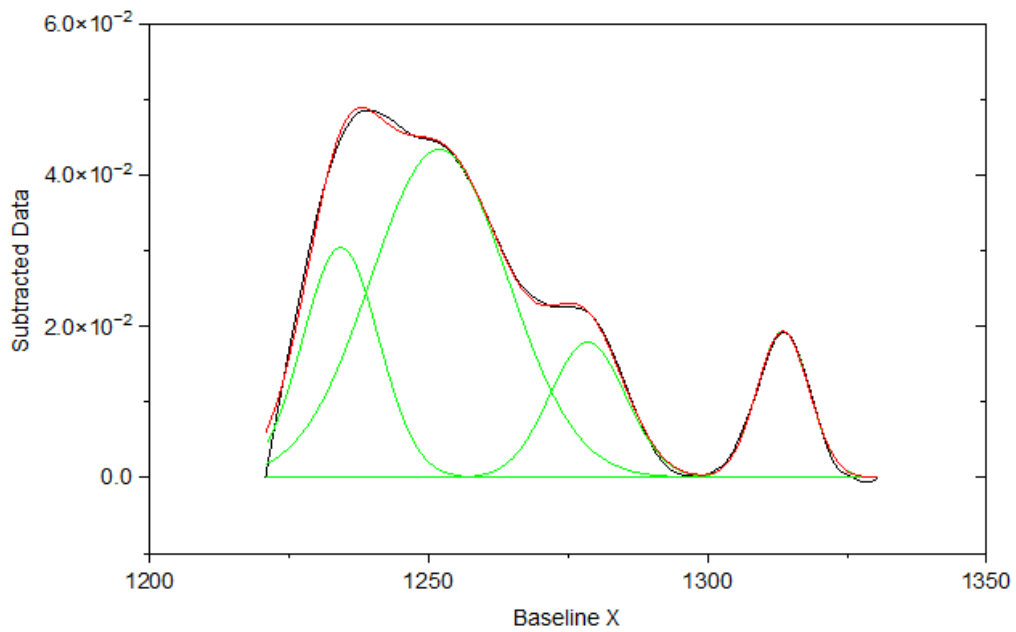
Corresponding FTIR graph – S1P2



Fitting Results

Peak Index	Peak Type	Area Intg	FWHM	Max Height	Center Grvty	Area IntgP
1	Gaussian	0.63413	16.37918	0.0374	1234.04825	27.20067
2	Gaussian	1.29098	30.54429	0.03994	1253.44442	55.37578
3	Gaussian	0.22576	13.54481	0.01566	1279.25619	9.68394
4	Gaussian	0.18043	10.66292	0.0159	1312.61844	7.73961

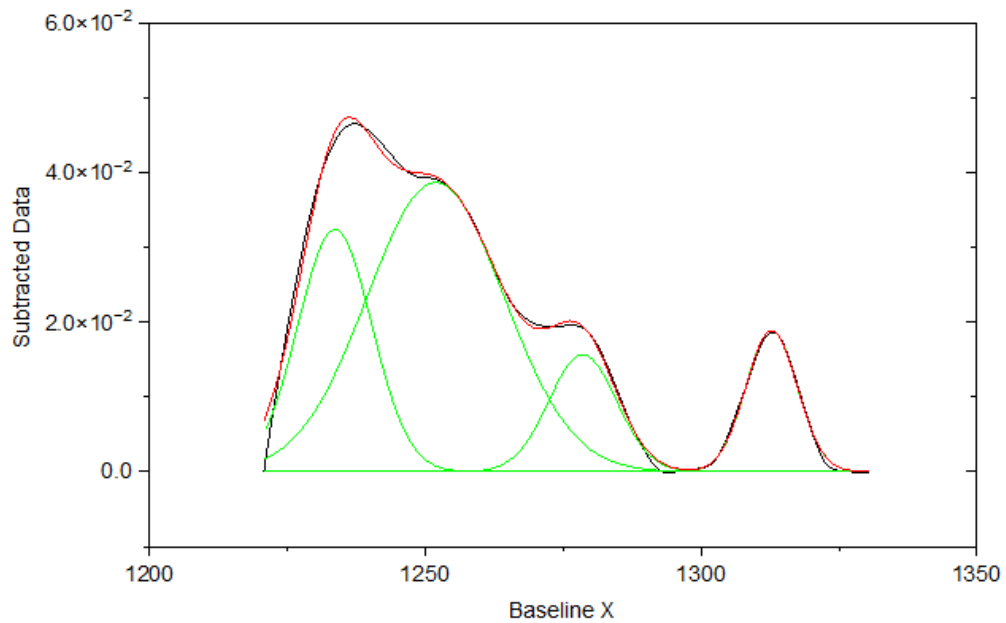
Corresponding FTIR graph – S2P1



Fitting Results

Peak Index	Peak Type	Area Intg	FWHM	Max Height	Center Grvty	Area IntgP
1	Gaussian	0.50566	15.99599	0.03041	1234.22659	21.39305
2	Gaussian	1.3272	28.92412	0.04335	1251.89205	56.1505
3	Gaussian	0.30532	16.05713	0.01786	1278.4801	12.91735
4	Gaussian	0.22547	10.95034	0.01935	1313.50601	9.5391

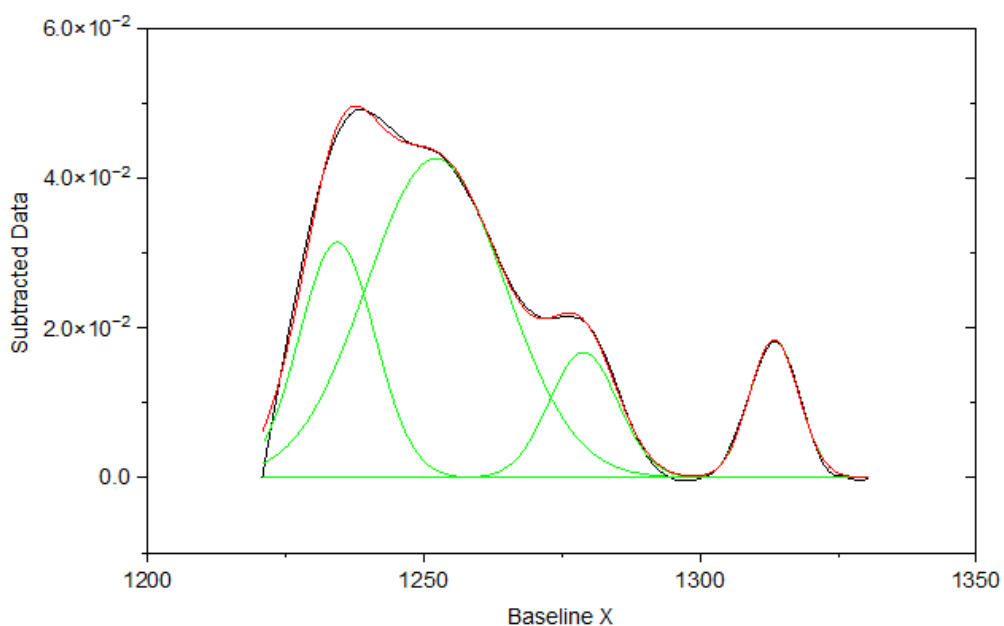
Corresponding FTIR graph – S2P2



Fitting Results

Peak Index	Peak Type	Area Intg	FWHM	Max Height	Center Grvty	Area IntgP
1	Gaussian	0.52807	15.76644	0.03234	1233.58822	24.21761
2	Gaussian	1.19297	29.16546	0.03866	1251.86063	54.71063
3	Gaussian	0.24058	14.44323	0.01565	1278.54057	11.03322
4	Gaussian	0.21889	10.91698	0.01884	1312.79084	10.03854

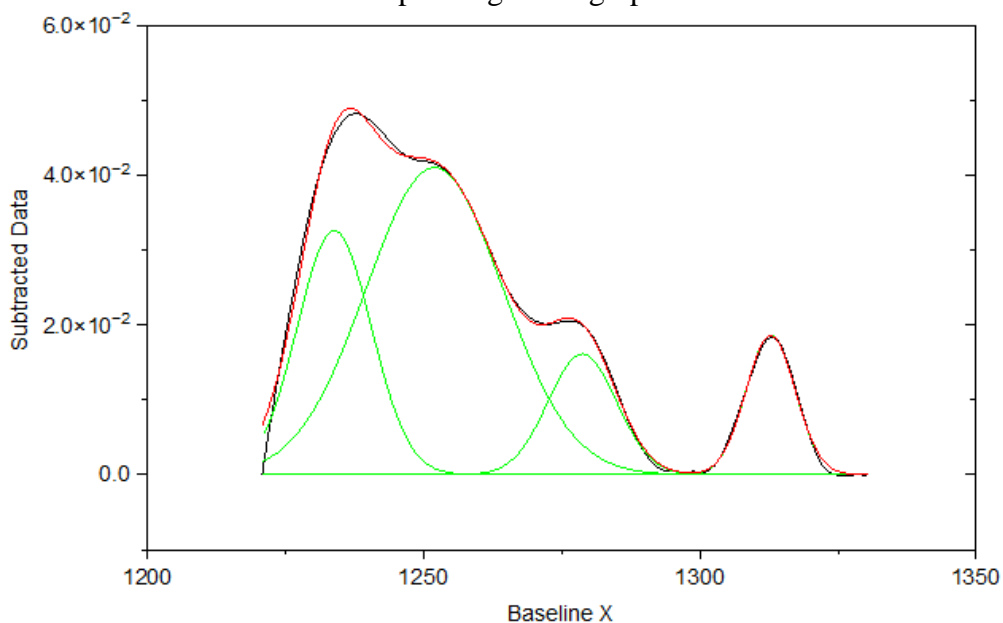
Corresponding FTIR graph – S3P1



Fitting Results

Peak Index	Peak Type	Area Intg	FWHM	Max Height	Center Grvty	Area IntgP
1	Gaussian	0.52475	16.06359	0.03142	1234.29042	22.62072
2	Gaussian	1.3287	29.48503	0.04259	1252.16004	57.27723
3	Gaussian	0.26114	14.64957	0.01675	1278.87458	11.25694
4	Gaussian	0.20519	10.49137	0.01837	1313.41064	8.84511

Corresponding FTIR graph – S3P2

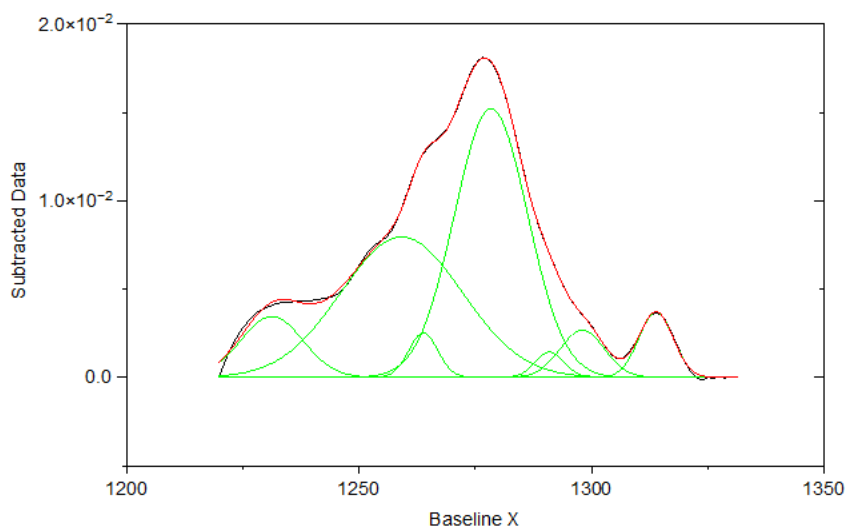


Fitting Results

Peak Index	Peak Type	Area Intg	FWHM	Max Height	Center Grvty	Area IntgP
1	Gaussian	0.53345	15.78242	0.03258	1233.80131	23.62474
2	Gaussian	1.26631	29.19541	0.04099	1251.94987	56.08065
3	Gaussian	0.25074	14.60531	0.01613	1278.71167	11.10421
4	Gaussian	0.20752	10.48527	0.01859	1312.82674	9.19041

1.0 wt% genipin-ELP filament (chapter 5.2.2.1)

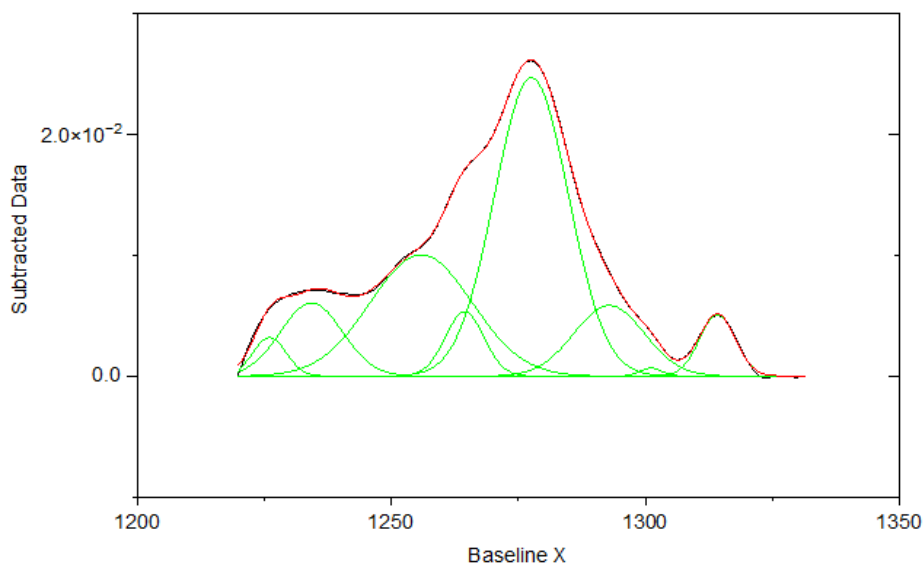
Filament location 1



Fitting Results

Peak Index	Peak Type	Area Intg	FWHM	Max Height	Center Grvty	Area IntgP
1	Gaussian	0.25964	30.70971	0.00795	1259.15114	36.43133
2	Gaussian	0.01982	7.41712	0.00251	1263.81188	2.78073
3	Gaussian	0.30064	18.57679	0.0152	1278.39255	42.18314
4	Gaussian	0.0111	7.29274	0.00143	1290.98882	1.55783
5	Gaussian	0.03194	11.23843	0.00267	1298.01206	4.48209
6	Gaussian	0.0341	8.63708	0.00371	1313.89756	4.78476
7	Gaussian	0.05545	15.74602	0.00346	1231.22755	7.78011

Filament location 2



Fitting Results

Peak Index	Peak Type	Area Intg	FWHM	Max Height	Center Grvty	Area IntgP
1	Gaussian	0.45148	17.15817	0.02472	1277.58198	44.1805
2	Gaussian	0.05085	8.98401	0.00532	1264.40898	4.97592
3	Gaussian	0.25268	23.63621	0.01004	1255.86588	24.72647
4	Gaussian	0.09173	14.34876	0.00606	1234.26207	8.97601
5	Gaussian	0.02539	7.71692	0.00318	1225.98362	2.48505
6	Gaussian	0.1014	16.29279	0.00585	1292.8655	9.92244
7	Gaussian	0.00355	5.05214	6.60583E-4	1301.13084	0.34763
8	Gaussian	0.04482	8.27364	0.00509	1314.20315	4.38599

## Appendix C

### *Swell Capacity in cross-linked ELP membranes (Chapter 3)*

<b>PMDI</b>	w <sub>d1</sub>	w <sub>d2</sub>	w <sub>d3</sub>	w <sub>s1</sub>	w <sub>s2</sub>	w <sub>s3</sub>	[% ]1	[% ]2	[% ]3	Average	St.Dev.
0.1%	42.00	39.52	46.60	43.90	40.94	49.41	4.52	3.59	6.03	4.72	1.23
0.2%	181.58	97.72	96.76	188.50	104.55	100.90	3.81	6.99	4.28	5.03	1.72
0.3%	47.49	49.67	43.95	51.16	53.80	46.72	7.73	8.31	6.30	7.45	1.03

<b>Genipin</b>	w <sub>d1</sub>	w <sub>d2</sub>	w <sub>d3</sub>	w <sub>s1</sub>	w <sub>s2</sub>	w <sub>s3</sub>	[% ]1	[% ]2	[% ]3	Average	St.Dev.
0.5%	145.45	174.04	128.26	155.60	183.64	139.00	6.98	5.52	8.37	6.96	1.43
1.0%	187.23	163.86	157.75	191.90	168.80	162.64	2.49	3.01	3.10	2.87	0.31
1.5%	29.81	20.85	20.83	30.34	21.40	21.57	1.78	2.64	3.55	2.66	0.89

<b>HDI</b>	w <sub>d1</sub>	w <sub>d2</sub>	w <sub>d3</sub>	w <sub>s1</sub>	w <sub>s2</sub>	w <sub>s3</sub>	[% ]1	[% ]2	[% ]3	Average	St.Dev.
ratio 1	44.36	53.62	97.77	45.48	55.08	99.94	2.52	2.72	2.22	2.49	0.25
ratio 4	48.7	49.33	87.41	49.89	50.41	89.69	2.44	2.19	2.61	2.41	0.21
ratio 12	45.58	55.00	82.11	46.59	56.43	83.45	2.22	2.60	1.63	2.15	0.49

## Appendix D

### *Print accuracy quantification in 1.0 wt% genipin 4% ELP prints (chapter 5.2.2.3.)*

Images printed samples incubation day 6

Sample 1 – Glovebox cross-linked (GB CL): 12 out of 25 pores printed

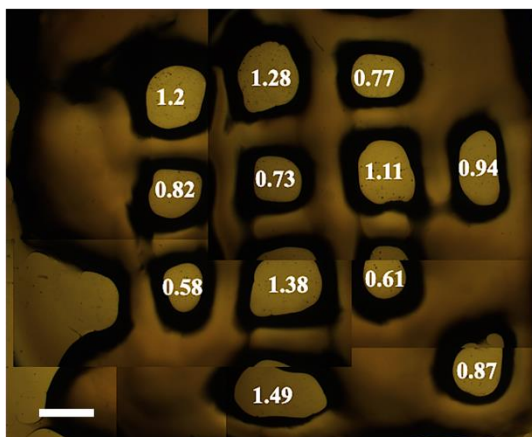


**Figure vi.1:** 1.0 wt% genipin 4% ELP printed Sample 1 after 6 days of incubation, showing measured surface area of successfully printed pores. Scale bar: 500  $\mu\text{m}$ .



**Figure vi.2:** 1.0 wt% genipin 4% ELP printed Sample 1 after 6 days of incubation, showing measured surface area of printed pores post glovebox cross-linking. Scale bar: 500  $\mu\text{m}$ .

Sample 2 – Fume hood cross-linked (FH CL): 9 out of 25 pores printed

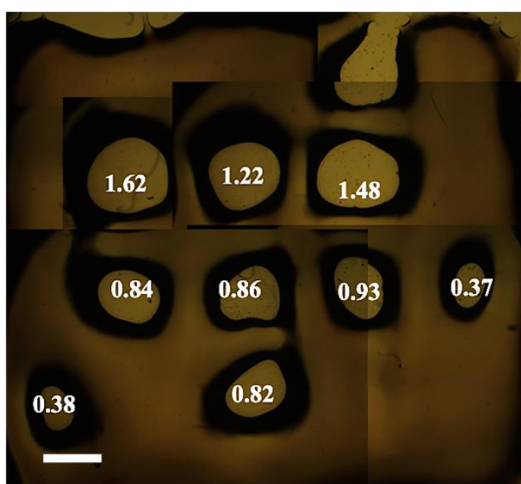


**Figure vi.3:** 1.0 wt% genipin 4% ELP printed Sample 2 after 6 days of incubation, showing measured surface area of successfully printed pores. Scale bar: 500  $\mu\text{m}$ .

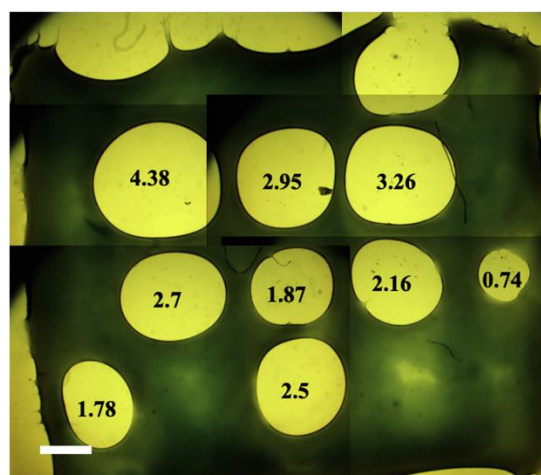


**Figure vi.4:** 1.0 wt% genipin 4% ELP printed Sample 2 after 6 days of incubation, showing measured surface area of printed pores post fume hood cross-linking. Scale bar: 500  $\mu\text{m}$ .

## Calculations

Printed pores sizes [mm <sup>2</sup> ]			
Sample 1	GB CL	Sample 2	FH CL
1,2	3,16	1,62	4,38
0,82	3,61	1,22	2,95
0,58	2,62	1,48	3,26
1,28	2,83	0,84	2,7
0,73	2,07	0,86	1,87
1,38	2,54	0,93	2,16
1,49	2,41	0,37	0,74
0,77	2,38	0,38	1,78
1,11	3,23	0,82	2,5
0,61	2,34	-	-
0,94	2,89	-	-
0,87	1,92	-	-
Average pore sizes [mm <sup>2</sup> ]			
0,98	2,67	0,95	2,48
Standard Deviations			
0,30	0,50	0,43	1,03
Pore size increase [%]			
Glovebox CL		Fume hood CL	
171,65		162,21	

## Print Accuracy in comparison to desired 2.56mm<sup>2</sup>

	Sample 1	Sample 2	Average	St.Dev.
Post Printing	104,17	96,96	37,67	0,96
Post CL	38,35	36,98	100,56	5,09

Images printed samples incubation day 7

Sample 1 – Glovebox cross-linked (GB CL): 16 out of 25 pores printed

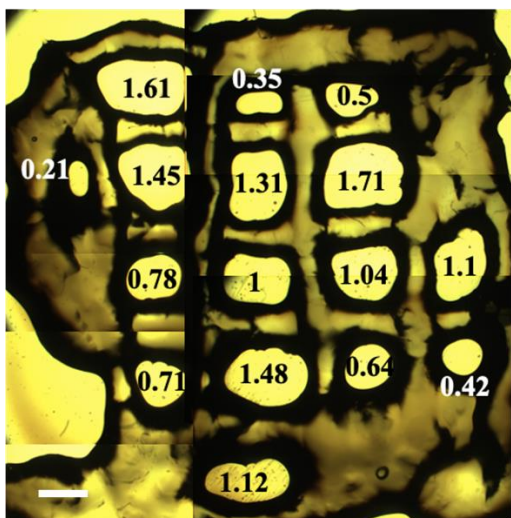


**Figure vi.5:** 1.0 wt% genipin 4% ELP printed Sample 1 after 7 days of incubation, showing measured surface area of successfully printed pores. Scale bar: 500  $\mu\text{m}$ .

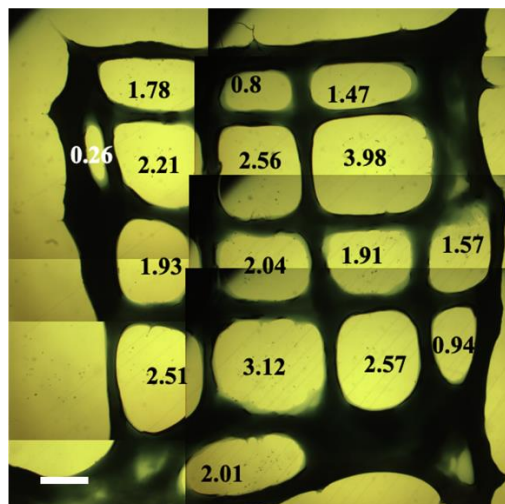


**Figure vi.6:** 1.0 wt% genipin 4% ELP printed Sample 1 after 7 days of incubation, showing measured surface area of printed pores post glovebox cross-linking. Scale bar: 500  $\mu\text{m}$ .

Sample 2 – Fume hood cross-linked (FH CL): 15 out of 25 pores printed, 16 pores post cross-linking

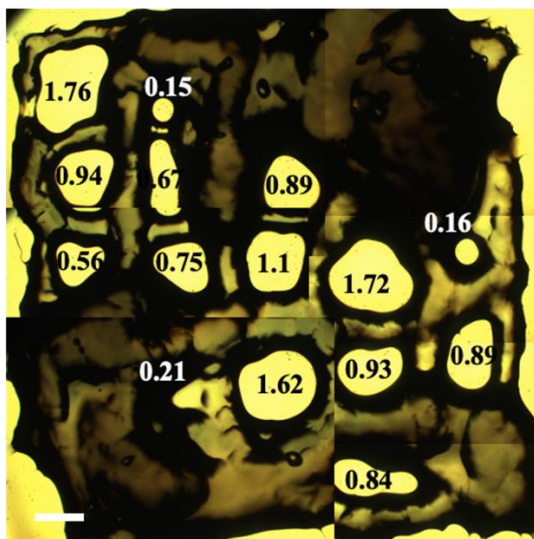


**Figure vi.7:** 1.0 wt% genipin 4% ELP printed Sample 2 after 7 days of incubation, showing measured surface area of successfully printed pores. Scale bar: 500  $\mu\text{m}$ .

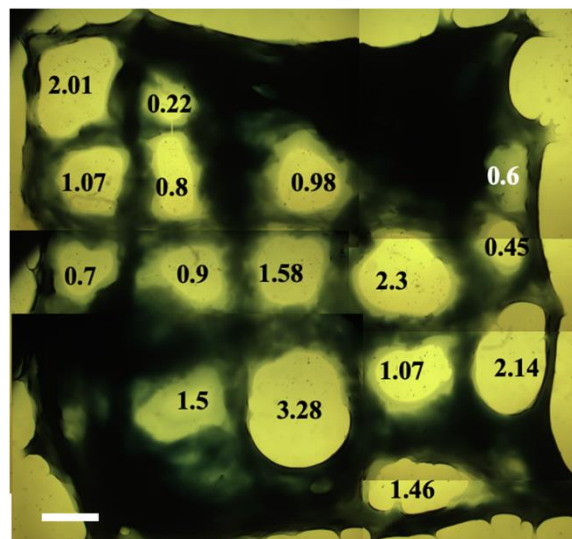


**Figure vi.8:** 1.0 wt% fenipin 4% ELP printed Sample 2 after 7 days of incubation, showing measured surface area of printed pores post fume hood cross-linking. Scale bar: 500  $\mu\text{m}$ .

## Calculations

Printed pores sizes [mm <sup>2</sup> ]			
Sample 1	GB CL	Sample 2	FH CL
1,61	1,78	1,76	2,01
0,21	0,26	0,94	1,07
1,45	2,21	0,56	0,70
0,78	1,93	0,15	0,22
0,71	2,51	0,67	0,80
0,35	2,01	0,75	0,90
1,31	0,80	0,21	1,50
1,00	2,56	0,89	0,98
1,48	2,04	1,10	1,58
1,12	3,12	1,62	3,28
0,50	1,47	1,72	2,30
1,71	3,98	0,93	1,07
1,04	1,91	0,84	1,46
0,64	2,57	0,16	0,60
1,10	1,57	0,89	0,45
0,42	0,94	0,00	2,14
Average pore sizes [mm <sup>2</sup> ]			
0,96	1,98	0,82	1,32
Standard Deviations			
0,47	0,90	0,55	0,80
Pore size increase [%]			
Glovebox CL		Fume hood CL	
105,18		59,67	

## Print Accuracy in comparison to desired 2.56mm<sup>2</sup>

	Sample 1	Sample 2	Average	St.Dev.
Post Printing	37,67	32,2	34,94	3,87
Post CL	77,29	51,42	64,36	18,3